Metal-Organic Frameworks as Templates for Highly Active Heterogeneous Catalysts

Renata Lippi

A thesis submitted for the degree of
Doctor of Philosophy

Department of Chemistry
School of Physical Sciences
The University of Adelaide

December 2017

Supervisors:

Prof. Christian J. Doonan
Dr Danielle F. Kennedy
Prof. Christopher J. Sumby

Table of contents

Abstract

Metal-organic frameworks (MOFs) are a class of porous materials, formed by inorganic nodes coordinated by organic linkers. MOFs have been extensively studied for applications in gas absorption, molecular separation, and catalysis. Recently, MOFs have been demonstrated to be excellent templates for functional materials. This work explores the use of MOFs as sacrificial templates to synthesise high performing catalysts and investigates the templating process.

Chapter 1 introduces MOFs and the advantages of their use as templates for the synthesis of functional materials, supported by examples of reported MOF-templated materials. The limited application of reducing atmosphere in MOF-templating and the lack of understanding of the templating mechanism are identified as opportunities of contribution to the field. In addition, the relevance of catalysts for renewable H_2 conversion into methane and ammonia is discussed. Lastly, high-throughput experimentation and powder X-ray diffraction are presented as tools for catalyst investigation.

Chapter 2 describes a systematic study of a manganese-based MOF and two post-synthetically metalated versions of the MOF with rhodium. The MOFs were used as precursors for CO_2 hydrogenation catalysts. The transformation of the MOFs into the active catalysts occurred under reactive conditions (80% H_2/CO_2). The structure of the MOF-templated catalysts and partially decomposed samples were characterized using a range of techniques (powder X-ray diffraction, electron microscopy, and X-ray photoelectron spectroscopy). Rh was demonstrated to assist in the templating process by decomposing the organic components of the MOF to form a mesh of Rh^0 nanoparticles and MnO or $MnCO_3$ crystals, dependent on the metalation conditions.

Chapter 3 presents a highly active CO_2 methanation catalyst derived from a Ru-impregnated zirconium MOF. In this case, after decomposition under reducing conditions (80% H_2 and 20% CO_2, at 4 bar and 350 °C), the MOF-templated catalyst was composed of Ru^0 nanoparticles evenly distributed on nano-ZrO_2 crystals. This catalyst displayed remarkable activity, with H_2 conversions of 96% and CH_4 selectivity of 99% and outperformed all tested controls, including a commercial benchmark (10 to 30% Ni/SiO_2) and samples with the same chemical composition. The structure achieved by the MOF-templating method underpined the high activity and was characterized using powder X-ray diffraction, electron microscopy and X-ray photoelectron spectroscopy.

Chapter 4 investigates how different Ru/Zr-MOF components affect the catalytic performance and final structure of the MOF-templated catalysts. In this study different organic linkers, active metals and node metal were evaluated for CO_2 methanation. In addition, in operando powder X-ray diffraction experiments clarified the phase transition during the MOF-templating of the active catalyst.

Lastly, chapter 5 extends the concept of the MOF-templating method used in Chapter 3 and 4 to a different reaction, NH_3 synthesis. A cerium MOF impregnated with ruthenium was used as catalyst precursor. The unpromoted catalyst displayed high activity at low pressures (30 and 50 bar), outperforming the tested controls. The structure was found to be composed of Ru^0 nanoparticles evenly distributed on nano-CeO_2 crystals. This synthesis route was shown to provide the catalysts with high activity by controlling the active metal distribution and final morphology.

Declaration

I certify that this work contains no material which has been accepted for the award of any other degree or diploma in my name, in any university or other tertiary institution and, to the best of my knowledge and belief, contains no material previously published or written by another person, except where due reference has been made in the text. In addition, I certify that no part of this work will, in the future, be used in a submission in my name, for any other degree or diploma in any university or other tertiary institution without the prior approval of the University of Adelaide and where applicable, any partner institution responsible for the joint-award of this degree.

I give consent to this copy of my thesis when deposited in the University Library, being made available for loan and photocopying, subject to the provisions of the Copyright Act 1968.

I acknowledge that copyright of published works contained within this thesis resides with the copyright holder(s) of those works.

I also give permission for the digital version of my thesis to be made available on the web, via the University's digital research repository, the Library Search and also through web search engines, unless permission has been granted by the University to restrict access for a period of time.

04/12/2017

Date

Acknowledgments

This work would not have been possible without the help and support of several people, to only some of whom it is possible to give particular mention here.

Above all, my deepest appreciation goes to my supervisors Dr Danielle Kennedy, Prof. Christian Doonan, and Prof. Chris Sumby for all I have learned from them and for their continuous guidance and persistent support at all stages of this work. I would also like to thank them for encouraging and helping me to shape my ideas and interests. – *Thanks!*

I would like to express my sincere gratitude to Mr. Ian Madsen for all his time dedicated mentoring me in powder X-ray diffraction technique and for his insightful comments and suggestions.

I am deeply indebted to Shaun Howard, Hector Barron, Chris Easton, Cam Coghlan, Lynne Waddington, Aaron Seeber, Yeşim Gözükara, Qinfen Gu, and Nathan Webster for their assistance and advices in many different technical aspects of this work.

I am particularly grateful for the constructive comments and warm encouragement from Ben Muir, David Alexander, Xavier Mullet and Jim Patel. I also would like to thank the Sumby-Doonan group members for the helpful conversations, our discussions always made me see my own work under a new perspective.

I offer my special thanks to my colleagues Jack Wang, Krystina Lamb, Sam Yick, Christian Vogt, Kaycee Low, Robert Madiona, Nathan Brosnahan and Ashley Murphy, for volunteering their time to assist me at beamtimes, – *you guys are legends!* – and for their technical advice and encouragement in challenging times. I am indebted to the Australian Synchrotron for beamtime grants to carry out some of the most exciting experiments of this work.

I would like to show my appreciation to the University of Adelaide for the Beacon of Enlightenment Ph.D. Scholarship and to CSIRO for the Ph.D. Top-up Scholarship, their generous support allowed me to pursue an international scientific career. It has been fantastic to be part of two renowned organisations and to have the opportunity to develop this work and meet inspiring professionals and friends.

I also would like express my gratitude to Christine, Mark, Jack and Harry Evans for hosting me in Adelaide and for making me feel part of their family. Thanks Sarah Kushinsky for our daily chats and all the support. I also thank my friends near and far for all the support regardless of the distance. Last but not least, I want to thank my parents, Irene and Alfredo Lippi, for their love and never-ending support.

Muito obrigada!

List of abbreviations

Abbreviation	**Meaning**
$[Rh(CO)_2Cl]_2$	Di-µ-chloro-tetracarbonyldirhodium(I)
Al-MIL-53	Aluminium (III) terephthalate
Ar	Argon
BDC^{2-}	Terephthalate
BET	Brunauer, Emmett and Teller method for specific surface area
BSE	Backscattered electrons
BTC^{3-}	benzene-1,3,5-tricarboxylate
C	Carbon
@C	Embedded in carbon
Ce	Cerium
CeO_2	Cerium (IV) oxide
Ce-UiO-66	Cerium (IV) terephthalate
CH_4	Methane
CO	Carbon monoxide
CO_2	Carbon dioxide
DFT	Density functional theory
DMF	N,N-Dimethylformamide
EDS	Energy dispersive spectroscopy
ESI	Eletronic supporting information a.k.a. supporting information
ex situ	"under conditions different from the process conditions"
Fe	Iron
GC	Gas chromatography
GL(30)	Peak profile with 30% Gaussian contribution and 70% Lorentzian contribution
H_2	Dihydrogen
H_2BDC	Terephthalic acid
HAADF	High-angle annular dark-field imaging
HKUST-1	Copper (II) benzene-1,3,5-tricarboxylate
HR-TEM	High-resolution transmission electron microscopy
HT	High-throughput
in situ	"under process conditions"
IWI	Incipient wetness impregnation
Lvol-IB or lvol or Lvol	Volume weighted column height calculated via integral breadth a.k.a. apparent crystallite size
M^0	Generic metal (0)
MCx	Generic metal carbide
MIL-101 or Cr-MIL-101	Chromium (III) terephthalate

Abbreviation	Meaning
Mn	Manganese
$MnCO_3$	Manganese (II) carbonate
MnMOF	MOF with Mn (II) trimers and deprotonated bis(4-(4’-carboxyphenyl)-3,5- dimethylpyrazolyl)methane ligands
MnMOF-Rh	MnMOF post-synthetically metalated with Rh (I)
MnO	Manganese (II) oxide
MOF	Metal-organic framework
MOF-5	Zinc (II) terephthalate
MOx	Generic metal oxide
MS or Mass spec	Mass spectrometry or mass spectrometer
MTcat	MOF-templated catalyst
N	Nitrogen
N_2	Dinitrogen
NH_3	Ammonia
NP	Nanoparticle
PSM	Post-synthetic modification
PSMet	Post-synthetic metalation
PtG	Power-to-Gas
PXRD	Powder X-ray diffraction
Rh	Rhodium
Ru	Ruthenium
$RuCl_3$	Ruthenium (III) chloride
S_{CH4}	Selectivity for methane
S_{CO}	Selectivity for carbon monoxide
SCXRD	Single-crystal X-ray diffraction
SEM	Scanning electron microscopy
SI	Supporting information
STEM	Scanning transmission electron microscopy
STY	Space Time Yield (mol of product per time per mass of catalyst)
TEM	Transmission electron microscopy
TGA	Thermogravimetric analysis
UiO-66	Zirconium (IV) terephthalate
WHSV	Weight-hourly space velocity (volumetric flow per mass of catalyst)
X_{CO2}	Conversion of carbon dioxide
X_{H2}	Conversion of dihydrogen
XPS	X-ray photoelectron spectroscopy
Zr	Zirconium
ZrO_2	Zirconium (IV) oxide

*Other chemical elements may be referred to by their standard symbol

Chapter 1

1. Introduction

1.1. Metal-organic frameworks

Metal-organic frameworks (MOFs) consist of inorganic nodes (metal ions or clusters) coordinated by organic linkers to form continuous two or three dimensional structures[1] (Figure 1). MOFs typically possess ultra-high porosity and pore volumes with examples showing BET specific surface areas over 6000 m^2/g.[2-3] Although MOFs are well known for their high degree of crystallinity, non-crystalline MOFs (amorphous, glass and liquid) have also been reported.[4-5] The number of new MOFs reported in the literature is growing each year as the essentially limitless combination of different inorganic nodes and organic linkers give rise to an extensive variety of topologies and the potential to tailor pore functionality.[6] MOFs are commonly synthesised using ‘one-pot’ solvothermal synthesis methods, however the functionality of the as-synthesised materials can be tuned via post-synthetic modification (PSM) techniques including, covalent functionalisation,[7] linker exchange,[8] post synthetic metalation,[9] and cation exchange at the metal node.[10]

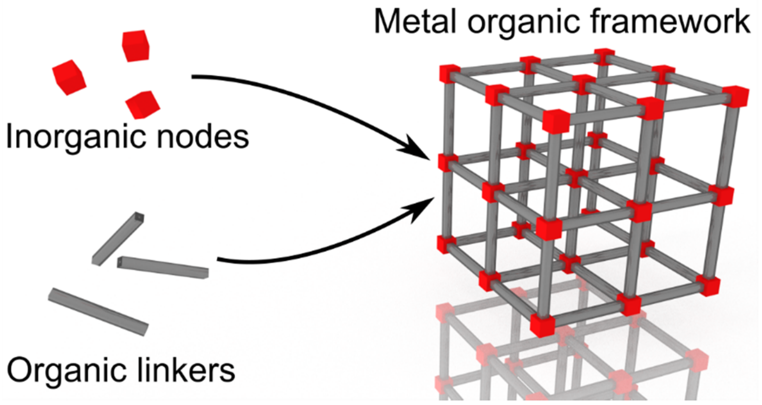

Figure 1: Scheme showing how organic and inorganic components comprise a MOF with primitive cubic (pcu) topology, such as MOF-5.

Due to their highly porous structures and tunable pore shape, size and functionality MOFs have been extensively studied for applications to molecular separation,[11] gas storage,[12-13] catalysis,[14] and drug delivery.[15]

Catalysis is an established area in MOF chemistry.[16-22] Catalysis comprises the decrease of the overall activation energy of a reaction by the interaction of the reactants with another substance, a catalyst, which is not consumed during the process, this interaction results in a decrease of the transition state energy or a reaction pathway change. Catalysts can be in the same phase as the reactants (homogeneous catalysts) or in a different phase (heterogeneous catalysts). Heterogeneous catalysis are solids that interact with reactants in the liquid phase or in the gas phase, and provide active sites that allow adsorption of reactants, formation of intermediate molecules and desorption of products. Furthermore, due to the ease of separation from the reaction medium heterogeneous catalysts make up a large proportion of catalysts employed in industrial processes.[23] The use of MOFs as heterogeneous catalysts takes advantage of their solid state and versatile structure that allow catalytically active sites to be immobilised within their framework structure whilst the porosity offers accessibility to these sites by reactant molecules and diffusion of products.

1.1.1. MOFs as heterogeneous catalysts

Catalytically active metal sites can exist in MOFs: as coordinatively unsaturated inorganic nodes; as metals bound to node or linker; and as metals confined within the framework pores (Figure 2). These possibilities are briefly discussed and exemplified in this section.

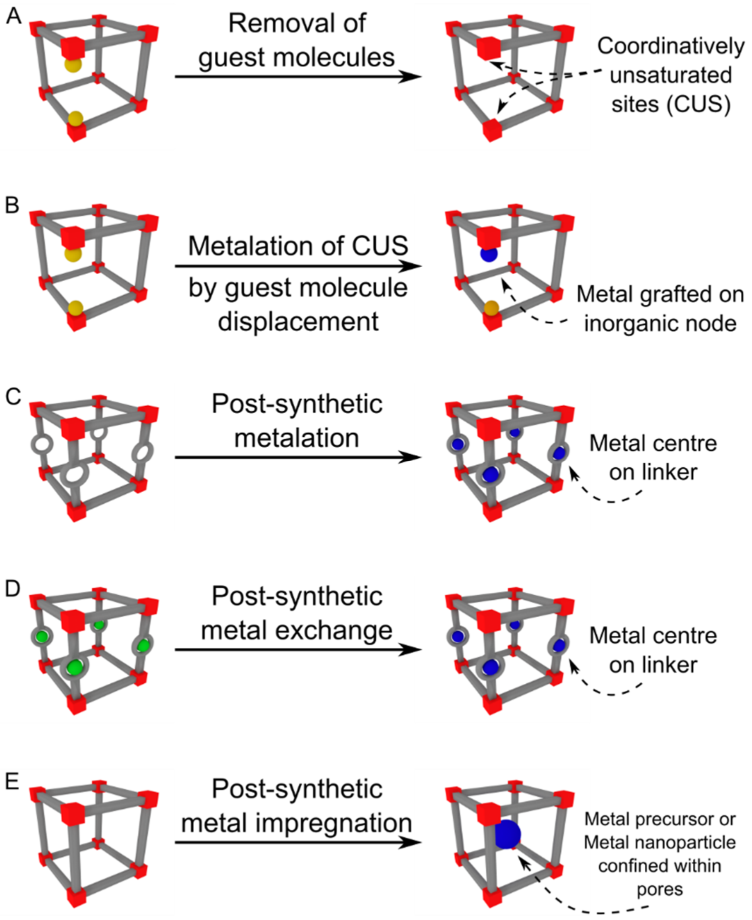

Figure 2: Examples of procedures to generate catalytically active metal sites in MOFs.

1.1.1.1. Coordinatively unsaturated sites (CUS)

A number of MOF frameworks can be synthesised that are composed of metal nodes that possess coordinatively unsaturated sites (CUS) *i.e.* they have free binding sites available for guest molecules.[7, 24] Typically these sites are occupied by non-structural solvent molecules, which when removed create an unsaturated metal site with Lewis acidic character (Figure 2A). These coordinatively unsaturated sites can be directly used as active sites for catalysis.[16, 24-26] or they can be functionalised to achieve a targeted property.[27] As an example of the former, Schlichte *et al.* have demonstrated that upon removal of water from the metal nodes of HKUST-1 (Copper (ii) benzene-1,3,5-tricarboxylate, a.k.a. Cu-BTC) the MOF acted as a Lewis acid for the activation of benzaldehyde during the cyanosilylation in heptane.[28] An example of functionalising the CUS of a metal node is represented by the post-synthetic grafting of the CUS of Cr-MIL-101. Here, ethylenediamine molecules are grafted on to unsaturated Cr sites to generate a catalyst with high activity for Knoevenagel condensation.[27] Metalation of CUS (Figure 2B) has been demonstrated for UiO-66 impregnated with vanadium. Characterisation indicated that the V^{5+} atoms were attached to the inorganic nodes of the MOF where linkers were absent.[29] Lastly, cation exchange of Zn^{2+} by Ni^{2+} at the inorganic node of MFU-4*l* has been shown to produce a highly active and selective catalyst for dimerisation of ethylene to 1-butene, the Ni-containing nodes are demonstrated to act as immobilised molecular catalysts. These examples demonstrate how CUS can act as catalytic sites or can allow organic or metallic species to bind to it in order to improve the MOF catalytic activity.

1.1.1.2. Metalated organic linkers

Metal ions bound to MOF linkers can combine the selectivity of transition metal-based homogeneous catalysts with the separation advantages of heterogeneous catalysts.[30] In order to create catalytic sites analogous to some homogeneous catalysts, one approach is the direct synthesis of a MOF using metalated linkers (Figure 2D, left).[31] Another strategy involves the introduction or exchange of metallic species in the organic linkers of a MOF by post-synthetic metalation (PSMet) techniques (Figure 2C, D).[9] A review of reactions catalysed by MOFs linkers has been reported by Mondloch *et al.*[30] A specific example of PSMet is the work of Burgun *et al.* who have used a Mn-based MOF metalated with Rh^{1+} as catalyst for the catalytic carbonylation of MeBr and MeI. In this study the immobilisation of Rh onto the linker within a highly crystalline MOF allowed the investigation of single-site catalysis by single crystal X-ray diffraction studies. The linker moiety in that system, namely bis(1-pyrazolyl)methane, is commonly used in homogeneous organometallic catalysts, *e.g.* for hydroamination,[32-33] and immobilisation of these catalysts is important for their recyclability.[34] this clearly illustrates the potential of MOFs as heterogeneous catalysts.

1.1.1.3. Metal species embedded in MOFs

The two previous sections discussed metal centres immobilised onto the framework components, however, metal species can also be confined to the MOF pores in order to produce embedded metal nanoparticles (Figure 2E).[24, 35] Catalysis using nanoparticles embedded within MOFs (NP@MOFs) take advantage of the nanoparticles catalytically active surface whilst allowing diffusion of reactants and products through the MOF pores. In addition, the framework can assist in stabilising the nanoparticles, avoiding their agglomeration or the need for coatings. Reviews[36-38] on the use of NP@MOFs for heterogeneous catalysis indicate a large interest in these composites and reveal liquid phase catalysed reactions as the focus of application of NP@MOFs catalysts. For example, Shen *et al.* have used UiO-66-NH_2 as support for Pd^0 nanoparticles to achieve the photocatalytic reduction of aqueous Cr(VI).[39] In the gas phase, Fischer's group impregnated MOF-5 with copper nanoparticles for methanol synthesis from synthesis gas (72 vol% H_2, 4 vol% CO_2, 10 vol% CO, and 14 vol% He) at 220 °C,[40-41] however, they observed the collapse of the MOF under catalytic conditions. Liang *et al.* have impregnated Al-MIL-53 with palladium nanoparticles which showed complete CO oxidation at 115 °C (reactive gas mixture containing 1 vol% CO, 21 vol% O_2 and 78 vol% Ar), however, its catalytic activity and crystallinity were affected after five cycles,[42] indicating that the catalyst was not stable under those conditions.

Independent of the location of the catalytic site, MOF catalysts have been largely tested for liquid phase catalysis and these early studies suggest that they have a huge potential for application to the synthesis of fine chemicals.[43] In contrast, reports of MOF-catalysts for gas phase reactions are usually limited to low temperature reactions and in many cases the catalysts display signs of decomposition. In addition, to their low thermal stability, MOFs commonly suffer structural damage from exposure to moisture and over wide pH ranges, mostly due to the weak coordination bonds between linkers and inorganic nodes.[44] However, very recent work has shown that the collapse of the MOF structures can yield materials with structural properties that cannot be easily accessed by other synthetic methods.

1.1.2. MOF conversion to materials

The use of MOFs as sacrificial templates (MOF-templating or MOF-mediated synthesis) for the synthesis of inorganic nanostructures has seen a rapid growth in the last few years. The hybrid composition and controlled structure of MOFs, ensures a regular arrangement of the inorganic nodes spaced by organic ligands. These extended structures can assist in the synthesis of nanoporous carbons (C), metal (M^0), metal oxides (MO_x) and their composite materials with excellent control of morphology and spatial composition. Examples of such materials have been applied for adsorption, electrochemistry and catalysis. It is worth mentioning that reports on MOF-derived materials frequently misuse the terms “pyrolysis” and “calcination” to refer to the heat-treatment used. Here, as defined by IUPAC[*], “pyrolysis” suggests heat-treatment in an inert atmosphere, whereas “calcination” is used for heat-treatment in air or oxygen-containing atmosphere.[45]

1.1.2.1. Non-catalytic MOF-derived materials

1.1.2.1.1. Carbon-containing materials

Upon collapse of the crystalline MOF structure, the organic linkers act as carbon source for the synthesis of amorphous or graphitic carbon; whereas the metal nodes may agglomerate to form more stable MO_x nanoparticles. The distance between nodes imposed by the linkers and the formation of carbon matrix may lead to a size control of the nanoparticles. Furthermore,

---

[*] International Union of Pure and Applied Chemistry

the C matrix can assist in stabilising/supporting these nanoparticles. MOF-templating can also be used for the synthesis of metal-free nanoporous carbon. For example, nanoporous carbon has been produced via pyrolysis of MOF-5, the removal of the metal occurred during the pyrolysis process as a result of the volatility of Zn at 1000 °C. At lower temperatures, ZnO is formed embedded within a porous C matrix, whilst temperature increase causes the Zn^{2+} to reduce to metal and leads to its evaporation.[†] The resulting Zn-free nanoporous carbon displayed good H_2 capture properties as well as good electrochemical properties for electrode application.[46] However, MO_x, MC_x, M^0 and C composites are the most common product of the pyrolysis of MOFs. The metal species formed depends on the temperature used and the Gibbs free energy of the reaction of the metal oxide with the present reductant.[47] An example of MO_x embedded in C is given by Banerjee *et al.* who produced high surface area Fe_3O_4@C by pyrolysis of Fe-MIL-53 in Ar. The MOF-derived material was tested as adsorbent for pollutant (oil and dye) removal with the advantage of being able to be recovered from liquids by magnetic separation.[48] The pyrolysis of Zn and Mg MOFs at 650 °C yielded their respective MO_x embedded in porous carbon; at 1000 °C, Zn-free porous carbon and MgO embedded in porous carbon, respectively. Notably, the all four derived materials retained the morphology of the parent MOFs.[49] These examples demonstrate how pyrolysis of MOFs can lead to the 'templating' of nanoporous carbon doped with metal oxides or free of metals.

1.1.2.1.2. Carbon-free materials

The removal of carbon from the MOF-derived materials can be achieved via direct calcination (air) or via two steps: pyrolysis (N_2 or Ar) followed by calcination (air). For instance, α-Fe_2O_3 anode materials for lithium battery application were obtained via two steps: pyrolysis of Fe-MIL-88 yielded particles of FeO_x@C, which upon calcination for the removal of carbon produced clusters of α-Fe_2O_3 nanoparticles. The particles of FeO_x@C and the α-Fe_2O_3

[†] Zn^0 boiling point is 907 °C

nanoparticle clusters both inherited the morphology of the parent MOF crystals. The direct calcination of Fe-MIL-88, also yielded α-Fe_2O_3 with similar morphology to the MOF, however with lower surface area and different electrochemical performance.[50] Although not discussed by the authors, assessment of the powder diffraction patterns suggests smaller hematite crystallite size via direct calcination and evidence of an additional phase (PXRD[‡] reflections at 56 °2θ and between 65 and 70 °2θ), further indicating differences between the two methods. Using the two-step synthesis approach, a 6 wt%CeO_2/CuO/Cu_2O composite was synthesised by pyrolysis followed by calcination of Ce-impregnated HKUST-1. The high level of dispersion of CeO_2 on the final composite is suggested by the lack of observable PXRD reflections for CeO_2 and superior electrochemical performance as an anode material for Li batteries.[51] Synthesis of doped MO_x have also been achieved via MOF templating where Yue *et al.* synthesised Y-doped ZrO_2 for solid oxide fuel cells electrode application. A bimetallic MOF (Zr,Y-UiO-66) underwent pyrolysis followed by calcination to yield Y-doped ZrO_2. The authors hypothesised that, firstly, ZrO_2 and Y_2O_3 are formed in a carbon matrix and then react to form the doped metal oxide.[52] Applications that require porous, mixed or doped metal oxides material, such as electrodes, may take advantage of the controlled morphology and elemental distribution that MOF-templating route offers.

1.1.2.2. MOF-derived catalysts

Inorganic heterogeneous catalysts are another class of functional materials that greatly benefit from synthetic methods that provide superior morphology and composition control. Given that traditional heterogeneous catalysts are usually composed of M^0 and MO_x moieties, the use of MOF-derived catalysts is flourishing area. Even though MOFs themselves can be used as catalysts, their low chemical and thermal stability limit their application and recyclability (as discussed in section 1.1.1). Catalytically active M^0 or MO_x species are

---

[‡] Powder X-ray diffraction

commonly supported in porous supports in order to avoid sintering of the particles whist allowing diffusion of reactants. These supports include porous C, silica, alumina, zeolites, etc. Below, some examples of C-supported and carbon-free catalysts are presented.

1.1.2.2.1. Carbon-supported MOF-derived catalysts

MOF-mediated synthesis of C-supported M^0, MO_x and/or metal carbide catalysts is usually achieved via pyrolysis of the parent MOF. Kim *et al.* firstly tested pristine HKUST-1 as an excellent catalyst for the aerobic oxidation of primary alcohols, however, the Cu-MOF displayed signs of degradation affecting its recyclability. On the other hand, pyrolysis of HKUST-1 (Ar, 800 °C, 6 h) lead to a stable Cu@C catalyst, which displayed conversions of over 90% for aerobic oxidation. After a number of runs, the catalyst could be regenerated at 800 °C under an inert atmosphere to achieve the original catalytic performance.[53] The same MOF was used as template for Cu/Cu_2O supported on porous carbon. In this example, the amount of C was increased by synthesis of a phenolic polymer within HKUST-1 prior to its pyrolysis. The final composite of $Cu/Cu_2O@C$ had ~60 wt% C and was used as a catalyst for the reduction of 4-nitrophenol to 4-aminophenol by $NaBH_4$. The MOF-derived Cu catalyst displayed higher catalytic performance than other Cu-based catalysts with turnover rate comparable to Au-based catalysts. This improved activity is believed to be combination of high loading of Cu (33 to 38 wt%) with small particle size (40 nm) supported on porous carbon.[54]

The MOF-templating synthesis method can also assist with tuning the catalysts by doping the carbon matrix and synthesising alloy nanoparticles.[55] For example, Long *et al.* decomposed mixed metal MOFs with linkers containing N and C to produce alloy nanoparticles supported on graphitic C doped with N. They observed high activity of these mixed-metal catalysts compared to single metal equivalents. The controlled-size alloy nanoparticles (20 nm) were contained in a shell of graphitic carbon doped with N. The supported Co-Ni alloy nanoparticles were tested for a range of transfer hydrogenation of nitriles achieving high conversions throughout.[56]

Metal carbides can also be produced via pyrolysis of MOFs. Pyrolysis of Fe-BTC yielded iron carbide embedded in microporous carbon, where the Fe loading and size of Fe_3C nanoparticles of Fe in the final catalyst could be reduced by impregnation of the parent MOF with furfuryl alcohol. The catalytic performance of this catalyst was superior to several reported catalysts.[57] Molybdenium carbides (MoC_x) have been prepared from mixed metal MOFs[58] or from the synthesis of MOFs in the presence of molybdenum-based polyoxometalates.[59] Both materials showed promising results for application as electrocatalysts for hydrogen evolution reaction.

Lastly, MOF-derived metal oxides embedded in porous carbon (MO_x@C) can be modified to improve its catalytic properties. The following example shows the use of several steps to fine-tune the chemistry of the final catalyst, whilst retaining the nanoporosity and metal distribution resultant from the MOF-templating method. Molybdenum phosphide embedded in porous carbon was synthesised in 4 steps: chemical vapour deposition of UiO-66 with MoO_3, pyrolysis of MoO_3/UiO-66 to yield MoO_2/ZrO_2@C; acidic leaching of ZrO_2 with $HF_{(aq)}$ resulting in MoO_2@C; and finally, MoO_2@C is reacted with PH_3 to form MoP@C. The MOF-derived catalyst exhibited high catalytic activity for hydrogen evolution reaction due to the small nanoparticles accessible via the porous matrix.[60]

Pyrolysis of MOFs can yield a range of C-supported catalysts including metal, metal oxides and metal carbides. In addition, rational design of the final catalyst can be achieved by functionalising the parent MOF or via chemical treatment of the derived material.

1.1.2.2.2. Carbon-free MOF-derived catalysts

Catalysts derived from MOFs can also be synthesised via calcination (one or two-steps), this route will generate MO_x free of carbon, as described in section 1.1.2.1.2. In this section, more complex designs of MOF-templates that have yielded sophisticated catalysts are presented.

Doped metal oxide catalysts can be synthesised using a mixed metal MOF-template. For instance, a porous catalyst consisting of K-doped CeO_2 was synthesised from the calcination of a Ce and K mixed-metal MOF (Ce:K = 3:1). The MOF-derived catalyst was used for oxidation of *o*-xylene and compared to another K-doped CeO_2 synthesised via precipitation method. The MOF-templated catalyst displayed catalytic activity far superior than the control catalyst, as a result of the nanoparticulate morphology and effective embedding of K^+ within CeO_2 crystals.[19] Another advantage of using MOFs as catalyst precursors is the possibility of controlling the elemental distribution in 3D. In a crystalline MOF, the location of the inorganic nodes is fairly accurate and functionalisation of the linkers allows the insertion of a secondary metal at defined locations within the MOF (Figure 2C, D). Therefore, the precursor will have a defined spacing between the different metals, which can lead to a great dispersion of the metals in the final catalyst. For this reason, Abney *et al.* prepared a mixed-metal MOF via post-synthetic metalation of the chelating sites of Ce-UiO-67-BIPY with Cu^{2+} and after calcination obtained CuO/CeO_2 catalysts for CO oxidation with a high level of Cu dispersion.[61] Impregnation of a MOF with a secondary metal precursor (Figure 2E) is another strategy to tailoring the composition of the templated catalyst. As illustrated by the calcination of W-impregnated UiO-66, which produced WO_x/ZrO_2 with high surface acidity and high catalytic activity for the acetalisation of benzaldehyde.[62]

In addition to thermal treatment, other methods have been applied for the templating of catalysts using MOFs. Starting with a mixed metal MOF, ZnCo-ZIF, Lan *et al.* were able to produce three different catalysts by changing the templating conditions: calcination of the ZnCo-ZIF, yielded ZnO-Co_3O_4; sulfurisation in liquid phase, yielded ZnS-CoS[§]; and calcination followed by phosphorisation was carried to synthesise Zn_3P_2-CoP. The MOF-templated materials were doped with Pt and tested for water splitting, displaying enhanced photocatalytic activity for hydrogen evolution.[63] Precursors combining MOFs and metal oxides are another route to tailor properties of the derived materials. For example, core-shell nanoparticles of hematite embedded in TiO_2 were synthesised by coating Fe-MIL-101 with TiO_2 prior to calcination. The MOF-derived photocatalyst doped with Pt had a synergistic effect on the photocatalytic activity for hydrogen evolution under visible light, whilst the separate oxides were not active under those conditions.[64]

1.1.3. Overview and challenges for MOF-derived materials

MOFs have emerged in the past two decades offering the opportunity for the rational design of materials at nanometric scale. MOFs and their derivatives have shown improvement in material performance for a range of applications. Interest in MOF-derived materials is evident by a number of very recent reviews focusing in MOF-derived materials for applications in electrochemistry[65-69] and catalysis.[47, 66, 69-71] These reviews offer several more examples of materials obtained from MOFs, categorising them by application,[65-66, 68, 71] nature of the derived material,[69-70] metal species,[47, 70] and preparation techniques.[67]

Thermal treatment has been identified as the most common method to carry out MOF-templating, and it is performed either in inert atmosphere (pyrolysis) or in oxidising atmosphere (calcination). As a general rule, pyrolysis of MOFs results in porous carbon or in carbon-supported nanoparticles of M^0, MO_x or MC_x, whereas calcination leads to the synthesis of MO_x nanoparticles (Figure 3). Pyrolysis followed by calcination, as a two-step method, also

---

[§] Carbon quantification for these samples is not available.

leads to the synthesis of MO_x nanoparticles. Even though differences in the final materials by direct and two-step calcination are not clear, at least one example shows that the two-step thermal treatment, *i.e.* pyrolysis followed by calcination, leads to higher surface area MO_x nanoparticles.[50] Porous carbon can also be prepared by leaching the metals out of MOF-derived $M^0/MO_x@C$. Interestingly, few reports have studied MOF-templating via thermal treatment in H_2 gas[72-73] and the effect that reducing conditions may have in MOF transformation is not clear.

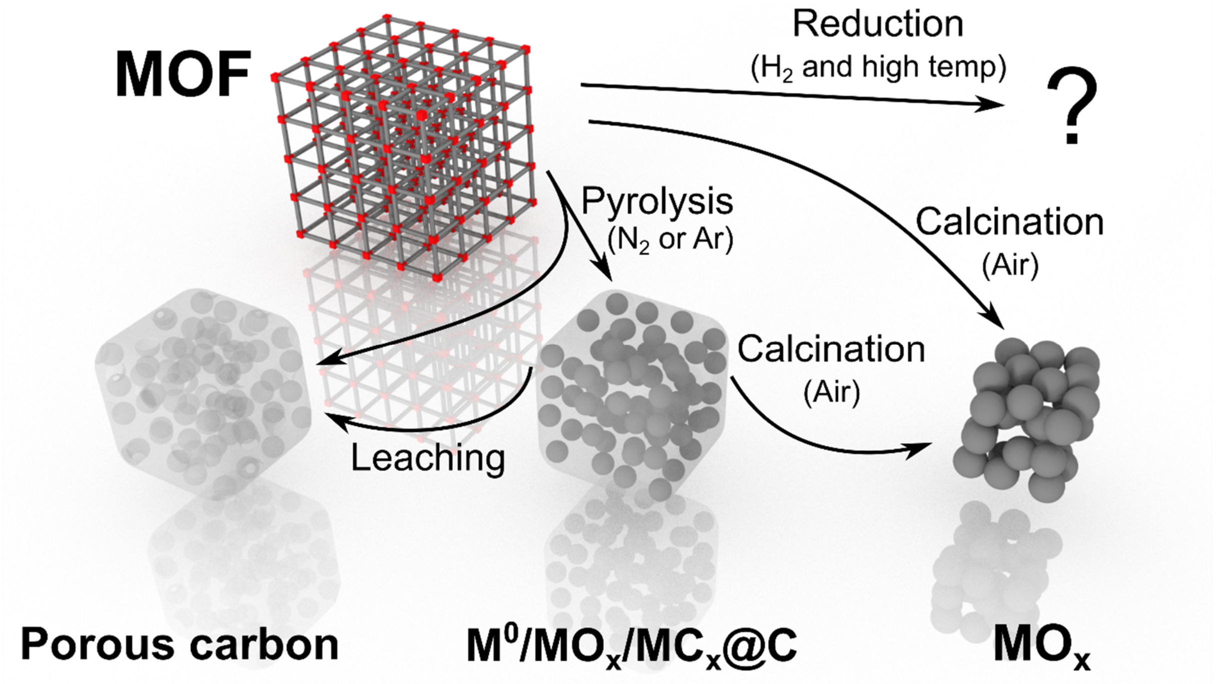

Figure 3: MOF-templating methods and the resulting materials. In general, pyrolysis of MOFs will produce metal, metal oxide and/or metal carbide nanoparticles embedded in carbon ($M^0/MO_x/MC_x@C$). Porous carbon can be synthesised from a MOF via direct pyrolysis or via pyrolysis followed by acidic leaching of the embedded metal species. Direct calcination or pyrolysis followed by calcination of the MOF results in metal oxide nanoparticles. Interestingly, the derived materials frequently retain the parent MOF topology. Thermal treatment in highly reducing conditions, *i.e.* in high concentrations of H_2 gas, have not been largely explored.

Apart from the advantages of using MOFs to produce inorganic nanomaterials, all reviews above mentioned[47, 65-71] have highlighted the current limited knowledge of the MOF-templating mechanism as a limitation in the synthesis and properties of the final material. Efforts to address this issue are exemplified by the use of *in situ* TEM and XRD with hot-stages to observe in real-time the pyrolysis of a Ni-based MOF into Ni@C. The MOF-derived catalyst displayed high catalytic activity for the reaction of 4-nitrophenol (4-NP) to 4-aminophenol (4-AP) with $NaBH_4$. The researchers observed the annealing of Ni nanoparticles, which became larger with increasing temperatures until they started detaching from the carbon matrix above 600 °C. This observation led to optimisation of the catalyst synthesis conditions.[74]

Shen *et al.* have also raised their concern with MOF-derived catalysts been limited to liquid phase reactions whilst there is also potential for application of these materials in gas phase reactions.[66] Gas phase reactions may equally benefit from controlled nanoparticle size, porosity, and elemental dispersion of these nanomaterials, as shown for the Fischer-Tropsch reaction.[57, 75] Demonstrating the opportunity for the development of catalysts for important gas phase industrial processes by MOF-templating.

The field of research on MOFs and MOF-derived materials is highly interdisciplinary, as it involves organic chemistry, structural characterisation (*e.g.* Powder X-ray diffraction), surface chemistry, and application specific knowledge (*e.g.* catalysis or electrochemistry). One of the limitations identified during this research is the lack of protocols for characterisation and testing of MOFs and MOF-derived materials. Characterisation of the materials can be frequently found to be incomplete and non-MOFs controls may not be presented for the application investigated, resulting in an incomplete understanding of the MOF-templated materials. This is pronounced by the novelty and popularity of the field.

1.2. Renewable H_2 conversion

To address climate change, shifting the global economy away from fossil resources is essential. Fossil resources are largely applied as fuels for transportation, electricity generation and in the synthesis of chemicals. Examples of fossil derived chemicals are petroleum-derived monomers for plastics production (*e.g.* polyethylene), whilst another example is H_2 gas, which is an important chemical feedstock largely produced from steam reforming of fossil natural gas. Renewables can directly replace fossil fuel-based energy and can also be employed to generate commercially important chemicals that are currently derived from the fossil fuel industry, such as H_2.

1.2.1. Energy

In the energy scenario, renewable sources are increasingly contributing to the global energy production. In Australia, renewables generated 17.3% of electricity in 2016, with the highest contribution from hydro (7.3%) and wind (5.3%).[76] In South Australia, renewable energy is largely harvested and accounts for 41.2% of the locally generated electricity (34.7% wind and 7.5% solar) with gas and coal complementing it with 36.4% and 20.9% respectively.[77] However, the intermittent electricity generation from renewable sources hinders its full potential and has caused the increasing demand for renewable energy storage systems and processes.[78] Energy generated in excess to demand at a given moment can be stored and later be made available when demand of energy is higher than the generation.

Renewable energy can be stored in batteries, as gravitational energy (pumped hydroelectricity) or in chemicals, for example.[79] Batteries have great electricity storage potential however limited availability of their components at battery-grade purity levels is anticipated to limit their applications.[80] An example of renewable energy storage in chemicals is using renewable electricity (solar or wind) to electrolyse water into H_2 and O_2; H_2 can then be stored and used as a clean fuel or as feedstock.[81]

A high volumetric energy density is a desired to facilitate storage and transportation of fuels. Hydrogen gas has a high specific energy (141.8 MJ/kg)[82], however its low volumetric mas density (0.08 kg/m^3)[83] results in a very low volumetric energy density (0.0113 MJ/L).

Increasing H_2 gas volumetric mass and energy densities requires high pressures (*e.g.* 800 bar) or extremely low temperatures, as liquid H_2 exists below -252 °C. [84] In addition, H_2 has a wide explosive and flammability range (4 to 75 vol% H_2 in air).[85] All these inherent properties of H_2 make it difficult to be stored and transported, therefore causing it to be an impractical fuel for many applications. Storage of H_2 by interaction with materials,[84] including MOFs,[12] have greatly improved the volumetric storage density. Considering these advances in storage of H_2, a transition to a hydrogen economy would require significant upgrade of the distribution and storage currently in place. Alternatively, H_2 can be converted into synthetic natural gas via CO_2 methanation using CO_2 captured from air. In the renewable energy scenario, this process is known as Power-to-Gas (PtG).[86-89] Walker *et al.* compared PtG to a number of energy storage systems, including H_2 fuel and batteries, and outlined the following advantages of synthetic natural gas from PtG systems:[90]

- Compatibility with existing natural gas infrastructure, *e.g.* distribution grids, electricity plants, motors, etc.;
- Safer storage and transportation compared to pure H_2;
- Storage for long periods of time and transportation without significant energy loss;
- Flexibility to generate electrical energy or to be used as mobility fuels;
- Higher energy density.

In order to integrate PtG to a renewable energy scenario, improvements in catalysts technology for CO_2 methanation reaction may be necessary. These include higher conversion of H_2, higher selectivity to methane (the main component of natural gas), and low operation temperature and pressure, for example.

1.2.2. Chemicals

As previously discussed, fossil-derived H_2 is an important feedstock for chemicals, particularly for ammonia synthesis. Ammonia is an important commodity for agriculture and mining, fixation of dinitrogen is achieved through the energy demanding Haber-Bosch process.

The reaction takes place over iron or ruthenium based catalysts, at pressures ranging from 100 to 300 bar and temperatures from 300 to 500 °C.[91] It is estimated that 2% of the global energy is used for the production of NH_3.[92] Currently, H_2 used in ammonia synthesis is obtained from steam reforming of natural gas, which is considered a non-expensive source for H_2. The side product of steam reforming, carbon monoxide, is then transformed into CO_2 via water-gas shift reaction before being released into the atmosphere. The large global demand for NH_3 for fertiliser production, for example, makes this process a major source of fossil-derived CO_2 emissions, estimated to contribute about 2.5% of the global emissions.[92]

Synthesising renewable H_2 is considerably more expensive than steam reforming, consequently the cost to produce NH_3 will be escalated. Therefore reduction of costs in NH_3 synthesis processes are crucial for the transition to a renewable-based economy. The development of new, more active catalysts may be the key to cost reduction by reducing the energy requirement (temperature and pressure) and improving the process conversion.

1.3. Methods for catalyst investigation

1.3.1. High-throughput experimentation

Catalysts are critical for our economy, as over 80% of chemical processes involve at least one catalytic step.[93] They are also complex materials, therefore, understanding the reaction mechanism in heterogeneous catalysis and precisely defining active sites is often challenging. Hence empirical studies are crucial for catalyst development and optimisation.

High-throughput (HT) experimentation has its origins related to combinatorial chemistry. Both combinatorial chemistry and HT experimentation are well developed methods in biochemistry,[94] a field in which these terms are often used interchangeably. However, combinatorial chemistry consists of the rational design and preparation of libraries of samples, whereas HT experimentation is the systematic and simultaneous testing of a large number of samples. Typically, HT experiments will involve parallel testing of samples providing data for multiple samples under uniform conditions in a short period of time. As heterogeneous catalysts are often multicomponent materials (combining active metal, support, and promoters), naturally, combinatorial chemistry and HT experimentation have been incorporated in catalyst research for evaluation and optimisation of these components.[93, 95-97] In addition to chemical composition, heterogeneous catalysts are also sensitive to variables such as morphology (resultant of preparation method), reaction conditions and time.

Catalyst development with high-throughput methodology can be separated in three stages: primary screening, optimisation, and scale-up.[96, 98] The first stage consists of a parallel screening of samples to identify potential catalysts. The second stage will comprise validation and optimisation of the catalysts identified in the previous stage. At this stage, variables such as composition, synthesis methods, reaction conditions and stability are optimised in a number of HT-experiments. The third stage involves scaling up of the optimised catalyst, testing at pilot plants and further developments for its commercialisation.

This work focuses on the use of HT-experimentation for the optimisation of catalysts. The catalytic tests were performed in a 48-channel catalyst testing rig with parallel fixed-bed microreactors (Figure 4). The MOF-templated catalysts discussed in this work underwent validation and optimisation experiments using this HT catalyst testing rig. The parallel testing allowed the comparison of a number of samples with different composition and in replicate, while comparing to benchmarks and other controls to validate the observed data. In addition, long-term stability tests of over 200 hours were performed simultaneously for all samples. By using microreactors, we were able to test tens of milligrams of each sample, significantly decreasing the financial investment to synthesise a large number of variant samples, otherwise impossible at the gram scale.

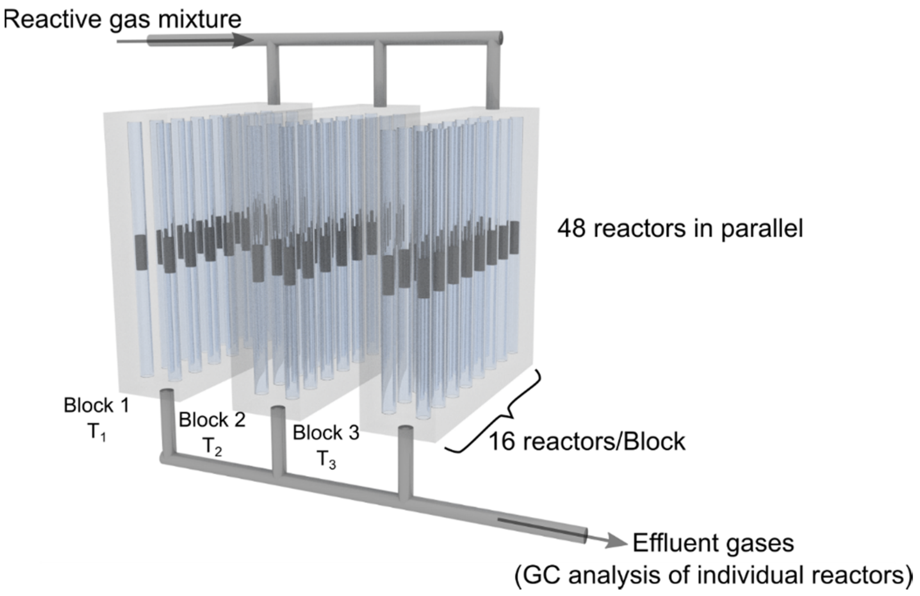

Figure 4: Illustration of 48-channel HT catalysis testing rig used in this work. The microreactors are evenly fed with the reactive gas mixture, but are divided in three temperature-independent blocks. Effluent gases are analysed using a gas chromatograph.

1.3.2. Powder X-ray diffraction (PXRD)

Powder X-ray diffraction (PXRD) is a technique based on the constructive interference of monochromatic X-rays and atoms of a crystalline material. The atoms in a crystalline structure are arranged in (hkl) planes regularly spaced (d-spacing) and scattered X-rays will present constructive interference if the incident angle and d-spacing satisfy Bragg's Law:[99]

$$2 \cdot d \cdot \sin(\theta) = n \cdot \lambda \qquad \text{(Eq. 1)}$$

Where:

- d is (hkl) interplanar spacing (d-spacing);
- θ is diffraction angle;
- n is diffraction order (n = integer);
- λ is X-ray beam wavelength.

The incidence of a monochromatic X-ray beam on a polycrystalline solid will result in a diffraction pattern of intensity versus diffraction angle (2θ). This pattern contains peaks with features such as position, intensity, width and shape, in addition to a background. These features can be analysed and correlated to composition, structure and instrument involved in the analysis as indicated in Table 1. Regarding sample information, PXRD patterns can be used for phase identification by fingerprint analysis, in which reflection positions and relative intensities are matched with the pattern of a known structure using databases; in addition, peak width can indicate the crystallite size of a phase. In a multiphase sample, the relative intensities of a phase are indicative of the amount of this phase in the sample and can be quantified via full pattern analysis methods (Appendix 1). Finally, the pattern background contains information about disordered phases, *e.g.* amorphous phases, present in the sample or in the environment.

Table 1: Relation of pattern features with analysis information, structural source and possible instrument interference.

Pattern feature	Information from analysis	Sample related factors	Instrument and experimental factors
Background	Diffuse scattering	Fluorescence; Disorder; Local structure	Air scatter; Detector noise; Sample holder
Peak position	Qualitative phase analysis; Lattice parameters	Unit cell dimensions; Macro-strain	Wavelength; Zero point error; Sample height
Intensity	Quantitative phase analysis; Crystal structure	Amount of phase; Atomic coordinates; Temperature factors; Absorption; Site occupancies	Amount of sample; Lorentz-polarisation; and others diffraction factors
Peak profile (width and shape)	Sample broadening	Size of crystallites; Micro-strain; Defects	Diffractometer geometry; Slit sizes; Type of detector; X-ray source

PXRD analysis does not require sample preparation or specific environment, and samples can be analysed at varying temperature and in controlled atmosphere, making it a great technique for *in situ* analysis. *In situ* PXRD analysis allows the study of a sample under simulated process conditions, in catalysis, it can allow the observation of a phase transition that a catalyst may undergo during activation and under reaction conditions, providing a better understanding of the active phase and its formation.

1.4. Research questions and aims

This project set out to investigate catalyst synthesis mediated by metal-organic framework templates. The research questions underlying this research are:

- Can metal nanoparticles be synthesised via MOF-templating in a H_2-containing atmosphere?
- Can MOFs assist in the synthesis of high-performing catalysts for gas phase reactions?
- What is the mechanism of MOF-templating?
- How do MOF components affect the final catalyst?

The following chapters of this thesis describe the investigation of MOF-templating for heterogeneous catalysts for CO_2 hydrogenation and NH_3 synthesis reactions.

Rhodium metal is known to be an active catalyst for CO_2 hydrogenation, morphology and dispersion control should be considered for the synthesis of high performing Rh^0 catalysts. Therefore, MOF-templating was evaluated as a new synthesis route for Rh^0 nanoparticles. Chapter 2 investigates the MOF-mediated synthesis of catalysts in a reducing atmosphere with H_2 concentrations of 5% and 80%. To ensure controlled dispersion of the Rh precursor in the template, a Mn-based MOF containing one third of its linkers with free chelating sites was selected as a template. Post synthetic metalation of these sites with Rh^{1+} species provided a homogeneous distribution of Rh throughout the template. The pristine MOF (MnMOF) and its Rh-metalated versions (MnMOF-Rh) were subjected to CO_2 hydrogenation conditions, 350 °C and 4 bar in a flow of 80% H_2 and 20% CO_2. This highly reducing condition caused the collapse of the framework samples: MnMOF-Rh produced Rh^0 nanoparticles of controlled size, the nanoparticles formed a porous mesh around larger crystals of MnO, $MnCO_3$ and other salts; whilst MnMOF formed MnO crystals embedded in a N-containing amorphous carbon phase. In addition, in a separate experiment, MnMOF and MnMOF-Rh were treated at 350 °C in 5% H_2/Ar atmosphere. The samples derived from the reduction in 5% H_2 displayed intermediate characteristics between the template MOFs and the templated catalysts. Comparison of the MOFs with the samples derived from treatment in 5% H_2 and the templated catalysts provided insights into the templating mechanism. Notably, Rh was found to assist with the removal of the organic linkers to produce the final catalysts.

The successful synthesis of metal nanoparticles of controlled size reported in Chapter 2 provided the basis to explore other catalytic systems. Accordingly, in Chapter 3 a MOF-templated Ru^0/ZrO_2 catalyst is reported. The catalyst was derived from a Ru^{3+} impregnated Zr-MOF, since Ru is known to be a highly active metal for CO_2 methanation and ZrO_2 is also known to be a good catalyst support material. The catalyst was templated under CO_2 hydrogenation conditions, 350 °C and 4 bar in a flow of 78% H_2 and 22% CO_2, and displayed remarkable conversion of reactants and selectivity for methane production. Interestingly, Ru^{3+} directly impregnated on ZrO_2 displayed inferior performance compared to the MOF-templated catalyst. Characterisation of the system demonstrated that the MOF-templated catalyst was composed of nanocrystals of ZrO_2 nanocrystals decorated with Ru^0 nanoparticles. The excellent morphological control provided by the MOF-templating underpinned the high performance of the catalyst.

Chapter 4 examines the templating mechanism of Ru^0/ZrO_2 catalyst described in the previous chapter. The phase transition from MOF into the templated catalyst was studied in an *in operando* PXRD experiment. The collapse of the MOF formed an amorphous phase which crystallised into ZrO_2 at higher temperatures. In addition, catalytic performance was evaluated by the analysis of the effluent gas composition and indicated no methane production for the amorphous phase and increasing production during the formation of ZrO_2. This chapter also demonstrates that the Ru^0 NPs on the MOF were present in an amorphous phase and that heat treatment of the template MOF in 5% H_2/Ar produced crystalline RuO_2 with poor catalytic performance. The effect of MOF components on the templating of the catalyst was studied by testing and characterising samples derived from template MOFs with different linkers, Ru loadings, impregnated metals and MOF node.

To evaluate the MOF-templating technique for a different gas phase reaction, Chapter 5 expands the MOF-templating route described in the previous chapters for the production of catalysts for ammonia synthesis reaction. MOF-templated catalysts Ru/ZrO_2 and Ru/CeO_2 were evaluated for ammonia synthesis alongside a commercial Fe-based catalyst. The MOF-templated catalyst Ru/CeO_2 was activated under NH_3 synthesis conditions, at 400 °C and 10 bar in a flow of 75%H_2 and 25%N_2, and studied for lower pressures in parallel with Ru-based non-MOF controls. The MOF-templated catalyst displayed remarkable activity at 30 and 50 bar, outperforming a benchmark catalyst by producing higher amounts of NH_3 per mass of Ru. This exemplifies the potential of MOF-templating under reducing conditions to obtain highly active catalysts owing to the synthesis of metal nanoparticles of controlled size.

1.5. References

1. Batten, S. R.; Champness, N. R.; Chen, X. M.; Garcia-Martinez, J.; Kitagawa, S.; Ohrstrom, L.; O'Keeffe, M.; Suh, M. P.; Reedijk, J., Terminology of Metal-Organic Frameworks and Coordination Polymers (Iupac Recommendations 2013). *Pure Appl. Chem.* **2013**, *85*, 1715-1724.

2. Peng, Y.; Krungleviciute, V.; Eryazici, I.; Hupp, J. T.; Farha, O. K.; Yildirim, T., Methane Storage in Metal–Organic Frameworks: Current Records, Surprise Findings, and Challenges. *J. Am. Chem. Soc.* **2013**, *135*, 11887-11894.

3. Mason, J. A.; Veenstra, M.; Long, J. R., Evaluating Metal-Organic Frameworks for Natural Gas Storage. *Chem. Sci.* **2014**, *5*, 32-51.

4. Bennett, T. D., et al., Melt-Quenched Glasses of Metal–Organic Frameworks. *J. Am. Chem. Soc.* **2016**, *138*, 3484-3492.

5. Bennett, T. D.; Cheetham, A. K., Amorphous Metal–Organic Frameworks. *Acc. Chem. Res.* **2014**, *47*, 1555-1562.

6. Chung, Y. G.; Camp, J.; Haranczyk, M.; Sikora, B. J.; Bury, W.; Krungleviciute, V.; Yildirim, T.; Farha, O. K.; Sholl, D. S.; Snurr, R. Q., Computation-Ready, Experimental Metal–Organic Frameworks: A Tool to Enable High-Throughput Screening of Nanoporous Crystals. *Chem. Mater.* **2014**, *26*, 6185-6192.

7. Cohen, S. M., Postsynthetic Methods for the Functionalization of Metal-Organic Frameworks. *Chem. Rev.* **2012**, *112*, 970-1000.

8. Kim, M.; Cahill, J. F.; Su, Y.; Prather, K. A.; Cohen, S. M., Postsynthetic Ligand Exchange as a Route to Functionalization of 'Inert' Metal–Organic Frameworks. *Chem. Sci.* **2012**, *3*, 126.

9. Evans, J. D.; Sumby, C. J.; Doonan, C. J., Post-synthetic Metalation of Metal-Organic Frameworks. *Chem. Soc. Rev.* **2014**, *43*, 5933-5951.

10. Kim, M.; Cahill, J. F.; Fei, H. H.; Prather, K. A.; Cohen, S. M., Postsynthetic Ligand and Cation Exchange in Robust Metal-Organic Frameworks. *J. Am. Chem. Soc.* **2012**, *134*, 18082-18088.

11. Li, J.-R.; Sculley, J.; Zhou, H.-C., Metal–Organic Frameworks for Separations. *Chem. Rev.* **2011**, *112*, 869-932.

12. Suh, M. P.; Park, H. J.; Prasad, T. K.; Lim, D.-W., Hydrogen Storage in Metal–Organic Frameworks. *Chem. Rev.* **2011**, *112*, 782-835.

13. He, Y.; Zhou, W.; Qian, G.; Chen, B., Methane Storage in Metal-Organic Frameworks. *Chem. Soc. Rev.* **2014**, *43*, 5657-5678.

14. García-García, P.; Müller, M.; Corma, A., MOF Catalysis in Relation to Their Homogeneous Counterparts and Conventional Solid Catalysts. *Chem. Sci.* **2014**.

15. Tan, L.-L.; Li, H.; Qiu, Y.-C.; Chen, D.-X.; Wang, X.; Pan, R.-Y.; Wang, Y.; Zhang, S. X.-A.; Wang, B.; Yang, Y.-W., Stimuli-Responsive Metal-Organic Frameworks Gated by Pillar[5]Arene Supramolecular Switches. *Chem. Sci.* **2015**, *6*, 1640-1644.

16. Liu, J.; Chen, L.; Cui, H.; Zhang, J.; Zhang, L.; Su, C.-Y., Applications of Metal-Organic Frameworks in Heterogeneous Supramolecular Catalysis. *Chem. Soc. Rev.* **2014**, *43*, 6011-6061.

17. Zhu, L.; Liu, X.-Q.; Jiang, H.-L.; Sun, L.-B., Metal–Organic Frameworks for Heterogeneous Basic Catalysis. *Chem. Rev.* **2017**, *117*, 8129-8176.

18. Huang, Y.-B.; Liang, J.; Wang, X.-S.; Cao, R., Multifunctional Metal-Organic Framework Catalysts: Synergistic Catalysis and Tandem Reactions. *Chem. Soc. Rev.* **2017**, *46*, 126-157.

19. Wang, H.; Liu, M.; Guo, S.; Wang, Y.; Han, X.; Bai, Y., Efficient Oxidation of O-Xylene over CeO2 Catalyst Prepared from a Ce-MOF Template: The Promotion of K+ Embedding Substitution. *Mol. Catal.* **2017**, *436*, 120-127.

20. Cirujano, F. G., MOFs Vs Zeolites: Carbonyl Activation with M(Iv) Catalytic Sites. *Catal. Sci. Technol.* **2017**.

21. Zhao, M.; Ou, S.; Wu, C.-D., Porous Metal–Organic Frameworks for Heterogeneous Biomimetic Catalysis. *Acc. Chem. Res.* **2014**, *47*, 1199-1207.

22. Furukawa, H.; Cordova, K. E.; O'Keeffe, M.; Yaghi, O. M., The Chemistry and Applications of Metal-Organic Frameworks. *Science* **2013**, *341*, 1230444.

23. Dumesic, J. A.; Huber, G. W.; Boudart, M., Principles of Heterogeneous Catalysis. In *Handbook of Heterogeneous Catalysis*, Ertl, G.; Knözinger, H.; Schüth, F.; Weitkamp, J., Eds. Wiley-VCH Verlag GmbH & Co. KGaA: 2008.

24. Gascon, J.; Corma, A.; Kapteijn, F.; Xamena, F. X. L. I., Metal Organic Framework Catalysis: Quo Vadis? *ACS Catal.* **2014**, *4*, 361-378.

25. Fujita, M.; Kwon, Y. J.; Washizu, S.; Ogura, K., Preparation, Clathration Ability, and Catalysis of a Two-Dimensional Square Network Material Composed of Cadmium(Ii) and 4,4'-Bipyridine. *J. Am. Chem. Soc.* **1994**, *116*, 1151-1152.

26. Vermoortele, F.; Valvekens, P.; De Vos, D., Chapter 8 Catalysis at the Metallic Nodes of MOFs. In *Metal Organic Frameworks as Heterogeneous Catalysts*, The Royal Society of Chemistry: 2013; pp 268-288.

27. Hwang, Y. K.; Hong, D. Y.; Chang, J. S.; Jhung, S. H.; Seo, Y. K.; Kim, J.; Vimont, A.; Daturi, M.; Serre, C.; Ferey, G., Amine Grafting on Coordinatively Unsaturated Metal Centers of MOFs: Consequences for Catalysis and Metal Encapsulation. *Angew. Chem. Int. Ed.* **2008**, *47*, 4144-4148.

28. Schlichte, K.; Kratzke, T.; Kaskel, S., Improved Synthesis, Thermal Stability and Catalytic Properties of the Metal-Organic Framework Compound Cu3(BTC)(2). *Microporous Mesoporous Mater.* **2004**, *73*, 81-88.

29. Nguyen, H. G. T.; Schweitzer, N. M.; Chang, C. Y.; Drake, T. L.; So, M. C.; Stair, P. C.; Farha, O. K.; Hupp, J. T.; Nguyen, S. T., Vanadium-Node-Functionalized UiO-66: A Thermally Stable MOF-Supported Catalyst for the Gas-Phase Oxidative Dehydrogenation of Cyclohexene. *ACS Catal.* **2014**, *4*, 2496-2500.

30. Mondloch, J. E.; Farha, O. K.; Hupp, J. T., Chapter 9 Catalysis at the Organic Ligands. In *Metal Organic Frameworks as Heterogeneous Catalysts*, The Royal Society of Chemistry: 2013; pp 289-309.

31. Kitagawa, S.; Noro, S.-i.; Nakamura, T., Pore Surface Engineering of Microporous Coordination Polymers. *Chem. Commun.* **2006**, 701-707.

32. Burling, S.; Field, L. D.; Messerle, B. A.; Rumble, S. L., Late Transition Metal Catalyzed Intramolecular Hydroamination: The Effect of Ligand and Substrate Structure. *Organometallics* **2007**, *26*, 4335-4343.

33. Kennedy, D. F.; Messerle, B. A.; Rumble, S. L., Application of Uv-Vis Spectroscopy to High Throughput Screening of Hydroamination Catalysts. *New J. Chem.* **2009**, *33*, 818-824.

34. Tregubov, A. A.; Vuong, K. Q.; Luais, E.; Gooding, J. J.; Messerle, B. A., Rh(I) Complexes Bearing N,N and N,P Ligands Anchored on Glassy Carbon Electrodes: Toward Recyclable Hydroamination Catalysts. *J. Am. Chem. Soc.* **2013**, *135*, 16429-16437.

35. El-Shall, M. S.; Abdelsayed, V.; Khder, A. E. R. S.; Hassan, H. M. A.; El-Kaderi, H. M.; Reich, T. E., Metallic and Bimetallic Nanocatalysts Incorporated into Highly Porous Coordination Polymer Mil-101. *J. Mater. Chem.* **2009**, *19*, 7625-7631.

36. Aijaz, A.; Xu, Q., Catalysis with Metal Nanoparticles Immobilized within the Pores of Metal–Organic Frameworks. *J. Phys. Chem. Lett.* **2014**, *5*, 1400-1411.

37. Rosler, C.; Fischer, R. A., Metal-Organic Frameworks as Hosts for Nanoparticles. *CrystEngComm* **2015**.

38. Yang, Q.; Xu, Q.; Jiang, H.-L., Metal-Organic Frameworks Meet Metal Nanoparticles: Synergistic Effect for Enhanced Catalysis. *Chem. Soc. Rev.* **2017**, *46*, 4774-4808.

39. Shen, L. J.; Wu, W. M.; Liang, R. W.; Lin, R.; Wu, L., Highly Dispersed Palladium Nanoparticles Anchored on UiO-66(NH2) Metal-Organic Framework as a Reusable and Dual Functional Visible-Light-Driven Photocatalyst. *Nanoscale* **2013**, *5*, 9374-9382.

40. Hermes, S.; Schroter, M. K.; Schmid, R.; Khodeir, L.; Muhler, M.; Tissler, A.; Fischer, R. W.; Fischer, R. A., Metal@MOF: Loading of Highly Porous Coordination Polymers Host Lattices by Metal Organic Chemical Vapor Deposition. *Angew. Chem. Int. Ed.* **2005**, *44*, 6237-6241.

41. Muller, M.; Hermes, S.; Kaehler, K.; van den Berg, M. W. E.; Muhler, M.; Fischer, R. A., Loading of MOF-5 with Cu and ZnO Nanoparticles by Gas-Phase Infiltration with Organometallic Precursors: Properties of Cu/ZnO@MOF-5 as Catalyst for Methanol Synthesis. *Chem. Mater.* **2008**, *20*, 4576-4587.

42. Liang, Q.; Zhao, Z.; Liu, J.; Wei, Y. C.; Jiang, G. Y.; Duan, A. J., Pd Nanoparticles Deposited on Metal-Organic Framework of Mil-53(Al): An Active Catalyst for CO Oxidation. *Acta Phys. Chim. Sin.* **2014**, *30*, 129-134.

43. Dhakshinamoorthy, A.; Opanasenko, M.; Cejka, J.; Garcia, H., Metal Organic Frameworks as Heterogeneous Catalysts for the Production of Fine Chemicals. *Catal. Sci. Technol.* **2013**, *3*, 2509-2540.

44. Howarth, A. J.; Liu, Y.; Li, P.; Li, Z.; Wang, T. C.; Hupp, J. T.; Farha, O. K., Chemical, Thermal and Mechanical Stabilities of Metal–Organic Frameworks. *Nat. Rev. Mater.* **2016**, *1*, 15018.

45. *Iupac: Compendium of Chemical Terminology,* 2nd ed.; Blackwell Scientific Publications: Oxford, 1997.

46. Liu, B.; Shioyama, H.; Akita, T.; Xu, Q., Metal-Organic Framework as a Template for Porous Carbon Synthesis. *J. Am. Chem. Soc.* **2008**, *130*, 5390-5391.

47. Oar-Arteta, L.; Wezendonk, T.; Sun, X.; Kapteijn, F.; Gascon, J., Metal Organic Frameworks as Precursors for the Manufacture of Advanced Catalytic Materials. *Mater. Chem. Front.* **2017**, *1*, 1709-1745.

48. Banerjee, A.; Gokhale, R.; Bhatnagar, S.; Jog, J.; Bhardwaj, M.; Lefez, B.; Hannoyer, B.; Ogale, S., MOF Derived Porous Carbon-Fe3O4 Nanocomposite as a High Performance, Recyclable Environmental Superadsorbent. *J. Mater. Chem.* **2012**, *22*, 19694-19699.

49. He, Y.; Shang, J.; Zhao, Q.; Gu, Q.; Xie, K.; Li, G.; Singh, R.; Xiao, P.; Webley, P. A., A Comparative Study on Conversion of Porous and Non-Porous Metal–Organic Frameworks (MOFs) into Carbon-Based Composites for Carbon Dioxide Capture. *Polyhedron* **2016**, *120*, 30-35.

50. Xu, X.; Cao, R.; Jeong, S.; Cho, J., Spindle-Like Mesoporous A-Fe2O3 Anode Material Prepared from MOF Template for High-Rate Lithium Batteries. *Nano Lett.* **2012**, *12*, 4988-4991.

51. Wang, L.; Wang, X.; Meng, Z.; Hou, H.; Chen, B., MOF-Templated Thermolysis for Porous Cuo/Cu2O@CeO2 Anode Material of Lithium-Ion Batteries with High Rate Performance. *J. Mater. Sci.* **2017**, *52*, 7140-7148.

52. Yue, Z.; Liu, S.; Liu, Y., Yttria Stabilized Zirconia Derived from Metal-Organic Frameworks. *RSC Adv.* **2015**, *5*, 10619-10622.

53. Kim, B. R.; Oh, J. S.; Kim, J.; Lee, C. Y., Robust Aerobic Alcohol Oxidation Catalyst Derived from Metal–Organic Frameworks. *Catal. Lett.* **2016**, *146*, 734-743.

54. Niu, H. Y.; Liu, S. L.; Cai, Y. Q.; Wu, F. C.; Zhao, X. L., MOF Derived Porous Carbon Supported Cu/Cu2O Composite as High Performance Non-Noble Catalyst. *Microporous Mesoporous Mater.* **2016**, *219*, 48-53.

55. Wang, X.; Fan, X.; Lin, H.; Fu, H.; Wang, T.; Zheng, J.; Li, X., An Efficient Co-N-C Oxygen Reduction Catalyst with Highly Dispersed Co Sites Derived from a Znco Bimetallic Zeolitic Imidazolate Framework. *RSC Adv.* **2016**, *6*, 37965-37973.

56. Long, J.; Shen, K.; Chen, L.; Li, Y., Multimetal-MOF-Derived Transition Metal Alloy NPs Embedded in an N-Doped Carbon Matrix: Highly Active Catalysts for Hydrogenation Reactions. *J. Mater. Chem. A* **2016**, *4*, 10254-10262.

57. Santos, V. P., et al., Metal Organic Framework-Mediated Synthesis of Highly Active and Stable Fischer-Tropsch Catalysts. *Nat. Commun.* **2015**, *6*, 6451.

58. Xu, X. B.; Nosheen, F.; Wang, X., Ni-Decorated Molybdenum Carbide Hollow Structure Derived from Carbon-Coated Metal-Organic Framework for Electrocatalytic Hydrogen Evolution Reaction. *Chem. Mater.* **2016**, *28*, 6313-6320.

59. Wu, H. B.; Xia, B. Y.; Yu, L.; Yu, X.-Y.; Lou, X. W., Porous Molybdenum Carbide Nano-Octahedrons Synthesized via Confined Carburization in Metal-Organic Frameworks for Efficient Hydrogen Production. *Nat. Commun.* **2015**, *6*, 6512.

60. Yang, J.; Zhang, F.; Wang, X.; He, D.; Wu, G.; Yang, Q.; Hong, X.; Wu, Y.; Li, Y., Porous Molybdenum Phosphide Nano-Octahedrons Derived from Confined Phosphorization in Uio-66 for Efficient Hydrogen Evolution. *Angew. Chem. Int. Ed.* **2016**, *55*, 12854-12858.

61. Abney, C. W.; Patterson, J. T.; Gilhula, J. C.; Wang, L.; Hensley, D. K.; Chen, J.; Foo, G. S.; Wu, Z.; Dai, S., Controlling Interfacial Properties in Supported Metal Oxide Catalysts through Metal-Organic Framework Templating. *J. Mater. Chem. A* **2017**, *5*, 13565-13572.

62. Wang, P.; Feng, J.; Zhao, Y.; Wang, S.; Liu, J., MOF-Derived Tungstated Zirconia as Strong Solid Acids toward High Catalytic Performance for Acetalization. *ACS Appl. Mater. Interfaces* **2016**, *8*, 23755-23762.

63. Lan, M.; Guo, R.-M.; Dou, Y.; Zhou, J.; Zhou, A.; Li, J.-R., Fabrication of Porous Pt-Doping Heterojunctions by Using Bimetallic MOF Template for Photocatalytic Hydrogen Generation. *Nano Energy* **2017**, *33*, 238-246.

64. deKrafft, K. E.; Wang, C.; Lin, W., Metal-Organic Framework Templated Synthesis of Fe2O3/TiO2 Nanocomposite for Hydrogen Production. *Adv. Mater.* **2012**, *24*, 2014-2018.

65. Xia, W.; Mahmood, A.; Zou, R.; Xu, Q., Metal-Organic Frameworks and Their Derived Nanostructures for Electrochemical Energy Storage and Conversion. *Energy Environ. Sci.* **2015**, *8*, 1837-1866.

66. Shen, K.; Chen, X.; Chen, J.; Li, Y., Development of MOF-Derived Carbon-Based Nanomaterials for Efficient Catalysis. *ACS Catal.* **2016**, *6*, 5887-5903.

67. Cao, X.; Tan, C.; Sindoro, M.; Zhang, H., Hybrid Micro-/Nano-Structures Derived from Metal-Organic Frameworks: Preparation and Applications in Energy Storage and Conversion. *Chem. Soc. Rev.* **2017**, *46*, 2660-2677.

68. Xie, Z.; Xu, W.; Cui, X.; Wang, Y., Recent Progress in Metal–Organic Frameworks and Their Derived Nanostructures for Energy and Environmental Applications. *ChemSusChem* **2017**, *10*, 1645-1663.

69. Kaneti, Y. V.; Tang, J.; Salunkhe, R. R.; Jiang, X. C.; Yu, A. B.; Wu, K. C. W.; Yamauchi, Y., Nanoarchitectured Design of Porous Materials and Nanocomposites from Metal-Organic Frameworks. *Adv. Mater.* **2017**, *29*.

70. Song, Y.; Li, X.; Sun, L.; Wang, L., Metal/Metal Oxide Nanostructures Derived from Metal-Organic Frameworks. *RSC Adv.* **2015**, *5*, 7267-7279.

71. Zhao, S.-N.; Song, X.-Z.; Song, S.-Y.; Zhang, H.-j., Highly Efficient Heterogeneous Catalytic Materials Derived from Metal-Organic Framework Supports/Precursors. *Coord. Chem. Rev.* **2017**, *337*, 80-96.

72. Chen, D.; Huang, M.; He, S.; He, S.; Ding, L.; Wang, Q.; Yu, S.; Miao, S., Ru-MOF Enwrapped by Montmorillonite for Catalyzing Benzene Hydrogenation. *Appl. Clay Sci.* **2016**, *119*, 109-115.

73. Wang, Z.; Li, X.; Yang, Y.; Cui, Y.; Pan, H.; Wang, Z.; Chen, B.; Qian, G., Highly Dispersed Beta-Nis Nanoparticles in Porous Carbon Matrices by a Template Metal-Organic Framework Method for Lithium-Ion Cathode. *J. Mater. Chem. A* **2014**, *2*, 7912-7916.

74. Xu, D.; Pan, Y.; Chen, M.; Pan, Q.; Zhu, L.; Xue, M.; Zhang, D.; Fang, Q.; Qiu, S., Synthesis and Application of a MOF-Derived Ni@C Catalyst by the Guidance from an in Situ Hot Stage in Tem. *RSC Adv.* **2017**, *7*, 26377-26383.

75. An, B.; Cheng, K.; Wang, C.; Wang, Y.; Lin, W., Pyrolysis of Metal–Organic Frameworks to Fe3O4@Fe5C2 Core–Shell Nanoparticles for Fischer–Tropsch Synthesis. *ACS Catal.* **2016**, *6*, 3610-3618.

76. *Clean Energy Australia Report*; Clean Energy Council: 2016.

77. *South Australian Electricity Report*; Australia Energy Market Operator: 2016.

78. Tarca, S.; Roughan, M.; Ertugrul, N.; Bean, N., Dispatchability of Wind Power with Battery Energy Storage in South Australia. *Energy Procedia* **2017**, *110*, 223-228.

79. Ibrahim, H.; Ilinca, A.; Perron, J., Energy Storage Systems—Characteristics and Comparisons. *Renew. Sustainable Energy Rev.* **2008**, *12*, 1221-1250.

80. Olivetti, E. A.; Ceder, G.; Gaustad, G. G.; Fu, X., Lithium-Ion Battery Supply Chain Considerations: Analysis of Potential Bottlenecks in Critical Metals. *Joule* **2017**, *1*, 229-243.

81. Shaner, M. R.; Atwater, H. A.; Lewis, N. S.; McFarland, E. W., A Comparative Technoeconomic Analysis of Renewable Hydrogen Production Using Solar Energy. *Energy Environ. Sci.* **2016**, *9*, 2354-2371.

82. Probstein, R. F.; Hicks, R. E., *Synthetic Fuels*; Courier Corporation, 2006.

83. *Crc Handbook of Chemistry and Physics*, 98th ed.; CRC Press, 1977.

84. Züttel, A., Materials for Hydrogen Storage. *Materials Today* **2003**, *6*, 24-33.

85. White, A. G., Cccxxv.-Limits for the Propagation of Flame in Inflammable Gas-Air Mixtures. Part I. Mixtures of Air and One Gas at the Ordinary Temperature and Pressure. *Journal of the Chemical Society, Transactions* **1924**, *125*, 2387-2396.

86. Gillessen, B.; Heinrichs, H. U.; Stenzel, P.; Linssen, J., Hybridization Strategies of Power-to-Gas Systems and Battery Storage Using Renewable Energy. *Int. J. Hydrogen Energy* **2017**, *42*, 13554-13567.

87. Götz, M.; Lefebvre, J.; Mörs, F.; McDaniel Koch, A.; Graf, F.; Bajohr, S.; Reimert, R.; Kolb, T., Renewable Power-to-Gas: A Technological and Economic Review. *Renew. Energy* **2016**, *85*, 1371-1390.

88. Gutierrez-Martin, F.; Rodriguez-Anton, L. M., Power-to-Sng Technology for Energy Storage at Large Scales. *Int. J. Hydrogen Energy* **2016**, *41*, 19290-19303.

89. Walspurger, S.; Haije, W. G.; Louis, B., CO2 Reduction to Substitute Natural Gas: Toward a Global Low Carbon Energy System. *Isr. J. Chem.* **2014**, *54*, 1432-1442.

90. Walker, S. B.; Mukherjee, U.; Fowler, M.; Elkamel, A., Benchmarking and Selection of Power-to-Gas Utilizing Electrolytic Hydrogen as an Energy Storage Alternative. *Int. J. Hydrogen Energy* **2016**, *41*, 7717-7731.

91. van der Ham, C. J. M.; Koper, M. T. M.; Hetterscheid, D. G. H., Challenges in Reduction of Dinitrogen by Proton and Electron Transfer. *Chem. Soc. Rev.* **2014**, *43*, 5183-5191.

92. Pfromm, P. H., Towards Sustainable Agriculture: Fossil-Free Ammonia. *J. Renew. Sustain. Energy* **2017**, *9*.

93. Farrusseng, D., High-Throughput Heterogeneous Catalysis. *Surf. Sci. Rep.* **2008**, *63*, 487-513.

94. Liu, R.; Li, X.; Lam, K. S., Combinatorial Chemistry in Drug Discovery. *Curr. Opin. Chem. Biol.* **2017**, *38*, 117-126.

95. Hendershot, R. J.; Snively, C. M.; Lauterbach, J., High-Throughput Heterogeneous Catalytic Science. *Chemistry: A European Journal* **2005**, *11*, 806-814.

96. Turner, H. W.; Volpe, A. F.; Weinberg, W. H., High-Throughput Heterogeneous Catalyst Research. *Surf Sci* **2009**, *603*, 1763-1769.

97. Newsam, J. M.; Schuth, F., Combinatorial Approaches as a Component of High-Throughput Experimentation (Hte) in Catalysis Research. *Biotechnol. Bioeng.* **1999**, *61*, 203-216.

98. Moulijn, J. A.; Pérez-Ramírez, J.; Berger, R. J.; Hamminga, G.; Mul, G.; Kapteijn, F., High-Throughput Experimentation in Catalyst Testing and in Kinetic Studies for Heterogeneous Catalysis. *Catal. Today* **2003**, *81*, 457-471.

99. Bragg, W. L., The Diffraction of Short Electromagnetic Waves by Crystals. *Proceedings of the Cambridge Philosophical Society* **1913**, 43-57.

Chapter 2

Insights into MOF-templating of Rh^0 nanoparticles under reducing conditions

Renata Lippi,[†‡] Campbell J. Coghlan,[†] Shaun C. Howard,[‡] Christopher D. Easton,[‡]
Qinfen Gu,[§] Christopher J. Sumby,[†] Danielle F. Kennedy,*[‡] Christian J. Doonan*[†]

[†]Centre for Advanced Nanomaterials, Department of Chemistry, The University of Adelaide, Adelaide, South Australia 5005, Australia.
[‡]CSIRO Manufacturing, Clayton, Victoria 3168, Australia.
[§]Australian Synchrotron, Clayton, Victoria 3168, Australia.

Manuscript to be submitted

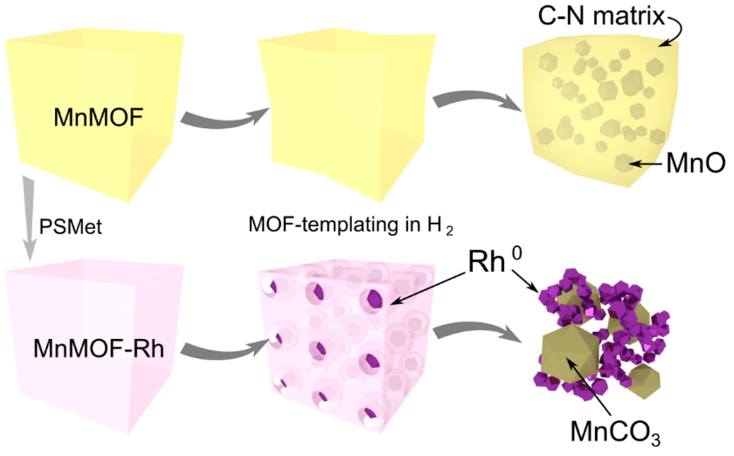

2.1. Summary

Rhodium is a catalyst of interest for a range of reactions, including CO_2 hydrogenation. The research presented in this chapter investigates MOF-templating of a Rh^0-based catalyst under reducing conditions. To the best of our knowledge, this is the first report of a Rh material derived from a MOF. A manganese based MOF was selected for this study as it contains linkers with available chelating sites for the Rh^I precursor to bind. The MOF-templating route was studied for the pristine MOF and its Rh-metalated variant under different concentrations of H_2 and time periods (5% H_2/Ar for 4 h and 80%H_2/CO_2 for 90 h). The different treatments resulted in different templating stages: template MOF, partially decomposed MOF and MOF-templated catalyst. Characterisation of these samples provided insights into the templating mechanism, and the role that the secondary metal, Rh, plays in the MOF decomposition.

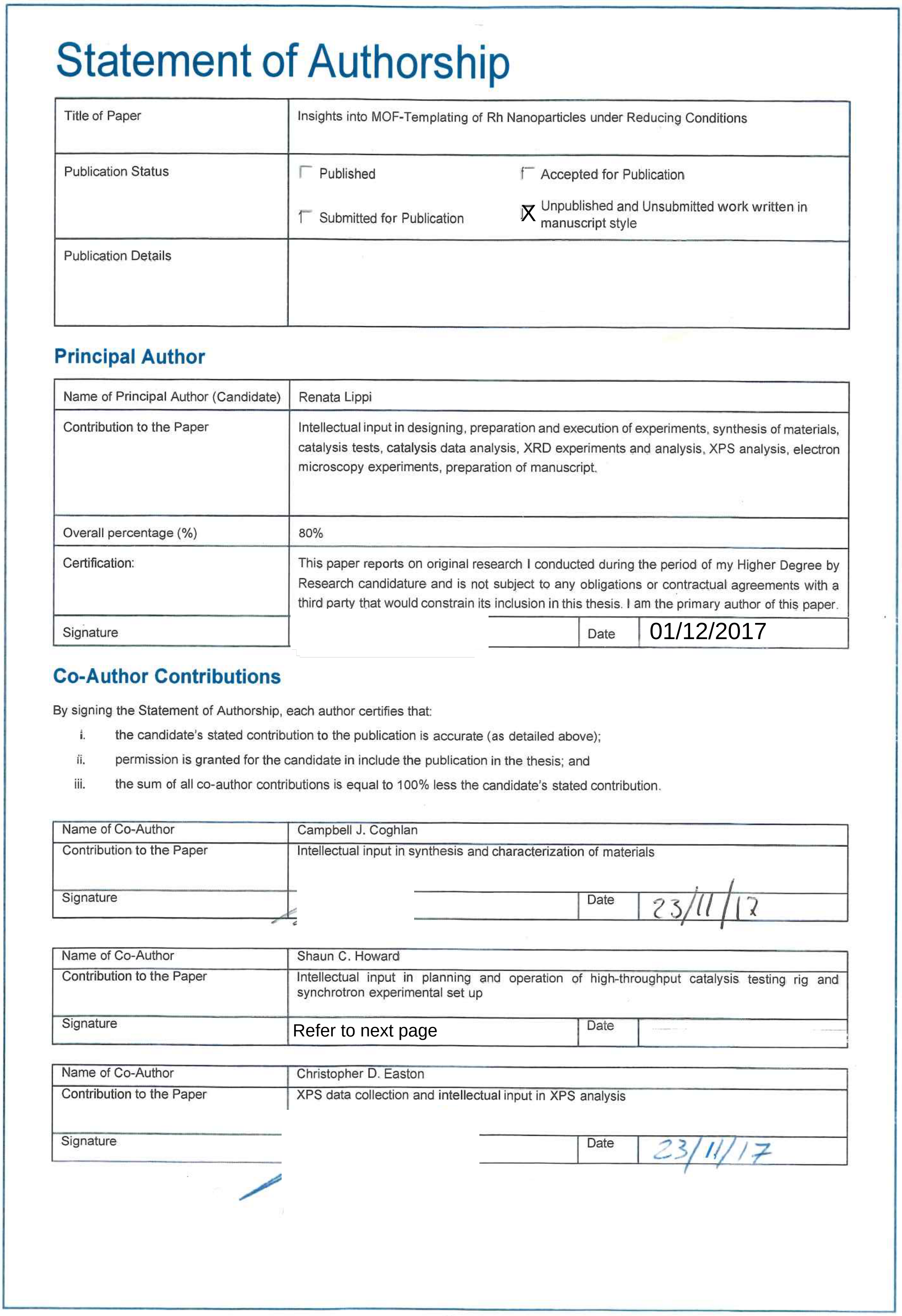

Statement of Authorship

Title of Paper	Insights into MOF-Templating of Rh Nanoparticles under Reducing Conditions
Publication Status	☐ Published ☐ Accepted for Publication ☐ Submitted for Publication ☒ Unpublished and Unsubmitted work written in manuscript style
Publication Details	

Principal Author

Name of Principal Author (Candidate)	Renata Lippi		
Contribution to the Paper	Intellectual input in designing, preparation and execution of experiments, synthesis of materials, catalysis tests, catalysis data analysis, XRD experiments and analysis, XPS analysis, electron microscopy experiments, preparation of manuscript.		
Overall percentage (%)	80%		
Certification:	This paper reports on original research I conducted during the period of my Higher Degree by Research candidature and is not subject to any obligations or contractual agreements with a third party that would constrain its inclusion in this thesis. I am the primary author of this paper.		
Signature		Date	01/12/2017

Co-Author Contributions

By signing the Statement of Authorship, each author certifies that:

i. the candidate's stated contribution to the publication is accurate (as detailed above);

ii. permission is granted for the candidate in include the publication in the thesis; and

iii. the sum of all co-author contributions is equal to 100% less the candidate's stated contribution.

Name of Co-Author	Campbell J. Coghlan		
Contribution to the Paper	Intellectual input in synthesis and characterization of materials		
Signature		Date	23/11/17

Name of Co-Author	Shaun C. Howard		
Contribution to the Paper	Intellectual input in planning and operation of high-throughput catalysis testing rig and synchrotron experimental set up		
Signature	Refer to next page	Date	

Name of Co-Author	Christopher D. Easton		
Contribution to the Paper	XPS data collection and intellectual input in XPS analysis		
Signature		Date	23/11/17

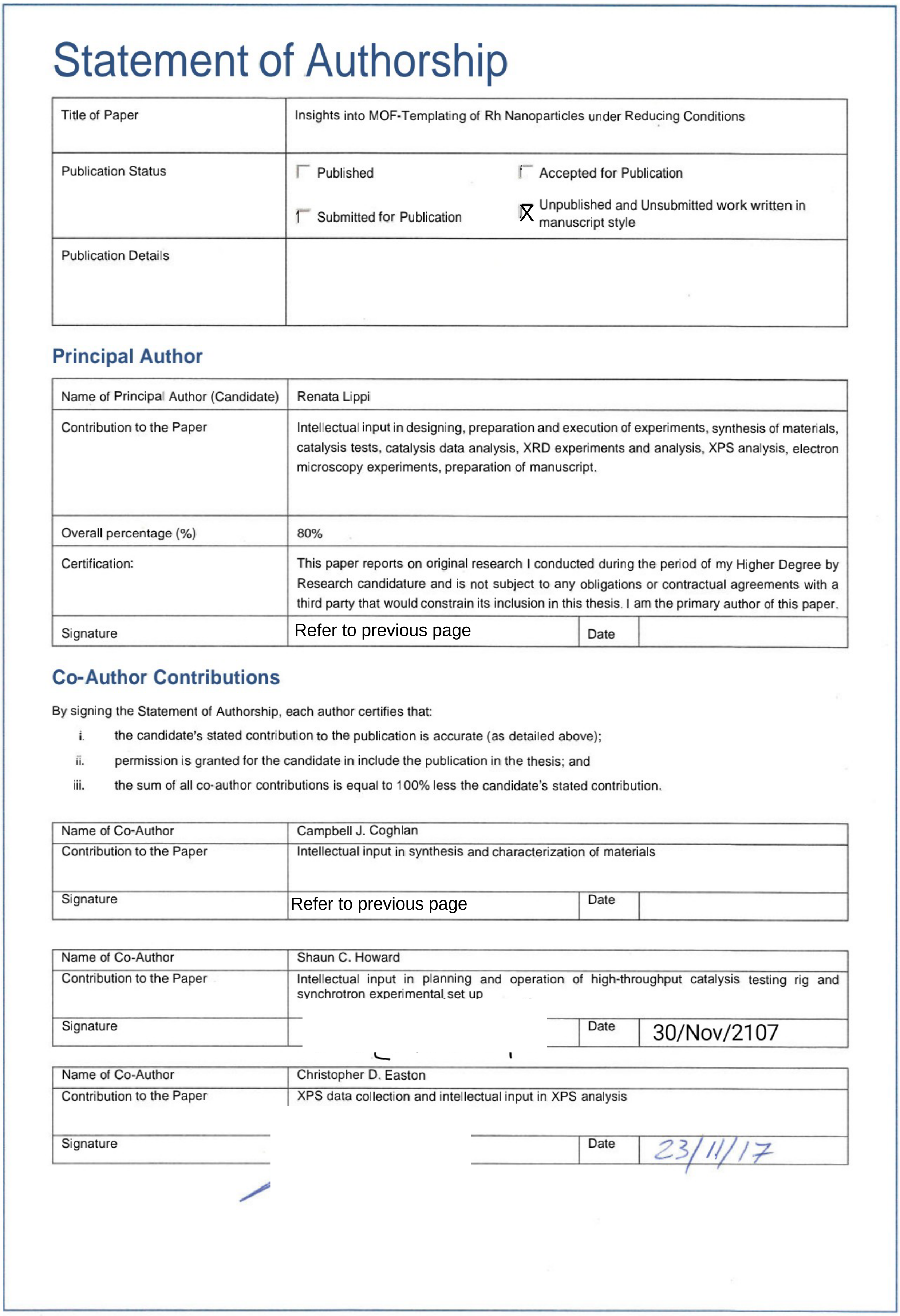

Statement of Authorship

Title of Paper	Insights into MOF-Templating of Rh Nanoparticles under Reducing Conditions
Publication Status	☐ Published ☐ Accepted for Publication ☐ Submitted for Publication ☒ Unpublished and Unsubmitted work written in manuscript style
Publication Details	

Principal Author

Name of Principal Author (Candidate)	Renata Lippi		
Contribution to the Paper	Intellectual input in designing, preparation and execution of experiments, synthesis of materials, catalysis tests, catalysis data analysis, XRD experiments and analysis, XPS analysis, electron microscopy experiments, preparation of manuscript.		
Overall percentage (%)	80%		
Certification:	This paper reports on original research I conducted during the period of my Higher Degree by Research candidature and is not subject to any obligations or contractual agreements with a third party that would constrain its inclusion in this thesis. I am the primary author of this paper.		
Signature	Refer to previous page	Date	

Co-Author Contributions

By signing the Statement of Authorship, each author certifies that:

i. the candidate's stated contribution to the publication is accurate (as detailed above);

ii. permission is granted for the candidate in include the publication in the thesis; and

iii. the sum of all co-author contributions is equal to 100% less the candidate's stated contribution.

Name of Co-Author	Campbell J. Coghlan		
Contribution to the Paper	Intellectual input in synthesis and characterization of materials		
Signature	Refer to previous page	Date	

Name of Co-Author	Shaun C. Howard		
Contribution to the Paper	Intellectual input in planning and operation of high-throughput catalysis testing rig and synchrotron experimental set up		
Signature		Date	30/Nov/2107

Name of Co-Author	Christopher D. Easton		
Contribution to the Paper	XPS data collection and intellectual input in XPS analysis		
Signature		Date	23/11/17

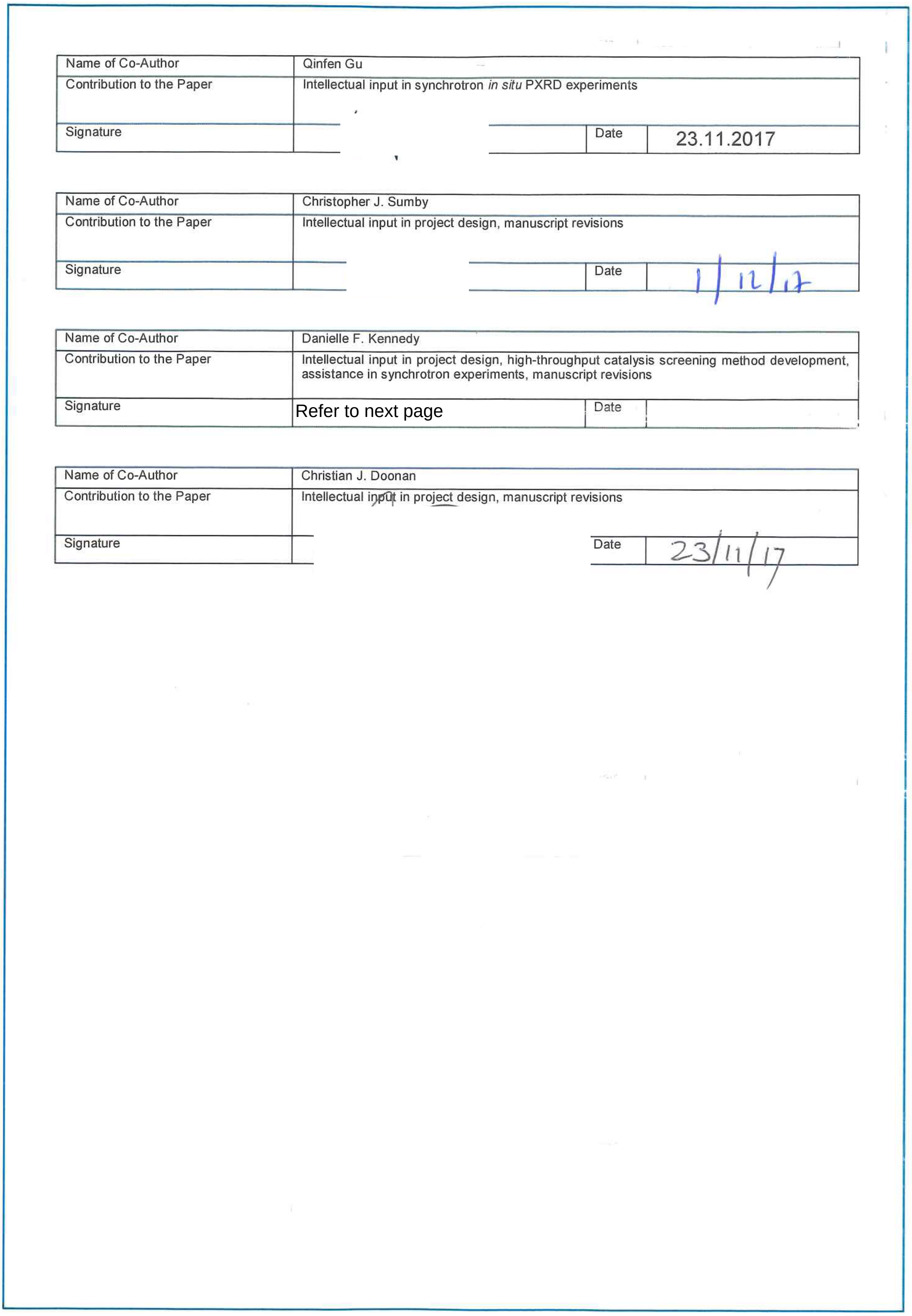

Name of Co-Author	Qinfen Gu		
Contribution to the Paper	Intellectual input in synchrotron *in situ* PXRD experiments		
Signature		Date	23.11.2017

Name of Co-Author	Christopher J. Sumby		
Contribution to the Paper	Intellectual input in project design, manuscript revisions		
Signature		Date	1/12/17

Name of Co-Author	Danielle F. Kennedy		
Contribution to the Paper	Intellectual input in project design, high-throughput catalysis screening method development, assistance in synchrotron experiments, manuscript revisions		
Signature	Refer to next page	Date	

Name of Co-Author	Christian J. Doonan		
Contribution to the Paper	Intellectual input in project design, manuscript revisions		
Signature		Date	23/11/17

Name of Co-Author	Qinfen Gu		
Contribution to the Paper	Intellectual input in synchrotron *in situ* PXRD experiments		
Signature		Date	23.11.2017

Name of Co-Author	Christopher J. Sumby		
Contribution to the Paper	Intellectual input in project design, manuscript revisions		
Signature	Refer to previous page	Date	

Name of Co-Author	Danielle F. Kennedy		
Contribution to the Paper	Intellectual input in project design, high-throughput catalysis screening method development, assistance in synchrotron experiments, manuscript revisions		
Signature		Date	26/11/2017

Name of Co-Author	Christian J. Doonan		
Contribution to the Paper	Intellectual input in project design, manuscript revisions		
Signature	Refer to previous page	Date	

2.2. Abstract

Manganese-based MOFs differentially metalated with Rh were used as sacrificial templates for Rh^0 nanocatalysts for CO_2 hydrogenation. The MOF-derived catalysts were templated *in situ* (80% H_2 and 20% CO_2, 350 °C) and displayed CO_2 conversion of up to 20% single-pass, with CH_4 as the main product observed. The used catalysts were compared to samples templated in 5% H_2/Ar at 350 °C using powder X-ray diffraction, electron microscopy, energy dispersive spectroscopy, and X-ray photoelectron spectroscopy. The *in situ* MOF-templated catalyst consisted of a mesh of Rh nanoparticles supported on crystals of MnO or $MnCO_3$, dependent on the composition of the post-synthetically metalated MOF. In the absence of Rh, the MOF-templating yielded MnO nanoparticles embedded in an amorphous carbon phase doped with N. The samples derived from reduction in 5% H_2 displayed characteristics of both the parent MOF and the MOF-templated catalysts, representing an intermediate phase. Characterisation of the samples reveals that formation of Rh^0 nanoparticles under a reducing atmosphere assisted with the removal of the MOF organic components, which allowed growth of MnO or $MnCO_3$ and the *in situ* formation of a mesh of catalytic Rh^0 nanoparticles.

2.3. Introduction

Heterogeneous catalysts are widely applied in chemical industry. Their facile separation and robustness make them more attractive for industrial applications than homogeneous catalysts. However, understanding the catalytic reaction mechanisms can be challenging as identification of catalytically active sites and reaction the intermediates is required.[1-4] Active sites typically compose a small fraction of the overall surface area of a catalyst, thus catalyst optimisation aims to increase the surface density of these sites. Therefore, synthesis methods that provide control over chemical composition and structure may facilitate (i) identification of active sites and (ii) increasing the surface density of active sites. Metal nanocatalysts are synthesised via physicochemical methods with attention to clusters size, morphology and available surface area.[5-8] However, developments of new synthetic approaches for catalytic materials with better composition and morphology control is desired to achieve long lasting and high performing catalysts.[5] Recently, MOF-mediated synthesis has been demonstrated as a potential new route for efficient catalysts.

Metal-organic frameworks (MOFs), are a class of porous materials made of inorganic nodes connected via organic linkers.[9] The large library of organic linkers and metal nodes available affords a vast number of possible structures.[10-11] Furthermore, the properties of MOFs can be tailored by the rational selection of these components. In addition, the functionality of synthesised MOF materials can be tuned by post synthetic modifications (PSM) techniques such as, covalent attachment, linker/cation exchange or addition of a secondary metal.[12-13] A significant body of research has focused on the gas capture,[14-16] separation,[17] and catalytic properties of MOFs.[18] Indeed a recent development in the area of MOF chemistry has been to use their porous networks as self-sacrificing templates[19-26] to yield uniquely structured materials for electrochemical[19] and catalytic[21, 24] applications. Among the highly active MOF-templated catalysts reported are composites of metal, metal oxides and porous carbon.[27-29] In these examples, the high activity of the MOF-derived catalysts has been attributed to factors, such as excellent control of secondary metal dispersion in the derived catalyst[27], nanoparticle size control,[28] and good nanoparticle dispersion on support.[29] The control provided by MOF-templating is hypothesised to be a consequence of the uniform spacing of inorganic and organic subunits in the template.[25] The underlying mechanism is not well understood, but insights into the mechanism lead to catalyst synthesis optimisation.[30] Normally, the parent MOF is treated at high temperature in inert atmosphere (pyrolysis) or in air (calcination) to yield the templated inorganic material.[20, 22, 26] In general, pyrolysis of a MOF produces metal or metal oxide nanoparticles embedded in carbon whereas calcination yields metal oxide nanoparticles alone. Of the limited examples where MOF-templating was carried out under a reducing atmosphere, H_2, the synthesis of metallic nanoparticles has been reported.[31-32] Metallic nanoparticles are employed in several catalytic reactions, such as oxidations, hydrogenations, and C-C coupling, which can greatly benefit from the control of nanoparticles dispersion, size and morphology.[5, 7-8] This led us to investigate the effect of reducing conditions in the synthesis of metallic nanocatalysts via MOF-templating.

Rhodium metal nanoparticles can be used as catalysts for both oxidation[33] and hydrogenation reactions,[34-37] including CO_2 hydrogenation.[37-39] Strategies to synthesise Rh^0 nanoparticles of controlled size include the use of solid supports, surfactants or polymeric stabilisers.[36, 40-41] To the best of our knowledge, MOF-templating method has not been explored for Rh materials.

Here, we explore the use of a Mn-based MOF, which can be post-synthetically metalated (PSMet) with Rh at precisely defined sites, as a template for a nanostructured Rh catalyst. The Rh-metalated MOF was thermally treated under CO_2 hydrogenation conditions (80% H_2/CO_2 at 350 °C) to produce the MOF-templated Rh^0 nanocatalyst "*in situ*". We use X-ray diffraction, electron microscopy, energy dispersive spectroscopy, and X-ray photoelectron spectroscopy to provide insight into the templating mechanism of this novel material and compare structure to control samples. Our data indicates that the presence of Rh in the MOF facilitated the decomposition of the organic linkers and, thus afforded the removal of carbon and nitrogen under reducing conditions. This resulted in crystals of MnO or $MnCO_3$ distributed in a mesh of Rh^0 nanoparticles of 6 to 9 nm in size.

2.4. Experimental methods

2.4.1. Synthetic procedures

MnMOF(1) The organic ligand bis(4-(4'-carboxyphenyl)-3,5-dimethylpyrazolyl)methane (H_2L) was synthesised according to Bloch, *et al.*[42] 1 was synthesised by solvothermal synthesis reported by Bloch *et al.*[43] In a typical synthesis, the organic ligand (63.2 mg H_2L) and the Mn salt (49.9 mg $MnCl_2{\cdot}4H_2O$) were dissolved in a mixture of DMF (8 mL) and water (4 mL). The solution was kept static at 100 °C for 24 h. The white precipitate formed was washed with DMF (5 x 20mL). The MOF structure was verified by PXRD.

Post-synthetic metalation (PSM) of **1** was achieved by soaking **1** in anhydrous acetonitrile with excess of di-μ-chloro-tetracarbonyldirhodium(I) (**1**·Rh_2) or with both di-μ-chloro-tetracarbonyldirhodium(I) and sodium tetrafluoroborate (**1**·Rh-BF_4) (Figure 1). After 48 hours, the solution was decanted and the PSM MOFs were washed with anhydrous acetonitrile (7 x 20mL CH_3CN) and dried under a stream of Ar.

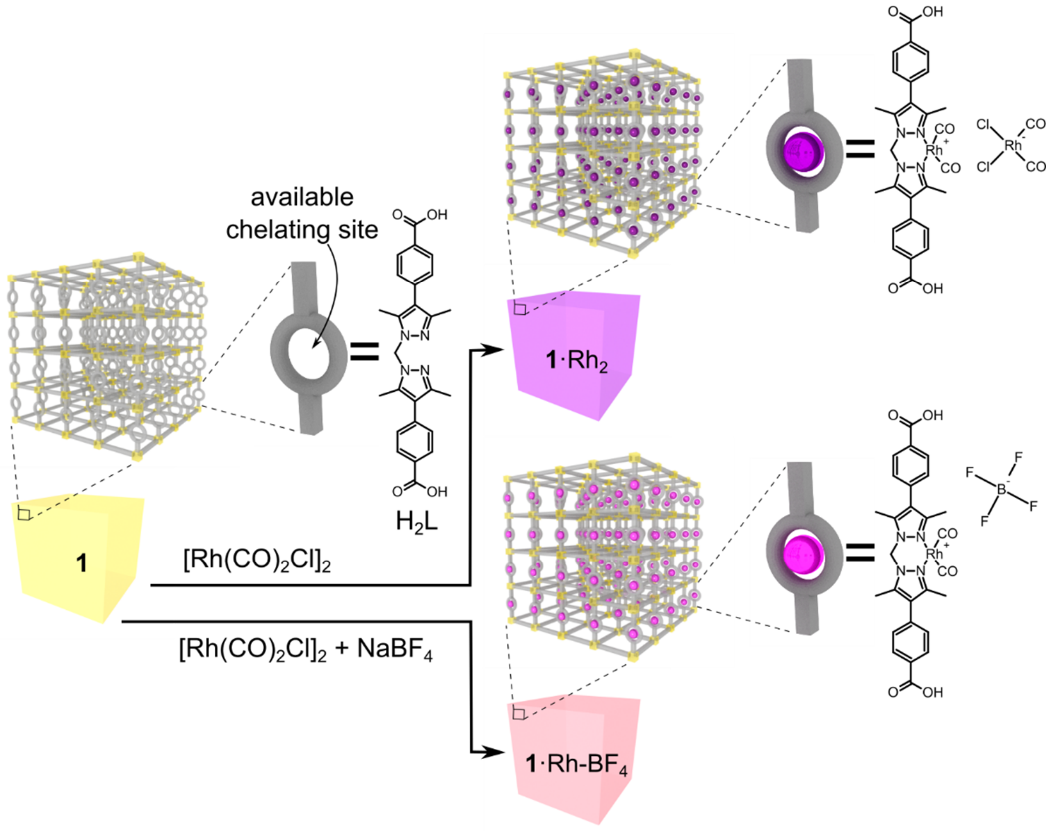

Figure 1: Scheme of post synthetic metalation of **1**. The linker (H_2L) has a bidentate bis-(3,5-dimethyl-pyrazolyl)methane coordination site. In **1**, one out of three di-pyrazole moieties are available chelating sites, with the remaining di-pyrazole moieties chelating the Mn nodes. The metalation of these sites with $[Rh(CO)_2Cl]_2$ yielded **1**$\cdot Rh_2$ and **1**$\cdot Rh\text{-}BF_4$ (right), depending on the reaction conditions as illustrated above.

2.4.2. Catalysis testing

Catalysis testing was performed in a multi-channel testing rig with parallel fixed-bed microreactors using a method described in detail in Lippi *et al.*[44] Each MOF (15 mg of **1**, 18.8 mg of **1**$\cdot Rh\text{-}BF_4$ and 18.7 mg of **1**$\cdot Rh_2$) was mixed with SiC (50 mg) and loaded into a different microreactor. In addition, a reactor filled with SiC (100 mg) was used as a negative control. The catalysis experiments started with a 30 min drying step, under Ar flow (1 ml/min per reactor) at 220 °C and 1 bar, to remove any solvent guest molecules within the MOF pores. Subsequently, a reactive gas mixture (2.9 mL/min per reactor, 71.4 vol% H_2, 17.9 vol% CO_2, and 10.7 vol% Ar) $H_2:CO_2 = 4:1$ was flowed through the reactors and activation was performed at 4 bar and 350 °C (Condition A). To evaluate the effect of space velocity, the flow of the reactive gas mix was increased to 4.7 mL/min per reactor (74.6 vol% H_2, 18.7 vol% CO_2, and 6.7 vol% Ar) H_2:CO_2 = 4:1, while keeping the temperature and pressure constant (Condition B). Flow was set back to match activation flow (2.9 mL/min per reactor, 71.4 vol% H_2, 17.9 vol% CO_2, and 10.7 vol% Ar) and catalysis testing was then performed at a lower temperature, 250 °C (Condition C). Lastly, the first reaction conditions (Condition A) were re-established in order to determine the stability of the catalyst and identify any hysteresis (Condition D).

Effluent gas composition for each individual reactor was analysed using an online gas chromatograph with He as carrier gas.

2.4.3. Controlled atmosphere thermal treatment

The samples **1**, **1**·Rh_2 and **1**·Rh-BF_4 were loaded into quartz crucibles. The crucibles were placed inside the quartz tube of a tube furnace with three hot zones, each zone independently controlled by a 1/16 DIN temperature controller (Watlow, USA). The temperature of each zone was calibrated prior to the experiment. The ends of the quartz tube were connected to in-house built gas connections. The upstream end was connected to the feed gas line and the downstream end was connected to an oil bubbler. One set of samples was treated in pure N_2 and another set in 5 vol% H_2 in Ar. All samples were treated at 350 °C for 4 h under continuous gas flow.

2.4.4. Powder X-ray diffraction

PXRD experiments were carried out at the Powder Diffraction Beamline at the Australian Synchrotron. A Mythen microstrip detector[45] was used for data collection.

***Ex situ* analysis:** The samples were loaded into special glass 0.7 mm wide capillaries (The Charles Supper Company, USA). The capillary was kept rotating during acquisition for better averaging of reflections. The beam energy during data acquisition was 16 keV (Figure 3) and 15 keV (Figure 4) with current of 200 mA.

***In situ* analysis:** For the experiments performed under a controlled atmosphere and variable temperature, the samples (**1** and **1**·Rh-BF_4) were loaded into open-ended special glass 0.7 mm wide capillaries (The Charles Supper Company, USA) glass wool was used to contain the powder within the capillary while allowing gas to flow. The capillary was kept oscillating during acquisition for better average of reflections. A hot-air blower positioned below the capillary was used for temperature control. A capillary holder adapted for controlled atmosphere experiments was connected to a gas manifold allowing the selection of gas. The beam energy during data acquisition was 17.9 keV with a current of 200 mA. The sample was first heated at 5 °C/min to 200 °C under Ar flow, then the gas flow was switched to a mixture of CO_2:H_2 = 1:3. The temperature profile for each sample is indicated in Figure 5.

2.4.5. Rietveld refinement

Phase identification of the collected patterns were obtained via the use of search and match algorithm in X'pert Highscore Plus (PANalytical, the Netherlands). The obtained phases were quantified via Rietveld refinement based quantitative phase analysis[46] using Topas V5 software.[47]

2.4.6. Transmission electron microscopy (TEM)

Samples were suspended in ethanol and deposited on carbon-coated copper TEM grids and allowed to dry. Grids were examined in a Tecnai 12 G2 TEM (FEI, The Netherlands), operating at 120 kV, and images were recorded with a MegaView III CCD (Olympus, Tokyo).

2.4.7. Scanning electron microscopy (SEM) and energy dispersive spectroscopy (EDS)

The samples loaded on TEM grids, as previously described, were placed on a SEM stage and examined using a Zeiss Merlin FESEM (Field Emission Scanning Electron Microscope) operated in the secondary electron (SE) mode and back-scattered mode (BSE). Energy dispersive spectroscopy (EDS) was used to identify elements present within the samples. The EDS system used was AZTEC, manufactured by Oxford Instruments Pty Ltd. An accelerating voltage of 15 kV was used for EDS mapping. The scale bars in the images are indicative of the magnification used.

2.4.8. X-ray photoelectron spectroscopy (XPS)

X-ray photoelectron spectroscopy (XPS) analysis was performed using an AXIS Nova spectrometer (Kratos Analytical Inc., Manchester, UK) with a monochromated Al Kα source at a power of 180 W (15 kV, 12 mA) and a hemispherical analyser operating in the fixed analyser transmission mode. The total pressure in the main vacuum chamber during analysis was typically between 10-9 and 10-8 mbar. Survey spectra were acquired at a pass energy of 160 eV. To obtain more detailed information about chemical structure, oxidation states etc., high resolution spectra were recorded from individual peaks at 40 eV pass energy (yielding a typical peak width for polymers of 1.0 eV).

Samples were filled into shallow wells of custom-built sample holders. Each specimen was analysed at an emission angle of 0° as measured from the surface normal. Assuming typical values for the electron attenuation length of relevant photoelectrons the XPS analysis depth (from which 95 % of the detected signal originates) ranges between 5 and 10 nm for a flat surface. As the actual emission angle is ill-defined for rough surfaces (ranging from 0° to 90°), the sampling depth may range from 0 nm to approximately 10 nm.

Quantification: Data processing was performed using CasaXPS processing software version 2.3.15 (Casa Software Ltd., Teignmouth, UK). All elements present were identified from survey spectra. The atomic concentrations of the detected elements were calculated using integral peak intensities and the sensitivity factors supplied by the manufacturer. Binding energies were referenced to the main C 1s peak at 284.8 eV. The accuracy associated with quantitative XPS is ca. 10% - 15%. Precision (i.e. reproducibility) depends on the signal/noise ratio but is usually much better than 5%. The latter is relevant when comparing similar samples.

2.5. Results and discussion

The synthesis MnMOF (**1**) and its post synthetic metalation (PSM) with $[Rh(CO)_2Cl]_2$ to yield **1**·$[Rh(CO)_2][RhCl_2(CO)_2]$ (**1**·Rh_2) were performed as described in our previous work.[43, 48] The inorganic nodes of **1** are composed of Mn trimers, which are coordinated by both the carboxylate and di-pyrazole moieties of L (Figure 1). Due to the stoichiometry of the metal node one third of all the organic linkers (L) in **1** presented free di-pyrazole moieties (Figure 1). These free sites are available to chelate transition metals via PSM. In the case of PSM with $[Rh(CO)_2Cl]_2$ (**1**·Rh_2), single crystal diffraction indicated occupancy of these sites greater than 90%.[43] In this report, the replacement of the *cis*-$[RhCl_2(CO)_2]^-$ anion by BF_4^- to yield **1**·$[Rh(CO)_2]BF_4$ (**1**·Rh-BF_4) was carried out to decrease the loading of Rh^I in the framework to provide a single Rh^I atom per available chelating site, as opposed to two found in to **1**·Rh_2. Evaluation by IR spectroscopy indicated the successful displacement of the counter-ion *cis*-$[RhCl_2(CO)_2]^-$ in **1**·Rh-BF_4 (Figure S2). Figure 1 provides a graphical representation of the structure of the MOFs tested in this work: **1**, **1**·Rh_2 and **1**·Rh-BF_4. The resulting overall loading of Rh in the MOFs is approximately 11 wt% and 6 wt% for **1**·Rh_2 and **1**·Rh-BF_4, respectively.

Rh and Ru are noble metals known to be very active for CO_2 hydrogenation.[6, 37, 39, 44] We recently reported the MOF-templating of a highly active Ru catalyst for CO_2 methanation, which presented controlled nanoparticle size and distribution over the support.[44] Therefore, we hypothesised that MOF-templating could also afford the synthesis of Rh nanoparticles of controlled size. In this report, **1** is selected as the template due to the homogeneous distribution of Rh that can be achieved through metalation of the chelating sites. Accordingly, **1**, **1**·Rh_2 and **1**·Rh-BF_4 were examined as precursors for producing CO_2 hydrogenation catalysts. Each of the MOFs were transformed into active catalysts under CO_2 hydrogenation reaction conditions; 350 °C and 4 bar under a flow of 80% H_2 and 20% CO_2 at 350 °C and 4 bar (i.e. CO_2 hydrogenation reaction conditions, Figure S5). Therefore, **1**-used, **1**·Rh_2-used, and **1**·Rh-BF_4-used will be applied to identify the *in situ* produced catalysts that are continuously tested over 90 h. For each sample, a gradual change in catalytic performance was observed over the first 25 h. We attribute this to the structural transition from the PSM MOF into the active catalyst. The two Rh containing samples initially displayed a maximum production of CH_4, 18 $mmol.min^{-1}.g_{MOF}^{-1}$ (4 hours) and 16 $mmol.min^{-1}.g_{MOF}^{-1}$ (8 hours) for **1**·Rh_2-used and **1**·Rh-BF_4-used, respectively, which decreased thereafter (Figure 2). The CH_4 production was accompanied by H_2 and CO_2 (Figure 2), which is strong evidence that methane was a product of CO_2 hydrogenation and not a result of the decomposition of the organic linkers. **1** and SiC were also tested as a controls and displayed negligible activity. The significantly lower CH_4 production, indicates that that **1**-used was inactive for the CO_2 hydrogenation and that Rh is a necessary component of the active catalyst.

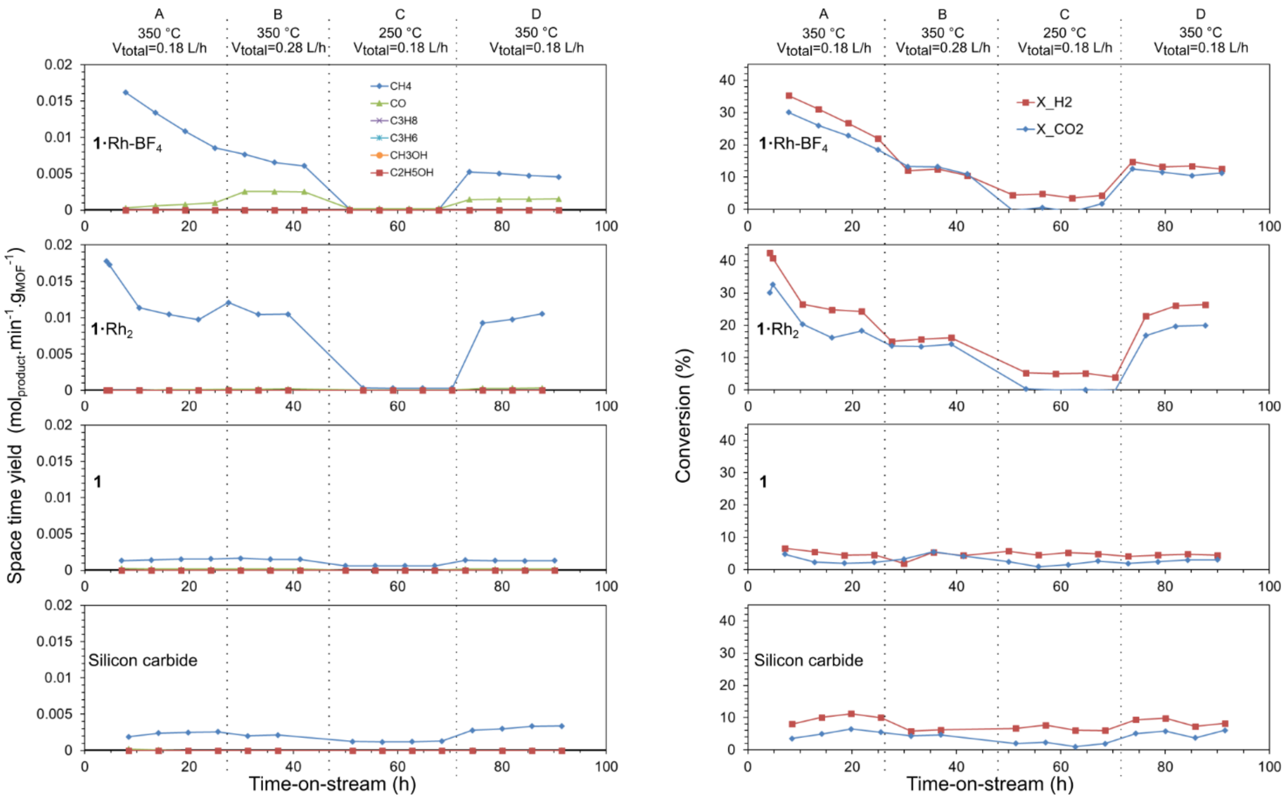

Figure 2: Space time yield (left) and reactant conversion (right) for the different precatalysts tested in parallel for CO_2 hydrogenation. The different testing conditions of temperature and total gas flow as indicated by the letters A to D (top). Catalysis testing of **1**, **1**·Rh-BF_4, **1**·Rh_2, and SiC (blank reactor) at 4 bar.

After activation and an initial deactivation period (Figure 2,Figure condition A), the catalysts displayed stable conversions for the duration of the experiment, 90 h (Figure 2). The Rh-containing samples displayed higher CH_4 production, however, **1**·Rh_2-used produced approximately double the amount of CH_4 per gram of MOF than **1**·Rh-BF_4-used (Figure S6), this difference can be correlated to Rh loading of the precatalysts, 11 and 6 wt% respectively. Divergent products (CH_4, CO, C_3H_8, C_3H_6) selectivity between **1**·Rh_2-used and **1**·Rh-BF_4-used (Figure S7) suggest that the differences between the MOF-derived catalysts in not only dependent upon the amount of Rh and is potentially related to other phases formed during the templating process.

The presence of different crystalline phases in each sample was determined by Rietveld-based quantitative phase analysis[46] on powder X-ray diffraction (PXRD) data of the used catalysts (Figure 3 and Table 1). The remaining material was examined by XPS and SEM/EDS experiments. The catalyst **1**·Rh-BF_4-used displayed a complex composition, containing cubic Rh^0, trigonal $MnCO_3$, Na salts, and at least one unidentified phase with a large unit cell as observed by the difference curve. The International Centre for Diffraction Data (ICDD) database was used for the search of possible phases which would be in agreement with the unidentified phase(s) without success. Considering the nature of the other identified phases and the peak profile, a low-ordered multi-component phase (possibly Mn, Na, F, Cl, O, Rh, C, and/or N) is hypothesised to be the source of those reflections. The presence of Na salts is explained by the poor solubility of NaCl in acetonitrile. This results in the incomplete removal of NaCl, a by-product from the reaction of $NaBF_4$ with the Rh dimer within the framework. A simpler composition was observed for **1**·Rh_2-used, with cubic Rh^0 and cubic MnO in the used catalyst. Silicon carbide (SiC) was also present in the diffractogram, as it was mixed with the catalyst as diluent for the performance testing, and was a remnant in the isolated sample. It is evident that the composition of the precatalyst affects the final catalyst composition and, therefore, its catalytic properties.

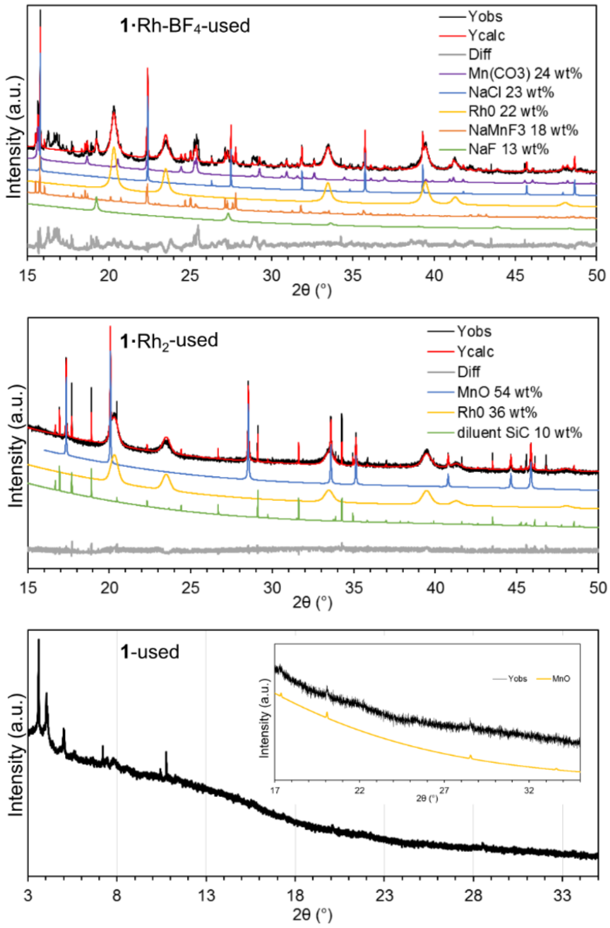

Figure 3: Experimental PXRD patterns (black) for the MOF-derived catalysts. The Rietveld refined pattern is shown in red and the difference curve in grey for the Rh-containing samples. The patterns offset below the diffractograms are the calculated patterns for the phases listed. Quantitative phase analysis results are listed in the legend. Analysis of the catalyst derived from **1** indicated the retention of the low angle peaks from the MOF and the presence of reflections of MnO (inset).

The diffractogram of the control sample, **1**-used, showed low angle reflections suggestive of the planes (0 0 1) and (1 1 0) of the pristine MOF even after prolonged time on stream. However, these reflections in **1**-used had broadened substantially and displayed decreased intensity consistent with a significant loss of crystallinity and partial collapse of the MOF. In addition, low intensity reflections of MnO were identified in the wide angle region (Figure 3). This indicates that in the absence of Rh, the MOF undergoes partial decomposition under reaction conditions, forming a relatively small amount of MnO crystals, as observed from the low intensity peaks.

The difference in Rh loading of the two template MOFs was reflected in Rietveld-based quantitative phase analysis (QPA). Rh^0 amounts for the derived catalysts **1**·Rh_2-used and **1**·Rh-BF_4-used were determined to be 40 wt% and 22 wt% respectively (excluding diluent SiC). The broad peaks for Rh^0 reflections is a result of the small crystallite sizes in this phase, which are in average 10 nm, as measured via TEM. Volume weighted column height or apparent crystallite size (Lvol-IB) was also calculated via Rietveld refinement.[49] The MOF templating route yielded Rh nanoparticles with an apparent size of 6 and 8 nm for **1**·Rh_2-used and **1**·Rh-BF_4-used, respectively. For both MOF-templated catalysts, Rh^0 nanoparticles were substantially smaller than the other particles. For example, the apparent size of MnO in **1**·Rh_2-used, was 90 nm. For **1**·Rh-BF_4-used, the apparent size of $MnCO_3$ was 32 nm and the Na salts were in the range of 20 to 200 nm (Table 1). The control **1**-used presented MnO crystals with apparent size of 64 nm; these crystals were smaller than the crystals generated in the Rh containing sample, **1**·Rh_2.

Table 1. Quantitative phase analysis (QPA) and volume weighted column height (Lvol-IB) calculated via Rietveld refinement.

Template MOF	**1**·Rh-BF_4	**1**·Rh_2	**1**
Phase	Rietveld QPA (wt%) Apparent crystallite size Lvol-IB		
Rh^0	22% 8.3 nm	40% 6.4 nm	-
MnO	-	60% 90 nm	N/A 64 nm
$MnCO_3$	24% 32 nm	-	-
NaCl	23% 213 nm	-	-
$NaMnF_3$	18% 89 nm	-	-
NaF	13% 21 nm	-	-

The majority of MOF-templated materials are synthesised via calcination in air or under an inert atmosphere at temperatures ranging from 300 to 1000 °C. The temperature of treatment is selected to exceed the thermal stability of the MOF, obtained via thermogravimetric analysis (TGA) in inert atmosphere or in air.[20-22, 26] The template MOFs **1**, **1**·Rh_2 and **1**·Rh-BF_4 displayed thermogravimetric stability up to 400 °C in N_2 (Figure S3). In this study the MOF-templating step occurs at a temperature below the thermal stability in N_2 (350 °C), however the presence of H_2 (80% H_2 and 20% CO_2) can affect the MOF stability. Accordingly, to evaluate the effect of the atmosphere composition in the templating of the catalyst, samples of **1** and **1**·Rh-BF_4 were treated *ex situ* at 350 °C under an inert (N_2) and reducing atmosphere (5% H_2 in N_2). The resulting samples (with added labels "N_2" or "5%H_2") were characterised and are compared to the MOF-derived catalysts below.

Pyrolysis of MOFs **1** and **1**·Rh-BF_4 produced amorphous samples (Figure 4); NaCl was present in the metalated MOF as noted above, and was not formed during pyrolysis. In contrast, under a mildly reducing atmosphere (5% H_2), the resulting samples (**1**-5%H_2 and **1**·Rh-BF_4-5%H_2) displayed low angle peaks which are in agreement with the planes (0 0 1) and (1 1 0) of **1**. This indicates that the samples heat-treated in 5% H_2 retained some structural features of the original MOF structure. No new phase was formed in **1**-5%H_2, whereas Rh^0 nanoparticles were formed in **1**·Rh-BF_4-5%H_2. Aside from Rh^0 nanoparticles, no other phases previously observed for **1**·Rh-BF_4-used were present. These Rh^0 nanoparticles had the same phase, cubic-Rh^0, as the ones formed during catalysis testing (**1**·Rh_2-used and **1**·Rh-BF_4-used) but were smaller in apparent size (Lvol-IB = 5.3 nm). As Rh^0 nanoparticles were not produced via pyrolysis, these samples were not further analysed.

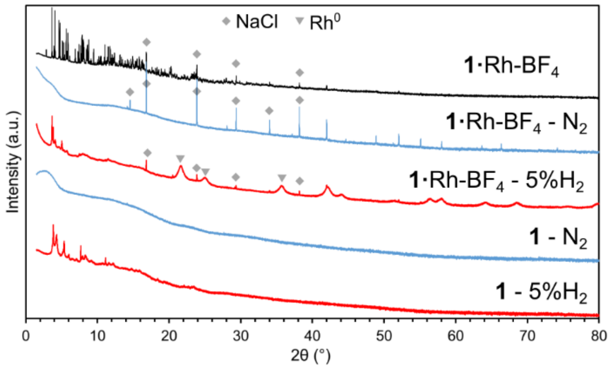

Figure 4: PXRD patterns of **1**·Rh-BF$_4$ as-synthesised and samples resulting from the thermal treatment of **1** and **1**·Rh-BF$_4$ samples (Rh^0 Lvol-IB 5.3) nm. Samples reduced (red) and calcined (blue) as indicated by the legends.

In situ MOF-templating of the catalyst was investigated in temperature and atmosphere controlled PXRD experiments. In these experiments, the phase transitions of **1** and **1**·Rh-BF$_4$ were observed while subjecting these samples to simulated CO_2 hydrogenation reaction conditions: drying in 100% Ar flow from room temperature to 200 °C; followed by a flow of 75% H_2 and 25% CO_2 and temperature ramp to 350 °C (Figure 5). The crystalline structure of **1**·Rh-BF$_4$ was stable during the drying step, and abruptly collapsed on exposure to H_2-containing gas mixture at 200 °C. At 350 °C, increased intensity was observed in the region corresponding to Rh^0 reflections revealing the formation of the Rh nanoparticles (Figure S9). The sharp peak around 14° 2θ was identified as a reflection from NaCl, a by-product of the PSM step. Following the collapse of the MOF, this NaCl reflection displayed increasing intensity due to further growth of these crystals. Upon reaching 300 °C, the intensity of NaCl reflections start to decrease, possibly due to formation of $NaMnF_3$ and NaF, phases observed in **1**·Rh-BF$_4$-used. Other phases present in **1**·Rh-BF$_4$-used were not observed, thus indicating that they may only form after a prolonged exposure (10-25 h) to reactive gases (time restrictions when using the synchrotron source prevented further examination). The crystallinity of the control sample **1** was retained throughout the extended period of exposure to Ar and CO_2

hydrogenation conditions (H_2 + CO_2), indicating that the presence of Rh in the template MOF was required for the fast collapse of the structure under catalytic conditions.

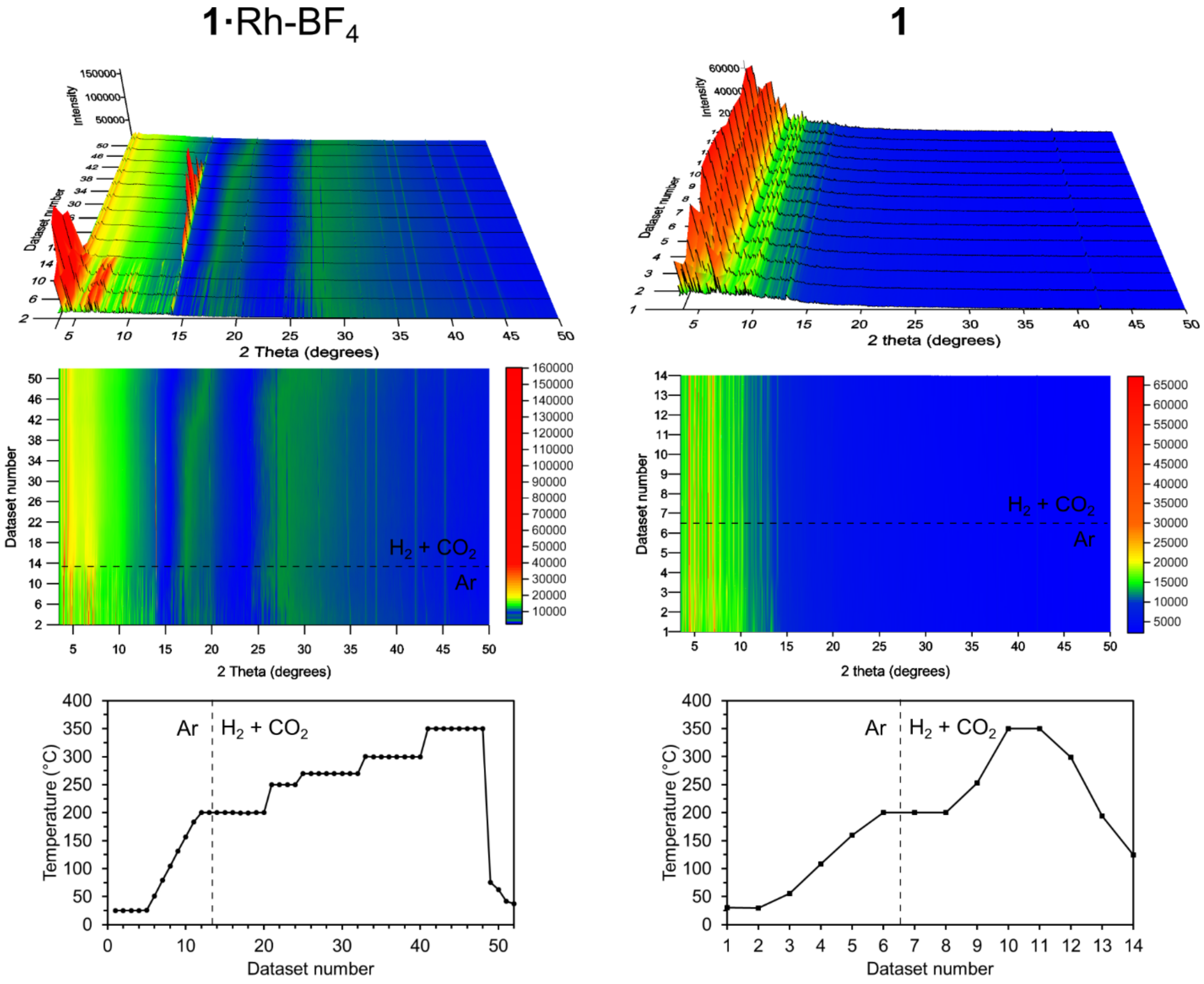

Figure 5: *In situ* PXRD study for **1**·Rh-BF_4 and **1**. The 3D plots present the intensity (z axis) versus diffraction angle (x axis) for each data set (y axis). The heat maps display a different perspective of the dataset looking down the intensity axis. The different colours indicate different intensities according to the legend. The temperature at each dataset is shown on the bottom charts, in addition, the change of atmosphere is displayed on the heat maps as well as on the temperature charts. The structure of **1**·Rh-BF_4 collapsed as soon as the atmosphere was switched to the reactive gas mix, the shift of the green colour in the final datasets around 18° and 32° 2θ highlight the formation of Rh^0 at 350 °C (see SI for comparison). Non-metalated **1** was stable throughout the whole experiment. Reactive gas mixture (75% H_2 and 25% CO_2). Experiment performed at synchrotron photon energy of 17.9 keV.

The morphology of the MOF-derived samples produced after catalysis testing (used samples) and after tube furnace reduction (5% H_2) were studied by TEM (Figure 6), SEM and

EDS (Figure 7). The catalyst **1**·Rh-BF_4-used consisted of a mesh of Rh nanoparticles in the range of 6 to 15 nm (histogram in Figure S10) among larger crystals of varying sizes ranging from 30 to 300 nm. Interestingly, at lower magnification it was possible to observe that these crystalline composite meshes retained the shape of the much larger original plate shaped monoclinic MOF crystals, another sign that the MOF served as a sacrificial template.[44] EDS mapping confirmed that the nanoparticles were composed of Rh and that the larger crystals were in agreement with the phases observed in the diffractogram, i.e. $MnCO_3$ and Na salts.

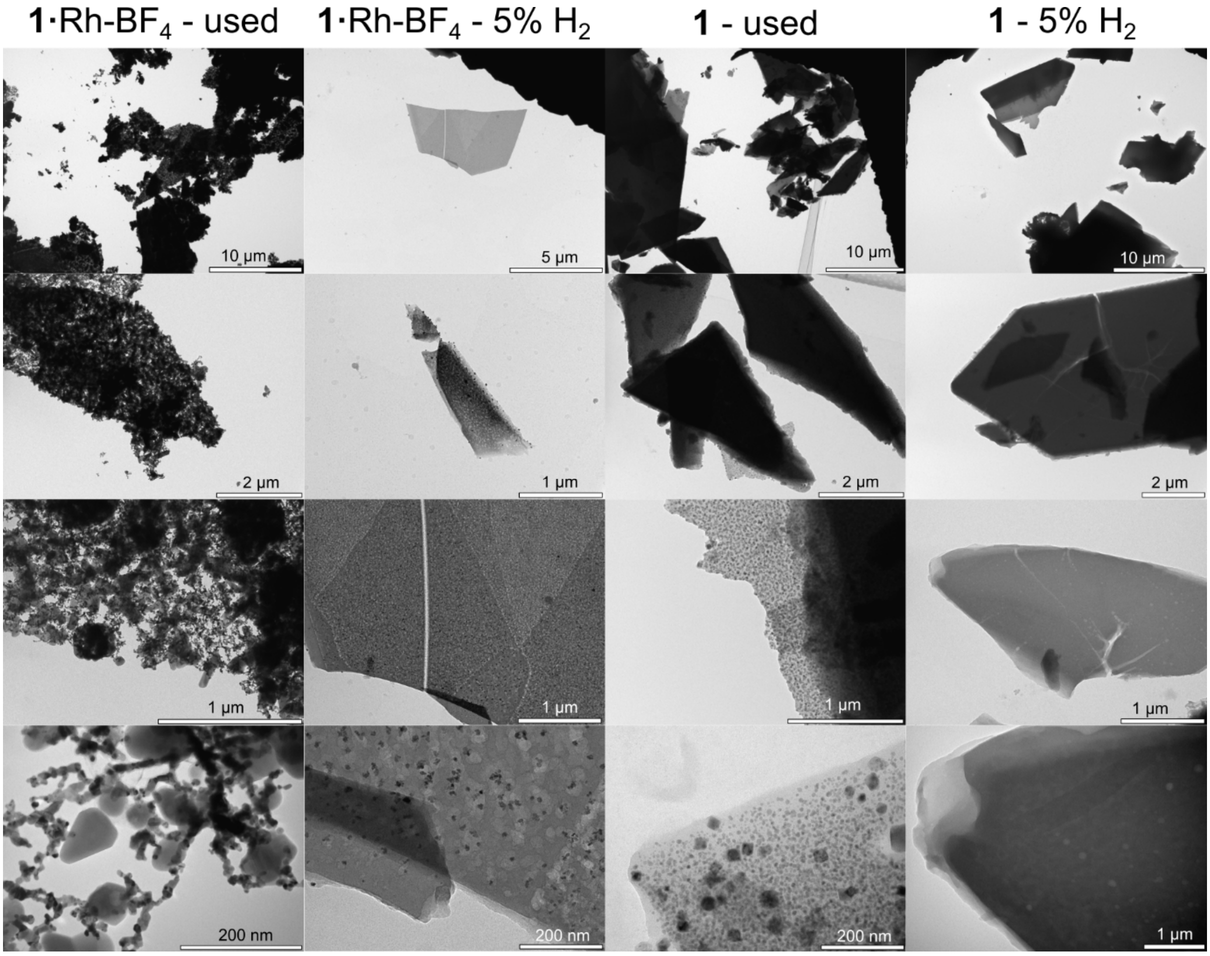

Figure 6: Transmission electron microscopy of the samples derived from **1** and **1**·Rh-BF_4 after catalysts tests ("used") and after reducing treatment ("5% H_2"). In the first two columns, Rh nanoparticles are distinguished by the darker colour due to the electron density of Rh. Scale bars are indicative of the magnification.

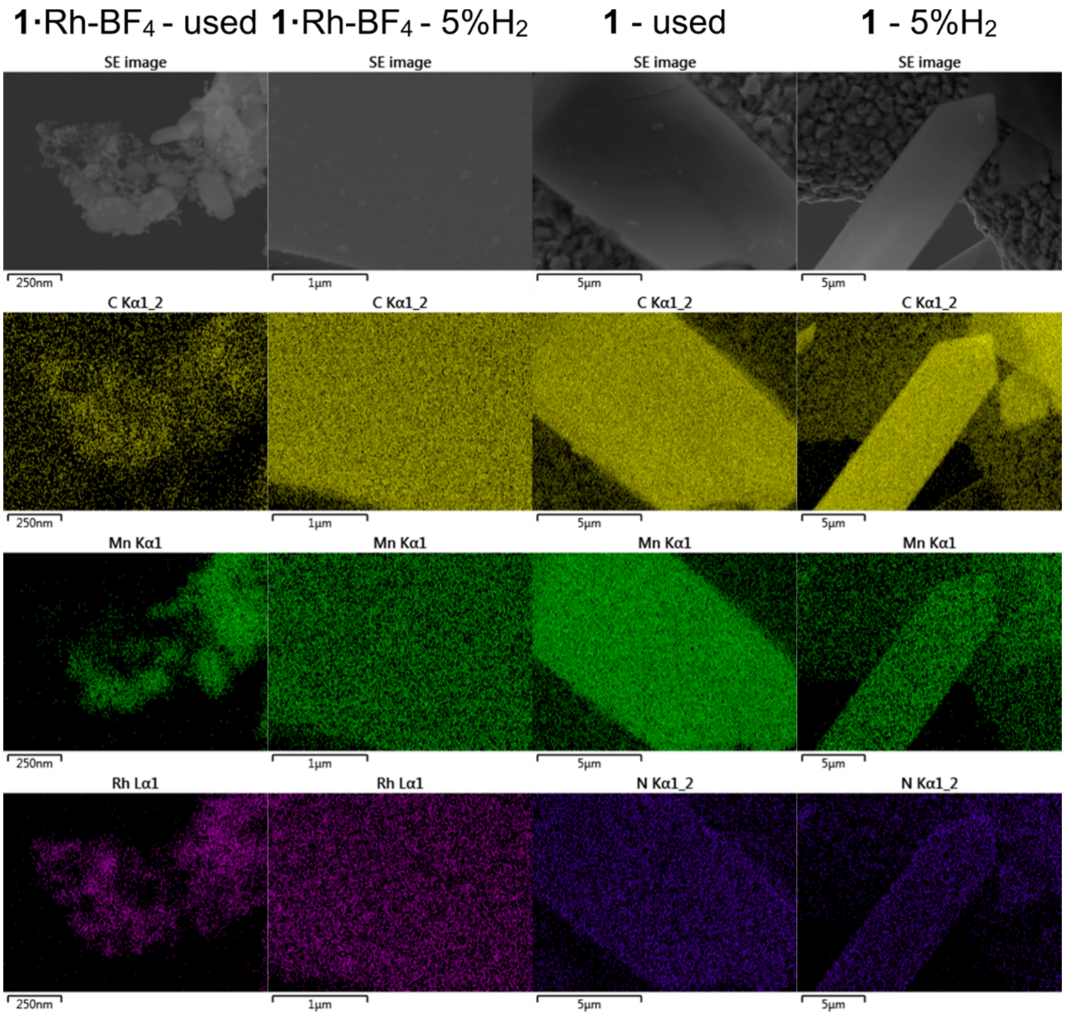

Figure 7: Scanning electron microscopy and energy dispersive spectroscopy maps of metalated samples used: following catalysis testing, and 5% H_2: following reduction in a tube furnace.

The sample **1**·Rh-BF_4-5%H_2 had smaller Rh nanoparticles, from 3 to 12 nm (histogram in Figure S10), embedded in larger lower electron density porous particles, which we hypothesise is a porous C doped with N amorphous matrix. EDS mapping confirmed that the high dispersion of Rh exists in the carbon-rich phase. This reduced sample, **1**·Rh-BF_4-5%H_2, displays characteristics of an intermediate material between the template MOF **1**·Rh-BF_4 and the activated catalyst **1**·Rh-BF_4-used, where the Rh nanoparticles are being formed, but the MOF linkers are not fully decomposed and Mn crystalline phases, *e.g.* MnO and $MnCO_3$, are absent (Figure 8).

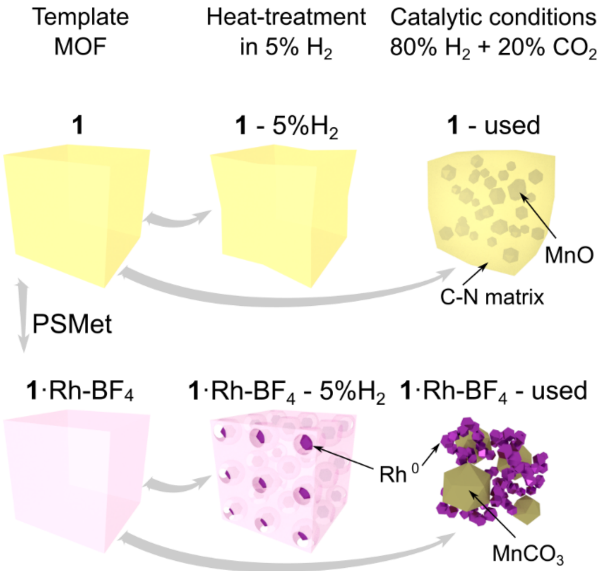

Figure 8: Simplified illustration of the structures of **1** and **1**·Rh-BF_4 after heat treatment in 5% H_2 and after CO_2 hydrogenation catalysis testing.

As for the non-metalated MOF (**1**), small medium electron density crystals embedded in N-doped carbon were present in **1**-used (Figure 6 and 8). The crystals had been identified in PXRD as MnO derived from the aggregation of the Mn trimers in **1** (Figure 3). Lastly, **1**-5%H_2 consisted of low electron density micrometric particles, and no crystals or nanoparticles embedded within those particles were observed. This was in agreement with PXRD analysis that showed a partial loss of crystallinity, but no other crystalline phase formed.

The surface of the template MOFs (**1** and **1**·Rh-BF_4), the reduced samples and the used catalysts (Figure 8) were analysed by XPS. Firstly the elements on the surface are quantified and discussed, followed by a detailed analysis of the binding energy of Mn 2p, Rh 3d, N 1s using high resolution spectra. The six samples are compared to investigate whether the reduced sample is a possible intermediate state of the MOF-templating process and to better understand the mechanism of this transformation.

Surface elemental quantification by XPS for the template MOFs and MOF-derived samples from reduction in 5% H_2 and used for CO_2 hydrogenation catalysis testing are displayed in Table 2. For the metalated MOF **1**·Rh-BF_4, a loss of 14 at% of carbon from its surface was observed after catalysis testing, indicating that the used catalyst still presents a significant amount of adventitious carbon. In particular, the surface of Na salts (NaCl, NaF and $NaMnF_3$) appear to be largely covered by carbon, considering surface characterisation (XPS) versus bulk characterisation (PXRD). In contrast, N contained in the parent MOF linkers is completely absent in the used catalyst, evidence of the complete decomposition of the organic linkers. As a result of the linker decomposition, other elements which were in the interior of the MOF become exposed and display higher relative amounts, *e.g.* Mn.

Table 2: Quantitative elemental analysis by X-ray photoelectron spectroscopy for the MOFs and MOF-derived samples.

Atomic %	**1**·Rh-BF_4	**1**·Rh-BF_4-5%H_2	**1**·Rh-BF_4-used	**1**	**1**-5%H_2	**1**-used[a]
C	72	73	62	74.8	74.7	73.0
N	10	9.5	0	9.9	9.7	7.3
Mn	2.62	3.5	6.8	2.8	3.8	5.2
O	11.7	11.4	18	11.54	11.5	13.1
Rh	0.78	1.17	6.4	-	-	-
Cl	0.3	0.43	0.65	0.1	0.1	0.2
Na	0.13	0.08	1.63	0.11	-	0.1
F	1.7	0.35	2.2	-	-	-
B	0.37	0.41	2.3	0.12	-	0.4
Si	-	-	-	0.39	0.24	0.6
S	0.32	-	-	0.16	-	-

[a] Normalised data (details in SI)

The sample **1**·Rh-BF_4-5%H_2 derived from heat treatment of **1**·Rh-BF_4 in 5% H_2 displayed a lower amount of exposed Rh (1.2%) than **1**·Rh-BF_4-used (6.4%) but a higher amount than its precursor **1**·Rh-BF_4 (0.78%), indicating an intermediate state between the MOF as-synthesised and the used catalyst. The compositions of C, N, Mn and O remain unchanged when comparing **1**·Rh-BF_4 and **1**·Rh-BF_4-5%H_2 providing evidence that the synthesis of Rh nanoparticles occurs as a first step, which then assists in the catalytic decomposition of the organic linkers. Analysis of the bare MOF supports this theory as there is only a small difference in the element composition among **1**, and the samples derived from reduction (**1**-5%H_2) and catalysis treatment (**1**-used). Nitrogen quantification was 9.9, 9.7 and 7.3% for **1**, **1**-5%H_2, and **1**-used, respectively and even after 90 h on stream only 26% of the N is lost in the absence of Rh. Mn quantification indicates an increase in surface Mn, possibly due to the formation of MnO crystals close to the surface.

Analysis of the high resolution XPS spectra clarified the state of the surface elements of the MOFs (**1** and **1**·Rh-BF_4) at different stages of decomposition (as-synthesised, reduced in 5%H_2 and used). Starting with Mn, a strong satellite peak for Mn 2p relative to the main peak was observed for both **1** and **1**·Rh-BF_4 (Figure 9). Resolved satellite peaks on the high binding energy side of the Mn $2p^{3/2}$ peak is consistent with MnO references.[50-52] However, the overall peak shape and the intensity of the satellite peak relative to the main peak differs from reference Mn oxide materials. The distinctive peak shape is attributed to the unique local environment of the Mn in the MOF framework, where the Mn trimer is coordinated by O and N from the organic linkers. Satellite peaks for Mn oxides have been reported to arise from shake-up processes[50] that occur as a result of photoelectrons that lose energy through the promotion of valence electrons from an occupied state to a higher unoccupied level.[53] It is reasonable to assume that in the case of **1** and **1**·Rh-BF_4 this shake-up results in unusually intense satellite peaks due to the coordination of the Mn node by the chelating di-pyrazole moiety. Therefore, the presence of the shake-up for Mn 2p is indicative of the coordination of the inorganic node by the organic linkers and provides strong evidence for the presence of the MOF structure. After reduction of the MOFs, a minor increase in the intensity of the satellite peak for **1**-5%H_2 and **1**·Rh-BF_4-5%H_2 was observed when comparing to the samples prior to reduction. The relative fraction of intensity for the satellite peak for each spectra was determined using component fitting, with the ratio of this peak for **1**-5%H_2 w.r.t. **1** being 1.15, and for **1**·Rh-BF_4-5%H_2 w.r.t. **1**·Rh-BF_4 being 1.17. This minor increase can be attributed to a cleaner surface of the material after the reduction treatment. Thus despite the partial loss of crystallinity observed with PXRD, the inorganic nodes are still likely coordinated by the organic linkers in a disordered structure. In contrast, after catalysis testing, the satellite peak intensity for the Mn 2p peak is reduced for **1**·Rh-BF$_4$-used, due to the formation of $MnCO_3$, with an intensity ratio of 0.71. Further, the lack of N signal for **1**·Rh-BF$_4$-used indicates the complete removal of the di-pyrazole moiety from the surface. The satellite peak is reduced further for **1**-used, with relative intensity ratio of 0.24 w.r.t. **1**, and whose spectral envelope becomes similar to oxide forms such as MnO. This confirms that long term testing of **1** for CO_2 hydrogenation caused the formation of MnO on the surface and loss of the Mn trimer present in the original MOF.

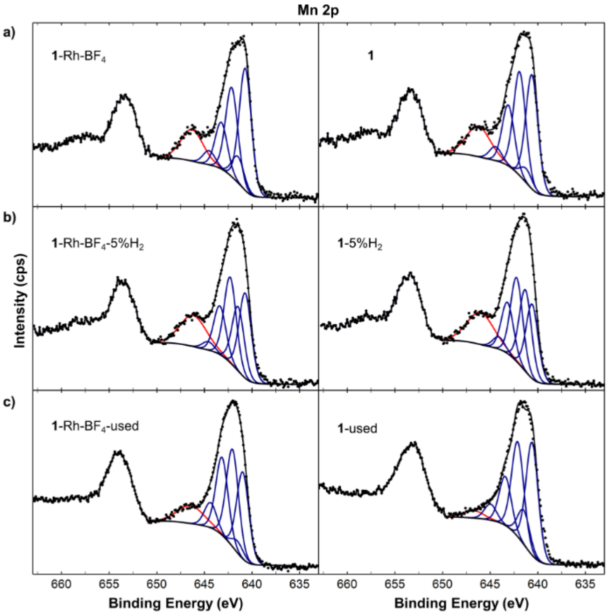

Figure 9: Selected, representative high resolution Mn 2p spectra of **1** and **1**·Rh-BF$_4$ (a) after heat treatment in 5% H_2 (b) and after CO_2 hydrogenation catalysis testing (c). Fitting of the Mn $2p^{3/2}$ peak was undertaken using standard GL(30) components. Red component accounts for intensity in region associated with a satellite peak.

For the Rh containing samples, **1**·Rh-BF$_4$-used contains a significant fraction of Rh^0 based on the component fitting of the Rh 3d peak (Figure 10), whereas the sample reduced in a tube furnace, **1**·Rh-BF$_4$-5%H$_2$, can be fit with three doublets of roughly equal proportions (i.e. Rh^0, Rh^I and Rh^{III}). The low binding energy doublet is associated with Rh^0. The remaining two doublets are assigned to Rh^I and Rh^{III}, where Rh^I is Rh bound to the linker as shown in Figure 1, and Rh^{III} is Rh still bound to the linker but oxidised due to exposure to air at the surface (these are not representative of the bulk material). Both Rh oxidation states were identified in the original report of this MOF by Bloch *et al.* using single-crystal X-ray diffraction (SCXRD).[43] Combined with the Rh^{0} observed, this can be interpreted as the presence of both Rh nanoparticles and of Rh binding to the linker. Lastly, for **1**·Rh-BF$_4$ as-synthesised, the high binding energy doublet dominates the spectrum, in agreement with a large amount of Rh binding to di-pyrazole moieties.

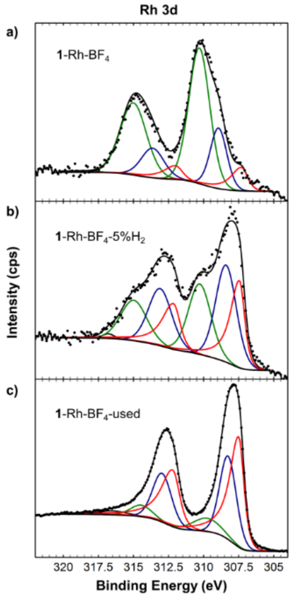

Figure 10: Selected, representative high resolution Rh 3d spectra of **1**·Rh-BF$_4$ (a) after heat treatment in 5% H_2 (b) and after CO_2 hydrogenation catalysis testing (c). The red doublets were assigned to Rh^{0}, blue for both Rh^{I} and Rh_2O_3, and green for Rh^{III} (SI). From the first report of this MOF by Bloch *et al.*, both Rh^{I} and Rh^{III} were identified by SCXRD,[43] where Rh^{III} was formed from the oxidation of Rh^{I}. Peak assignments for Rh^{I} and Rh^{III} from the literature were used for peak assignment as detailed in Table S4.

For the parent samples **1** and **1**·Rh-BF$_4$ and reduced samples, **1**-5%H_2 and **1**·Rh-BF$_4$-5%H_2, the high resolution N 1s spectra could be fit with the model ligand components (as described in SI) at approximately 399.5 eV and 401.1 eV (Figure 11). Comparing the MOFs with the reduced samples, the higher binding energy component MC2 has increased in intensity relative to MC1. In addition, MC1 has shifted to a lower binding energy position consistent with the original di-pyrazole moiety. This is still present with considerable intensity, in agreement with the surface decomposition of a fraction of the organic ligands and with the preferential decomposition of the ligands bridging the Mn nodes. The templated catalyst **1**-used required a modification of the fitting components, where the spectrum is dominated by a peak at 398.8 eV. The higher binding energy contributions have significantly reduced, but still comprise a considerable amount of overall N in the sample, indicating that the ligand has likely decomposed, and N has now formed a different phase. Lastly, N is not detected for **1**·Rh-BF_4-used indicating that not only has the ligand is decomposed, but N has been completely removed from the structure during the catalysis tests.

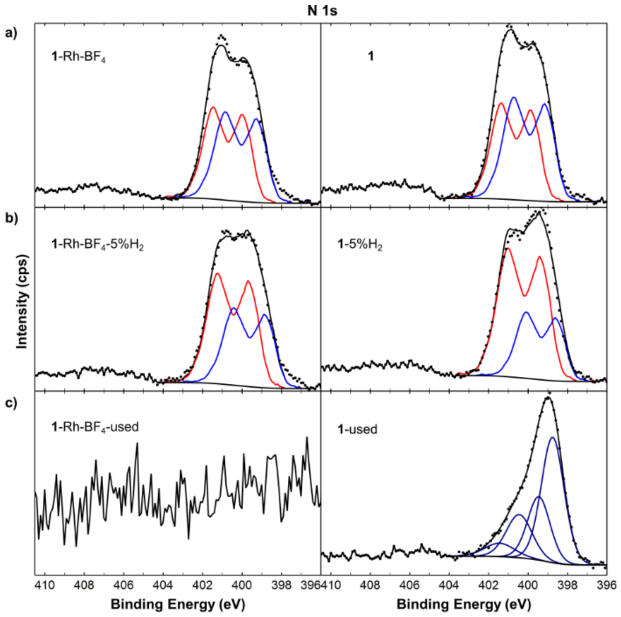

Figure 11: Selected, representative high resolution N 1s spectra of **1** and **1**·Rh-BF_4 (a) after heat treatment in 5% H_2 (b) and after CO_2 hydrogenation catalysis testing (c). Fitting of the N 1s peak for all samples except (c) was undertaken using a model component based on experimental data, specifically data collected from the H_2L linker presented in Figure S13c. The blue component at lower binding energy (MC1) is assigned to the linker flanked by two Mn nodes in the MOF while the higher binding energy component (MC2) in red represents the ligand coordinated with Mn.

2.6. Conclusions

In this study we describe the use of Rh-metalated Mn-MOFs as templates for Rh^0 nanoparticles. The MOF-templating occurred under highly reducing conditions (80% H_2 and 20% CO_2 at 350 °C), as opposed to commonly used pyrolysis and calcination methods. To the best of our knowledge, this is the first report of MOF-derived Rh material. The MOF-derived nanoparticles were applied as catalysts for CO_2 hydrogenation. The chemical composition of the template MOF influenced the composition of the active catalyst and the chemical selectivity obtained. The catalyst derived from **1**·Rh_2 had the simplest composition, Rh^0 nanoparticles and MnO microcrystals. In comparison, the addition of the counter-ion BF_4^- in the template **1**·Rh-BF_4 resulted in a catalyst with Rh^0 nanoparticles, $MnCO_3$ and other Na-phases.

The thorough characterization of the samples by PXRD, electron microscopy and XPS allowed us to understand the MOF-templating mechanism for this MOF-derived catalyst. As illustrated in Figure 8, Rh^0 is formed by reduction of the Rh atoms within the metalated MOF in the presence of H_2 gas. These Rh^0 nanoparticles dispersed in a porous C-matrix then assist with the decomposition of the organic ligands, due to Rh^0 hydrogenolysis properties,[54-56] until the final catalyst is composed of a 3D mesh of Rh nanoparticles, $MnCO_3$ or MnO and other salts depending on the counter-ion. In the absence of Rh, the reducing treatment does not affect the MOF significantly; loss of crystallinity is observed after reduction, but the organic ligands and the Mn atoms are not substantially reacted and display similar properties to the as-synthesised MOF. However, long term exposure to CO_2 hydrogenation reaction conditions caused the full decomposition of the framework, as the final material has substantially lost both crystallinity and the binding state of the elements. Interestingly, the catalyst derived from **1** was composed of MnO crystals embedded in an amorphous phase containing both C and N. As such a phase is not observed in the Rh-containing catalyst, this result provides further evidence that the Rh hydrogenolysis properties facilitate the removal of these elements. Understanding the mechanism of MOF-templating in H_2 may permit the synthesis of different metallic nanoparticles of controlled size for numerous applications, including catalysis.

2.7. Acknowledgements

Aspects of this work were undertaken at the Powder diffraction beamline of the Australian Synchrotron. The authors acknowledge the Science and Industry Endowment Fund (SIEF), the Commonwealth Scientific and Industrial Research Organisation (CSIRO) and the University of Adelaide for funding this research. RL acknowledges the University of Adelaide for the Beacon of Enlightenment PhD Scholarship.

2.8. References

1. Zaera, F., The Surface Chemistry of Heterogeneous Catalysis: Mechanisms, Selectivity, and Active Sites. *The Chemical Record* **2005**, *5*, 133-144.

2. Roduner, E., Understanding Catalysis. *Chem. Soc. Rev.* **2014**, *43*, 8226-8239.

3. Taylor, H. S., A Theory of the Catalytic Surface. *Proc. R. Soc. London, A* **1925**, *108*, 105-111.

4. Zhang, S.; Nguyen, L.; Zhu, Y.; Zhan, S.; Tsung, C.-K.; Tao, F., In-Situ Studies of Nanocatalysis. *Acc. Chem. Res.* **2013**, *46*, 1731-1739.

5. Cuenya, B. R., Synthesis and Catalytic Properties of Metal Nanoparticles: Size, Shape, Support, Composition, and Oxidation State Effects. *Thin Solid Films* **2010**, *518*, 3127-3150.

6. Frontera, P.; Macario, A.; Ferraro, M.; Antonucci, P., Supported Catalysts for CO2 Methanation: A Review. *Catalysts* **2017**, *7*.

7. White, R. J.; Luque, R.; Budarin, V. L.; Clark, J. H.; Macquarrie, D. J., Supported Metal Nanoparticles on Porous Materials. Methods and Applications. *Chem. Soc. Rev.* **2009**, *38*, 481-94.

8. Campelo, J. M.; Luna, D.; Luque, R.; Marinas, J. M.; Romero, A. a., Sustainable Preparation of Supported Metal Nanoparticles and Their Applications in Catalysis. *ChemSusChem* **2009**, *2*, 18-45.

9. Batten, S. R.; Champness, N. R.; Chen, X. M.; Garcia-Martinez, J.; Kitagawa, S.; Ohrstrom, L.; O'Keeffe, M.; Suh, M. P.; Reedijk, J., Terminology of Metal-Organic Frameworks and Coordination Polymers (Iupac Recommendations 2013). *Pure Appl. Chem.* **2013**, *85*, 1715-1724.

10. Furukawa, H.; Cordova, K. E.; O'Keeffe, M.; Yaghi, O. M., The Chemistry and Applications of Metal-Organic Frameworks. *Science* **2013**, *341*, 1230444.

11. Chung, Y. G.; Camp, J.; Haranczyk, M.; Sikora, B. J.; Bury, W.; Krungleviciute, V.; Yildirim, T.; Farha, O. K.; Sholl, D. S.; Snurr, R. Q., Computation-Ready, Experimental Metal–Organic Frameworks: A Tool to Enable High-Throughput Screening of Nanoporous Crystals. *Chem. Mater.* **2014**, *26*, 6185-6192.

12. Cohen, S. M., Postsynthetic Methods for the Functionalization of Metal-Organic Frameworks. *Chem. Rev.* **2012**, *112*, 970-1000.

13. Evans, J. D.; Sumby, C. J.; Doonan, C. J., Post-synthetic Metalation of Metal-Organic Frameworks. *Chem. Soc. Rev.* **2014**, *43*, 5933-5951.

14. He, Y.; Zhou, W.; Qian, G.; Chen, B., Methane Storage in Metal-Organic Frameworks. *Chem. Soc. Rev.* **2014**, *43*, 5657-5678.

15. Furukawa, H.; Cordova, K. E.; O'Keeffe, M.; Yaghi, O. M., The Chemistry and Applications of Metal-Organic Frameworks. *Science* **2013**, *341*, 974-+.

16. Suh, M. P.; Park, H. J.; Prasad, T. K.; Lim, D.-W., Hydrogen Storage in Metal–Organic Frameworks. *Chem. Rev.* **2011**, *112*, 782-835.

17. Li, J.-R.; Sculley, J.; Zhou, H.-C., Metal–Organic Frameworks for Separations. *Chem. Rev.* **2011**, *112*, 869-932.

18. Corma, A.; Garcia, H.; Xamena, F. X. L. I., Engineering Metal Organic Frameworks for Heterogeneous Catalysis. *Chem. Rev.* **2010**, *110*, 4606-4655.

19. Xia, W.; Mahmood, A.; Zou, R.; Xu, Q., Metal-Organic Frameworks and Their Derived Nanostructures for Electrochemical Energy Storage and Conversion. *Energy Environ. Sci.* **2015**, *8*, 1837-1866.

20. Song, Y.; Li, X.; Sun, L.; Wang, L., Metal/Metal Oxide Nanostructures Derived from Metal-Organic Frameworks. *RSC Adv.* **2015**, *5*, 7267-7279.

21. Shen, K.; Chen, X.; Chen, J.; Li, Y., Development of MOF-Derived Carbon-Based Nanomaterials for Efficient Catalysis. *ACS Catal.* **2016**, *6*, 5887-5903.

22. Cao, X.; Tan, C.; Sindoro, M.; Zhang, H., Hybrid Micro-/Nano-Structures Derived from Metal-Organic Frameworks: Preparation and Applications in Energy Storage and Conversion. *Chem. Soc. Rev.* **2017**, *46*, 2660-2677.

23. Xie, Z.; Xu, W.; Cui, X.; Wang, Y., Recent Progress in Metal–Organic Frameworks and Their Derived Nanostructures for Energy and Environmental Applications. *ChemSusChem* **2017**, *10*, 1645-1663.

24. Zhao, S.-N.; Song, X.-Z.; Song, S.-Y.; Zhang, H.-j., Highly Efficient Heterogeneous Catalytic Materials Derived from Metal-Organic Framework Supports/Precursors. *Coord. Chem. Rev.* **2017**, *337*, 80-96.

25. Oar-Arteta, L.; Wezendonk, T.; Sun, X.; Kapteijn, F.; Gascon, J., Metal Organic Frameworks as Precursors for the Manufacture of Advanced Catalytic Materials. *Mater. Chem. Front.* **2017**, *1*, 1709-1745.

26. Kaneti, Y. V.; Tang, J.; Salunkhe, R. R.; Jiang, X. C.; Yu, A. B.; Wu, K. C. W.; Yamauchi, Y., Nanoarchitectured Design of Porous Materials and Nanocomposites from Metal-Organic Frameworks. *Adv. Mater.* **2017**, *29*.

27. Wang, H.; Liu, M.; Guo, S.; Wang, Y.; Han, X.; Bai, Y., Efficient Oxidation of O-Xylene over CeO2 Catalyst Prepared from a Ce-MOF Template: The Promotion of K+ Embedding Substitution. *Mol. Catal.* **2017**, *436*, 120-127.

28. Santos, V. P., *et al.*, Metal Organic Framework-Mediated Synthesis of Highly Active and Stable Fischer-Tropsch Catalysts. *Nat. Commun.* **2015**, *6*, 6451.

29. Niu, H. Y.; Liu, S. L.; Cai, Y. Q.; Wu, F. C.; Zhao, X. L., MOF Derived Porous Carbon Supported Cu/Cu2O Composite as High Performance Non-Noble Catalyst. *Microporous Mesoporous Mater.* **2016**, *219*, 48-53.

30. Xu, D.; Pan, Y.; Chen, M.; Pan, Q.; Zhu, L.; Xue, M.; Zhang, D.; Fang, Q.; Qiu, S., Synthesis and Application of a MOF-Derived Ni@C Catalyst by the Guidance from an *in situ* Hot Stage in Tem. *RSC Adv.* **2017**, *7*, 26377-26383.

31. Chen, D.; Huang, M.; He, S.; He, S.; Ding, L.; Wang, Q.; Yu, S.; Miao, S., Ru-MOF Enwrapped by Montmorillonite for Catalyzing Benzene Hydrogenation. *Appl. Clay Sci.* **2016**, *119*, 109-115.

32. Wang, Z.; Li, X.; Yang, Y.; Cui, Y.; Pan, H.; Wang, Z.; Chen, B.; Qian, G., Highly Dispersed Beta-Nis Nanoparticles in Porous Carbon Matrices by a Template Metal-Organic Framework Method for Lithium-Ion Cathode. *J. Mater. Chem. A* **2014**, *2*, 7912-7916.

33. Senkan, S.; Kahn, M.; Duan, S.; Ly, A.; Leidholm, C., High-Throughput Metal Nanoparticle Catalysis by Pulsed Laser Ablation. *Catal. Today* **2006**, *117*, 291-296.

34. Jacinto, M. J.; Kiyohara, P. K.; Masunaga, S. H.; Jardim, R. F.; Rossi, L. M., Recoverable Rhodium Nanoparticles: Synthesis, Characterization and Catalytic Performance in Hydrogenation Reactions. *Applied Catalysis A: General* **2008**, *338*, 52-57.

35. Ye, X.-R.; Lin, Y.; Wang, C.; Engelhard, M. H.; Wang, Y.; Wai, C. M., Supercritical Fluid Synthesis and Characterization of Catalytic Metal Nanoparticles on Carbon Nanotubes. *J. Mater. Chem.* **2004**, *14*, 908-908.

36. Yan, N.; Yuan, Y.; Dyson, P. J., Rhodium Nanoparticle Catalysts Stabilized with a Polymer That Enhances Stability without Compromising Activity. *Chem. Commun.* **2011**, *47*, 2529-2531.

37. Karelovic, A.; Ruiz, P., CO2 Hydrogenation at Low Temperature over Rh/Gamma-Al2O3 Catalysts: Effect of the Metal Particle Size on Catalytic Performances and Reaction Mechanism. *Appl. Catal., B* **2012**, *113*, 237-249.

38. Buchel, R.; Baiker, A.; Pratsinis, S. E., Effect of Ba and K Addition and Controlled Spatial Deposition of Rh in Rh/Al2O3 Catalysts for CO2 Hydrogenation. *Appl. Catal., A* **2014**, *477*, 93-101.

39. Karelovic, A.; Ruiz, P., Mechanistic Study of Low Temperature CO2 Methanation over Rh/TiO2 Catalysts. *J. Catal.* **2013**, *301*, 141-153.

40. Yuan, Y.; Yan, N.; Dyson, P. J., Advances in the Rational Design of Rhodium Nanoparticle Catalysts: Control via Manipulation of the Nanoparticle Core and Stabilizer. *ACS Catal.* **2012**, *2*, 1057-1069.

41. Jiang, B., *et al.*, Mesoporous Metallic Rhodium Nanoparticles. *Nat. Commun.* **2017**, *8*, 15581.

42. Bloch, W. M.; Doonan, C. J.; Sumby, C. J., Using Hinged Ligands to Target Structurally Flexible Copper(Ii) MOFs. *CrystEngComm* **2013**, *15*, 9663-9671.

43. Bloch, W. M.; Burgun, A.; Coghlan, C. J.; Lee, R.; Coote, M. L.; Doonan, C. J.; Sumby, C. J., Capturing Snapshots of Post-Synthetic Metallation Chemistry in Metal–Organic Frameworks. *Nat. Chem.* **2014**, *6*, 906-912.

44. Lippi, R., *et al.*, Highly Active Catalyst for CO_2 Methanation Derived from a Metal Organic Framework Template. *J. Mater. Chem. A* **2017**, *5*, 12990-12997.

45. Schmitt, B.; Bronnimann, C.; Eikenberry, E. F.; Gozzo, F.; Hormann, C.; Horisberger, R.; Patterson, B., Mythen Detector System. *Nucl. Instrum. Methods Phys. Res., Sect. A* **2003**, *501*, 267-272.

46. Madsen, I. C.; Scarlett, N. V. Y.; Riley, D. P.; Raven, M. D., Quantitative Phase Analysis Using the Rietveld Method. In *Modern Diffraction Methods*, Wiley-VCH Verlag GmbH & Co. KGaA: 2012; pp 283-320.

47. *Topas V5: General Profile and Structure Analysis Software for Powder Diffraction Data*, Bruker AXS GmbH: Karlsruhe, Germany, 2012.

48. Burgun, A.; Coghlan, C. J.; Huang, D. M.; Chen, W.; Horike, S.; Kitagawa, S.; Alvino, J. F.; Metha, G. F.; Sumby, C. J.; Doonan, C. J., Mapping-out Catalytic Processes in a Metal–Organic Framework with Single-Crystal X-Ray Crystallography. *Angew. Chem. Int. Ed.* **2017**, *56*, 8412-8416.

49. *Powder Diffraction: Theory and Practice*; The Royal Society of Chemistry: Cambridge, UK, 2008; Vol. 24, p 2-3.

50. Oku, M.; Hirokawa, K.; Ikeda, S., X-Ray Photoelectron Spectroscopy of Manganese—Oxygen Systems. *J. Electron Spectrosc. Relat. Phenom.* **1975**, *7*, 465-473.

51. Biesinger, M. C.; Payne, B. P.; Grosvenor, A. P.; Lau, L. W. M.; Gerson, A. R.; Smart, R. S. C., Resolving Surface Chemical States in Xps Analysis of First Row Transition Metals, Oxides and Hydroxides: Cr, Mn, Fe, Co and Ni. *Appl. Surf. Sci.* **2011**, *257*, 2717-2730.

52. Di Castro, V.; Polzonetti, G., Xps Study of Mno Oxidation. *J. Electron Spectrosc. Relat. Phenom.* **1989**, *48*, 117-123.

53. Casey, P.; McCoy, A. P.; Bogan, J.; Byrne, C.; Walsh, L.; O'Connor, R.; Hughes, G., *In situ* Investigations into the Mechanism of Oxygen Catalysis on Ruthenium/Manganese Surfaces and the Thermodynamic Stability of Ru/Mn-Based Copper Diffusion Barrier Layers. *J. Phys. Chem. C* **2013**, *117*, 16136-16143.

54. Holgado, M. J.; Rives, V., Hydrogenolysis of Light-Hydrocarbons on Rh/Tio2 - Catalysts Reduced at High-Temperature. *React. Kinet. Catal. Lett.* **1986**, *32*, 215-219.

55. Carter, J. L.; Cusumano, J. A.; Sinfelt, J. H., Hydrogenolysis of N-Heptane over Unsupported Metals. *J. Catal.* **1971**, *20*, 223-229.

56. Sinfelt, J. H., Catalytic Hydrogenolysis over Supported Metals. *Catalysis Reviews* **1970**, *3*, 175-205.

2.9. Supporting information

Insights into MOF-templating of Rh^0 nanoparticles under reducing conditions

A. Experimental methods

A.1 Materials

All materials were used as provided by the manufacturer, unless stated otherwise. Di-μ-chloro-tetracarbonyldirhodium(I) ($[Rh(CO)_2Cl]_2$) 97% Sigma Aldrich (Australia), sodium tetrafluoroborate ($NaBF_4$) 98% Sigma Aldrich (Australia), Manganese(II) chloride ($MnCl_2$) 98% Sigma Aldrich (Australia), N-N-dimethylformamide (DMF) 99.8% Merck Pty. Ltd. (Australia), anhydrous acetonitrile (CH_3CN) max. 0.005% H_2O Merck Pty. Ltd. (Australia), Silicon Carbide (SiC) 99% 300-355 μm Beijing HWRK Chem Co., Ltd. (China). Water was deionized by reverse osmosis. All gases used were supplied by Coregas (Australia) including custom made mixtures: nitrogen (N4); Argon (N5); Helium (N5); Hydrogen (N5); 25% carbon dioxide with hydrogen balance; and 2.52% ethane, 2.82% ethene, 2.53% acetylene, 2.44% methane, 2.48% carbon dioxide, 2.53% carbon monoxide, 2.51% hydrogen with argon balance, 5% hydrogen with argon balance.

A.2 Thermogravimetric analysis (TGA)

Samples were loaded into Al_2O_3 crucibles and evaluated using a Mettler Toledo TGA 2. The samples were heated to 800 °C at 10 °C/min under N_2 purge gas at 30 mL/min. The sample was allowed to equilibrate at 25 °C in N_2 before the analysis, this section is not shown in the thermogram.

B. Supporting results

B.1 MOF Characterization

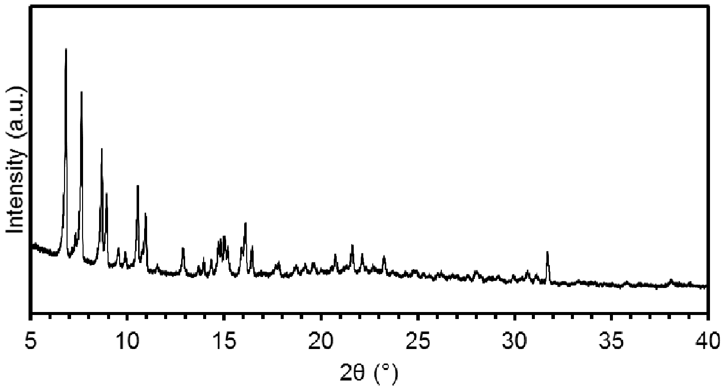

Figure S1: PXRD of 1-Rh-BF$_4$ with Cu radiation.

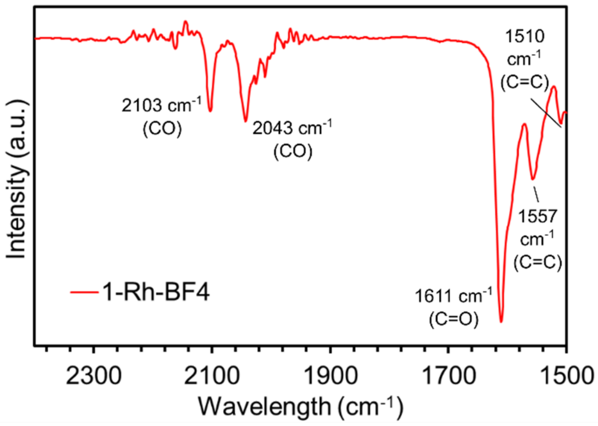

Figure S2: IR spectrum of **1**-Rh-BF$_4$. The displacement of the counter-ion $[Rh(CO)_2Cl_2]^-$ by $[BF_4]^-$ in the MOF is confirmed by the presence of only two major peaks in the region from 2200 and 1900 cm^{-1}. In contrast, the presence of the counter-ion $[Rh(CO)_2Cl_2]^-$ in **1**-Rh$_2$ contributes to a total of five different absorption wavelengths in this region.[1-2]

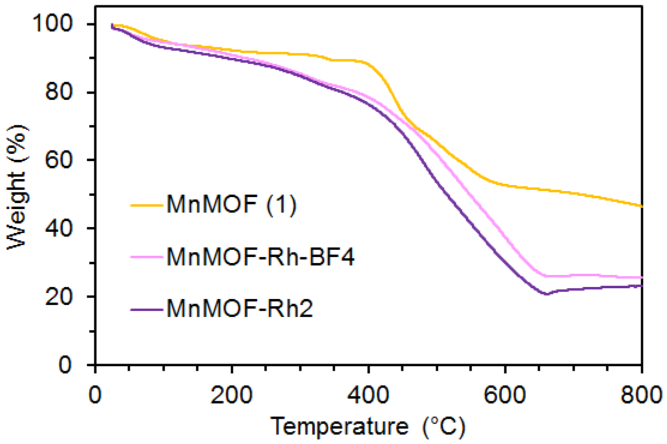

Figure S3: Thermogravimetric analysis of **1**, **1**-Rh-BF_4 and **1**-Rh_2 in N_2 (40 mL/min). Both MnMOF (**1**) and its post synthetically metalated versions display high thermal stability up to 400 °C. From 100 to 400 °C MnMOF (**1**) loses 7 wt% and both **1**-Rh-BF_4 and **1**-Rh_2 lose 17 wt%.

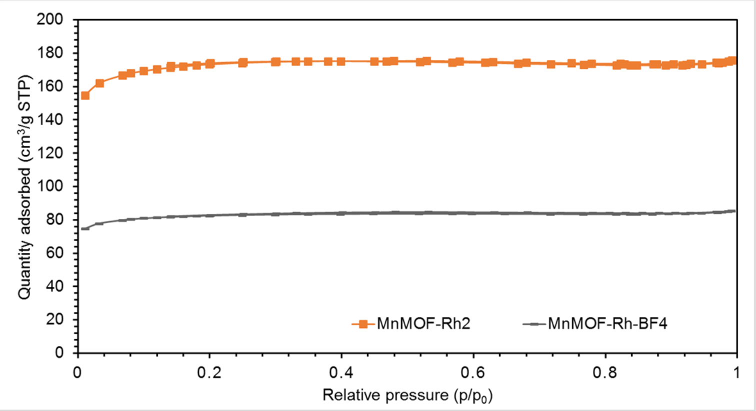

Figure S4: N_2 adsorption isotherm for **1**-Rh-BF_4 and **1**-Rh_2.

Table S1. BET surface area results. The low surface area for **1**-Rh-BF_4 is explained by the presence of NaCl crystals (by-product of the counter-ion exchange) likely blocking some of the pores.

Sample	BET surface area (m^2/g)
1-Rh_2	581.5
1-Rh-BF_4	276.6

B.2 Catalysis results

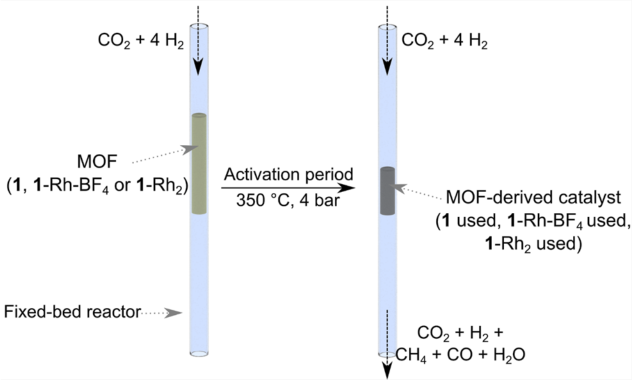

Figure S5: Scheme of *in situ* catalyst activation. Fixed-bed microreactor loaded with MOF (left) and MOF-templated catalyst (right) activated under reaction conditions, i.e. in situ.

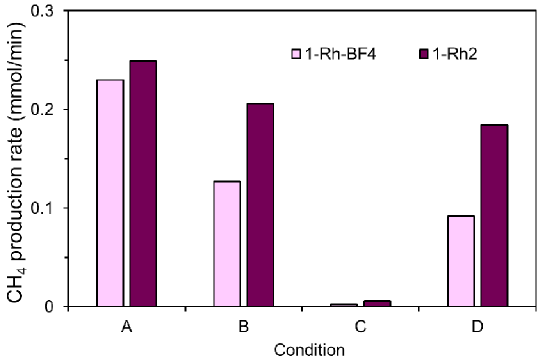

Figure S6: Comparison of average CH_4 production for **1**-Rh-BF_4 and **1**-Rh_2. A lower production rate of CH_4 is observed for the sample where the counter-ion $[Rh(CO)Cl_2]^-$ has been displaced. In condition D **1**-Rh_2 produces approximately double the amount of CH_4 than **1**-Rh-BF_4.

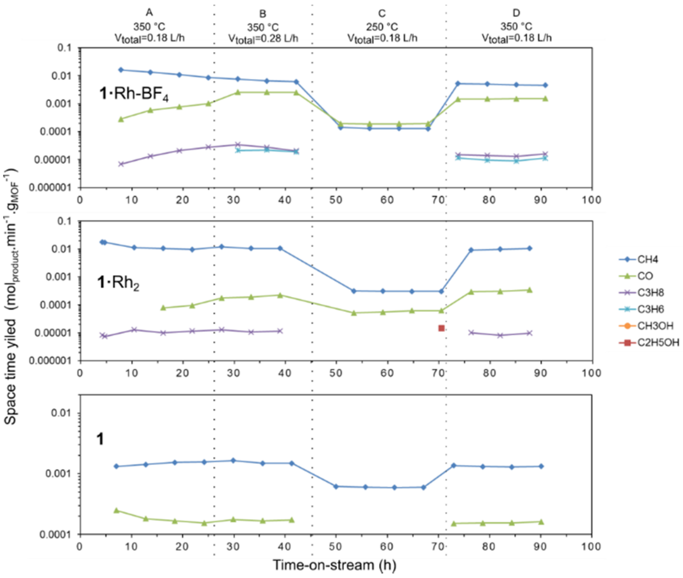

Figure S7: Space-time yield in logarithmic scale for the different precatalysts tested in parallel for CO_2 hydrogenation (Figure 2). Scale used to display with clarity the presence of products in trace amounts.

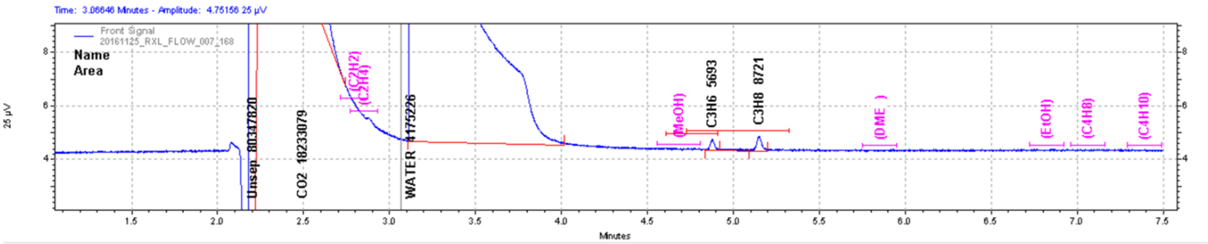

Figure S8: Example of chromatogram of effluent gas from **1**-Rh-BF_4-used. The authors note that the presence of C2 products could not be evaluated due to the proximity of their retention time with CO_2 and water, which were present in high amounts in the gas effluent. However, the presence of C3 is clearly visible.

B.3 XRD

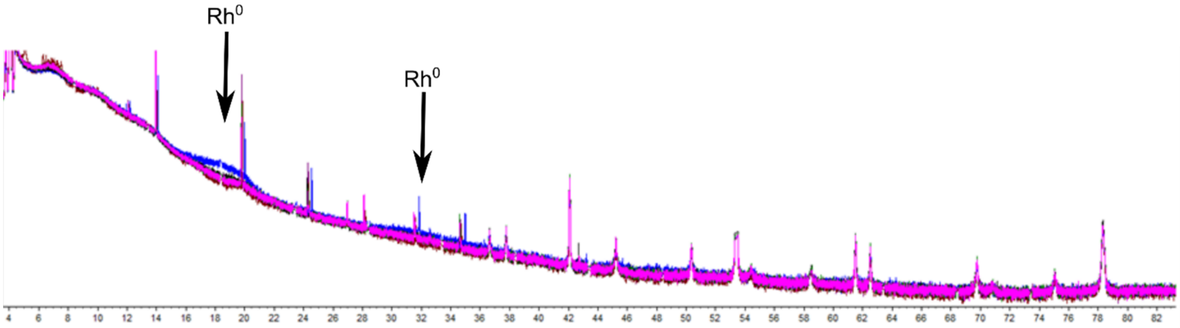

Figure S9: Comparison of XRD patterns from datasets 18, 30 and 50 of **1**·Rh-BF$_4$ in situ XRD experiment (Figure 5). Intensity increase is observed around 19° and 32°, where Rh^0 reflections are expected, indicating the formation of Rh^0 nanoparticles. The shift of other peaks is due to thermal expansion as temperature varied in the course of this experiment.

B.4 TEM nanoparticle sizing

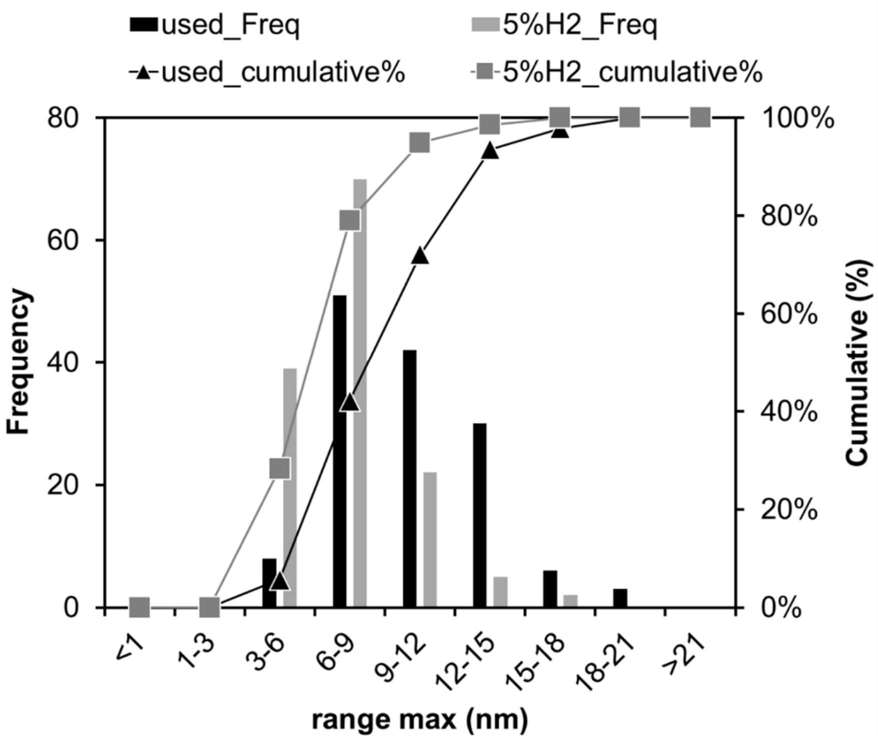

Figure S10: Histogram of Rh^0 nanoparticles size distribution **1**·Rh-BF$_4$-5%H$_2$ and **1**·Rh-BF$_4$-used.

B.5 EDS mapping

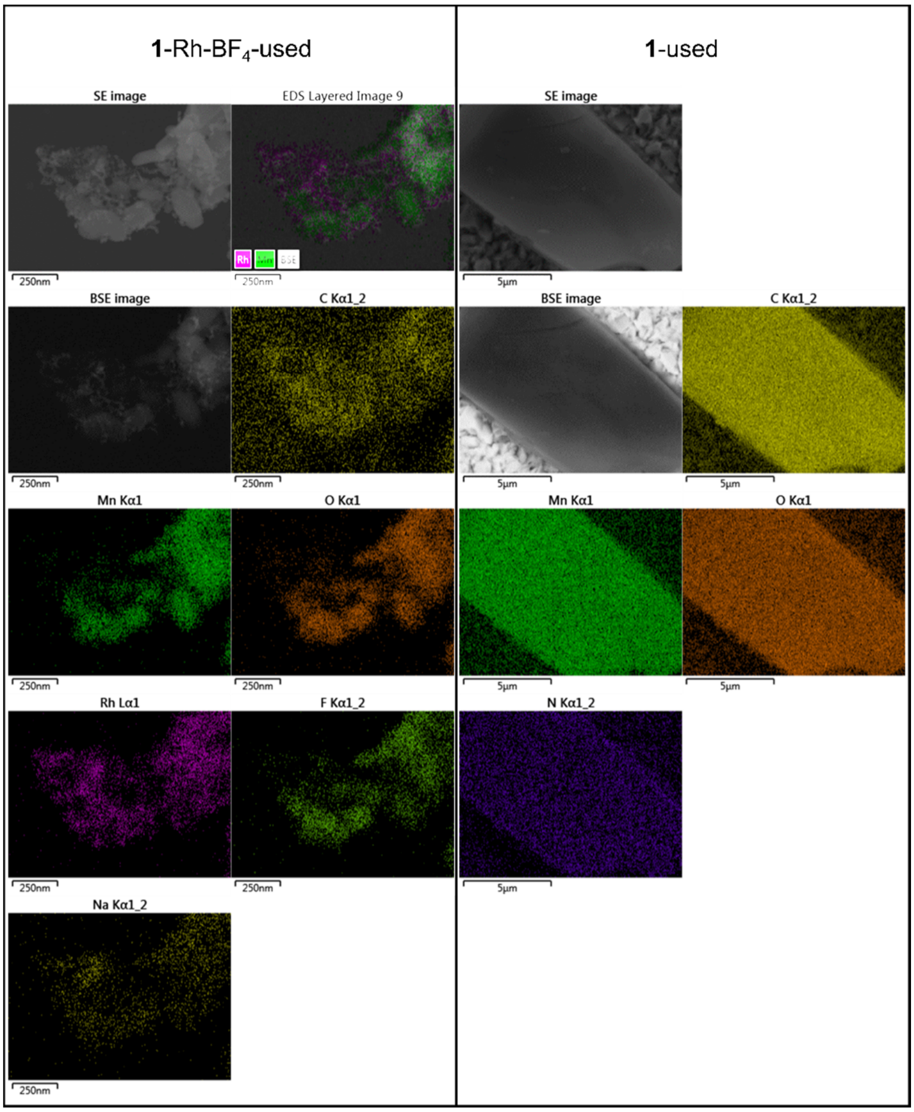

Figure S11: SEM and EDS element maps for **1**-Rh-BF$_4$ and **1** after catalysis testing (used).

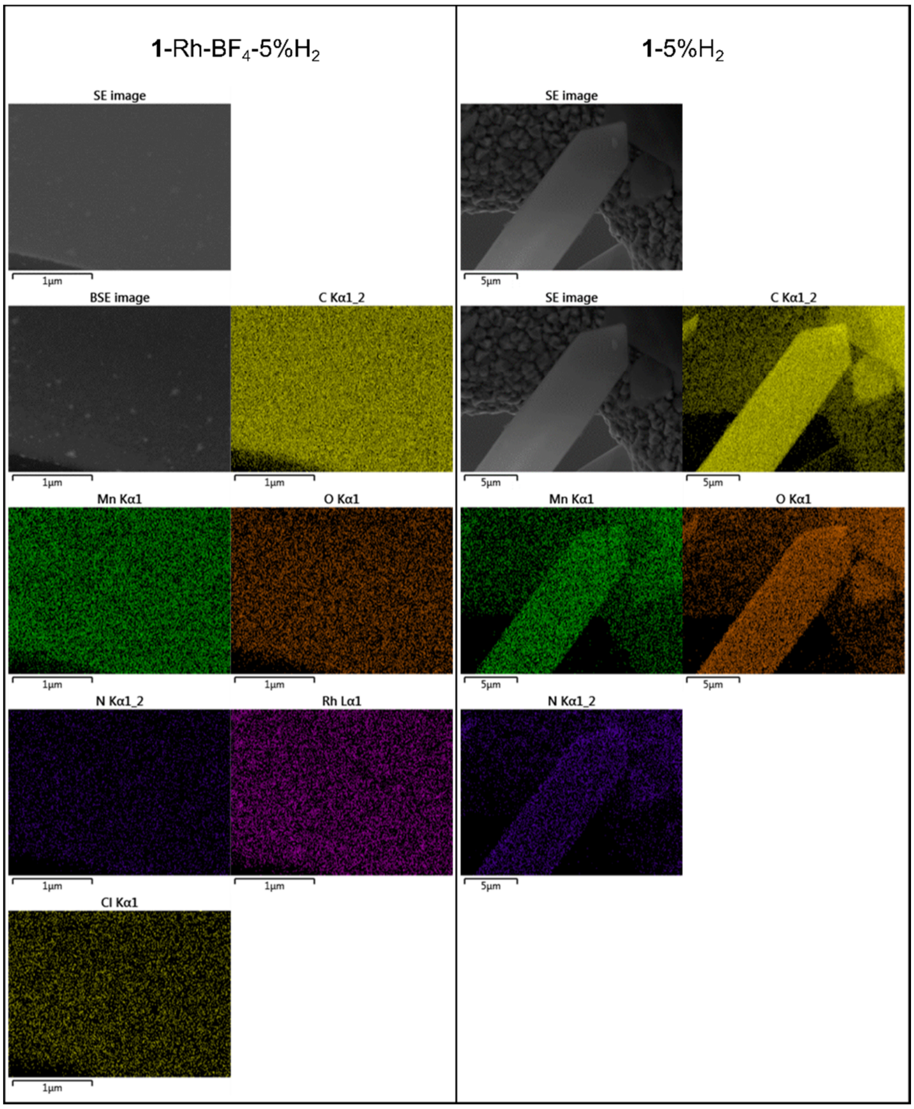

Figure S12: SEM and EDS element maps for **1**-Rh-BF_4 and **1** after reduction in 5%H_2.

B.6 X-ray photoelectron spectroscopy

B.7 Elemental quantification

Table S2: XPS elemental composition.

Elements	Atomic composition (%) ± standard deviation					
	MnMOF (1)	1-5%H2	1 used (normalized)	1-Rh-BF4	1-Rh-BF4-5%H2	1-Rh-BF4 used
C	74.83 ± 0.01	74.72 ± 0.29	73.0	72.1 ± 0.21	73.14 ± 0.37	62.06 ± 0.14
N	9.93 ± 0.28	9.7 ± 0.06	7.3	9.99 ± 0.3	9.51 ± 0.58	-
Mn	2.85 ± 0.08	3.76 ± 0.27	5.2	2.62 ± 0.02	3.51 ± 0.07	6.76 ± 0.39
O	11.54 ± 0.08	11.5 ± 0.01	13.1	11.7 ± 0.06	11.41 ± 0.16	18.04 ± 0.11
Rh	-	-	-	0.78 ± 0.03	1.17 ± 0.07	6.42 ± 0.08
Cl	0.1 ± 0	0.1 ± 0.01	0.2	0.3 ± 0.01	0.43 ± 0.01	0.65 ± 0.04
Na	0.11 ± 0.06	-	0.1	0.13 ± 0.08	0.08 ± 0.01	1.63 ± 0.29
F	-	-	-	1.72 ± 0.08	0.35 ± 0.09	2.15 ± 0.41
B	0.12 ± 0.06	-	0.4	0.37 ± 0.04	0.41 ± 0.06	2.31 ± 0.23
Si	0.39 ± 0	0.24 ± 0.04	0.6	-	-	-
S	0.16 ± 0.01	-	-	0.32 ± 0.08	-	-

Table S3: Data collected for **1**-used and normalization to remove excess of SiO_2 contaminant. [a] Estimated value

Elements (atomic %)	**1** used	**1** used (Excluding excess of SiO_2)	**1** used (Normalized)
C	45.78 ± 0.47	45	73.0
N	4.54 ± 0.33	4.5	7.3
Mn	3.18 ± 0.01	3.18	5.2
O	33.22 ± 0.11	8.1	13.1
Rh	-	-	-
Cl	0.14 ± 0.01	0.14	0.2
Na	0.04 ± 0.02	0.04	0.1
F	-	-	-
B	0.27 ± 0.14	0.27	0.4
Si	12.85 ± 0.12	0.4[a]	0.6
S	-	-	-
total	98.98	61.63	100.0

B.8 High resolution spectra

Rh 3d

Fitting of the Rh 3d peak was undertaken using a combination of Lorentizian assimetric for Rh^0 and GL(30) components for the remaining contributions. A peak separation of 4.7 eV was used for each doublet. A single component was included at high binding energy to account for peak asymmetry that was not accounted for by the existing components.

Table S4: Rh $3d^{3/2}$ peak positions based on fitting presented in Figure 10 and tentative peak assignments based on literature values.

	Peak position (eV) and tentative assignment for Rh $3d^{3/2}$					
Sample	Doublet 1 (red)		Doublet 2 (blue)		Doublet 3 (green)	
1-Rh-BF4	307.3	Ru^0 (Ref 3)	308.9	Rh(I)^	310.3	Rh(III)&
1-Rh-BF4-5%H2	307.4	Ru^0	308.4	Rh(I)^and Rh_2O_3 (Ref 4)	310.3	Rh(III)&
1-Rh-BF4-used	307.5	Ru^0	308.3	Rh_2O_3 (Ref 4)	309.8	Rh(III)&

^Rh(I) has binding energy values in the literature at 308.3 eV[4] and 309 eV[5] for $Rh_2(CO)_4Cl_2$ and 308.5 eV and 308.3 eV for (acrylic resin)-NC-Rh(PPh3)2Cl and (acrylic resin)-NC-Rh, respectively[6]. &Rh(III) has binding energy values in the range of 309.3 – 310.4 eV[3]

N 1s

High resolution N 1s spectra of the ligand (H_2L) component of the MOF was collected to assist with the nitrogen peak assignment. The ligand H_2L is prepared via a 2 step synthesis, starting from bis(3,5-dimethylpyrazol-1-yl)methane, iodination to give (bis(3,5-dimethyl-4-iodopyrazol-1-yl)methane) and Suzuki coupling to give the ligand (H_2L). These 3 compounds were examined and for the first two compounds, a pair of peaks are observed in the N 1s spectra at approximately 398.8 eV (imine) and 400.4 eV (amine) with an intensity ratio (N2:N3) of 44:56. For the third step, where a pair of benzene rings with an acid group on either end are added and represents the ligand used in 1, both peaks are shifted to higher binding energy (399.2 eV and 400.7 eV) (Figure S11).

For the parent samples **1** and **1**·Rh-BF4, the high resolution N 1s spectra could be fit with two components at approximately 399.5 eV and 401.1 eV (Figure 11), representing a further shift to higher binding energy compared to the ligand spectra (Figure S11c). Upshifting of N components upon coordination has been observed previously, for example for Pd and Mn coordination of bipyridine.[7] However it is noted that the binding energy shift seen here is significant compared to the original di-pyrazole spectrum, where organic N components in the range of 401 to 402 eV would generally be associated with N+, such as quaternary amine.[8-9] For **1**·Rh-BF_4, the sample presented a shoulder on the lower binding energy side of the spectra (398.4 eV) which would represent a small contribution consistent with nitride. Interestingly, using the original ligand (H_2L) N 1s spectrum as a model fit component, the N 1s for both parent samples can be fit using 2 components with a ratio of approximately 1:1. The peak position of the lower binding energy component (MC1) is consistent with the original ligand spectrum, while the other component (MC2) is shifted by approximately +0.7 eV. Based on this fit, the higher binding energy contribution would represent the ligand coordinated with the Mn, while the lower binding energy contribution would represent the ligand flanked by two Mn nodes in the MOF structure. Considering this hypothesis, the ratio between the two components MC1:MC2 should be 1:2, instead of 1:1. We believe that this difference is due to either surface orientation or a different stoichiometry on the surface of the MOF comparing to the interior.

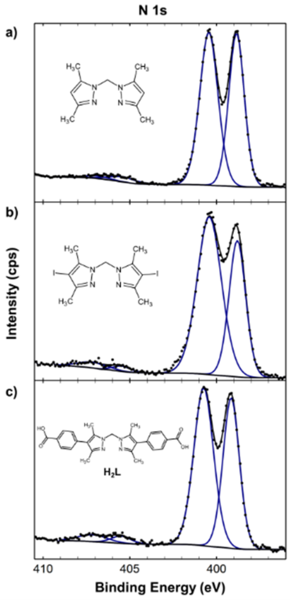

Figure S13: Selected, representative high resolution N 1s spectra of Bis(3,5-dimethylpyrazol-1-yl)methane (a), bis(3,5-dimethyl-4-iodo-1H-pyrazol-1-yl)methane (b), and H_2L (c). Spectra are fitted using standard GL(30) components.

C. References

1. Bloch, W. M.; Burgun, A.; Coghlan, C. J.; Lee, R.; Coote, M. L.; Doonan, C. J.; Sumby, C. J., Capturing Snapshots of Post-Synthetic Metallation Chemistry in Metal–Organic Frameworks. Nat. Chem. 2014, 6, 906-912.

2. Burgun, A.; Coghlan, C. J.; Huang, D. M.; Chen, W.; Horike, S.; Kitagawa, S.; Alvino, J. F.; Metha, G. F.; Sumby, C. J.; Doonan, C. J., Mapping-out Catalytic Processes in a Metal–Organic Framework with Single-Crystal X-Ray Crystallography. Angew. Chem. Int. Ed. 2017, 56, 8412-8416.

3. Goldshleger, N. F.; Azbel, B. I.; Isakov, Y. I.; Shpiro, E. S.; Minachev, K. M., Selective Rhodium-Containing Zeolite Catalysts for Cyclodimerization of Bicyclo 2.2.1 Hepta-2,5-Diene. J. Mol. Catal. A: Chem. 1996, 106, 159-168.

4. Okamoto, Y.; Ishida, N.; Imanaka, T.; Teranishi, S., Active States of Rhodium in Rhodium Exchanged Y-Zeolite Catalysts for Hydrogenation of Ethylene and Acetylene and Dimerization of Ethylene Studied with X-Ray Photoelectron-Spectroscopy. J. Catal. 1979, 58, 82-94.

5. Nefedov, V. I.; Shubochk.Ef; Kolomnik.Is; Baranovs.Ib; Kukolev, V. P.; Golubnic.Ma; Shubochk.Lk; Poraikos.Ma; Volpin, M. E., X-Ray Electron Spectroscopy in Studying Rhodium Complexes. Zh. Neorg. Khim. 1973, 18, 845-848.

6. Giannandrea, R.; Mastrorilli, P.; Zaccaria, G.; Nobile, C. F., Hydrogenation of Organic Substrates by Isocyanide Polymer-Bound Rh(Pph(3))(3)Cl. J. Mol. Catal. A: Chem. 1996, 109, 113-117.

7. Leng, W.; Ge, R.; Dong, B.; Wang, C.; Gao, Y., Bimetallic Docked Covalent Organic Frameworks with High Catalytic Performance Towards Tandem Reactions. RSC Adv. 2016, 6, 37403-37406.

8. Beamson, G.; Briggs, D., High Resolution Xps of Organic Polymers: The Scienta Esca300 Database; Wiley, 1992.

9. Easton, C. D.; Bullock, A. J.; Gigliobianco, G.; McArthur, S. L.; MacNeil, S., Application of Layer-by-Layer Coatings to Tissue Scaffolds - Development of an Angiogenic Biomaterial. J. Mater. Chem. B 2014, 2, 5558-5568.

Chapter 3

Highly active catalyst for CO_2 methanation derived from a metal organic framework template

Renata Lippi,[†‡] Shaun C. Howard,[‡] Hector Barron,[ϕ] Christopher D. Easton,[‡] Ian C. Madsen,[§]
Lynne, J. Waddington,[‡] Christian Vogt,[‡ ±] Matthew R. Hill,[‡] Christopher J. Sumby,[†]
Christian J. Doonan,*[†] Danielle F. Kennedy*[‡]

[‡]CSIRO Manufacturing, Clayton, Victoria 3168, Australia.
[†]Centre for Advanced Nanomaterials, Department of Chemistry, The University of Adelaide, Adelaide, South Australia 5005, Australia.
[ϕ]CSIRO Data61, Docklands, Victoria 3008, Australia
[§]CSIRO Mineral Resources, Clayton, Victoria 3168, Australia
[±]School of Chemistry, Monash University, Clayton, Victoria 3800, Australia

Published in Journal of Materials Chemistry A, ***2017****, 5, pp. 12990-12997.*
Reproduced with permission from the Royal Society of Chemistry.

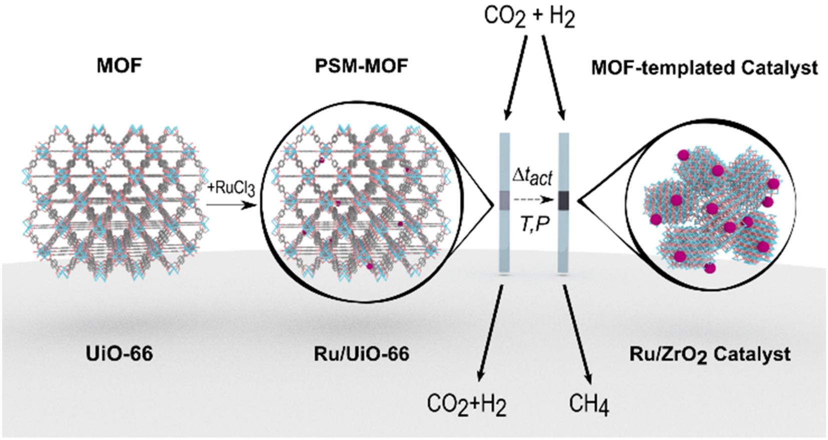

3.1. Summary

The successful synthesis of metal nanoparticles described in Chapter 2 prompted exploration of different MOF systems for the templating of catalytic active metal nanoparticles. In this chapter, the use of a zirconium MOF impregnated with $RuCl_3$ was explored as a template for CO_2 methanation catalysts. The final catalyst was templated under CO_2 methanation reaction conditions (80% H_2 and 20% CO_2), and displayed remarkable catalytic activity (X_{H2}=96%) for this gas phase reaction. The MOF-templated catalyst was tested alongside different controls and demonstrated superior H_2 conversion and selectivity to CH_4. The structure of the final catalyst was characterised and found to be composed of clusters of monoclinic and tetragonal ZrO_2 decorated with Ru^0 nanoparticles. Comparison to samples with equivalent chemical composition, demonstrates that the morphology and metal distribution achieved via the MOF-templating process was critical for the high activity of this catalyst.

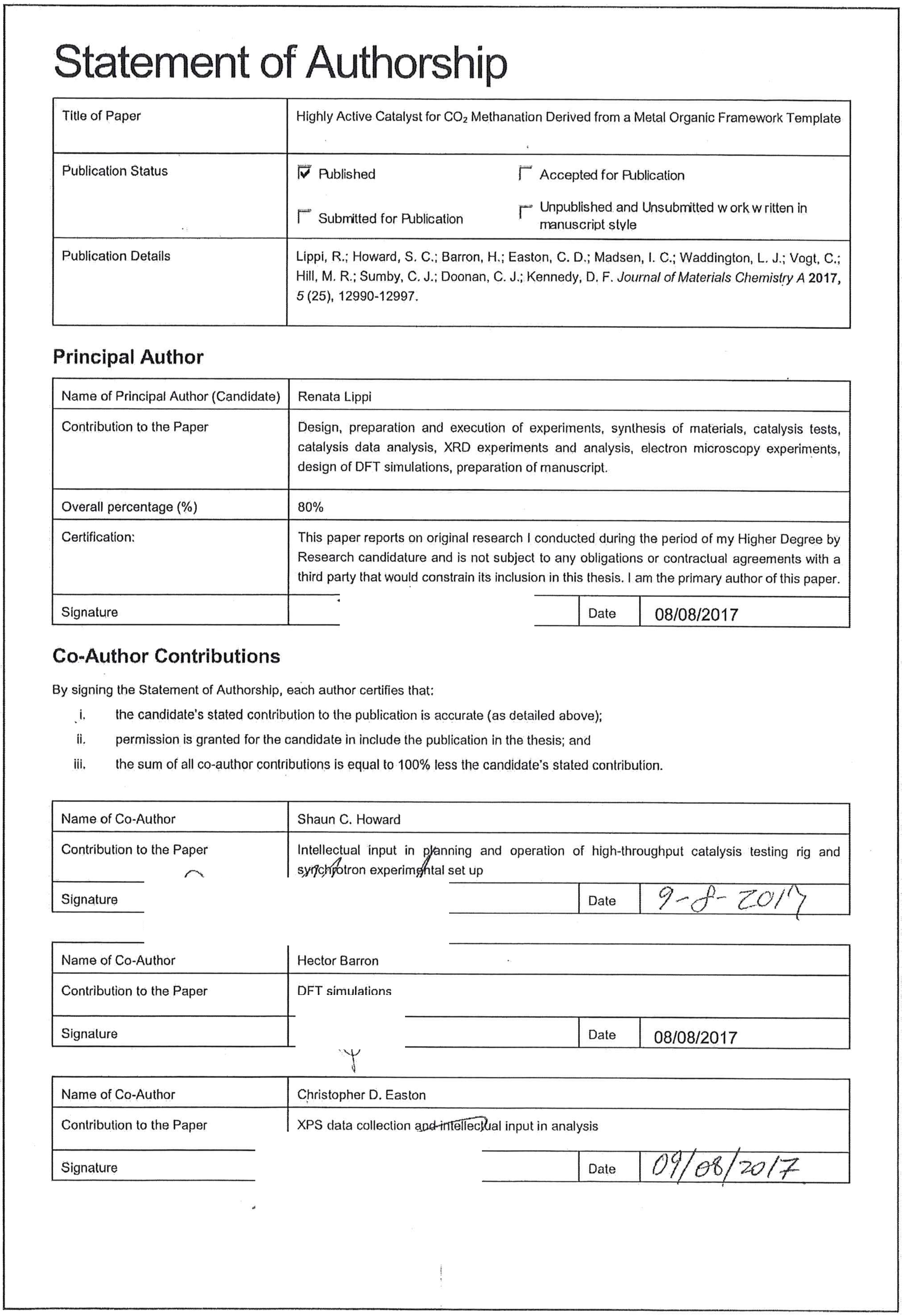

Statement of Authorship

Title of Paper	Highly Active Catalyst for CO_2 Methanation Derived from a Metal Organic Framework Template
Publication Status	☑ Published ☐ Accepted for Publication ☐ Submitted for Publication ☐ Unpublished and Unsubmitted work written in manuscript style
Publication Details	Lippi, R.; Howard, S. C.; Barron, H.; Easton, C. D.; Madsen, I. C.; Waddington, L. J.; Vogt, C.; Hill, M. R.; Sumby, C. J.; Doonan, C. J.; Kennedy, D. F. *Journal of Materials Chemistry A* **2017**, *5* (25), 12990-12997.

Principal Author

Name of Principal Author (Candidate)	Renata Lippi		
Contribution to the Paper	Design, preparation and execution of experiments, synthesis of materials, catalysis tests, catalysis data analysis, XRD experiments and analysis, electron microscopy experiments, design of DFT simulations, preparation of manuscript.		
Overall percentage (%)	80%		
Certification:	This paper reports on original research I conducted during the period of my Higher Degree by Research candidature and is not subject to any obligations or contractual agreements with a third party that would constrain its inclusion in this thesis. I am the primary author of this paper.		
Signature		Date	08/08/2017

Co-Author Contributions

By signing the Statement of Authorship, each author certifies that:

i. the candidate's stated contribution to the publication is accurate (as detailed above);
ii. permission is granted for the candidate in include the publication in the thesis; and
iii. the sum of all co-author contributions is equal to 100% less the candidate's stated contribution.

Name of Co-Author	Shaun C. Howard		
Contribution to the Paper	Intellectual input in planning and operation of high-throughput catalysis testing rig and synchrotron experimental set up		
Signature		Date	9-8-2017

Name of Co-Author	Hector Barron		
Contribution to the Paper	DFT simulations		
Signature		Date	08/08/2017

Name of Co-Author	Christopher D. Easton		
Contribution to the Paper	XPS data collection ~~and intellectual~~ input in analysis		
Signature		Date	09/08/2017

Name of Co-Author	Lynne J. Waddington		
Contribution to the Paper	Assistance in microscopy experiments		
Signature		Date	17/08/2017

Name of Co-Author	Ian C. Madsen		
Contribution to the Paper	Intellectual input in XRD experimental analysis		
Signature		Date	9th August 2017

Name of Co-Author	Christian Vogt		
Contribution to the Paper	Assistance in larger scale catalysis tests		
Signature		Date	13/08/2017

Name of Co-Author	Matthew R. Hill		
Contribution to the Paper	Intellectual Input in project design		
Signature		Date	18/10/2017

Name of Co-Author	Cristopher J. Sumby		
Contribution to the Paper	Intellectual input in project design, manuscript revisions		
Signature		Date	23/11/17

Name of Co-Author	Christian J. Doonan		
Contribution to the Paper	Intellectual input in project design, manuscript revisions		
Signature		Date	23/11/17

Name of Co-Author	Danielle F. Kennedy		
Contribution to the Paper	Intellectual input in project design, High-throughput catalysis screening method development, assistance in synchrotron experiments, manuscript revisions		
Signature		Date	10/08/2017

3.2. Abstract

The conversion of CO_2 into chemicals of commercial interest is a rapidly expanding area of research. Here, we present a highly active and stable CO_2 methanation catalyst that is derived from a Ru-impregnated zirconium-based metal-organic framework (MOF) material. The Ru-doped MOF is transformed, under reaction conditions, into an active catalyst which yields CO_2 conversions of 96% and a CH_4 selectivity of 99%. We demonstrate that the final catalyst was composed of a mixture of Ru-nanoparticles supported on monoclinic and tetragonal ZrO_2 nanoparticles. Notably, such catalytic activity has only been achieved using the MOF templating strategy. Catalysts of the same composition were synthesized via different methods but were less active for CO_2 methanation.

3.3. Introduction

In the past two decades, anthropogenic carbon dioxide (CO_2) emissions have become a major environmental concern. This can be attributed to the effect of atmospheric CO_2 concentrations on the global climate patterns.[1-2] Accordingly, efforts from the international community are underway to limit the increase in average global temperature to a maximum of 2 °C.[3] One strategy for controlling CO_2 emissions is Carbon Capture and Utilization (CCU). However, for CCU to be economically viable an energy efficient processes must be developed for utilising CO_2 as a carbon source which will enable its use for producing commodity chemicals aligned to industrial needs.[4]

One pathway to CO_2 utilisation is hydrogenation to value added products.[5] The Sabatier reaction (also known as CO_2 methanation), fully reduces CO_2, over a catalyst, to produce methane which can be directly used as a fuel.[6] This reaction may find use in the future as part of power-to-gas technology where hydrogen is produced from renewable energy sources such as wind or solar power.[7-8] A key challenge for the realisation of this process is improvement in existing catalyst technologies. For example, directions in this field include the synthesis of high surface area catalysts, improving CO_2 conversion, minimising unwanted CO production, addressing poor long-term catalyst stability, low methane production rates and reducing the reaction temperatures.[9-11] Nickel catalysts on various supports have been widely studied due to its natural abundance and relatively low cost. However, most Ni catalysts suffer from deactivation due to carbon deposition, sintering, and chemical poisoning.[9-12] Given these limitations other metals, such as ruthenium[13] have been explored as potential catalysts. Although, Ruthenium-based catalysts are relatively more expensive, they are very stable and known to be highly active for CO_2 methanation.[9-11, 14-15] With respect to catalytic supports, Al_2O_3, TiO_2, SiO_2, CeO_2 and ZrO_2 are most common.[9-11, 16-19] The metal-oxide support has a significant impact on the activity of catalysts in the CO_2 methanation reaction. A salient example is ZrO_2, which exists in three phases: monoclinic, tetragonal and cubic. Studies have shown that the respective phases affect CO_2 conversion for Ni-based catalysts.[16, 18-19] Indeed, supports comprised of a combination of two ZrO_2 phases were shown to yield more active catalysts.[19]

Metal-organic frameworks (MOFs) are well-known for their applications in gas absorption, molecular separation,[20-21] sensors and catalysis.[20] Recent reports have shown that these materials can be used as templates to synthesise catalysts with unique morphologies.[22-25] For example, Santos et al. have recently reported the synthesis of highly active MOF-derived iron carbide catalyst for Fischer-Tropsch synthesis.[26-27] It is noteworthy that the novel structure of the MOF derived catalyst described in this work could not be obtained by other methods.[26] Additionally, MOF-derived catalysts have also been reported for photocatalytic hydrogen production, the reduction of nitro aromatics and for the aerobic oxidation of alcohols, respectively.[28-31] These previous studies led us to hypothesise that a Ru-impregnated Zr-MOF may yield a composite active towards CO_2 methanation. Accordingly, here we report that infiltrating the pores of UiO-66 with $RuCl_3$ gives rise to a precursor of a highly active, stable and selective, *in situ* generated MOF-derived catalyst for CO_2 methanation at low pressure and mid-range temperature.

3.4. Experimental

3.4.1. Catalyst precursor synthesis

The methanation catalyst precursors are defined as xRu/UiO-66, where x = 0.25, 0.5, 0.75, 1, 1.25, 1.5, 1.75 or 2 wt% of Ru on the zirconium terephthalate MOF, UiO-66. They were synthesised by addition of $RuCl_3$ into the pores of activated UiO-66 via the Incipient Wetness Impregnation (IWI) method[32] to achieve the desired loading x. Detailed method in ESI.

3.4.2. CO_2 methanation reaction catalysis

The catalysts were activated *in situ* under methanation reaction conditions. We then evaluated the catalytic performance of the xRu/UiO-66 derived catalyst for CO_2 methanation under different pressure and temperature conditions. In a typical experiment, 20 mg of xRu/UiO-66 was loaded into a fixed-bed microreactor and, after an *in situ* drying step, the synthesis gas mixture was flowed through the bed. The synthesis gas mixture contained either a stoichiometric ratio of H_2 and CO_2 (H_2:CO_2 =4:1) and Ar tracer gas (H_2, 77.6 vol%; CO_2, 19.4 vol%; Ar, 3 vol%), or H_2:CO_2 =3.5:1 with Ar as tracer gas (H_2, 75.44 vol%; CO_2, 21.56 vol%; Ar, 3 vol%). The ratios used for each experiment are indicated in the figure captions. Throughout the experiments the temperature and pressure were controlled and effluent gas samples were analysed by a gas chromatograph. Considering that CO_2 is less expensive and more abundant, the limiting reactant in the Sabatier reaction is H_2, which would ideally be obtained from non-fossil-based sources. For this reason, performance was evaluated at stoichiometric ratios of H_2 and CO_2 and with a slight excess of CO_2. Thus, the authors chose to discuss performance in terms of H_2 conversion. Catalyst carbon content, CH_4 production and CO_2 conversion were evaluated for validation of the reported H_2 conversion. Other details can be found in the ESI.

3.5. Results and discussion

3.5.1. Catalyst activation

Figure 1A shows an initial increase in hydrogen conversion (X_{H2}) that can be attributed to catalyst activation. During this activation period, 60% mass loss was observed (Table S3) and mass spectrometry confirmed the loss of organic fragments from the pre-catalyst 1Ru/UiO-66 at 330 °C (Figure S14). After the activation, carbon products were derived from CO_2, as the carbon content of the MOF-derived catalyst was less than 2 wt% (Figure S11). High and stable H_2 conversions were observed from the MOF-derived CO_2 methanation catalysts. In particular, Figure 1A indicates that activation conditions above 330 °C afford X_{H2} above 94% and independent of pressure. However, 1Ru/UiO-66 derived catalysts activated and monitored at 250 and 300 °C took 13 h to stabilize, showing X_{H2} below 25% throughout the experiment. We note that increasing the reaction pressure at 350 °C reduced the activation period but had little impact on optimal conversion. Additionally, the catalyst showed remarkable selectivity for methane (S_{CH4}); 99.9% at all conditions tested (Figure 2C and 2D). The only by-product observed during this work was CO at very low concentrations (S_{CO} < 0.1%).

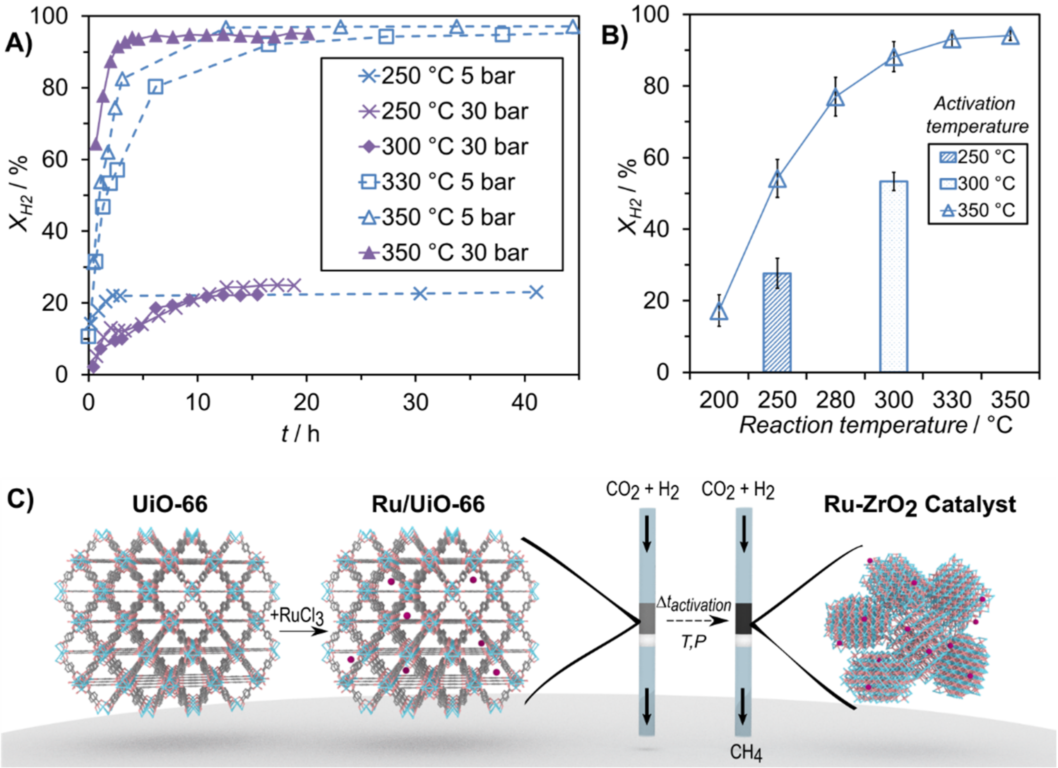

Figure 1: A) H_2 conversion (X_{H2}) during CO_2 methanation reactions using 1Ru/UiO 66 as the precatalyst under different reaction conditions. Reaction conditions: 20 mg of 1Ru/UiO 66, H_2:CO_2 = 4:1, Weight Hourly Space Velocity (WHSV) = 25 L·h 1·g 1. B) X_{H2} at different reaction temperatures and 5 bar for catalysts activated at 250, 300 or 350 °C. Reaction conditions: Activation at 30 bar for 22 hours, 50 mg of 1Ru/UiO 66, H_2:CO_2 = 4:1, WHSV = 43 L·h-1·g-1. C) Scheme of Ru/UiO 66 synthesis and in situ transformation into the MOF derived catalyst. Δtact = activation period.

3.5.2. Catalyst performance

To confirm that Ru is necessary for catalytic activity we carried out an analogous set of experiments with pure UiO-66. Under all conditions tested no X_{H2} was detected from this control. In addition, we found that X_{H2} was dependent on Ru loading. Figure 2A shows that conversions above 93% were observed for loadings higher than 0.75wt% of Ru on UiO-66. Accordingly, 1wt% Ru/UiO-66 (1Ru/UiO-66) was used for all other experiments. As a production rate indicator, we report the Weight Hourly Space Velocity (WHSV) in Figure 2B, which is the gas feed flow per catalyst mass unit. From an industrial perspective, it is desirable to maximize the production of methane using as little precious metal catalyst as possible. Therefore, a high WHSV associated with high X_{H2} is representative of an optimal catalyst. It is worth mentioning that 20 mg of 0.25Ru/UiO-66 yielded a catalyst with X_{H2} of 16% (Figure 2A) while, under the same conditions, 5 mg of 1Ru/UiO-66 provided X_{H2} of 78% (Figure 2B). Given that both reactors contained a total of 0.05 mg Ru these results confirm that the high activity of the MOF-templated catalyst is not achieved simply by the absolute amount of Ru, but depends on the structure of the catalyst.

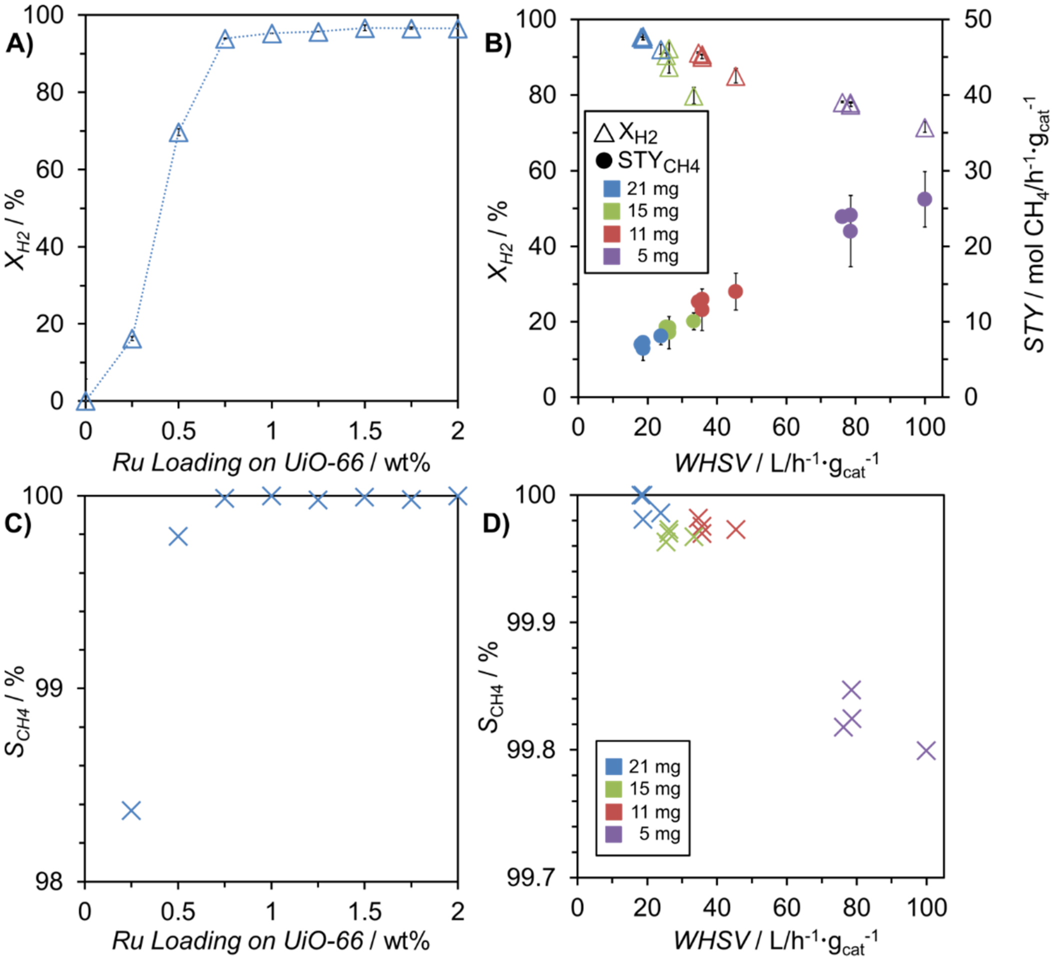

Figure 2: A) H_2 conversions (X_{H2}) and C) CH_4 selectivity (S_{CH4}) for catalysts derived from different loadings (x) of Ru on UiO-66. Reaction conditions: 20 mg of xRu/UiO-66, H_2:CO_2 = 4:1, WHSV = 19 L·h^{-1}·g^{-1}, 350 °C and 5 bar. B) X_{H2} and Space Time Yield for CH_4 (STY_{CH4}) for the MOF-derived catalysts and D) S_{CH4} for different conditions of WHSV (gas feed flow per catalyst mass unit), achieved using the indicated amounts of 1Ru/UiO-66 and different gas flows. Reaction conditions: H_2:CO_2 = 4:1, 350 °C and 5 bar. Error bars represent standard deviation over 40 h periods. CO was the only by-product observed.

In order to evaluate the performance of the 1Ru/UiO-66-derived catalyst a number of control samples were prepared (Figure 3). Ru was loaded onto several pre-made supports using identical IWI conditions to the MOF-based precatalyst; monoclinic zirconia ($pmZrO_2$), activated carbon (C), and mesoporous silica (SBA-15), to yield 1 wt% Ru loading. These control samples were then assessed for their catalytic performance for CO_2 methanation alongside 1Ru/UiO-66 and a commercially available Methanizer catalyst. We note that the MOF-based precatalyst undergoes significant mass loss during the *in situ* templating of the active catalyst. To ensure consistency, 20 mg of 1% Ru loaded on the different supports was used so that the absolute amount of Ru was equivalent in all experiments undertaken with different support materials. In all conditions tested, a significantly greater X_{H2} was observed for the MOF-derived catalyst (Figure 3). Furthermore, this catalyst was the most selective for methane and inhibited formation of the by-product CO which is commonly present in CO_2 methanation.[9-11] The catalyst's remarkable stability over isopressure periods of 40 h is evidenced by the small standard deviation bars, Figure 3, and the consistent conversion X_{H2} in Figure 1. Even after shutdown and exposure to air, deactivation was not observed for the derived catalyst (Figure S15).

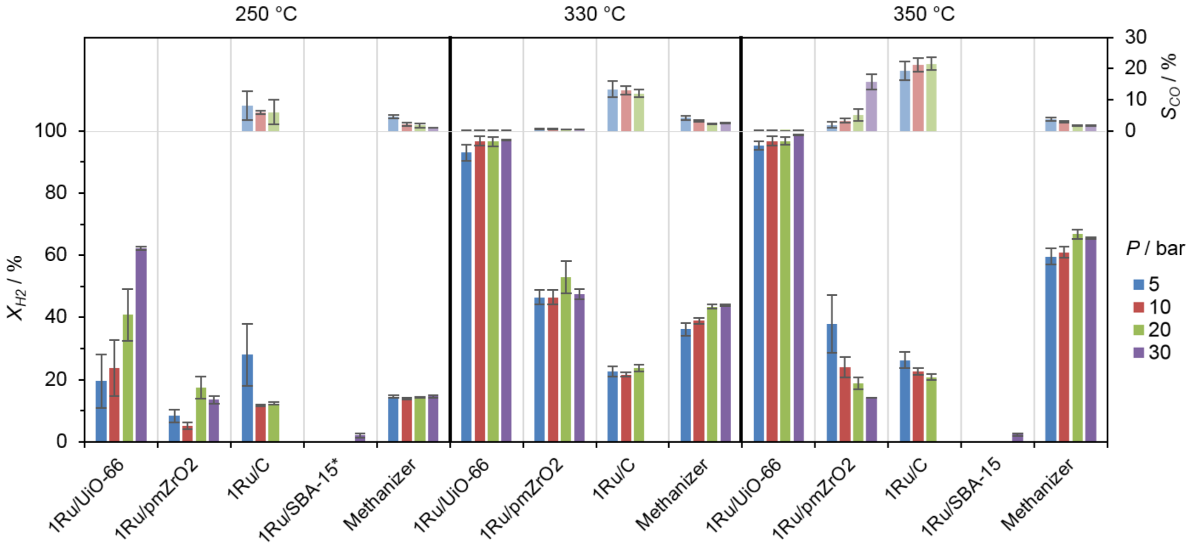

Figure 3: Average H_2 conversion (X_{H2}) and selectivity for CO (S_{CO}) by-product for samples at 250, 330 and 350 °C (left to right) with increasing reaction pressure conditions indicated by the colored bars. Average conversion values were obtained across isopressure periods of ~40 h. Total experiment time: 160 h. Reaction conditions: 20 mg of fresh sample as above, H_2:CO_2 = 3.5:1, gas flow= 14.3 mL·min^{-1}. Error bars represent standard deviation across an average of 3-4 measurements. *Tested at 270 °C.

In addition to high stability, the 1Ru/UiO-66-derived catalyst showed comparable or better activity than high-performing CO_2 methanation catalysts reported in the literature[14, 18-19, 33-36] and achieved conversions equivalent to the thermodynamic equilibrium of the Sabatier Reaction (Figure S15). The 1Ru/UiO-66-derived catalyst can be considered superior based on its combined performance characteristics: it requires a very small amount of catalyst to convert CO_2-rich streams at high gas flows conditions, it displays stable conversion in excess of 160 h, it is very selective for CH_4, has extremely low CO by-product formation, and operates at medium range temperatures (Figure 1B).

It is evident that the composition, in addition to the Ru loading, of the MOF-derived catalyst underpins its exceptional activity. This was confirmed by performing studies that showed, even at low concentrations, the presence of Ru was critical for catalytic performance; UiO-66 with no further treatment was inactive for CO_2 methanation. We also investigated whether the catalytic activity depended on the morphology of the template, UiO-66, in addition to the chemical composition. Accordingly, we prepared a solid mixture with the MOF precursors: $ZrCl_4$ and terephthalic acid (H_2BDC) in the molar ratio present in UiO-66, and then added $RuCl_3$ to produce a sample with chemical composition equivalent to the 1Ru/UiO-66. The catalytic activity of this sample was assessed at 350 °C and 5 bar and no methane production or H_2 conversion was detected. This provides strong evidence that the UiO-66 framework plays an important role in templating the structure of the active catalyst. This result is in agreement with previous studies[26] and is a further demonstration that MOFs can confer unique architectures to solid-state catalysts.

3.5.3. Powder X-Ray Diffraction

To elucidate the structure of the MOF-derived catalyst we performed a series of X-ray diffraction (XRD) experiments. We activated and tested the 1Ru/UiO-66 pre-catalyst at 250 ˚C, 300 ˚C and 350 ˚C (Figure 1B) and then recorded XRD patterns representative of each temperature after 20 and 100 hours on stream (Figure 4). Rietveld Refinement based quantitative phase analysis of the data indicates that both monoclinic (m-ZrO_2) and tetragonal (t-ZrO_2) phases of ZrO_2 are present with their respective ratios varying with reaction temperature and time. However, there were no peaks that could be attributed to the presence of a Ru^0 or RuO_2 phase. XRD reflections in diffractograms are affected by the relative amount of a phase, crystallinity and crystallite size. The catalyst contains only 3 wt% of Ru and Ru^0 nanoparticles are commonly found in an amorphous form.[37-38] Therefore, microscopy and elemental mapping were used to investigate the Ru phase (below). The MOF-derived catalyst activated at 350 ˚C yielded a greater proportion of m-ZrO_2 than the one activated at 250 ˚C. In addition, the catalyst activated at 350 ˚C performed better at 250 °C than the sample activated and kept at 250 °C. This infers a correlation between the amount of m-ZrO_2 present and activity (Figure 1A, 1B and 4). Catalyst samples activated and tested at 300 and 250 °C were less active

(Figure 1A and 1B), and contained more t-ZrO_2 (Figure 4). For these lower activation temperatures, the reaction time was observed to have an effect on composition and microstructure as well as on the conversion. This variation can be explained by the existence of a temperature threshold for the fast decomposition of 1Ru/UiO-66 under synthesis gas flow. Figure S14 shows the effluent composition during the activation of the MOF-derived catalyst in a single channel reactor connected to a mass spectrometer. An increasing loss of organic fragments was observed from 300 to 330 °C, at which point it reached a maxima, subsequently the conversion of the reagents and the production of CH_4 increased drastically. To further understand the changes in morphology under simulated reaction conditions, we performed controlled atmosphere and variable temperature (*in situ)* XRD of the precatalyst. This study at 1 bar confirmed that the MOF structure collapsed at 330 °C, in agreement with the loss of fragments observed by mass spectrometry, giving rise to an amorphous phase (Figure 5). This disordered phase, caused by the loss of the organic linkers, crystallizes into the ZrO_2 tetragonal and monoclinic phases at different rates depending on the temperature (Figure 4) to produce the active catalyst. Thermal decomposition of UiO-66 in air[39] and in N_2[40] atmosphere typically produce tetragonal ZrO_2. The high content of monoclinic ZrO_2 in the catalyst is explained by the presence of H_2O,[41] which is produced via CO_2 methanation during activation. This highlights the importance of the activation under reactive conditions to generate an active catalyst.

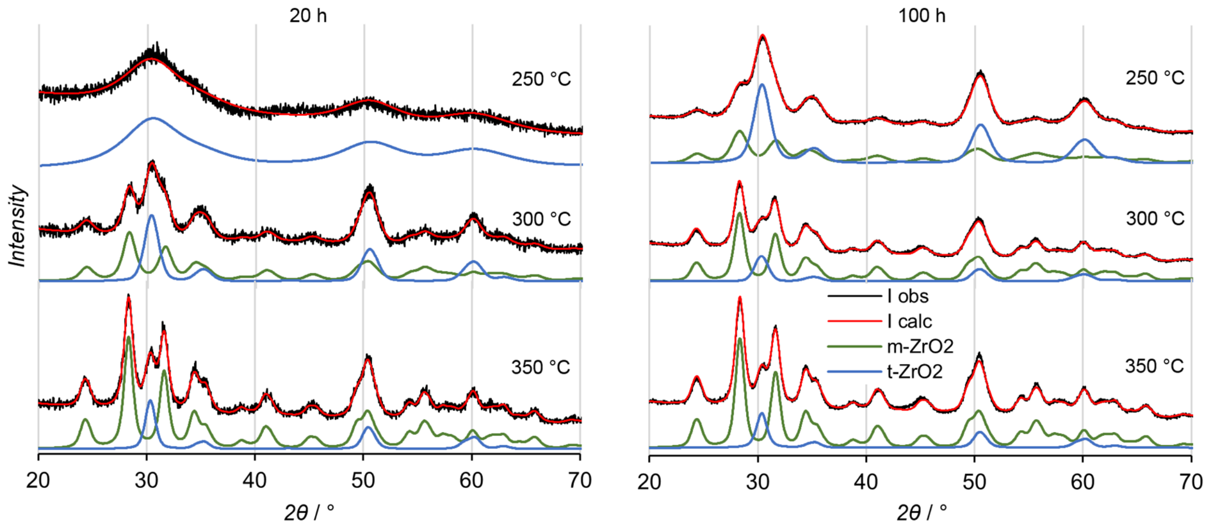

Figure 4: Diffractograms of MOF-derived catalysts activated at 250, 300 and 350 °C at 30 bar, after 20 h and after 100 h. Black lines indicate the collected data; red lines, the calculated profile from Rietveld quantitative phase analysis; and green and blue lines the individual contribution of each phase calculated by the Rietveld method (ESI). Diffractograms are offset for clarification.

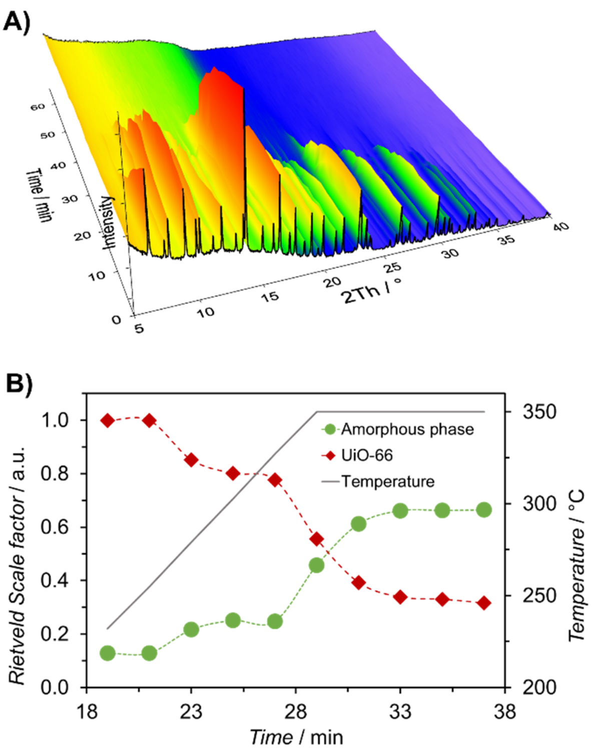

Figure 5: A) Controlled atmosphere and variable temperature (*In situ*) PXRD of 1Ru/UiO-66 in simulated reaction conditions. B) Rietveld refinement scale factor versus time and temperature for UiO-66 crystalline phase and the resulting amorphous phase. Experimental details can be found in the ESI.

3.5.4. Electron Microscopy

The microstructure of the MOF-derived catalyst was studied by Transmission Electron Microscopy (TEM) and Energy-dispersive X-ray Spectroscopy (EDS). The activated catalyst consisted of a hierarchical nanostructure. Nanoparticles of ZrO_2 in the range of 10 to 20 nm, in agreement with crystallite domain size obtained from XRD, were organized in clusters from 100 to 200 nm (Figure 6B). These clusters resembled the precursor 1Ru/UiO-66 crystals in size and shape (Figure 6A). Smaller Ru nanoparticles (Ru NPs) in the range of 2 to 5 nm were observed on the surface of the ZrO_2 particles (Figure 6C and 6D). EDS mapping infers that the Ru NPs are homogeneously dispersed on the ZrO_2 surfaces (Figure 7). The observed distribution of Ru is most likely due to the precursor MOF as a control sample of 1Ru/pmZrO_2 does not show the same spatial coincidence of Ru and Zr (Figure 7). Elemental mapping at higher magnification confirmed the presence of Ru NPs, additionally, the different spatial location of oxygen and Ru suggests that the nanoparticles consist of elemental Ru rather than Ru oxide (Figure 8 and S21). In summary, the microscopy data provide evidence that the MOF-derived catalyst is composed of larger ZrO_2 nanoparticles (10-20 nm) decorated by smaller Ru^0 NPs (2-5 nm).

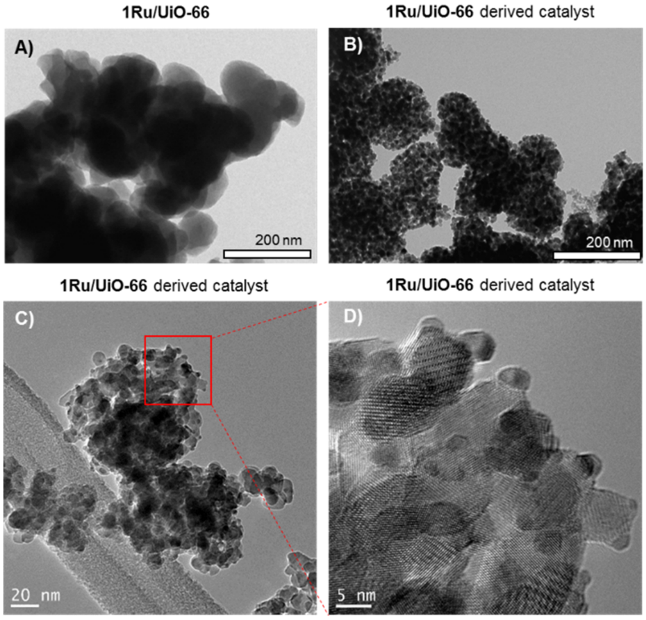

Figure 6: A) TEM of 1Ru/UiO-66 and of B) 1Ru/UiO-66 derived catalyst, the final catalyst is made of nanoparticle clusters which resemble the UiO-66 particles. C, D) HR-TEM of 1Ru/UiO-66 derived catalyst displaying the Ru particles (2-5 nm) supported on the ZrO_2 particles (10-20 nm). The MOF-derived catalyst was activated and tested at 350 °C, 30 bar for 100 h.

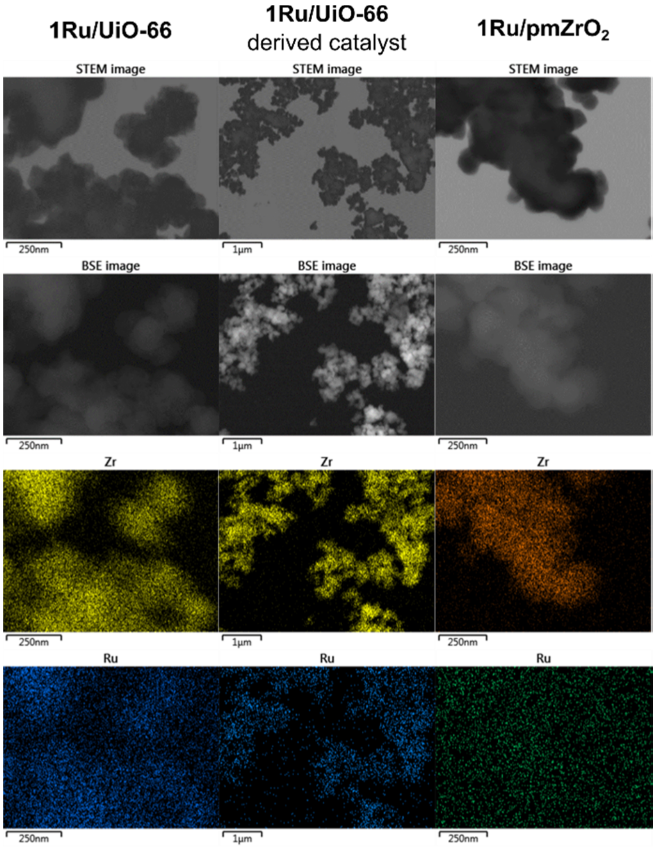

Figure 7: Microscopy images including STEM, backscattered electrons (BSE) and EDS elemental mapping of Zr and Ru for the precursor MOF, MOF-templated catalyst and Ru impregnated on pre-made monoclinic zirconia catalyst (1Ru/pmZrO_2). The elemental mapping of 1Ru/UiO-66 and the MOF-templated catalyst exhibited a great dispersion of Ru on the ZrO_2 particles. This level of dispersion was not observed for the 1Ru/pmZrO_2 catalyst, which presented most ZrO_2 particles Ru-free.

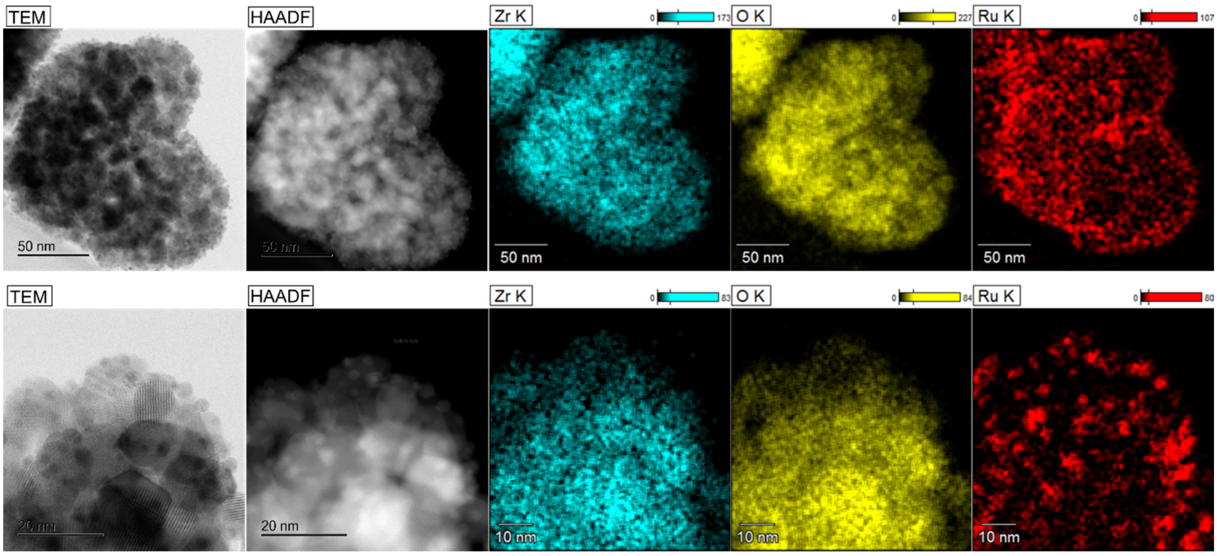

Figure 8: High resolution TEM, High-angle annular dark-field (HAADF) and EDS elemental mapping of 1Ru/UiO-66 templated catalyst. The MOF-templating method yielded a catalyst containing Ru

nanoparticles (2-5 nm) supported on ZrO_2 nanoparticles (10-20 nm). The oxygen map does not correlate with the Ru location, indicating the ruthenium to be Ru^0. Catalyst activated and tested at 350 °C and 30 bar.

3.5.5. X-ray photoelectron spectroscopy

The surface of the MOF-derived catalyst was examined by X-ray photoelectron spectroscopy (XPS). The high resolution spectra peak shape and binding energy position of the Ru is consistent with RuO_2 (Figure S24 and Table S7).[42] These results are in contrast to EDS maps that indicate the bulk of the nanoparticles consist of Ru^0, the presence of surface RuO_2 can be explained by oxidation of the surface Ru^0 atoms upon exposure to air.[43-44] The amount of Ru and Zr on the catalyst surface was quantified by XPS elemental analysis which afforded a Ru:Zr atomic ratio of 1:9. This value is significantly higher to the bulk Ru:Zr elemental quantification of 1:24 and provides further confirmation that the Ru nanoparticles supported on the ZrO_2 surface.

3.5.6. DFT Calculations

To provide insight into the structure of the catalyst precursor, Density Functional Theory (DFT) calculations were performed to evaluate the interaction between a Ru atom and the UiO-66 secondary building unit (SBU) (Figure 9). Cation exchange between Zr and Ru atoms during IWI was considered unlikely as the solvent is dried at 80 °C just after the addition of the $RuCl_3$ solution, not allowing a substantial amount of time for the exchange.[45] According to Table 1, the most favourable site for the 1Ru/UiO-66 is the configuration A, where the Ru atom is bonded to one oxygen and two zirconium atoms before the relaxation (High negative values of δE_{min} imply that some configurations are not allowed or stable, while low values indicate favourable configurations). Configuration B is the second most probable with an energy difference of -14 eV. This small energy difference is attributed to the fact that the final position of the Ru atom is similar to the initial configuration in both cases and remains bonded to the same atoms with very small change of configurations; while configurations C, D, and E undergo substantial configuration changes (Figure 9 and Table 1). Configurations A and B suggest that the Ru atom is coordinated to the metal node in a position normally occupied by a terephthalate linker. We note that this is consistent with previous studies which show that metal node defect sites in UiO-66 preferentially bind to other metals.[46-47] In this system, the post-synthetic metalation[48] of these defect sites may lead to the controlled distribution of Ru throughout the framework of the catalyst precursor MOF (Figure 7).

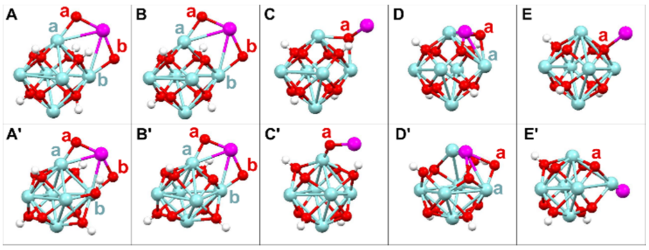

Figure 9: Initial (top) and final (bottom) configurations for the geometry optimization of different locations of Ru binding to the SBU. The spheres indicate atom position (Ru, magenta; O, red; Zr, blue and H, white). The most energetically favourable configurations A and B undergo subtle changes during the optimization, while configurations C, D and E undergo major changes

Table 1: Geometrical features and calculated energy for the configurations displayed in Figure 9.

Initial	Di Ru-O	Di Ru-Zr	Final	Df Ru-O	Df Ru-Zr	ETotal / eV	δEmin / eV
A	2.2a, 2.2b	3.4a, 3.4b	A’	2.0a, 2.0b	3.0a, 3.0b	-5681	0
B	2.2a, 2.2b	3.4a, 3.4b	B’	2.1a, 2.1b	3.0a, 3.0b	-5667	-14
C	2.1a	0.0a	C’	2.1a	0.0a	-5229	-452
D	2.1a, 0.0b	0.0a, 0.0b	D’	2.1a, 2.4b	2.8a, 2.9b	-5226	-455
E	0.0a	0.0a, 0.0b	E’	2.1b	2.8a, 2.9b	-4762	-919

$D_{i,f}$: Initial and final distances in Å. Sub-indexes a and b correspond to neighbouring atoms of each element (Figure 9). δE_{min} relates the maximum energy deviations observed from the lowest energy configuration with respect to Ru position

Upon the MOF collapse, during the activation period, the MOF loses its organic linkers and the MOF SBUs form a disordered (amorphous) phase before they rearrange to form ZrO_2 nanoparticles. Nanocrystalline ZrO_2 presents an excess of oxygen vacancies[49] which are responsible for the adsorption of CO_2 in the methanation process.[18-19] Ru species previously dispersed through the precursor MOF (1Ru/UiO-66) migrate to the surface of the nano-ZrO_2 and form Ru NPs. The high level of Ru NPs dispersion in the final catalyst is owed to the dispersion of Ru in the precursor MOF. In this study, the distribution of Ru NPs on nano-ZrO_2 matrix may underpin the exceptional activity of the MOF-derived catalyst. Accordingly, when the oxygen vacancies are associated with the hydrogenation properties of Ru NPs, a high activity for the CO_2 methanation was observed even at low Ru loading and at high WHSV.

3.6. Conclusions

We have identified a highly active catalyst for CO_2 methanation derived from Ru impregnated UiO-66. The final Ru/ZrO_2 catalyst displayed CO_2 conversions in the range of 96 to 98% when operating under high gas flow rates. In addition, it showed remarkable stability and high selectivity to methane for more than 160 h of testing. The combination of these reactive properties assures this catalyst superiority when comparing it to other cutting edge catalysts, however, poisoning tests have not yet been performed for this material. This work highlights that MOFs can confer unique morphology to heterogeneous catalyst systems via a templating strategy. Such *in situ* generation of the active catalyst by MOF-templating has the advantage of not requiring a calcination step at high temperatures or caustic chemical processing.[18-19, 24, 26, 35, 50-52] Furthermore, the precise spatial control of metal-oxide and organic components offered by MOF chemistry provides excellent potential for the design of new solid-state catalysts.

3.7. Acknowledgements

The authors would like to thank Nathan Brosnahan, Kaycee Low and Hao Wei. Aspects of this research were undertaken on the Powder Diffraction beamline at the Australian

Synchrotron, Victoria, Australia. This work was supported by CSIRO and the Science and Industry Endowment Fund is thanked for funding this research. R. Lippi acknowledges The University of Adelaide for the Beacon of Enlightenment Ph.D. Scholarship.

3.8. References

1. Song, C. S., Global Challenges and Strategies for Control, Conversion and Utilization of CO2 for Sustainable Development Involving Energy, Catalysis, Adsorption and Chemical Processing. *Catal. Today* **2006**, *115*, 2-32.

2. IPCC, Summary for Policymakers. In *Climate Change 2013: The Physical Science Basis. Contribution of Working Group I to the Fifth Assessment Report of the Intergovernmental Panel on Climate Change*, Stocker, T. F.; Qin, D.; Plattner, G.-K.; Tignor, M.; Allen, S. K.; Boschung, J.; Nauels, A.; Xia, Y.; Bex, V.; Midgley, P. M., Eds. Cambridge University Press: Cambridge, United Kingdom and New York, NY, USA, 2013; pp 1–30.

3. Iyer, G. C., et al., The Contribution of Paris to Limit Global Warming to 2 °C. *Environ. Res. Lett.* **2015**, *10*, 125002.

4. Aresta, M.; Dibenedetto, A.; Angelini, A., Catalysis for the Valorization of Exhaust Carbon: From CO2 to Chemicals, Materials, and Fuels. Technological Use of CO2. *Chem. Rev.* **2014**, *114*, 1709-1742.

5. Ampelli, C.; Perathoner, S.; Centi, G., CO2 Utilization: An Enabling Element to Move to a Resource- and Energy-Efficient Chemical and Fuel Production. *Philos. Trans. R. Soc. London, A* **2015**, *373*.

6. Thampi, K. R.; Kiwi, J.; Gratzel, M., Methanation and Photo-Methanation of Carbon-Dioxide at Room-Temperature and Atmospheric-Pressure. *Nature* **1987**, *327*, 506-508.

7. Gutierrez-Martin, F.; Rodriguez-Anton, L. M., Power-to-Sng Technology for Energy Storage at Large Scales. *Int. J. Hydrogen Energy* **2016**, *41*, 19290-19303.

8. Götz, M.; Lefebvre, J.; Mörs, F.; McDaniel Koch, A.; Graf, F.; Bajohr, S.; Reimert, R.; Kolb, T., Renewable Power-to-Gas: A Technological and Economic Review. *Renew. Energy* **2016**, *85*, 1371-1390.

9. Aziz, M. A. A.; Jalil, A. A.; Triwahyono, S.; Ahmad, A., CO2 Methanation over Heterogeneous Catalysts: Recent Progress and Future Prospects. *Green Chem.* **2015**, *17*, 2647-2663.

10. Gao, J.; Liu, Q.; Gu, F.; Liu, B.; Zhong, Z.; Su, F., Recent Advances in Methanation Catalysts for the Production of Synthetic Natural Gas. *RSC Adv.* **2015**, *5*, 22759-22776.

11. Ronsch, S.; Schneider, J.; Matthischke, S.; Schluter, M.; Gotz, M.; Lefebvre, J.; Prabhakaran, P.; Bajohr, S., Review on Methanation - from Fundamentals to Current Projects. *Fuel* **2016**, *166*, 276-296.

12. Ocampo, F.; Louis, B.; Kiwi-Minsker, L.; Roger, A.-C., Effect of Ce/Zr Composition and Noble Metal Promotion on Nickel Based Cexzr1−Xo2 Catalysts for Carbon Dioxide Methanation. *Appl. Catal., A* **2011**, *392*, 36-44.

13. Catalyst Used for Methanation of Carbon Dioxide, Preparation Method and Applications. CN104148065B, 2017.

14. Sharma, S.; Hu, Z.; Zhang, P.; McFarland, E. W.; Metiu, H., CO2 Methanation on Ru-Doped Ceria. *J. Catal.* **2011**, *278*, 297-309.

15. Carenco, S.; Sassoye, C.; Faustini, M.; Eloy, P.; Debecker, D. P.; Bluhm, H.; Salmeron, M., The Active State of Supported Ruthenium Oxide Nanoparticles During Carbon Dioxide Methanation. *J. Phys. Chem. C* **2016**, *120*, 15354-15361.

16. Yamasaki, M.; Habazaki, H.; Yoshida, T.; Akiyama, E.; Kawashima, A.; Asami, K.; Hashimoto, K.; Komori, M.; Shimamura, K., Compositional Dependence of the CO2 Methanation Activity of Ni/ZrO2 Catalysts Prepared from Amorphous Nizr Alloy Precursors. *Appl. Catal., A* **1997**, *163*, 187-197.

17. Perkas, N.; Amirian, G.; Zhong, Z.; Teo, J.; Gofer, Y.; Gedanken, A., Methanation of Carbon Dioxide on Ni Catalysts on Mesoporous ZrO2 Doped with Rare Earth Oxides. *Catal. Lett.* **2009**, *130*, 455-462.

18. Takano, H.; Kirihata, Y.; Izumiya, K.; Kumagai, N.; Habazaki, H.; Hashimoto, K., Highly Active Ni/Y-Doped ZrO2 Catalysts for CO2 Methanation. *Appl. Surf. Sci.* **2016**, *388*, 653-663.

19. Takano, H.; Shinomiya, H.; Izumiya, K.; Kumagai, N.; Habazaki, H.; Hashimoto, K., CO2 Methanation of Ni Catalysts Supported on Tetragonal ZrO2 Doped with Ca2+ and Ni2+ Ions. *Int. J. Hydrogen Energy* **2015**, *40*, 8347-8355.

20. Furukawa, H.; Cordova, K. E.; O'Keeffe, M.; Yaghi, O. M., The Chemistry and Applications of Metal-Organic Frameworks. *Science* **2013**, *341*, 1230444.

21. Cui, Y.; Li, B.; He, H.; Zhou, W.; Chen, B.; Qian, G., Metal–Organic Frameworks as Platforms for Functional Materials. *Acc. Chem. Res.* **2016**, *49*, 483-493.

22. Song, Y.; Li, X.; Sun, L.; Wang, L., Metal/Metal Oxide Nanostructures Derived from Metal-Organic Frameworks. *RSC Adv.* **2015**, *5*, 7267-7279.

23. Xia, W.; Mahmood, A.; Zou, R.; Xu, Q., Metal-Organic Frameworks and Their Derived Nanostructures for Electrochemical Energy Storage and Conversion. *Energy Environ. Sci.* **2015**, *8*, 1837-1866.

24. Yang, J.; Zhang, F.; Wang, X.; He, D.; Wu, G.; Yang, Q.; Hong, X.; Wu, Y.; Li, Y., Porous Molybdenum Phosphide Nano-Octahedrons Derived from Confined

Phosphorization in Uio-66 for Efficient Hydrogen Evolution. *Angew. Chem. Int. Ed.* **2016**, *55*, 12854-12858.

25. Shen, K.; Chen, X.; Chen, J.; Li, Y., Development of MOF-Derived Carbon-Based Nanomaterials for Efficient Catalysis. *ACS Catal.* **2016**, *6*, 5887-5903.

26. Santos, V. P., et al., Metal Organic Framework-Mediated Synthesis of Highly Active and Stable Fischer-Tropsch Catalysts. *Nat. Commun.* **2015**, *6*, 6451.

27. Wezendonk, T. A., et al., Elucidating the Nature of Fe Species During Pyrolysis of the Fe-Btc MOF into Highly Active and Stable Fischer–Tropsch Catalysts. *ACS Catal.* **2016**, *6*, 3236-3247.

28. deKrafft, K. E.; Wang, C.; Lin, W., Metal-Organic Framework Templated Synthesis of Fe2o3/Tio2 Nanocomposite for Hydrogen Production. *Adv. Mater.* **2012**, *24*, 2014-2018.

29. Niu, H. Y.; Liu, S. L.; Cai, Y. Q.; Wu, F. C.; Zhao, X. L., MOF Derived Porous Carbon Supported Cu/Cu2O Composite as High Performance Non-Noble Catalyst. *Microporous Mesoporous Mater.* **2016**, *219*, 48-53.

30. Sun, X.; Olivos Suarez, A. I.; Oar Arteta, L.; Rozhko, E.; Osadchii, D.; Bavykina, A.; Kapteijn, F.; Gascon, J., Metal-Organic-Framework Mediated Cobalt/N-Doped Carbon Hybrids as Efficient and Chemoselective Catalysts for the Hydrogenation of Nitroarenes. *Chemcatchem* **2017**, n/a-n/a.

31. Kim, B. R.; Oh, J. S.; Kim, J.; Lee, C. Y., Robust Aerobic Alcohol Oxidation Catalyst Derived from Metal–Organic Frameworks. *Catal. Lett.* **2016**, *146*, 734-743.

32. Campelo, J. M.; Luna, D.; Luque, R.; Marinas, J. M.; Romero, A. a., Sustainable Preparation of Supported Metal Nanoparticles and Their Applications in Catalysis. *ChemSusChem* **2009**, *2*, 18-45.

33. Garbarino, G.; Bellotti, D.; Riani, P.; Magistri, L.; Busca, G., Methanation of Carbon Dioxide on Ru/Al2O3 And ni/Al2O3 Catalysts at Atmospheric Pressure: Catalysts Activation, Behaviour and Stability. *Int. J. Hydrogen Energy* **2015**, *40*, 9171-9182.

34. Lu, B.; Kawamoto, K., Preparation of the Highly Loaded and Well-Dispersed Nio/SBA-15 for Methanation of Producer Gas. *Fuel* **2013**, *103*, 699-704.

35. Zhen, W. L.; Li, B.; Lu, G. X.; Ma, J. T., Enhancing Catalytic Activity and Stability for CO2 Methanation on Ni@MOF-5 Via Control of Active Species Dispersion. *Chem. Commun.* **2015**, *51*, 1728-1731.

36. Shin, H. H.; Lu, L.; Yang, Z.; Kiely, C. J.; McIntosh, S., Cobalt Catalysts Decorated with Platinum Atoms Supported on Barium Zirconate Provide Enhanced Activity and Selectivity for CO2 Methanation. *ACS Catal.* **2016**, *6*, 2811-2818.

37. Ohyama, J.; Sato, T.; Yamamoto, Y.; Arai, S.; Satsuma, A., Size Specifically High Activity of Ru Nanoparticles for Hydrogen Oxidation Reaction in Alkaline Electrolyte. *J. Am. Chem. Soc.* **2013**, *135*, 8016-8021.

38. Tee, S. Y.; Lee, C. J. J.; Dinachali, S. S.; Lai, S. C.; Williams, E. L.; Luo, H.-K.; Chi, D.; Hor, T. S. A.; Han, M.-Y., Amorphous Ruthenium Nanoparticles for Enhanced Electrochemical Water Splitting. *Nanotechnology* **2015**, *26*, 415401.

39. DeCoste, J. B.; Peterson, G. W.; Jasuja, H.; Glover, T. G.; Huang, Y. G.; Walton, K. S., Stability and Degradation Mechanisms of Metal-Organic Frameworks Containing the Zr6o4(OH)(4) Secondary Building Unit. *J. Mater. Chem. A* **2013**, *1*, 5642-5650.

40. Liu, S.-C.; Yue, Z.-F.; Liu, Y., Mesoporous Carbon–ZrO2 Composites Prepared Using Thermolysis of Zirconium Based Metal–Organic Frameworks and Their Adsorption Properties. *J. Porous Mater.* **2015**, *22*, 465-471.

41. Xie, S.; Iglesia, E.; Bell, A. T., Water-Assisted Tetragonal-to-Monoclinic Phase Transformation of ZrO2 at Low Temperatures. *Chem. Mater.* **2000**, *12*, 2442-2447.

42. Morgan, D. J., Resolving Ruthenium: Xps Studies of Common Ruthenium Materials. *Surf. Interface Anal.* **2015**, *47*, 1072-1079.

43. Bavand, R.; Yelon, A.; Sacher, E., X-Ray Photoelectron Spectroscopic and Morphologic Studies of Ru Nanoparticles Deposited onto Highly Oriented Pyrolytic Graphite. *Appl. Surf. Sci.* **2015**, *355*, 279-289.

44. Yao, Q.; Lu, Z.-H.; Yang, K.; Chen, X.; Zhu, M., Ruthenium Nanoparticles Confined in SBA-15 as Highly Efficient Catalyst for Hydrolytic Dehydrogenation of Ammonia Borane and Hydrazine Borane. *Sci. Rep.* **2015**, *5*, 15186.

45. Kim, M.; Cahill, J. F.; Fei, H. H.; Prather, K. A.; Cohen, S. M., Postsynthetic Ligand and Cation Exchange in Robust Metal-Organic Frameworks. *J. Am. Chem. Soc.* **2012**, *134*, 18082-18088.

46. Nguyen, H. G. T.; Schweitzer, N. M.; Chang, C. Y.; Drake, T. L.; So, M. C.; Stair, P. C.; Farha, O. K.; Hupp, J. T.; Nguyen, S. T., Vanadium-Node-Functionalized UiO-66: A Thermally Stable MOF-Supported Catalyst for the Gas-Phase Oxidative Dehydrogenation of Cyclohexene. *ACS Catal.* **2014**, *4*, 2496-2500.

47. Yang, D.; Odoh, S. O.; Wang, T. C.; Farha, O. K.; Hupp, J. T.; Cramer, C. J.; Gagliardi, L.; Gates, B. C., Metal–Organic Framework Nodes as Nearly Ideal Supports for Molecular Catalysts: Nu-1000- and UiO-66-Supported Iridium Complexes. *J. Am. Chem. Soc.* **2015**, *137*, 7391-7396.

48. Evans, J. D.; Sumby, C. J.; Doonan, C. J., Post-Synthetic Metalation of Metal-Organic Frameworks. *Chem. Soc. Rev.* **2014**, *43*, 5933-5951.

49. Cong, Y.; Li, B.; Yue, S.; Fan, D.; Wang, X.-j., Effect of Oxygen Vacancy on Phase Transition and Photoluminescence Properties of Nanocrystalline Zirconia Synthesized by the One-Pot Reaction. *J. Phys. Chem. C* **2009**, *113*, 13974-13978.

50. Toemen, S.; Abu Bakar, W. A. W.; Ali, R., Effect of Ceria and Strontia over Ru/Mn/Al2O3 Catalyst: Catalytic Methanation, Physicochemical and Mechanistic Studies. *J. CO2 Util.* **2016**, *13*, 38-49.

51. Abu Bakar, W. A. W.; Ali, R.; Toemen, S., Catalytic Methanation Reaction over Supported Nickel-Rhodium Oxide for Purification of Simulated Natural Gas. *J. Nat. Gas Chem.* **2011**, *20*, 585-594.

52. Abu Bakar, W. A. W.; Ali, R.; Toemen, S., Catalytic Methanation Reaction over Supported Nickel-Ruthenium Oxide Base for Purification of Simulated Natural Gas. *Sci. Iran.* **2012**, *19*, 525-534.

3.9. Supporting information

Highly active catalyst for CO_2 methanation derived from a metal-organic framework template

A. General considerations

All chemicals were used as provided by the manufacturer. Chemicals and respective suppliers: Zirconium Oxide nanoparticle (99+% ZrO_2 monoclinic, 40 nm, US3600) US Nano (USA), Charcoal activated powder R Grade LabServ (Australia), Methanizer packing 391160002 Agilent Technologies (Australia), ruthenium(III) cloride trihydrate ($RuCl_3 \cdot 3H_2O$) 99% PMO Pty Ltd (Australia), terephthalic acid 99% Acros Organics (Great Britain), dimethylformamide (DMF) 99.8% Merck Pty. Ltd. (Australia), zirconium chloride ($ZrCL_4$) 99.5% Sigma-Aldrich (Australia), hydrochloric acid (HCl) 32% Merck Pty. Ltd. (Australia), Pluronic® P-123 Sigma-Aldrich (Australia), Tetraethylorthosilicate (TEOS) 99% Merck Pty. Ltd. (Australia). Silicon Carbide (SiC) 99% 300-355 μm Beijing HWRK Chem Co., Ltd. (China). Water was deionized by reverse osmosis. All gases used were supplied by Coregas (Australia) including custom made mixtures: nitrogen (N4); Argon (N5); Helium (N5); Hydrogen (N5); 25% carbon dioxide with hydrogen balance; and 2.52% ethane, 2.82% ethene, 2.53% acetylene, 2.44% methane, 2.48% carbon dioxide, 2.53% carbon monoxide, 2.51% hydrogen with argon balance.

B. Syntheses Details

B.1 UiO-66

UiO-66 was synthesized according to Katz et al.[1] A 2 L Schott glass bottle was loaded with DMF (160 mL), $ZrCl_4$ (4 g) and 32% HCl (32 mL), the mixture was sonicated for 20 minutes. In a separate bottle, terephthalic acid was dissolved in DMF (320 mL) and then added to the $ZrCl_4$ solution. The bottle was sealed with a screw cap and placed in an oven at 80 °C for 20 hours. The resulting solid was isolated by vacuum filtration and it was washed with DMF (3x 300 mL) and ethanol (2x 300 mL). Subsequently, the solid was dried under vacuum for several hours. The synthesis of UiO-66 was confirmed by PXRD and TGA.

B.2 SBA-15

Mesoporous silica SBA-15 was synthesized according to the method of Cool et al.[2] In a 2 L round bottom flask, 1083 mL of water, 33 g of P123 and 166 mL of 4 M HCl solution were mixed using a mechanical stirrer for approximately 6 hours until complete dissolution. After resting for 16 hours, TEOS was added to the mixture and the solution was stirred at 452 rpm and 45 °C for 8 h. The resulting solution was let ageing in an oven at 80°C for 20 hours. The white solid phase formed after ageing was cooled down and recovered by filtering and washing it with deionized water (3x 200 mL). Next, the solid was dried at 60 °C for 20 h before being calcined in a Nabertherm muffle furnace at 500°C for 24 hours (heating at 1 °C/min, cool down at 2 °C/min). Before use, the material was crushed using a mortar and a pestle.

B.3 Ru/Support via IWI

In a typical experiment where the support was UiO-66, 1 wt% loading of Ru^0 in UiO-66 (**1Ru/UiO-66**) was achieved by the standard incipient wetness impregnation method of UiO-66 with an aqueous solution of $RuCl_3$. Finely ground UiO-66 solid (250 mg) was placed into an 8 mL glass vial and an aqueous $RuCl_3$ solution ($7.12 \cdot 10^{-5}$ M, 350 μL) was added followed by mixing of the resulting slurry to ensure that all the sample was in contact with the solution. The sample was dried in air at 80 °C to obtain **1Ru/UiO-66**. The same procedure was applied for different supports using the appropriate solution volume and concentration to yield the right loading as presented in Table S1. Different loadings of Ru on UiO-66 were achieved by using appropriate concentration of RuCl3.

The UiO-66 water uptake for the IWI was defined empirically. The total pore volume of approximately 0.4 cm^3/g was considered for the impregnation at first, however simple visual inspection indicated that it was not enough to create a homogeneous slurry. To define the water uptake for the IWI known amounts of water were added to UiO-66 until a homogeneous slurry was formed. The resulting value was 1.38 mL water/g UiO-66.

Table S1: Details of quantities used during the IWI procedure for different support materials.

Support	Volume aqueous solution to support mass (mL/g)	For 1% Ru loading RuCl3·3H2O solution concentration (g/mL)	RuCl3·3H2O solution concentration (mol/mL)
UiO-66	1.38	1.88·10-2	7.12·10-5
pmZrO2	0.636	4.07·10-2	1.54·10-4
Activated Carbon (C)	0.636	4.07·10-2	1.54·10-4
SBA-15	0.636	4.07·10-2	1.54·10-4

B.4 UiO-66 precursor mix ($ZrCl_4$+H_2BDC)

The preparation of UiO-66 precursors mix $ZrCl_4$ and terephthalic acid ($ZrCl_4$+H_2BDC) was designed considering the molecular formula of UiO-66, $C_{48}H_{24}O_{30}Zr_6$, in order to achieve the equivalent amount and ratio of Zr:BDC in 100 mg of UiO-66 ($6.15{\cdot}10^{-5}$ mol UiO-66), 86 mg of $ZrCl_4$ ($3.96\ {\cdot}10^{-4}$ mol $ZrCL_4$) was mixed with 61 mg of H_2BDC ($3.96{\cdot}10^{-4}$ mol H_2BDC), for the sample with Ru (Ru/$ZrCl_4$+H_2BDC), 2.5 mg of $RuCl_3{\cdot}3H_20$ (1 mg of Ru, $10{\cdot}10^{-6}$ mol Ru) was added to the solid mixture, this amount was chosen to simulate the Ru composition in **1Ru/UiO-66** when using 100 mg of UiO-66. These samples were kept under N_2 before the catalytic testing. For catalysis testing approximately 30 mg of the precursor mix was used since this amount is equivalent to 20 mg of UiO-66.

Table S2: Synthesis details and hydrogen conversion for the samples compared in this study.

	Synthesis details				**350 °C, 5 bar**	**350 °C, 5 bar**
Precatalyst acronym	Support	Metal precursor	Metal loading (wt%)	Impreg. method[a]	X_{H2} (%)	SD_{XH2}[b]
UiO-66	UiO-66	-	0	-	0	-
1Ru/UiO-66	UiO-66	$RuCl_3$	1	IWI	96.0	2.9
Ru/pmZrO_2	Pre-made ZrO_2 (monoclinic)	$RuCl_3$	1	IWI	38.0	9.2
Ru/C	Activated carbon	$RuCl_3$	1	IWI	26.3	2.6
Methanizer	SiO_2	Ni[c]	10-30	ND	59.6	2.6
Ru/SBA-15	SBA-15	$RuCl_3$	1	IWI	0[d]	-
$ZrCl_4$+H_2BDC	Dry mixture of solids	-	0	DM	0	-
Ru/$ZrCl_4$+H_2BDC	Dry mixture of solids	$RuCl_3$	1[e]	DM	0	-

[a]IWI: Incipient Wetness impregnation, ND: not disclosed, DM: solvent-free (dry) solid mixture; [b]Standard Deviation across isopressure periods; [c]Ni precursor not disclosed; [d] sample tested at 10 bar; [e]Equivalent to 1%**1Ru/UiO-66**

C. Thermogravimetric analysis (TGA)

The thermal analysis of 4 samples submitted were carried out using a Netzsch STA 449 F1 Jupiter with SiC furnace and S-type sensor. Samples were heated to 350 °C at a rate of 10°C/min under either 100% N_2 or 5% H_2 in N_2 purge gas at flowing rate of 40 mL/min. An empty alumina crucibles were run as blank for each method to correct for baseline. The STA analysis was initially run with an isothermal cycle for 5 min to allow the samples to equilibrate with the purge gas conditions. These sections are not shown in the thermograms.

A sample of UiO-66 was heated to 800 °C under N_2 to observe the full decomposition. This sample was evaluated using a Mettler Toledo TGA 2. UiO-66 (19 mg) was loaded into an empty alumina crucible heated to 800 °C at 10 °C/min under N_2 purge gas at flowing rate of 30 mL/min. the sample was allowed to equilibrate at 25 °C for 10 minutes before the analysis, this section is not shown in the thermogram.

Simultaneous Thermal Analysis (STA) was performed to evaluate the carbon content in the MOF-derived catalyst. After catalysis testing the used catalyst was loaded in an alumina pan and STA was performed in a Netzsch STA 449 F1 system fitted with a SiC Furnace and an S-type DTA sensor. The sample was heated to 1000ºC at 10ºC/min heating rate under Air purge gas 20 mL/min. An initial blank run was carried out to correct for the baseline. Evolved Gas Analysis (EGA) was performed with Pfeiffer Thermostar Quadrupole Mass Spectrometry coupled to the STA system in order to check for the volatiles.

D. Gas sorption analysis

The sample was degassed overnight at 150 °C. N_2 sorption was performed at 77 K using a Micromeritics ASAP 2020.

E. X-ray powder diffraction (XRD)

E.1 Laboratory source XRD

Where possible, samples were back-loaded into sample holders prior to the collection of XRD traces to minimize texture. Where insufficient sample was provided for back-loading, samples were instead loaded onto zero background plates. A Bruker D8 Advance X-ray Diffractometer operating under CuKα radiation (40kV, 40mA) equipped with a LynxEye detector was employed to obtain the XRD patterns. Samples were scanned over the 2θ range 3.5° to 130° with a step size of 0.02° and a count time of 0.4 second per step. 173/192 of the sensor strips on the LynxEye detector were used, to give an equivalent count time of 69.2 seconds per step.

E.2 Synchrotron source XRD (Gas controlled and variable temperature experiment)

Gas controlled and variable temperature XRD experiments were carried at the Powder Diffraction Beamline at the Australian Synchrotron. A Mythen microstrip detector[3] was used for data collection. The samples were loaded into open-ended special glass 0.7 mm wide capillaries (The Charles Supper Company, USA) glass wool was used to contain the powder within the capillary. The capillary was kept oscillating during acquisition. Temperature was controlled using a hot-air blower positioned below the capillary. The capillary holder was attached to a gas fitting, which was connected to a gas manifold allowing the selection of gas flow. The beam energy during data acquisition was 15 keV with a current of 200 mA. The sample was first heated to 220 °C under N_2 flow, then at 19 min, the gas flow was replaced with a mixture of CO_2:H_2 = 1:3. Upon reaching 350 °C, the temperature was kept constant.

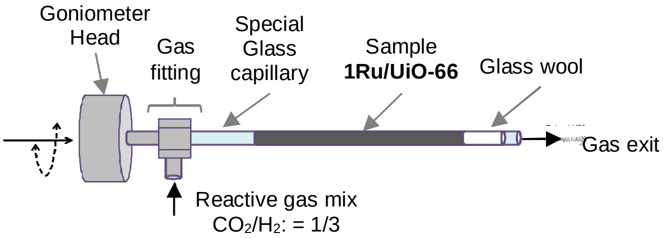

Figure S1: Gas controlled PXRD experiment sample holder setup.

E.3 Rietveld refinement of PXRD data

The quantitative phase and microstructure analysis of the laboratory source XRD data was performed using a whole-pattern, Rietveld based approach. The Rietveld method involves the development of a model which is used to generate a calculated XRD pattern. The model includes parameters such as crystal structure model for each phase, pattern background, wavelength, sample and instrument aberrations, etc. The then calculated pattern is compared with the observed data and the difference between observed and calculated is minimised through a least squares process by adjusting selected parameters in the model. These calculations were performed using the software TOPAS V5[4] in batch mode.

Synchrotron source was used for the gas controlled variable temperature PXRD of **1Ru/UiO-66**. Rietveld refinement of the scale UiO-66 and the resulting amorphous phase was performed in batch mode using Topas V5[4]. The Rietveld refinement of this XRD dataset was performed in batch mode starting with the diffractogram at 19min. The values refined for each diffractogram were used as input for the next. The background contribution for all diffractograms was fixed according to the refined values at 19min. Thereafter, the increase in the background was correlated with the generation of an amorphous phase.

F. Catalysis testing

Catalyst screening and optimization experiments were undertaken in a Flowrence® 48-channel catalysis rig manufactured by Avantium Ag.[5-6] (**Figure S2**). The tubular reactors had internal diameters of 2.0 mm, were 280 mm long and were constructed of either Hastaloy with a stainless steel frit or quartz with a quartz frit depending on the experiment. Hastalloy reactors were prepared with a base of 700 mg of SiC to a height of 11-13 cm to maintain the catalyst bed within the isothermal zone of the reactor which is 8 cm in length. Precatalyst masses of between 10 and 20 mg were diluted with coarse SiC to produce a catalyst bed volume between 50 and 200 uL in each reactor. Quartz reactors were loaded with quartz frits and undiluted precatalysts (~50 mg). The reactors were operated in co-current downstream mode and can operate at a maximum temperature of 750 °C, a maximum pressure of 160 bar and GHSVs of up to 100,000 h^{-1}.

This multichannel reactor was custom built for CSIRO and is comprised of 3 blocks of 16 reactors which can be independently temperature controlled allowing the concurrently testing of samples at different temperatures. Pressure is maintained with 2 backpressure manifolds each lined with a Teflon membrane, the gas feed and pressure is kept even for all reactors. Flow rates are modulated by EL-Flow Bronkhorst mass flow controllers. Effluent gases were diluted with nitrogen immediately after exiting reactors to provide enough volume to the GC analytics. The tracing line between the reactors and the GC was maintained at 120 °C.

All reactors were sequentially sampled by an on-line Gas Chromatograph 7890A Agilent (USA). The complete effluent analysis consisted of two methods performed in parallel on two GC channels: Front channel with an Agilent PoraBOND Q packed column (CP7352) with a TCD detector; and Auxiliary channel with an Agilent MolSieve 5A packed column (G3591-80046) with a TCD detector with negative polarity. In both channels, helium was used as sweep gas. Argon was mixed with the gas feed (3 vol% of argon in feed) as an internal standard required to calculate absolute flows.

Before the beginning of the experiments, a validation run was carried out with a Alfa Aesar Cu–ZnO–alumina catalyst for methanol synthesis, to perform a technical validation of the equipment. During this validation, various process parameters were studied: temperature: 260 and 300 °C; pressure: 10, 20 and 30 bar; H_2/CO molar ratio: 0.5, 1 and 2; GHSV: 4000, 8000, 16,000 h^{-1}. As expected, as this catalyst was designed for H_2/CO operations the product mixture is complex. The main product in this reaction was methanol. The data from this validation run showed that the equipment is capable of producing consistent and reproducible data.

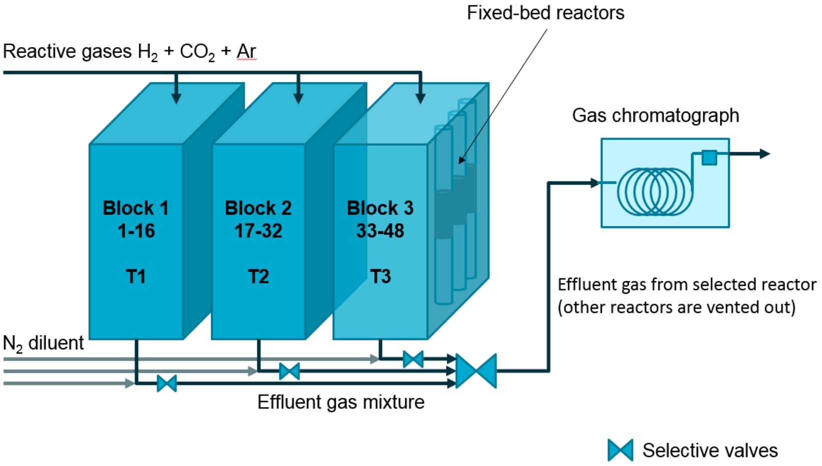

Figure S2: Diagram of the multi-channel rig used for the catalysis testing.

F.1 Experimental conditions

In a typical catalysis test, approximately 20 mg of precatalyst or catalyst mixed with 50 mg of SiC were loaded over a SiC bed inside a steel or quartz micro reactor and placed in the rig. The samples were then heated at 2 °C/min under a N_2 stream (3 mL/min) to 220 °C at 1 bar and kept for 20 min in order to remove guest solvent molecules from the samples. Next the samples were exposed to the reactive gas mixture and to set conditions of temperature (ramp rate of 5 °C/min) and pressure (4 bar/min) while the test was carried continuously for several hours. The reactive gas mixture had 3% argon and 97% CO_2 and H_2 either in a stoichiometric ratio (1 CO_2 : 4 H_2) or with H_2 as the limiting reactant (1 CO_2 : 3.5 H_2). Gas effluent composition was finally analyzed by a gas chromatograph (GC) as described above. It is important to mention that the CO_2 methanation is a volume reducing reaction, meaning that increasing pressure may improve the conversion of CO_2.[7] However, due to technical restrictions our studies were performed at 5 bar and above, for validation and comparison purposes the commercial catalyst Methanizer was included in the experiments.

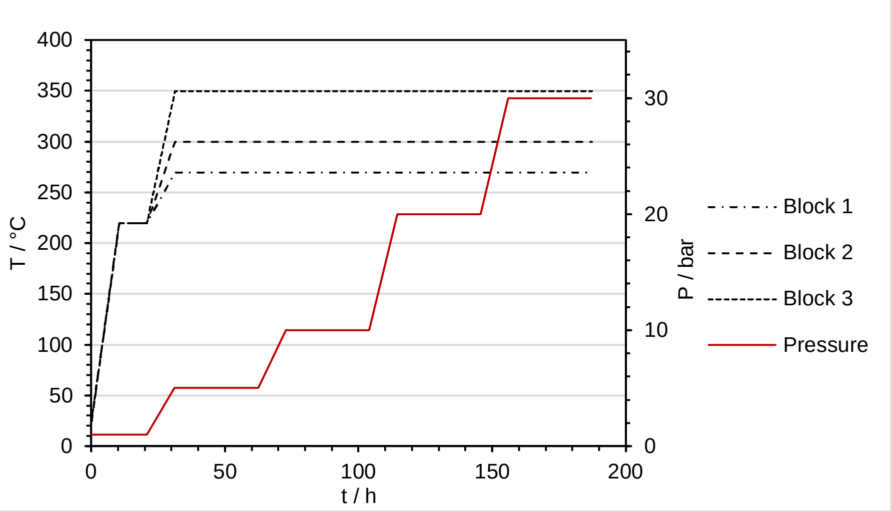

Figure S3: Experimental conditions versus time for the catalytic performance comparison of different supports (**Figure 3**). The first step at 1 bar and up to 220 °C was carried under N_2 and lasts for 20 min, it has been stretched in this plot for the purpose of observation.

G. Catalysis data analysis

G.1 Weight hourly space velocity (WHSV)

Weight hourly space velocity (WHSV) is defined as the volume of gas fed to each reactor per gram of final catalyst loaded per hour. Mass of final catalyst was defined as 35% of the precatalyst according to the mass loss measurements and to TGA.

$$WHSV\ (L \cdot h^{-1} \cdot g^{-1}) = \frac{\dot{V}_{gas\ fed\ in\ reactor}}{M_{final\ catalyst}} = \frac{\dot{V}_{H_2} + \dot{V}_{CO_2} + \dot{V}_{Ar}}{M_{pre-catalyst} * 0.35}$$

G.2 Quantitative analysis of reactor effluent gas via GC

For the quantitative analysis, the gas chromatograph (GC) was calibrated by flowing a gas mixture with known amounts of ethane, ethene, acetylene, methane, carbon dioxide, carbon monoxide, hydrogen and argon, supplied by Coregas, diluted with N_2 stream at different dilution ratios to define the factor$_i$ (area/%) used in the analysis and OpenLab software from Agilent was used to define species retention time.

$$x_{i\ effluent} = \frac{GC\ Area_i}{factor_i}$$

G.3 Conversion and selectivity calculations

Ar was added to the reactor gas feed as tracer gas. Since N_2 by-pass the reactor in order to dilute the gas effluent, just as Ar it does not react and thus its fraction in the gas effluent can be directly correlated with a total volume flow change. Both N_2 and Ar were used for verification.

$$\dot{V}_{reactor\ gas\ feed} = \dot{V}_{H_2 feed} + \dot{V}_{CO_2 feed} + \dot{V}_{Ar_{feed}}$$

$$\dot{V}_{total\ feed} = \dot{V}_{reactor\ gas\ feed} + \dot{V}_{by-pass\ N_2 feed}$$

$$\dot{V}_{total\ effluent} = \dot{V}_{H_2 effluent} + \dot{V}_{CO_2 effluent} + \dot{V}_{Ar_{effluent}} + \dot{V}_{N_2 effluent} + \sum_i \dot{V}_{product_i}$$

$$\dot{V}_{N_2 fed} = \dot{V}_{N_2 effluent} = \dot{V}_{total\ effluent} \cdot x_{N_2\ effluent} \leftrightarrow \dot{V}_{total\ effluent} = \frac{\dot{V}_{N_2 fed}}{x_{N_2\ effluent}}$$

$$\dot{V}_{Ar\,fed} = \dot{V}_{Ar\,effluent} = \dot{V}_{total\,effluent} \cdot x_{Ar\,effluent} \leftrightarrow \dot{V}_{total\,effluent} = \frac{\dot{V}_{Arfed}}{x_{Ar\,effluent}}$$

Species effluent volume flow

$$\dot{V}_{i\,effluent} = \dot{V}_{total\,effluent} \cdot x_{i\,effluent}$$

H_2 conversion values for single data points

$$X_{H_2} = \frac{\dot{V}_{H_2\,consumed}}{\dot{V}_{H_2\,fed}} = \frac{\dot{V}_{H_2\,fed} - \dot{V}_{H_2\,effluent}}{\dot{V}_{H_2\,fed}}$$

Reported multiple data points average H_2 conversion values

$$X_{H_2} = \frac{\sum\dot{V}_{H_2\,consumed}}{\sum\dot{V}_{H_2\,fed}} = \frac{\sum\dot{V}_{H_2\,fed} - \sum\dot{V}_{H_2\,effluent}}{\sum\dot{V}_{H_2\,fed}}$$

Reported average conversions were calculated for periods after catalyst activation, which varied from 4 up to 13 hours depending on the temperature.

Standard deviation for H_2 conversion presented in this work was calculated by the analysis of H_2 conversion values for single data points.

Selectivity was also confirmed by the absence of other products as observed in **Figure S4**.

$$S_{CH_4} = \frac{\dot{V}_{CH_4\,effluent}}{\dot{V}_{CO_2\,consumed}}$$

$$S_{CO} = \frac{\dot{V}_{CO\,effluent}}{\dot{V}_{CO_2\,consumed}}$$

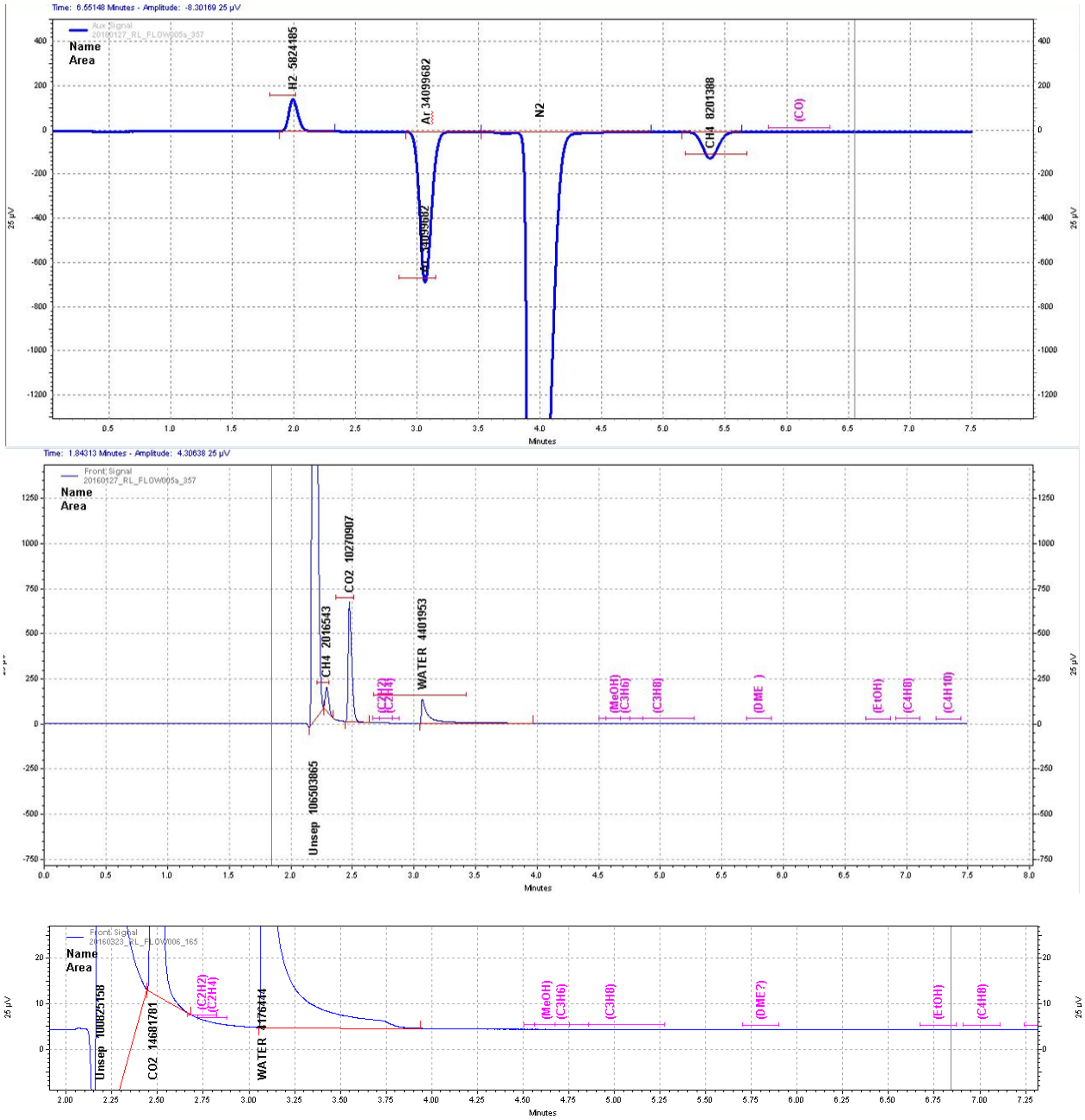

Figure S4: Example of the gas chromatograms obtained for each of the channels during the catalysis testing. The auxiliary channel (top) was used for H_2 and methane quantification and the front channel (middle) was used for CO_2 quantification and to verification of other products formation. CH_4 quantification was used to verify H_2 conversion numbers, as CO_2 could only be estimated as its peak position, on the tail of the unseparated gases peak, limited the accuracy of its quantification (bottom). This method was chosen because identification of small quantities of high molecular weight species was desired and we calibrated and trust the dosage of CO_2 to the reactor as discussed below.

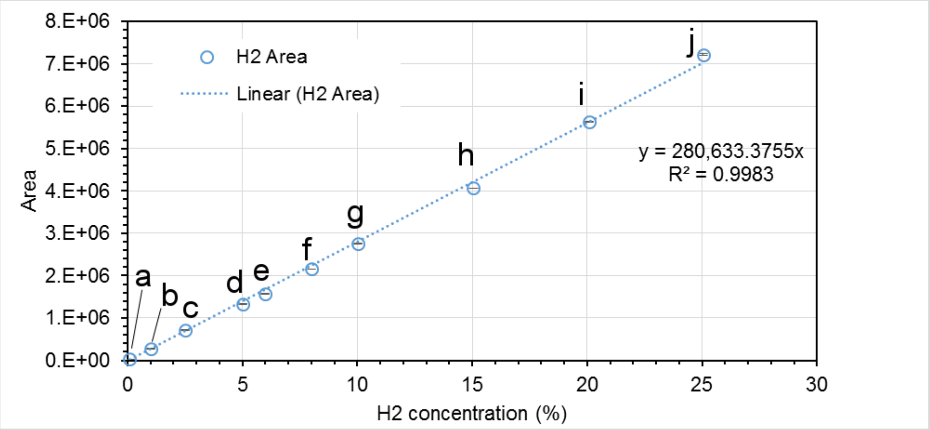

Figure S5: The H_2 calibration curve for the gas chromatograph and method used for this work. The peak shape at each concentration is displayed in **Figure S6**. Each point indicates the average of 3 to 4 injections for the same concentration. Error bars, present inside the markers, indicate standard deviation of the area.

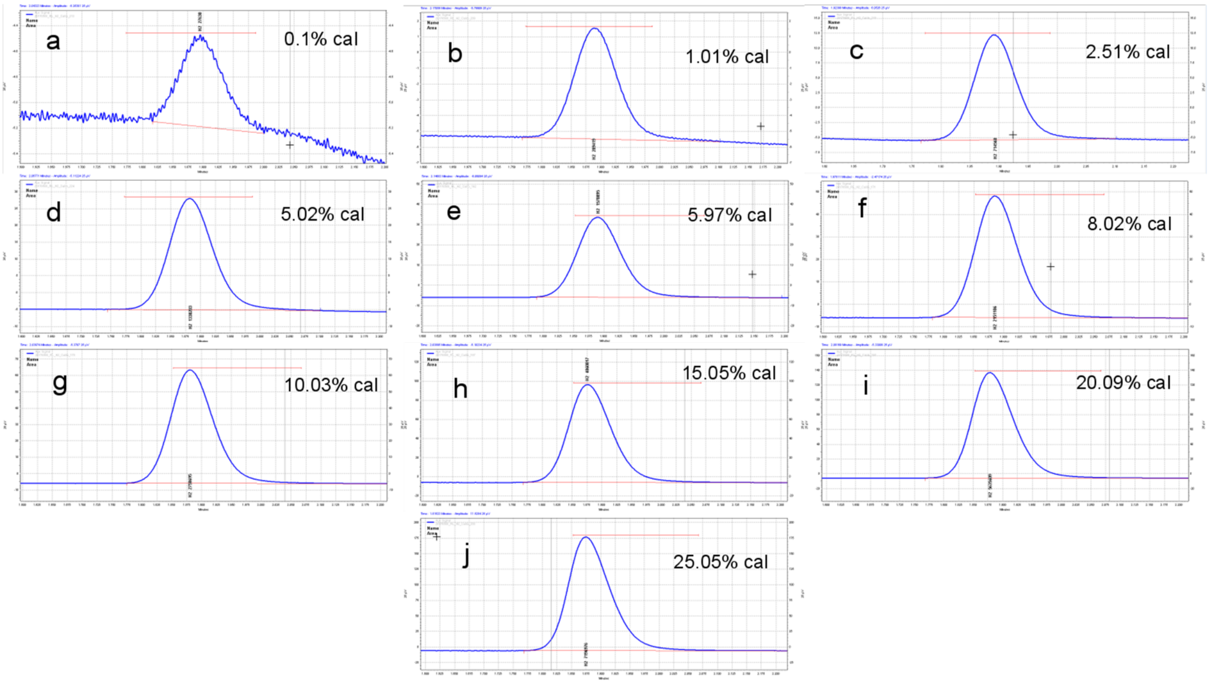

Figure S6: H_2 chromatogram peaks during calibration with different concentrations of H_2 as indicated in the figure.

G.4 Mass balance

Carbon balance was done by considering CH_4 production, CO_2 composition in the gas feed, absence of any other C-containing product and carbon content in catalyst. The CO_2 feed is accurately measured and according to the carbon mass balance method described below, the methane Yield (Y_{CH4}) is approximately equal to the CO_2 delivered to the reactor.

Gas feed composition (input) was controlled using EL-Flow Bronkhorst mass flow controllers calibrated by Bronkhorst. Spot checks are regularly done to verify the flow through each reactor. GC analysis of empty reactors are also performed to check the mass flow controllers' accuracy. In all experiments, empty reactors were added to the experiment and tested in parallel to verify the gas composition in the absence of catalysts. Composition of gas effluent was analysed using a GC.

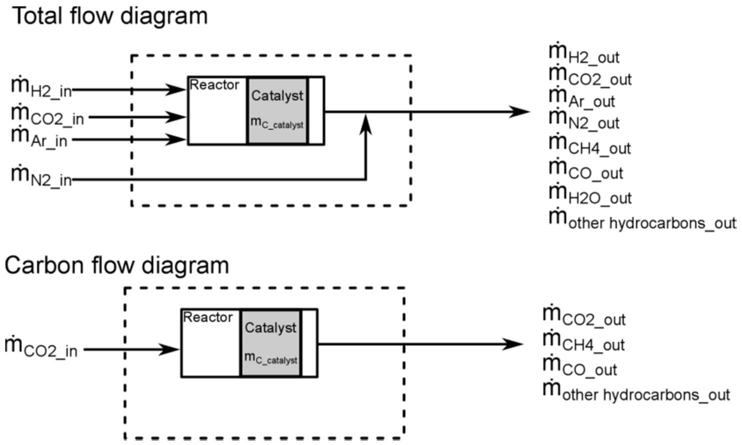

Figure S7: Flow diagram for all molecules (top) and for carbon-containing molecules only (bottom).

Below the mass balance for carbon-containing molecules.

$$input - output - accumulation = 0$$

Here, accumulation is defined as carbon deposited on the catalyst.

$$\dot{m}_{CO_{2_{in}}} - \dot{m}_{CO_{2_{out}}} - \dot{m}_{CH_{4_{out}}} - \dot{m}_{CO_{out}} - \dot{m}_{other\ hydrocarbons_{out}} - \dot{m}_{C_{catalyst}} = 0$$

- No other hydrocarbons were observed in the GC **Figure S4**, therefore

$$\dot{m}_{other\ hydrocarbons_{out}} = 0$$

- After activation of the catalyst there is no carbon left in the sample (**Figure S11**)

$$\dot{m}_{C_{catalyst}} \cong 0$$

- Selectivity of CO is less than 0.2% (**Figure 2D**)

$$\dot{m}_{CO_{out}} \cong 0$$

$$\dot{m}_{CO_{2\,in}} - \dot{m}_{CO_{2\,out}} - \dot{m}_{CH_{4\,out}} \cong 0$$

$$\dot{m}_{CO_{2\,in}} - \dot{m}_{CO_{2\,out}} \cong \dot{m}_{CH_{4\,out}} \xrightarrow{\div\left(\dot{m}_{CO_{2\,in}}\right)} \frac{\dot{m}_{CO_{2\,in}} - \dot{m}_{CO_{2\,out}}}{\dot{m}_{CO_{2\,in}}} \cong \frac{\dot{m}_{CH_{4\,out}}}{\dot{m}_{CO_{2\,in}}}$$

$$\frac{\dot{m}_{CO_{2\,in}} - \dot{m}_{CO_{2\,out}}}{\dot{m}_{CO_{2\,in}}} = X_{CO_2} \cong Y_{CH_4} = \frac{\dot{m}_{CH_{4\,out}}}{\dot{m}_{CO_{2\,in}}}$$

At stoichiometric ration H_2:CO_2 = 4:1, it is possible to compare the methane yield to the H_2 conversion for validation of the results.

$$\frac{\dot{m}_{CO_{2\,in}} - \dot{m}_{CO_{2\,out}}}{\dot{m}_{CO_{2\,in}}} = X_{CO_2} \cong Y_{CH_4} = \frac{\dot{m}_{CH_{4\,out}}}{\dot{m}_{CO_{2\,in}}} = \frac{\dot{m}_{H_{2\,in}} - \dot{m}_{H_{2\,out}}}{\dot{m}_{H_{2\,in}}} = X_{H_2}$$

This comparison is presented in **Figure S8**.

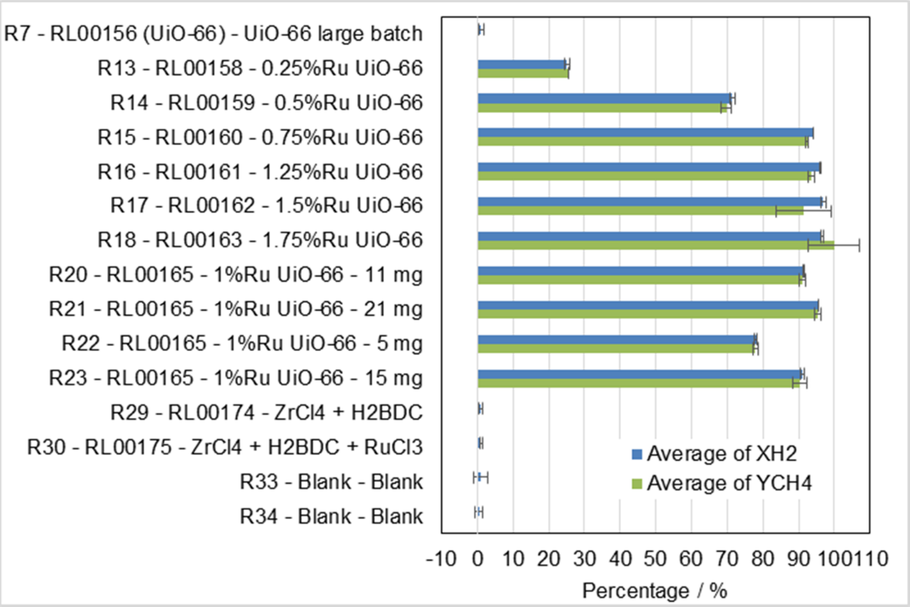

Figure S8: Example of verification of H_2 conversion (ml_$H_{2\ consumed}$/ml_$H_{2\ in}$) and CH_4 yield (ml_$CH_{4\ produced}$/ml_$CO_{2\ in}$) for different samples tested in parallel.

G.5 Transmission electron microscopy (TEM)

Figure 6A, 6B and S18: Samples were prepared for TEM as follows: aliquots of sample were suspended in ethanol, and applied to carbon-coated copper TEM grids. After air drying, grids were examined in a Tecnai 12 G2 TEM (FEI, The Netherlands), operating at 120 kV, and images were recorded with a MegaView III CCD (Olympus, Tokyo).

Figure 6C and 6D: High Resolution TEM was performed in a Tecnai F20 TEM (FEI, The Netherlands) equipped with STEM and EDS detectors operating at 200 kV.

Figure 8 and S21: TEM/STEM investigation was performed using a probe-corrected JEOL ARM200F (JEOL, USA) equipped with a cold field emission gun operating at 200 kV. High-angle annular dark-field (HAADF) images were acquired with inner and outer collection angles of 68 and 280 mrad, respectively, while bright field images were acquired with a maximum collection angle of 17 mrad. All images were acquired with a 20 ms dwell time and convergence angle of 25 mrad, resulting in a probe size about 0.1 nm and a current of 40 pA. The Energy-dispersive X-ray Spectroscopy (EDS) maps were acquired with a probe current of 155 uA.

G.6 Scanning electron microscopy (SEM/EDS)

Figure 7 and S19: The samples, which were mounted on TEM grids as described above, were placed on a STEM stage so that the samples could be imaged using a Zeiss Merlin FESEM (Field Emission Scanning Electron Microscope) operated in the secondary electron (SE) mode and back-scattered mode (BSE). SE images highlight topographical features whereas BSE imaging enhances elemental contrast and oxidation state differences so that low atomic elements or oxidated elements appear darker and higher atomic number elements or in the elemental state appear brighter. Energy dispersive spectroscopy (EDS) was used to identify elements present within the samples. The EDS system used was AZTEC, manufactured by

Oxford Instruments Pty Ltd. An accelerating voltage of 25 kV was used for EDS mapping. The magnifications used are indicative of the scale bars shown in the images.

G.7 X-ray photoelectron spectroscopy (XPS)

X-ray photoelectron spectroscopy (XPS) analysis was performed using an AXIS Ultra DLD spectrometer (Kratos Analytical Inc., Manchester, UK) with a monochromated Al K_α source at a power of 180 W (15 kV × 12 mA), a hemispherical analyser operating in the fixed analyser transmission mode and the standard aperture (analysis area: 0.3 mm × 0.7 mm) The total pressure in the main vacuum chamber during analysis was typically 10^{-8} mbar. Survey spectra were acquired at a pass energy of 160 eV. To obtain more detailed information about chemical structure, oxidation states etc., high resolution spectra were recorded from individual peaks at 40 eV pass energy (yielding a typical peak width for polymers of 0.9 – 1.0 eV).

The sample was filled into a shallow well of a custom-built sample holder where the sample was analysed at two different locations at a nominal photoelectron emission angle of 0^o w.r.t. the surface normal. Since the actual emission angle is ill-defined in the case of particles (ranging from 0^o to 90^o) the sampling depth may range from 0 nm to approx. 10 nm. In the case of a rough surface, such as the sample analyzed, the angle of emission vary greatly across the surface, making this technique more surface sensitive.

G.8 XPS Quantitative analysis

Data processing was performed using CasaXPS processing software version 2.3.15 (Casa Software Ltd., Teignmouth, UK). All elements present were identified from survey spectra. The atomic concentrations of the detected elements were calculated using integral peak intensities and the sensitivity factors supplied by the manufacturer. Correction of the binding energy scale for sample charging was based on the main C 1s peak, located at either 284.5 eV (sp2 hybridized carbon in C60) or 285 eV (aliphatic hydrocarbon). The accuracy associated with quantitative XPS is ca. 10% - 15%.

Si, Na and C shown in the analysis are sample contaminants.

Satellite peaks were observed on the high binding energy side of the Zr 3d peaks, as demonstrated in **Figure S22** and **S23**. A number of factors can contribute to the overall spectral shape. In terms of intrinsic contributions, in addition to an asymmetric tail on the higher binding energy side of the peak, spectral contributions from plasmons can occur as a result of coupling of core hole with collective electron oscillations for free-electron like metals[8] or shake-up peaks originating from π-π*transitions in aromatic and unsaturated species such as polystyrene.[9] Similar spectral shapes as observed herein at binding energies greater than the main Zr 3d doublet have been observed for polycrystalline pure[10] and oxidised[11] zirconium. In the case of ZrO_2-based ceramics,[12] a loss structure comprising of three peaks has been observed, which are assigned to excitation of ligand electrons in the valence band to the conduction band, bulk plasmon and excitation of a Zr core level, respectively. The binding energy shift from the main peak for the first two peaks matches that observed for **Figure S23**, noting that the binding energy ranged selected was not sufficient to collect the spectral region expected for the third peak. Considering the binding energy positions of the peaks, the overall spectral shape and the structure of the ligand-based MOF explored herein, the assignments obtained from ZrO_2-based ceramic are likely the closest representation for the loss structure observed herein for the Zr 3d peak.. The ratio of the Ru 3d and C 1s contributions to the total peak area of this spectral region were determined via fitting of the high resolution spectra using the protocol detailed by Morgan.[13] The ratio of intensity of the total Ru 3d and C 1s contributions was used to scale the total peak area of the Ru 3d / C 1s region defined in the survey spectra and thus calculate the elemental quantification of the catalyst. Satellite peaks were also assigned to the fitting of the Ru 3d and C 1s spectra, where Morgan attributed these to plasmons.[13]

G.9 DFT Simulations

The UiO-66 configurations were optimized by density functional theory (DFT) calculations performed using the SIESTA code[14] with the generalized gradient approximation of Perdew-Burke-Ernzerhof (PBE).[15] Norm-conserving Troullier-Martins pseudopotentials with scalar relativistic correction were used. The wave functions were expanded in a double-ζ polarized basis set (DζP). A 200 Ry cutoff for the density integration grid and a density matrix convergence criterion of $2x10^{-4}$ were chosen. A simple cubic superlattice with a cell size of 30 Å was used. In order to determine the most stable configuration, all atoms were allowed to relax until the Hellmann–Feynman forces were smaller than 5 $meV.Å^{-1}$ by using the conjugate gradient minimization method. These combinations of parameters have been successfully proven in different DFT studies.[16-17]

The atomic models were constructed from periodic unit cells of the catalyst precursor UiO-66. In each configuration the Ru atom is placed in different sites (**Figure 9**) with bond lengths of 2.1 Å and 3.4 Å between ruthenium and oxygen atoms and ruthenium and zirconium atoms respectively. Each configuration was relaxed prior to the geometry optimization.

H. Supporting results

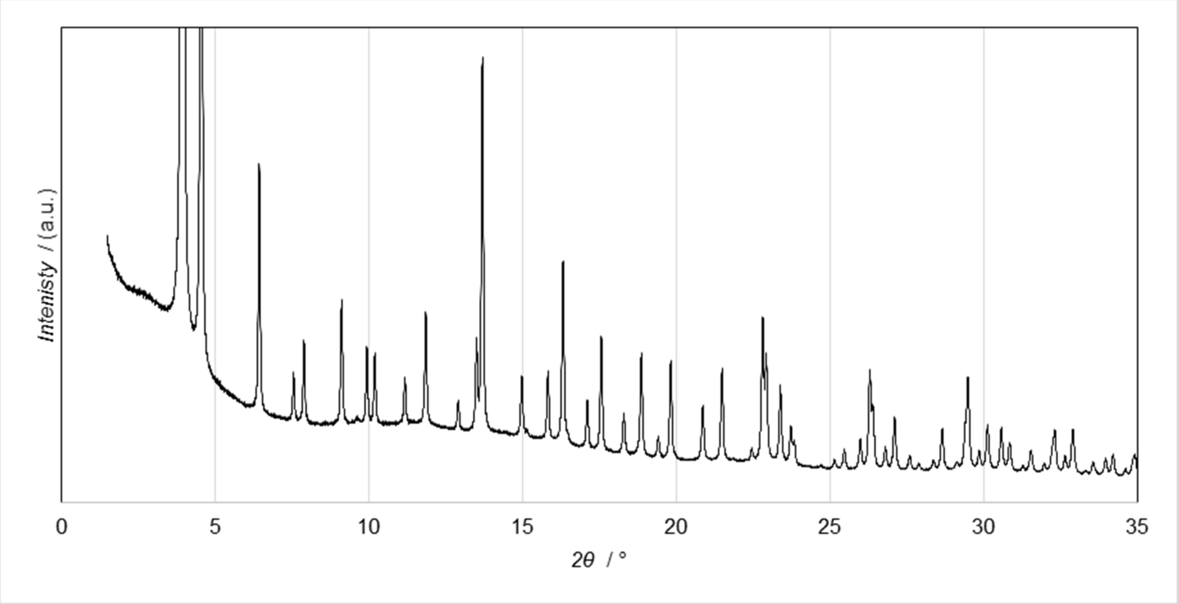

Figure S9: Synchrotron source (15 keV) X-ray diffractogram of Ru-impregnated UiO-66 (**1Ru/UiO-66**) pre-reduced in a tube furnace at 250 °C and 1 bar in 5% H_2-N_2 for 4 h. The UiO-66 structure persisted after the heat treatment and no Ru^0, RuO_2 or $RuCl_3$ phase is observed. **Figure S19** shows the presence of Cl in this sample, we believe the chlorine atoms are well dispersed within the framework due to the absence of chlorides reflections.

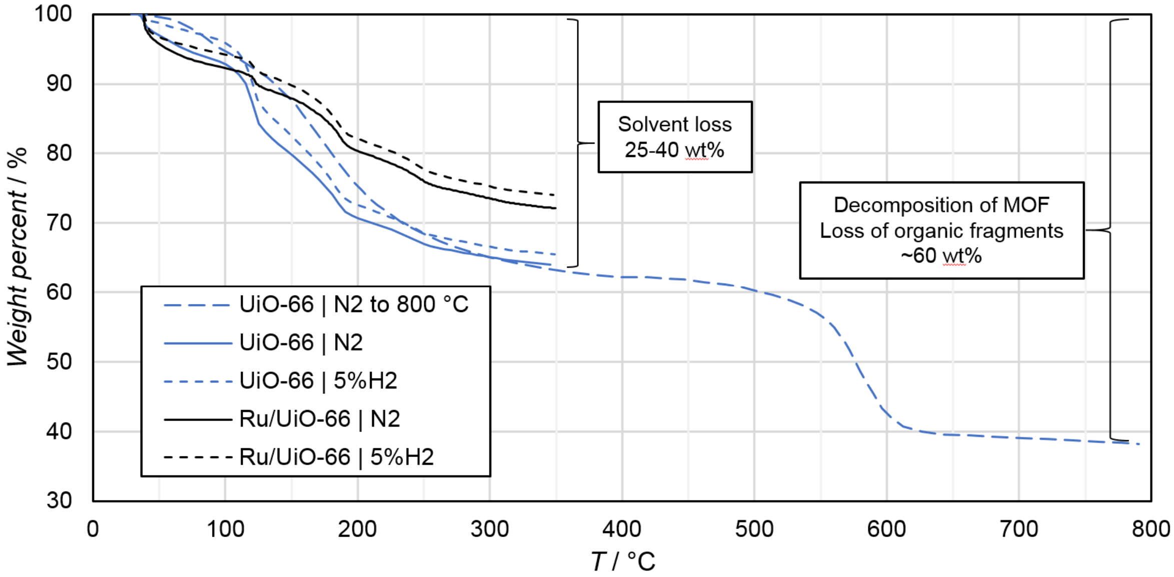

Figure S10: TGA thermograms of UiO-66 (blue) and **1Ru/UiO-66** (Black) in different purge gases (N_2 and 5%H_2/N_2). The presence of 5% H_2 did not seem to affect the stability of the MOF under 350 °C. In pure N_2, the decomposition of the framework (24 % mass loss) occurs after 400 °C. Since the weight loss differs minimally among these samples, we could conclude that a low concentration of H_2 (5 v%) was not enough for the decomposition of UiO-66 or **1Ru/UiO-66** below 350 °C.

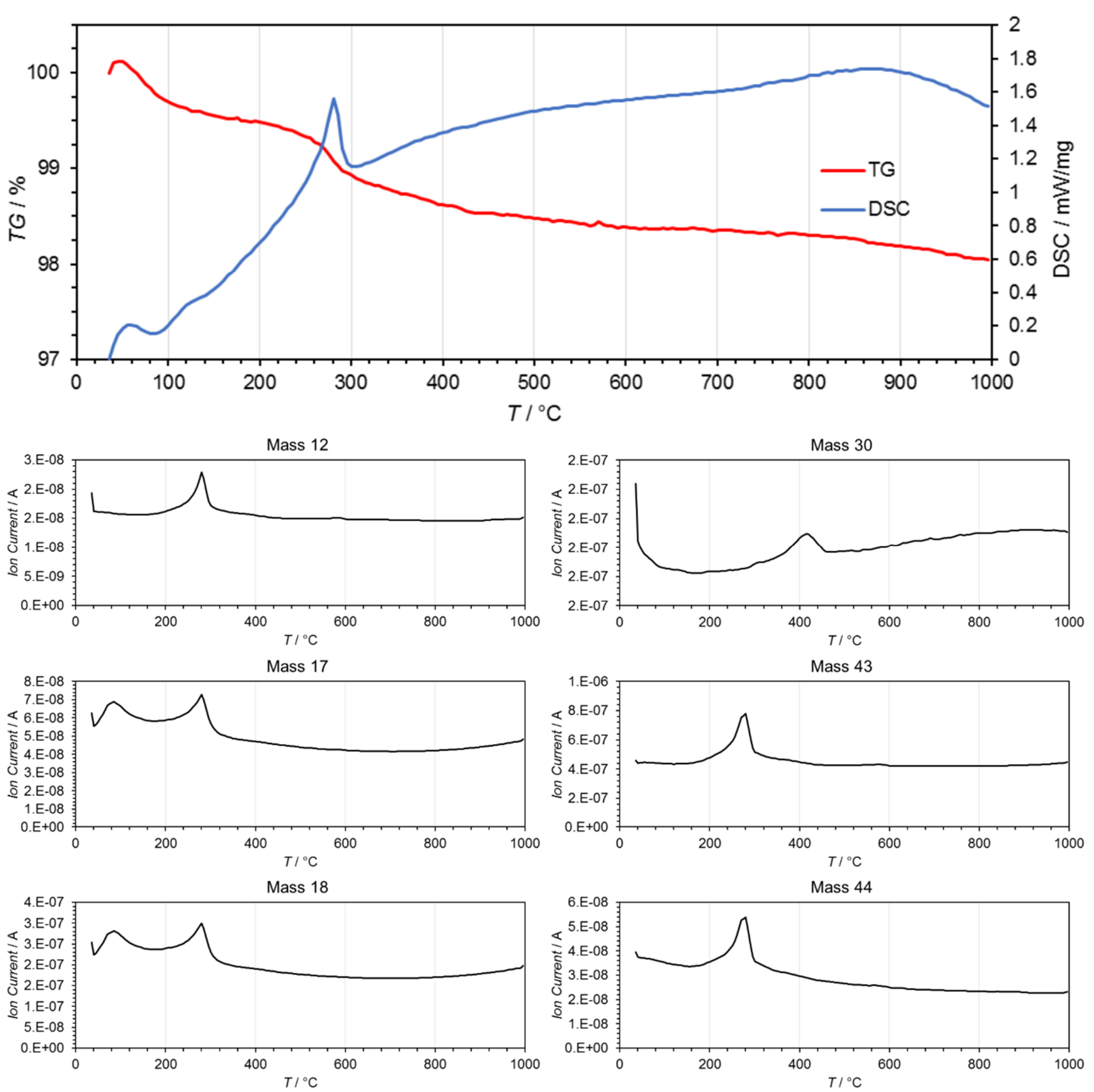

Figure S11: Simultaneous Thermal Analysis (STA) and Evolved Gas Analysis (EGA) of used MOF-derived catalyst performed in air. The TGA results shows less than 2% mass loss during the analysis, EGA confirmed the loss of carbon/carbon containing species (m=12, 30, 43 and 44) and H_2O (m=17 and 18). Thus, this is further evidence that no carbon is left in the catalyst after the *in situ* activation and the present carbon is adventitious. Sample: activated MOF-derived Ru-ZrO_2 catalyst after use at 350 °C, H_2:CO_2 = 4:1.

Table S3: Mass loss of **1Ru/UiO-66** during the catalyst activation. Weight of reactors were measured before precatalyst loading, after precatalyst catalyst loading and after catalysis test. The values below are difference between the loaded reactor weight, before and after catalysis. The mass loss around 60% can be related to the MOF decomposition (**Figure S12**).

Activation temp (°C)	Precatalyst **1Ru/UiO-66** (g)	MOF-derived catalyst (g)	Mass loss (wt%)
250	0.0534	0.0191	64
250	0.0504	0.0178	65
300	0.0487	0.0198	59
300	0.0475	0.0181	62
350	0.0454	0.0198	56
350	0.0462	0.0155	66

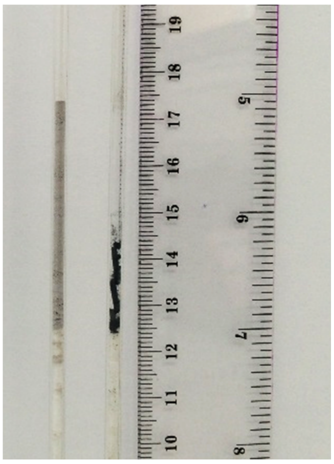

Figure S12: Photograph of **1Ru/UiO-66** as synthesized loaded in a micro-reactor (left) and of the activated MOF-derived Ru-ZrO_2 catalyst after use at 350 °C and 30 bar for 20 hours, $H_2 : CO_2 = 4 : 1$, WHSV = 25 $L \cdot h^{-1} \cdot g^{-1}$ (right). Ruler units are cm (left) and inches (right).

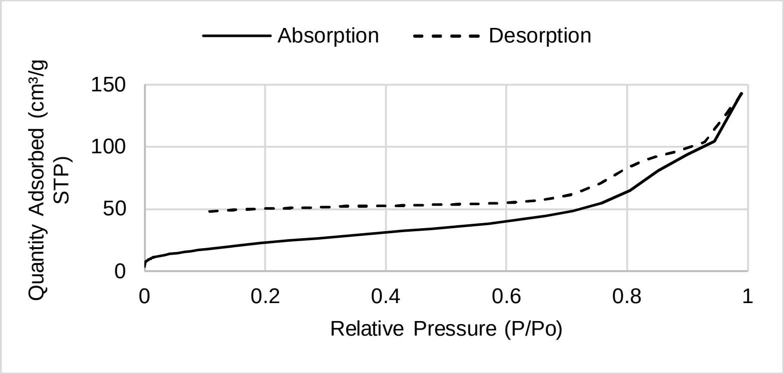

Figure S13: N_2 absorption isotherm at 77K for MOF-derived Ru-ZrO_2 catalyst after use. BET Surface area was found to be 60 m^2/g. Reaction conditions: 350 °C, 30 bar, H_2:CO_2 = 4:1, WHSV = 8.7 L·h-1·precatalyst g^{-1}.

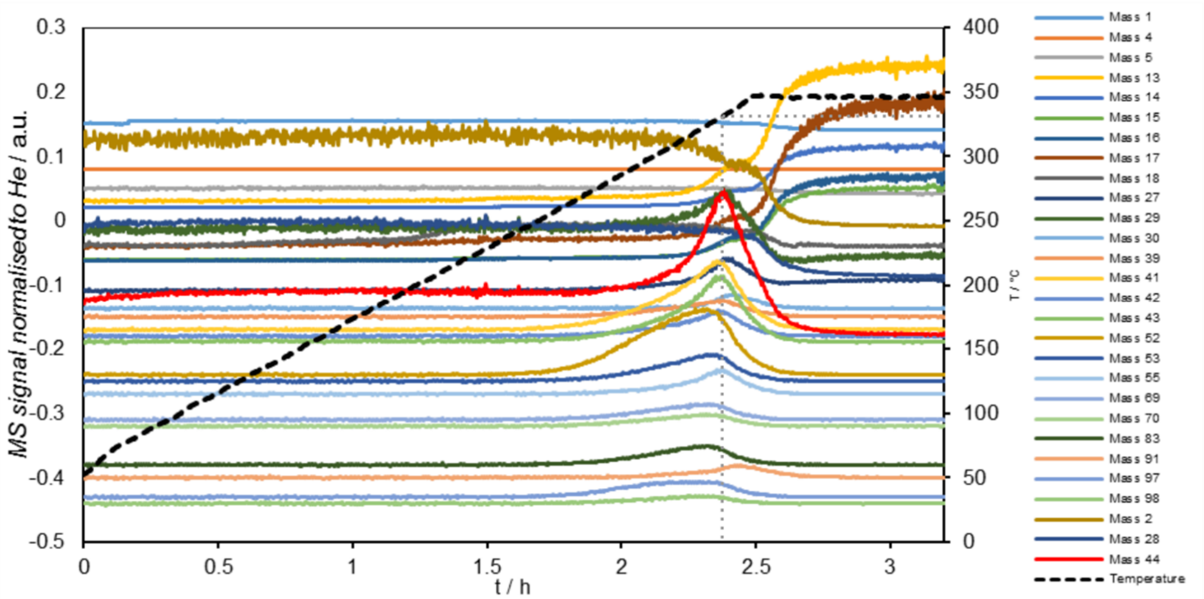

Figure S14: Mass spectral signal normalized to He tracing monitoring the activation of the MOF-derived catalyst. Several different organic fragments are detected by the mass spectrometer at 330 °C (dashed black line). Total experiment time: 3 h. Reaction conditions: 60 mg of **1Ru/UiO-66**, H_2:CO_2 = 3:1 (63.75% H_2, 21.25% CO_2 and 15% He), WHSV = 200 $L \cdot h^{-1} \cdot g_{cat}^{-1}$. Data was scaled and offset along the y axis for clarity.

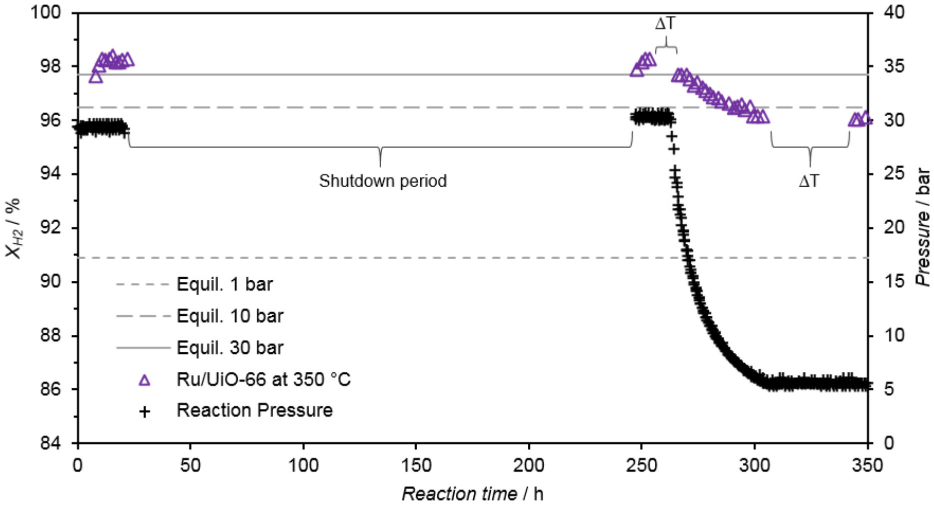

Figure S15: Triangle markers indicate the X_{H2} for the Ru-UiO-66 derived catalyst at 350 °C. Initially, the catalyst was tested at 30 bar before a long shutdown period, where the samples were cooled down to room temperature and exposed to air at atmospheric pressure. The sample was then tested again at 30 bar without any sign of deactivation. Next, it was tested at decreasing reaction pressure conditions to 5 bar (cross markers). The following periods where X_{H2} is absent are periods where the sample was tested at different temperatures (Figure 1B). For comparison, the gray lines indicate the X_{H2} calculated for the thermodynamic equilibrium at 350 °C and different pressures for CO_2 methanation with equal H_2 to CO_2 ratio[7]. Reaction conditions: 50 mg of **1Ru/UiO-66**, H_2:CO_2 = 4:1, WHSV = 43 L·h^{-1}·g^{-1}.

T	Reaction time 20 h	Reaction time 100 h
250 °C	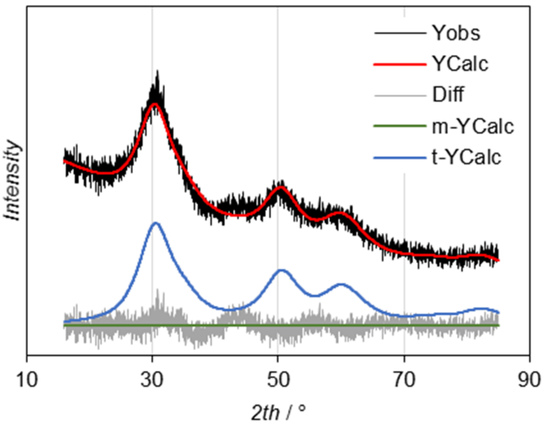	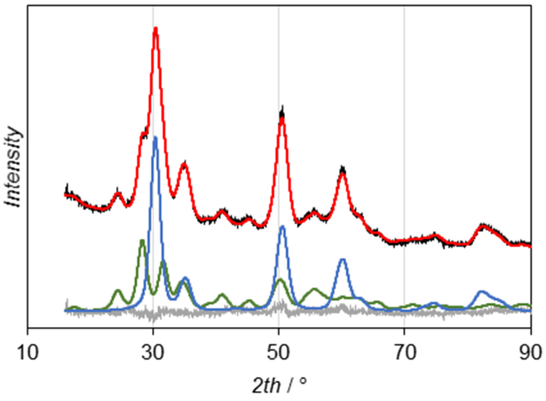
300 °C	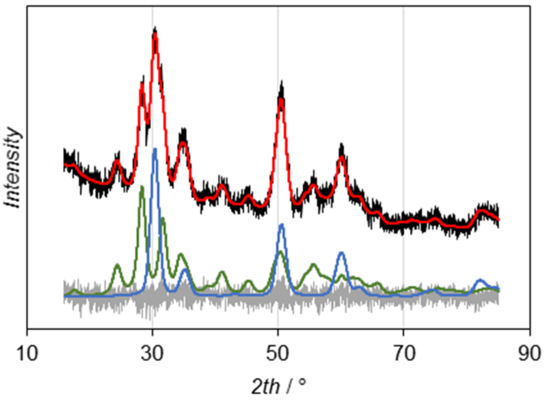	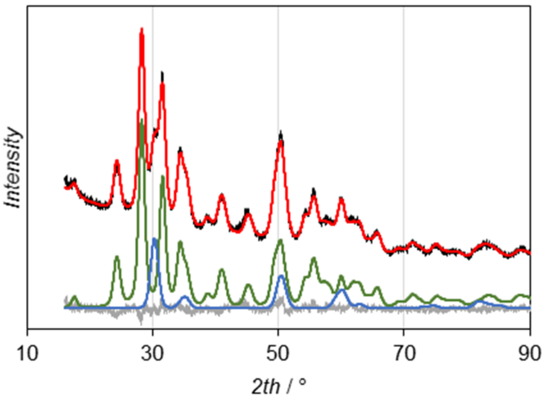
350 °C	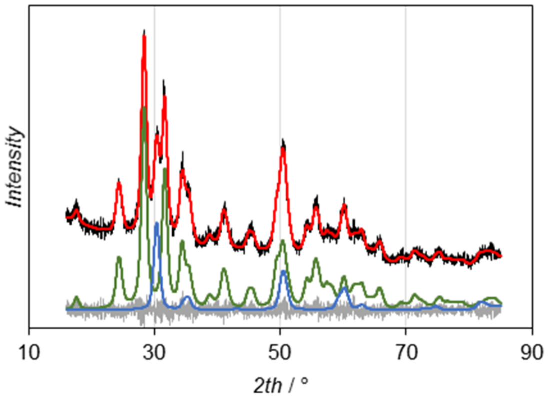	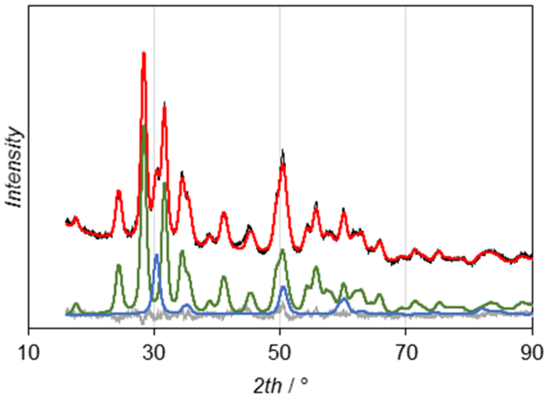

Figure S16: Analysis of PXRD data of the MOF-derived catalysts activated at different temperatures at during different reaction times. Observed XRD (Yobs), calculated XRD pattern through Rietveld method (Ycalc), difference curve (Diff), calculated contribution for the ZrO_2 monoclinic phase (m-Ycalc) and for the ZrO_2 tetragonal phase (t-Ycalc). No other phase (graphite, RuO_2 or Ru^0) was observed. Reaction conditions: 50 mg of **1Ru/UiO-66**, H_2:CO_2 = 4:1, WHSV = 43 L·h^{-1}·g^{-1} and 30 bar. Refined parameters and the weighted profile R factor (r_wp) can be found in **Table S4**.

Table S4: Rietveld refinement results according to reaction conditions.

Sample	Activation temp (°C)	Activation pressure (bar)	Reaction time (h)	Phase	Amount of phase (Wt%)	error	Rietveld Scale Factor	a (nm)	b (nm)	c (nm)	β (°)	r_wp	lvol - Crystallite domain size (nm)	error	e0 - micro strain	error
1	250	30	20	t-ZrO2	100	0.00	0.005789	3.589	3.589	5.225	90	5.80	1.84	0.00	0.02051	0.00
2	300	30	20	m-ZrO2	61.59	1.06	0.000623	5.156	5.202	5.329	99.38	5.48	8.32	0.72	0.00011	306.32
2	300	30	20	t-ZrO2	38.41	1.06	0.001628	3.602	3.602	5.185	90	5.48	7.73	0.59	0.00009	417.35
3	350	30	20	m-ZrO2	82.57	0.46	0.001486	5.151	5.208	5.322	99.22	4.85	12.09	0.47	0.00004	215.73
3	350	30	20	t-ZrO2	17.43	0.46	0.001312	3.600	3.600	5.197	90	4.85	10.92	1.03	0.01553	1.88
4	250	30	100	m-ZrO2	45.55	0.47	0.004795	5.160	5.194	5.323	99.43	2.32	6.68	0.25	0.00012	227.63
4	250	30	100	t-ZrO2	54.45	0.47	0.024072	3.595	3.595	5.185	90	2.32	6.49	0.12	0.00018	62.65
5	300	30	100	m-ZrO2	83.48	0.40	0.006676	5.154	5.206	5.321	99.30	2.98	10.47	0.20	0.00009	51.07
5	300	30	100	t-ZrO2	16.52	0.40	0.005531	3.597	3.597	5.201	90	2.98	8.23	0.48	0.01018	1.54
6	350	30	100	m-ZrO2	84.83	0.28	0.008906	5.151	5.207	5.318	99.24	2.87	11.88	0.21	0.00012	33.82
6	350	30	100	t-ZrO2	15.17	0.28	0.00667	3.600	3.600	5.191	90	2.87	10.14	0.60	0.0002	72.41

T / °C	20 h			100 h		
	m-ZrO_2	t-ZrO_2	X_{H2} / %	m-ZrO_2	t-ZrO_2	X_{H2} / %
250	0	100	23	48	52	28
300	52	48	22	86	14	53
350	82	18	96	88	12	96

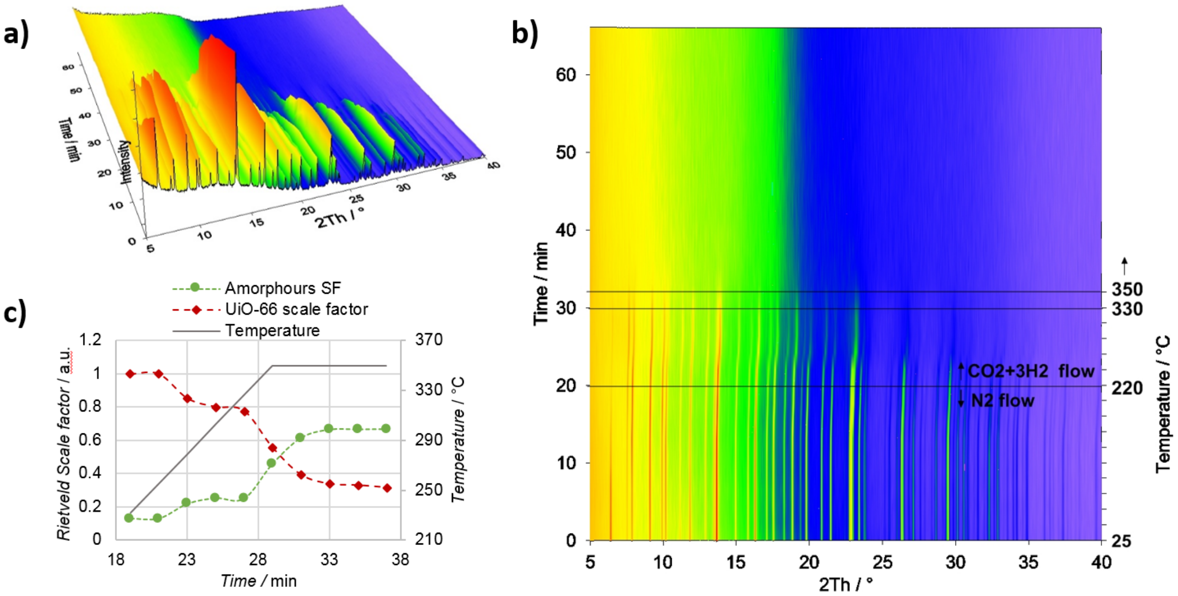

Figure S17: a, b) *In situ* variable temperature PXRD of **1Ru/UiO-66**. The sample was first heated to 220 °C under N_2 flow, then at 19 min, the gas flow was replaced with a mixture of CO_2:H_2 = 1:3. Upon reaching 350 °C, the temperature was kept constant. c) Rietveld refinement scale factor versus time and temperature for UiO-66 crystalline phase[18] and the resulting amorphous phase. Rietveld scale factor is a multiplier of the reflections of a certain phase (relative intensities within a phase are constant) and it can be correlated to the relative amount of the phase in the sample. A drastic decrease of the UiO-66 scale factor was observed simultaneously with the increase of the amorphous phase contribution. The Rietveld refinement of this XRD dataset was performed in batch mode starting with the diffractogram at 19min. The values refined for each diffractogram were used as input for the next. The background contribution for all diffractograms was fixed according to the refined values at 19min.

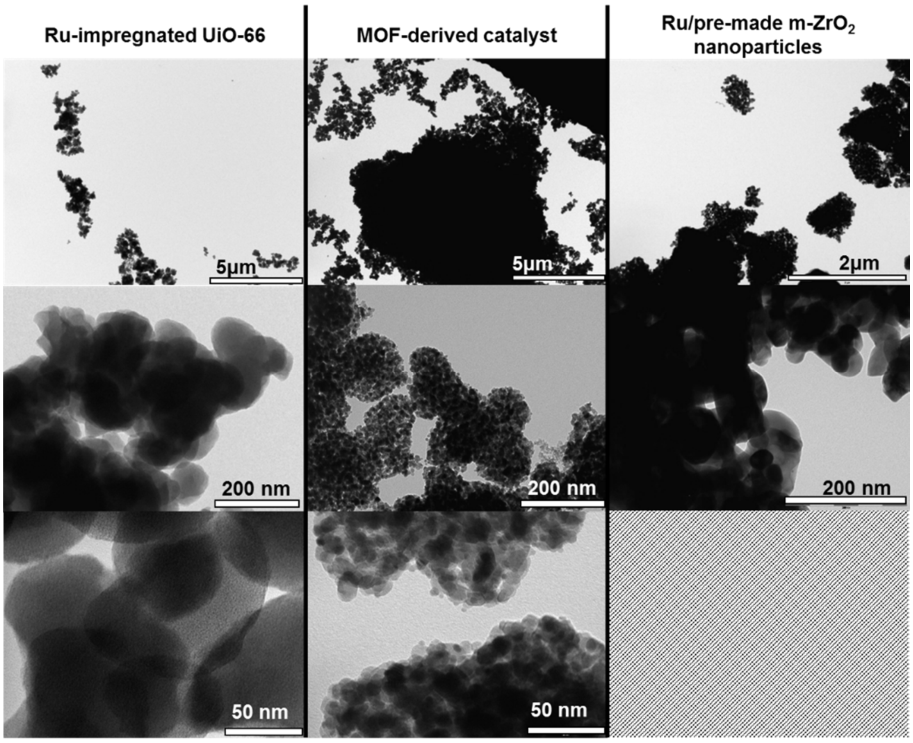

Figure S18: TEM images of **1Ru/UiO-66** pre-reduced in a tube furnace at 250 °C in 5% H_2-N_2 for 4 hours, UiO-66 framework was retained and confirmed by XRD (**Figure S9**) (left); MOF-derived catalyst activated at 350 °C and 30 bar (centre); and Ru/pmZrO2, Ru on premade m-ZrO_2, tested at 350 °C and 30 bar (right). The MOF-derived sample is composed of ZrO_2 nanoparticles, organized in clusters which resemble the UiO-66 crystals shape.

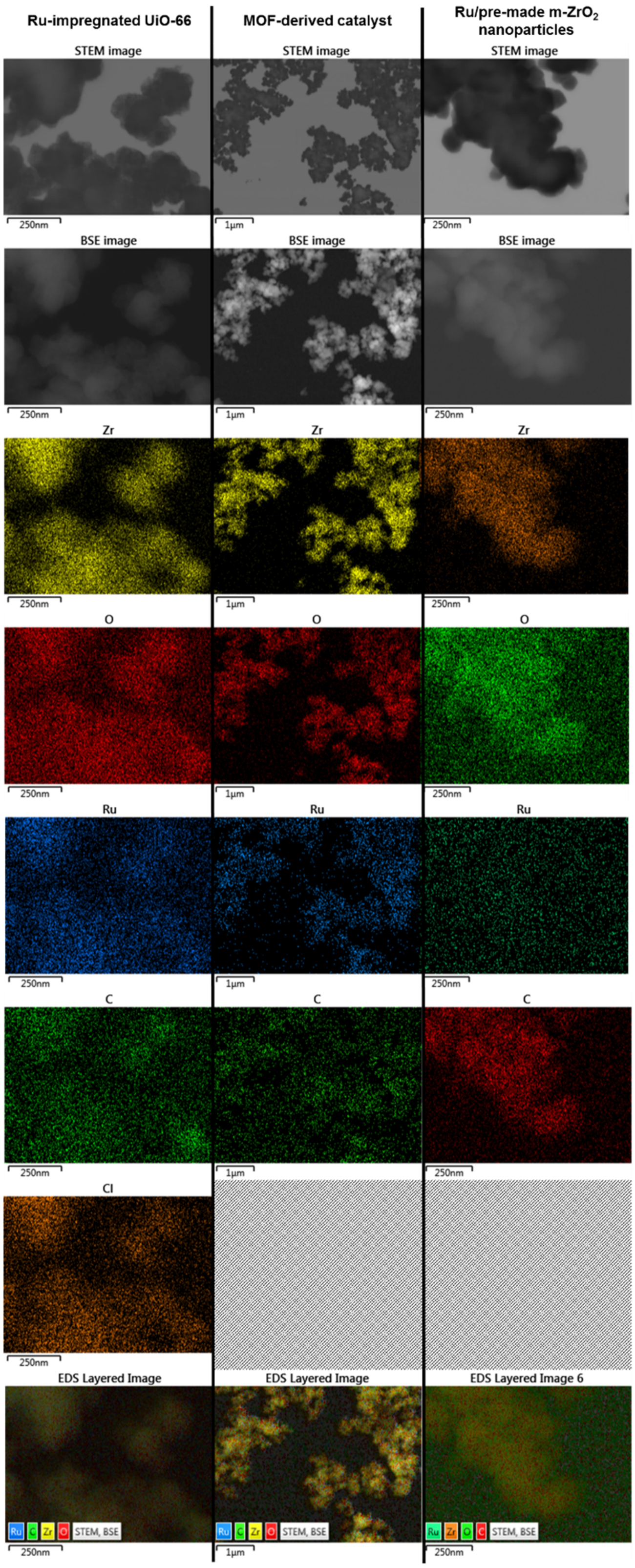

Figure S19: STEM, BSE images and EDS mapping of **1Ru/UiO-66** pre-reduced in a tube furnace at 250 °C in 5% H2-N2 for 4 hours, UiO-66 framework was retained and confirmed by XRD (**Figure S9**) (left); MOF-derived catalyst activated at 350 °C and 30 bar (centre); and Ru/pmZrO2, Ru on premade m-ZrO$_2$, tested at 350 °C and 30 bar (right). The comparison of these images indicate a homogeneous dispersion of ruthenium chloride within UiO-66 prior to the catalyst activation. The MOF-derived catalyst also contains Ru evenly dispersed, but no evidence of chloride. Lastly, Ru on pre-made m-ZrO_2 nanoparticles does not presents the same level of Ru dispersion over the ZrO_2 particles.

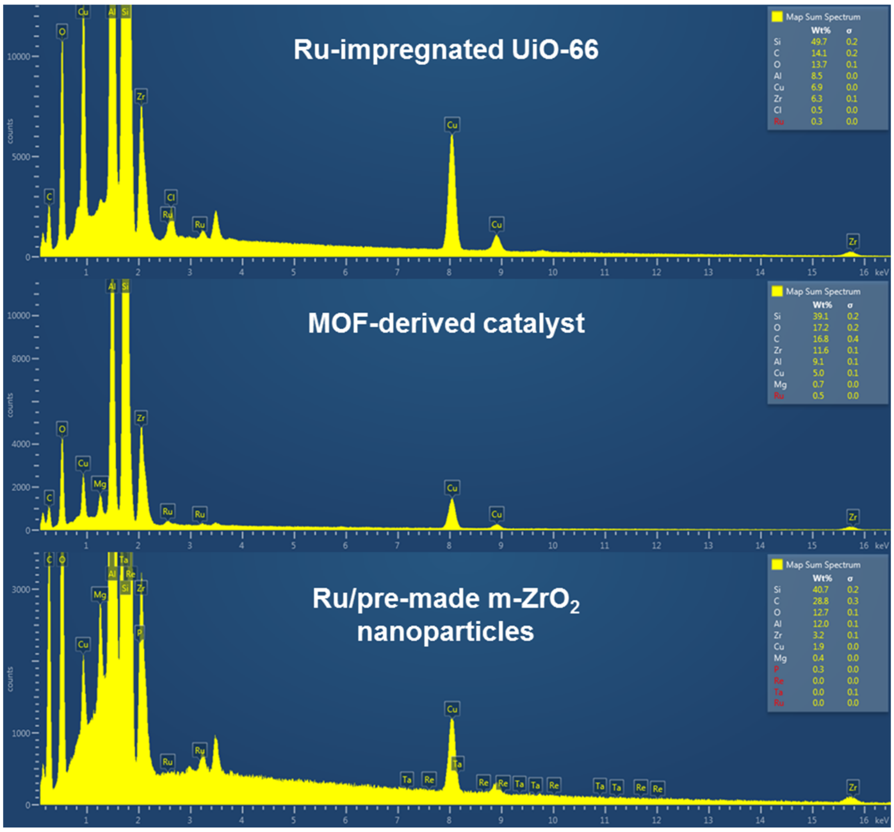

Figure S20: EDS quantitative elemental analysis for the mapping displayed in **Figure S19**.

Table S5: EDS Map Sum Spectrum quantitative analysis of MOF-derived catalyst from **Figure S20**.

Element	Wt %	σ
Si	39.1	0.2
O	17.2	0.2
C	16.8	0.4
Zr	11.6	0.1
Al	9.1	0.1
Cu	5.0	0.1
Mg	0.7	0.0
Ru	0.5	0.0

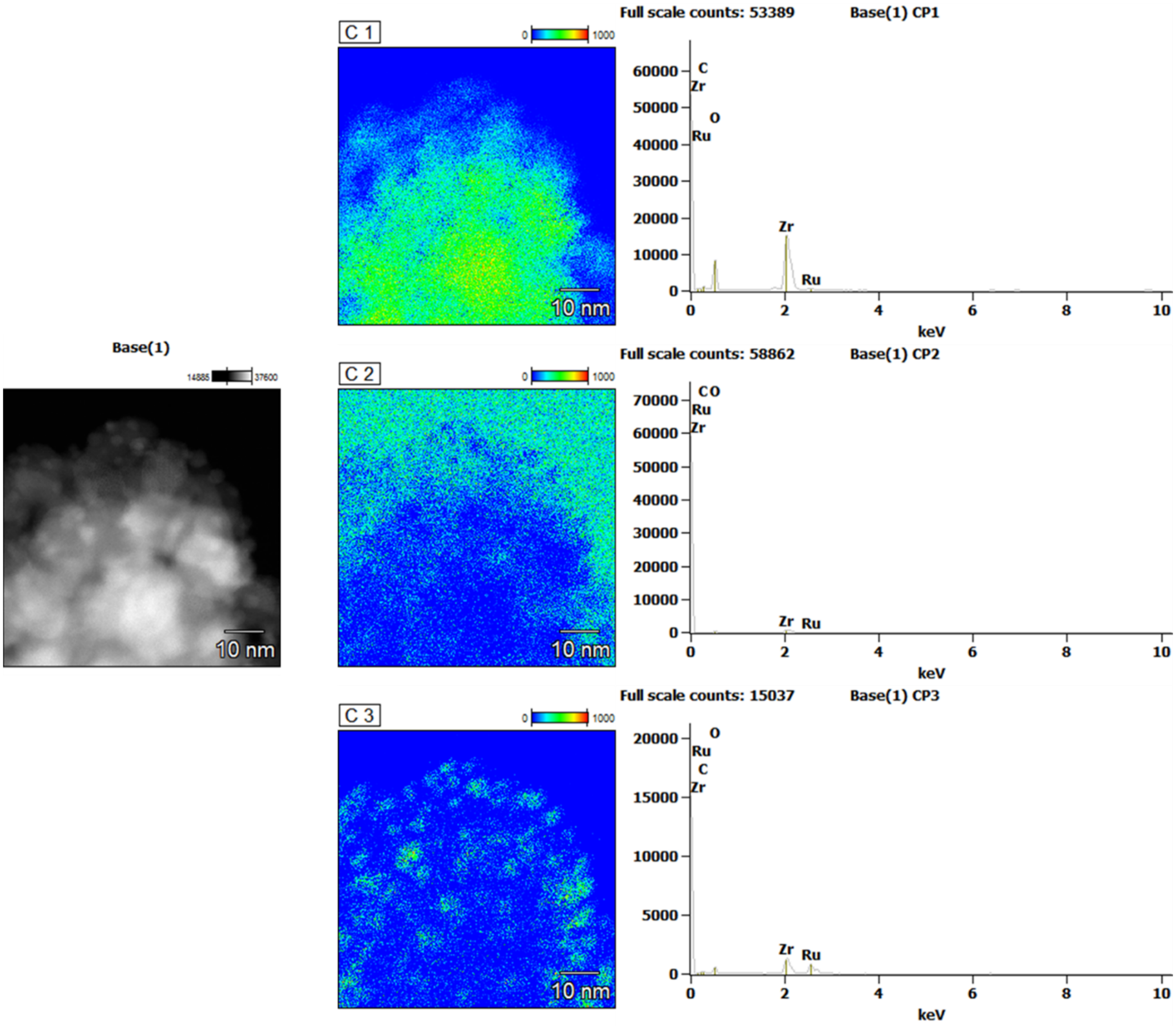

Figure S21: Compass analysis (multivariate statistical analysis) was used to separate the EDS data into regions with similar spectra. The analysis indicated 3 regions: Map C1 comprises the majority of the observable sample, C2 covers the background (sample-free region) and C3 highlights the Ru nanoparticles. Quantitative analysis of each area is shown below (**Table S6**)

Table S6: Quantitative analysis of the spectra shown in **Figure S21**. Map C3 indicated a much higher content of Ru compared to the other maps. In addition, the low O content in this map indicates Ru metal.

Map	C 1		C 2		C 3	
Element line	Wt.%	Error	Wt.%	Error	Wt.%	Error
C K	3.94	± 0.11	5.81	± 0.35	5.4	± 0.35
O K	31.31	± 0.21	21.75	± 0.59	18.59	± 0.37
Zr K	61.93	± 0.77	62.52	± 3.30	41.96	± 1.60
Ru L	2.82	± 0.11	9.92	± 0.50	34.05	± 0.70

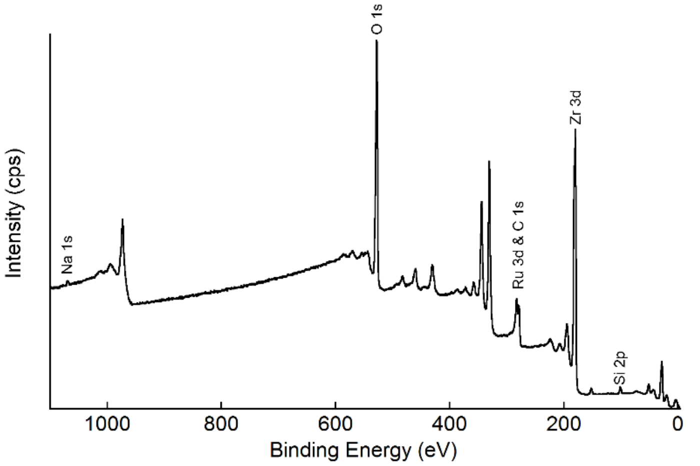

Figure S22: Selected, representative survey spectrum by XPS of the MOF-derived catalyst activated at 350 °C and 30 bar.

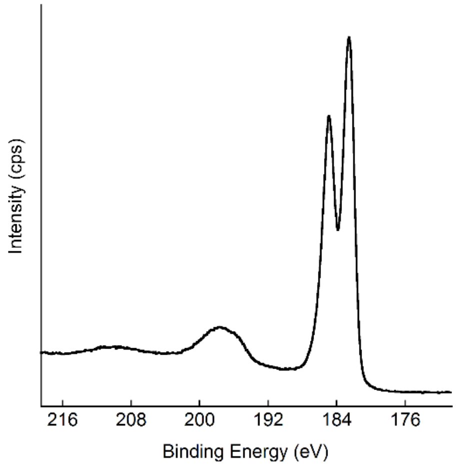

Figure S23: Selected, representative Zr 3d spectrum by XPS of the MOF-derived catalyst activated at 350 °C and 30 bar.

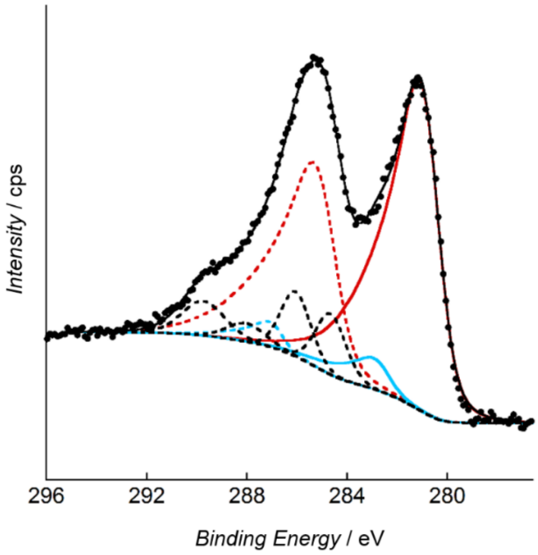

Figure S24: Selected, representative high resolution spectrum of the C 1s and Ru 3d region for the MOF-derived catalyst activated at 350 °C and 30 bar by XPS. Component assignments and fit parameters are provided in **Table S7**.

Table S7: XPS binding energies and fit parameters for MOF-derived catalyst activated at 350 °C.

BE (eV)	Component	Peak	Peak assignment	CasaXPS fitting parameter
280.7	Red (solid)	Ru 3d5/2	RuO2	LF(0.25,1,45,280)
284.9	Red (dashed)	Ru 3d3/2		LF(0.25,1,45,280)
282.6	Blue (solid)	Ru 3d5/2 sat	RuO2 satellite	LF(0.25,1,45,280)
286.8	Blue (dashed)	Ru 3d3/2 sat		LF(0.25,1,45,280)
284.7	Black (dashed)	C 1s	C-C, C-H	GL(30)
286	Black (dashed)	C 1s	C-O	GL(30)
287.9	Black (dashed)	C 1s	O-C-O, C=O	GL(30)
289.5	Black (dashed)	C 1s	CO2R, CO3	GL(30)

Table S8: Elemental composition of the MOF-derived catalyst activated at 350 °C and 30 bar by XPS.

Element	Mean Atomic%	Std. dev
O	53.75	1.96
Zr	23.97	1.66
C	15.74	0.16
Si	3.34	0.13
Ru	2.82	0.02
Na	0.38	0.01

I. References

1. Katz, M. J.; Brown, Z. J.; Colón, Y. J.; Siu, P. W.; Scheidt, K. a.; Snurr, R. Q.; Hupp, J. T.; Farha, O. K., A Facile Synthesis of UiO-66, UiO-67 and Their Derivatives. Chem. Commun. 2013, 49, 9449-51.

2. Meynen, V.; Cool, P.; Vansant, E. F., Verified Syntheses of Mesoporous Materials. *Microporous Mesoporous Mater.* **2009**, *125*, 170-223.

3. Schmitt, B.; Bronnimann, C.; Eikenberry, E. F.; Gozzo, F.; Hormann, C.; Horisberger, R.; Patterson, B., Mythen Detector System. *Nucl. Instrum. Methods Phys. Res., Sect. A* **2003**, *501*, 267-272.

4. *Topas V5: General Profile and Structure Analysis Software for Powder Diffraction Data*, Bruker AXS GmbH: Karlsruhe, Germany, 2012.

5. Gerbasi da Silva, A. J.; Claassens-Dekker, P.; Sallarès de Mattos Carvalho, A. C.; Manzolillo Sanseverino, A.; Pontes Bittencourt Quitete, C.; Szklo, A.; Falabella Sousa-Aguiar, E., Evaluation of Mos2 Based Catalysts for the Conversion of Syngas into Alcohols: A Combinatorial Approach. *J. Environ. Chem. Eng.* **2014**, *2*, 2148-2155.

6. van der Waal, J. K.; Klaus, G.; Smit, M.; Lok, C. M., High-Throughput Experimentation in Syngas Based Research. *Catal. Today* **2011**, *171*, 207-210.

7. Gao, J. J.; Wang, Y. L.; Ping, Y.; Hu, D. C.; Xu, G. W.; Gu, F. N.; Su, F. B., A Thermodynamic Analysis of Methanation Reactions of Carbon Oxides for the Production of Synthetic Natural Gas. *RSC Adv.* **2012**, *2*, 2358-2368.

8. Kurth, M.; Graat, P. C. J., Quantitative Analysis of the Plasmon Loss Intensities in X-Ray Photoelectron Spectra of Magnesium. *Surf. Interface Anal.* **2002**, *34*, 220-224.

9. Beamson, G.; Briggs, D., *High Resolution Xps of Organic Polymers: The Scienta Esca300 Database*; Wiley, 1992.

10. Lyapin, A.; Graat, P. C. J., Quantitative Analysis of the X-Ray Photoelectron Spectrum of Zirconium. *Surf. Interface Anal.* **2004**, *36*, 812-815.

11. Lyapin, A.; Jeurgens, L. P. H.; Graat, P. C. J.; Mittemeijer, E. J., Ellipsometric and Xps Study of the Initial Oxidation of Zirconium at Room Temperature. *Surf. Interface Anal.* **2004**, *36*, 989-992.

12. Hughes, A. E., Interfacial Phenomena in Y2o3-ZrO2-Based Ceramics: A Surface Science Perspective. In *Mater. Sci. Monogr.*, Janusz, N., Ed. Elsevier: 1995; Vol. Volume 81, pp 183-238.

13. Morgan, D. J., Resolving Ruthenium: Xps Studies of Common Ruthenium Materials. *Surf. Interface Anal.* **2015**, *47*, 1072-1079.

14. Soler, J. M.; Artacho, E.; Gale, J. D.; García, A.; Junquera, J.; Ordejón, P.; Sánchez-Portal, D., The Siesta Method for Ab Initio Order- N Materials Simulation. *J. Phys.: Condens. Matter* **2002**, *14*, 2745-2779.

15. Perdew, J. P.; Burke, K.; Ernzerhof, M., Generalized Gradient Approximation Made Simple. *Phys. Rev. Lett.* **1996**, *77*, 3865-3868.

16. Barron, H.; Fernández-Seivane, L.; López-Lozano, X., Systematic Study of the Adsorption of Thiol Molecules on a Au55 Nanoparticle. *physica status solidi (b)* **2014**, *251*, 1239-1247.

17. Barron, H.; Fernández-Seivane, L.; Weissker, H. C.; López-Lozano, X., Trends and Properties of 13-Atom Ag–Au Nanoalloys I: Structure and Electronic Properties. *J. Phys. Chem. C* **2013**, *117*, 21450-21459.

18. Valenzano, L.; Civalleri, B.; Chavan, S.; Bordiga, S.; Nilsen, M. H.; Jakobsen, S.; Lillerud, K. P.; Lamberti, C., Disclosing the Complex Structure of UiO-66 Metal Organic Framework: A Synergic Combination of Experiment and Theory. *Chem. Mater.* **2011**, *23*, 1700-1718.

Chapter 4

What happens during MOF templating? Synchrotron *in operando* PXRD study and systematic evaluation of MOF components for the synthesis of CO$_2$ methanation catalysts

Renata Lippi,[†‡] Shaun C. Howard,[‡] Ian C. Madsen,[§] Qinfen Gu, [±] Christopher J. Sumby,[†]
Christian J. Doonan,*[†] Danielle F. Kennedy*[‡]

[‡]CSIRO Manufacturing, Clayton, Victoria 3168, Australia.
[†]Centre for Advanced Nanomaterials, Department of Chemistry, The University of Adelaide, Adelaide, South Australia 5005, Australia.
[§]CSIRO Mineral Resources, Clayton, Victoria 3168, Australia
[±]Australian Synchrotron, Clayton, Victoria 3168, Australia.

Manuscript to be submitted

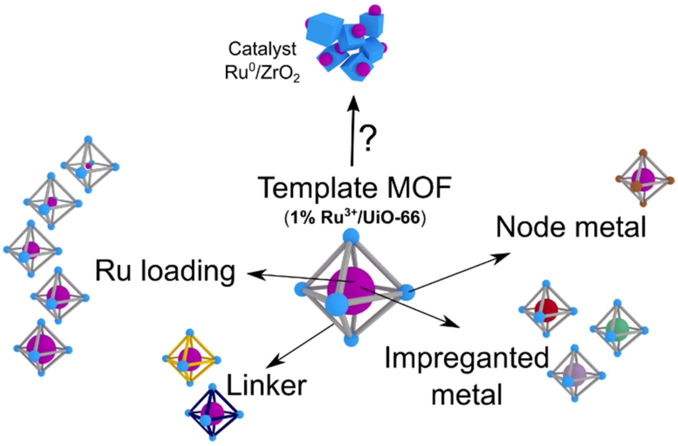

4.1. Summary

This chapter examines the templating of the highly active Ru^0/ZrO_2 catalyst identified in Chapter 3. The transformation that the MOF undergoes to form the active catalyst was investigated in a series of experiments to evaluate: catalyst activation in $5\%H_2$ vs *in situ* activation; Ru phase in the final catalyst; phase transformation during in situ activation via *in operando* PXRD; effect of MOF components in the templating of the catalyst, including linkers, Ru loading, impregnated metal, node metal. The systematic study presented in this chapter provides interesting insights in the MOF-templating mechanism and the effect of the individual components of the MOF on the templating of the catalyst and its catalytic activity.

Statement of Authorship

Title of Paper	What happens during MOF templating? Synchrotron in operando PXRD study and systematic evaluation of MOF components for the synthesis of CO_2 methanation catalysts
Publication Status	☐ Published ☐ Accepted for Publication ☐ Submitted for Publication ☒ Unpublished and Unsubmitted work written in manuscript style
Publication Details	

Principal Author

Name of Principal Author (Candidate)	Renata Lippi		
Contribution to the Paper	Intellectual input in designing, design, preparation and execution of experiments, synthesis of materials, catalysis tests, catalysis data analysis, XRD experiments and analysis, surface area analysis, electron microscopy experiments, preparation of manuscript.		
Overall percentage (%)	80%		
Certification:	This paper reports on original research I conducted during the period of my Higher Degree by Research candidature and is not subject to any obligations or contractual agreements with a third party that would constrain its inclusion in this thesis. I am the primary author of this paper.		
Signature		Date	29/11/2017

Co-Author Contributions

By signing the Statement of Authorship, each author certifies that:

i. the candidate's stated contribution to the publication is accurate (as detailed above);

ii. permission is granted for the candidate in include the publication in the thesis; and

iii. the sum of all co-author contributions is equal to 100% less the candidate's stated contribution.

Name of Co-Author	Shaun C. Howard		
Contribution to the Paper	Intellectual input in planning and operation of high-throughput catalysis testing rig and synchrotron experimental set up		
Signature		Date	20-Nov-2017

Name of Co-Author	Ian C. Madsen		
Contribution to the Paper	Intellectual input in Rietveld refinement of PXRD data		
Signature		Date	21\11\2017

Name of Co-Author	Qinfen Gu		
Contribution to the Paper	Intellectual input in synchrotron *in operando* PXRD experiments		
Signature		Date	23/11/2017

Name of Co-Author	Christopher J. Sumby		
Contribution to the Paper	Intellectual input in project design, manuscript revisions		
Signature	[redacted]	Date	23/11/17

Name of Co-Author	Christian J. Doonan		
Contribution to the Paper	Intellectual input in project design, manuscript revisions		
Signature	[redacted]	Date	23/11/17

Name of Co-Author	Danielle F. Kennedy		
Contribution to the Paper	Intellectual input in project design, high-throughput catalysis screening method development, assistance in synchrotron experiments, manuscript revisions		
Signature	[redacted]	Date	26/11/2017

4.2. Abstract

Metal-organic framework (MOF)-templating under reducing conditions has been investigated for the synthesis of Ru^0 nanocatalysts for CO_2 hydrogenation. A post synthetically modified template MOF 1wt%Ru/UiO-66 is used as template to examine (i) the effect of the concentration of H_2 in the catalyst templating, (ii) the effect of activation conditions on the phase of the active metal, and (iii) the structural transition from a MOF to active catalyst via *in operando* powder X-ray diffraction (PXRD). In addition, the structure and performance of catalysts formed from template MOFs with different Ru loading, various organic linkers, alternative impregnated metal and node metal were evaluated. These studies demonstrated that a high concentration of H_2 is a requirement for the synthesis of the highly active catalysts; Ru, present in the final catalyst as single crystal and amorphous nanoparticles, assists in driving the formation of ZrO_2; the ratio of monoclinic and tetragonal ZrO_2 is affected by the choice of template linker; and by replacing UiO-66 by a Ce analogue, Ru^0/CeO_2 nanocatalysts were synthesised, demonstrating the potential of MOF-templating to support metallic species on different metal oxides.

4.3. Introduction

Metal-organic frameworks (MOFs) are porous materials composed of inorganic nodes coordinated by organic linkers.[1] MOFs have been predominantly investigated for application to challenges in gas storage,[2-6] separation science,[7-9] and catalysis.[10-12] Recently, MOF-derived materials have attracted significant attention, evidenced by the large number of recent reviews.[13-20] Specifically, the use of MOFs as self-sacrificing templates for functional materials has been shown to significantly impact the composition and morphology of materials and, as a consequence, improve their performance, particularly for applications in the areas of electrochemistry[13, 15-17, 20] and catalysis.[14-15, 18-20] Their intrinsic porosity and the potential to tailor their periodic structures (*i.e.* spacing between inorganic nodes) make MOFs novel templates for the synthesis of functional materials that possess complex and controlled composition. A significant advantage of employing MOFs as templates is that MOF-derived materials often have structures and properties not achieved via other methods (*e.g.* morphology, porosity, particle size, phase/element distribution).[21-23]

MOF-templating is usually achieved via heat-treatment under inert (pyrolysis) or oxidising (calcination) atmospheres. Generally, pyrolysis yields metal, metal oxide or carbide nanoparticles embedded in a porous carbon matrix, whereas calcination leads to removal of carbon and formation of metal oxide nanoparticles. Only a few reports have explored the use of reducing conditions (*i.e.* thermal treatment in H_2) in MOF-templating,[24-25] In our previous work, we showed the MOF-templating of a highly active Ru^0/ZrO_2 catalyst carried under CO_2 methanation reaction conditions (80% H_2 and 20% CO_2 at 350 °C).[21] This exemplified the potential of using reducing atmospheres to synthesise metallic species with controlled distribution and morphology from MOFs.

Tailoring of the sacrificial MOF template has been successfully used to synthesise highly complex materials. For example, mixed-metal MOFs with N-containing linkers produced alloy nanoparticles embedded in a N-doped carbon matrix.[26] In addition, post-synthetic metalation of MOFs has been shown to provide excellent distribution of the secondary metal on the final material.[27-28] Despite these results, how the individual components of the MOF influence the templating route remains unknown.

The lack of a fundamental understanding of the MOF-templating mechanism has been identified as a limitation for the directed synthesis of new marterials.[13-20] Efforts in this direction have been reported by Xu *et al.* who investigated the pyrolysis of a Ni-MOF into Ni@C via *in* *situ* TEM. They observed the growth of Ni nanoparticles within a carbon matrix, the detachment of these nanoparticles from the matrix and consequent agglomeration at higher temperatures. This knowledge enabled optimisation of the catalyst synthesis conditions.[29] In summary, it is evident that understanding the mechanism of MOF-templating will lead to treatment optimisation and the development of more sophisticated structures.

Defining the phase transition that a catalyst may undergo during activation and under reaction conditions is key to understanding what the active phase is and how it is formed. Powder X-ray diffraction (PXRD) is a characterisation technique that relies on the diffraction of X-rays from the crystalline structure of the material.[30] Analysis of the resulting diffraction pattern provides precise identification and quantification of crystalline phases in a sample. This technique allows the analysis of the sample under various conditions, including controlled temperature and atmosphere. In this context, it is worthwhile to defining *in situ* and *in operando* characterisation methods. *In situ* characterisation is the study of a sample under simulated process conditions,[31] whereas *in operando* characterisation is the combination of *in situ* characterisation with another technique for verification of the process. *In operando* PXRD experiments for catalysts may, for example, track the reaction products or the conversion of reactants via effluent analysis using a mass spectrometer. The addition of this dimension to the analysis enables an accurate evaluation of the sample, but also adds complexity to the experiment.

Here we evaluate different aspects of the templating of CO_2 methanation catalysts derived from Ru/UiO-66 (Figure 1). The aspects related to the transformation mechanism include effect of H_2 concentration during activation and observation of phase transition during catalyst activation via *in operando* PXRD. In addition, aspects of the template MOF examined include, Ru loading, linker, impregnated metal and node metal.

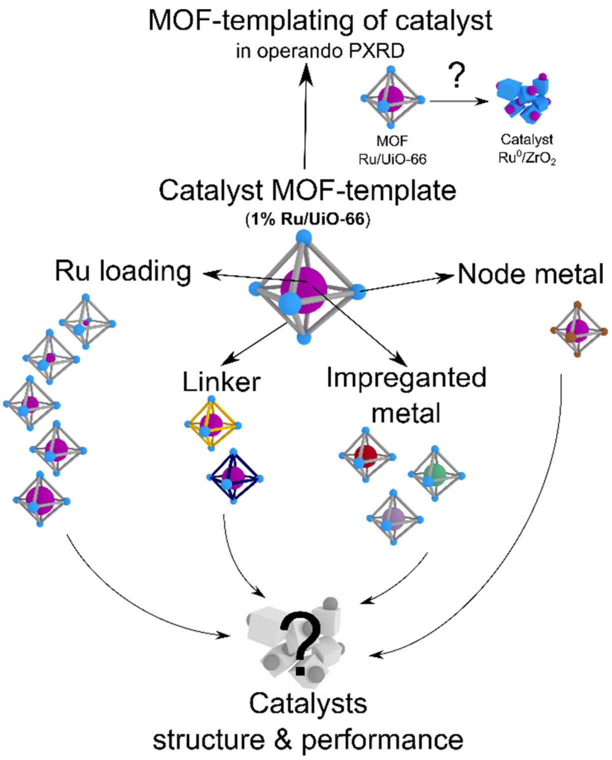

Figure 1: Summary of the scope of this study: templating conditions and MOF components (linker, impregnated metal and node metal) and their effect on the structure and catalytic performance of the derived materials.

4.4. Experimental

4.4.1. Synthesis

4.4.1. Metal-organic frameworks

UiO-66, **UiO-67**, **UiO-66-NH$_2$**, **UiO-66-PYDC**, and **UiO-66-PZDC** were synthesised based on the procedure described by Katz *et al.*[32] In a glass vial, the organic ligand (0.75 mmol) was dissolved in 10 mL of N-N-dimethylformamide (DMF). In a second glass vial, $ZrCl_4$ (0.54 mmol) and 1 mL of HCl were dissolved in 5 mL of DMF, the latter vial was sonicated for 20 min to ensure complete dissolution. Next, the $ZrCl_4$ solution was mixed to the ligand solution and the vial was sealed with Teflon-lined screw cap and placed in an aluminium heating block at 80 °C for 48 hours. The resulting precipitate was centrifuged, washed (4x10mL DMF and 2x10mL of ethanol) and dried at 110 °C for 48 hours.

The syntheses of **UiO-66-SO_3H** and **UiO-66-$(OH)_2$** were attempted based on the procedure reported by Foo *et al.*[33]. UiO-66-SO_3H was synthesised by dissolving H_2BDC-SO_3Na (1 g, 3.73 mmol), $ZrCl_4$ (869 mg, 3.73 mmol), and 16 ml of acetic acid in 148 ml of DMF. The solution was heated to 120 °C for 40 h. The precipitate was isolated by centrifugation and washed with DMF (3x 100 mL) and diethyl ether (DEE) (3x 100 mL). The solids were vacuum dried for 48 hours. UiO-66-$(OH)_2$ synthesis followed the same procedure using H_2BDC-$(OH)_2$ as the organic ligand.

Ce-UiO-66 was synthesised via solvothermal synthesis from $Ce(NH_4)_2(NO_3)_6$ and H_2BDC adapted from Lammert *et al.*[34] Detailed synthesis is described in Chapter 5.

4.4.1.1. Post-synthetic modification (PSM)

The samples were post-synthetically modified (PSM) by impregnation with an aqueous solution of a metal precursor ($RuCl_3$, $Zn(NO_3)_2$, $FeCl_3$, $CuCl_2$ or $Co(NO_3)_2$) using the incipient wetness impregnation method described in our previous work.[21] The loading of Ru was controlled by the concentration of the solution added to yield a sample with loadings of 0.25 to 2 wt % of Ru or 1 wt% of Zn, Fe, Cu, and Co on the MOF. Amounts for each sample are specified in Tables S2 and S3.

4.4.2. Powder X-ray Diffraction (PXRD)

Experiments performed at the powder diffraction beamline at the Australian Synchrotron used a Mythen-II strip detector[35] for pattern collection. Patterns were collected with 60 s of acquisition time at each of 2 different detector positions offset by 0.5° 2θ and later merged using PDViPeR[36] to remove gaps in the datasets resulting from gaps between the detector modules. For *ex-situ* XRD data collection, the powder samples were loaded in 0.7 mm special glass capillaries (Charles Supper, USA) and rotated about the long capillary axis during acquisition.

Samples analysed using laboratory source X-rays were back-loaded into flat plate sample holders prior to the collection of XRD patterns in order to minimise the effects of preferred orientation. Pattern collection took place using a Bruker D8 Advance X-ray Diffractometer with CuKα radiation (40kV, 40mA) using a LynxEye detector. Samples were scanned over the 2θ range 3.5° to 130° with a step size of 0.02° and acquisition time of 0.4 second per step. To give an equivalent count time of 69.2 seconds per step, 173/192 of the sensor strips on the LynxEye detector were used.

Synchrotron experiments were performed at 15 and 16 keV. Energy used for the collection of each pattern and any conversions of lab X-ray source data for comparison purposes are detailed in the supporting information (SI) provided.

4.4.2.1. Synchrotron *In operando* PXRD set up

For the *in operando* PXRD data collection, a flow-through cell designed by the Australian Synchrotron was used (Figure 2). The powder samples were loaded into open ended capillaries of outside diameter of 0.7 mm and wall thickness of 0.01mm. Fibrous quartz glass wool was inserted into the exit end of the capillary to prevent the sample being blown out by the applied gas flow. The capillary was mounted into the cell which was the fitted to the sample stage of the diffractometer. The gas inlet of the flow-through cell was connected to a gas mixing manifold using flexible nylon tubing (Figure S9). The gas manifold was connected to the capillary, pure N_2 and reactive gas mixture (25% CO_2 and 75% H_2). A flow meter was used to regulate the gas flow to 5 to 6 mL/min for both N_2 and the reactive gas mixture. The cell was oscillated through 40° about the long capillary axis during data acquisition in order to maximise the number of crystallites contributing to the diffraction process. The gas outlet of the flow-through cell was connected to an OmniStar GSD 320 O2 mass spectrometer (MS) (Pfeiffer Vacuum GmbH, Germany) using flexible nylon tubing due to the oscillation of the flow-through cell. Heating of the capillary was achieved using a hot air blower and the temperature controlled and measured using a thermocouple positioned about 1 mm beneath the capillary. The hot air blower temperature calibration was done by 15 high temperature calibration samples from 100 °C to 700 °C.

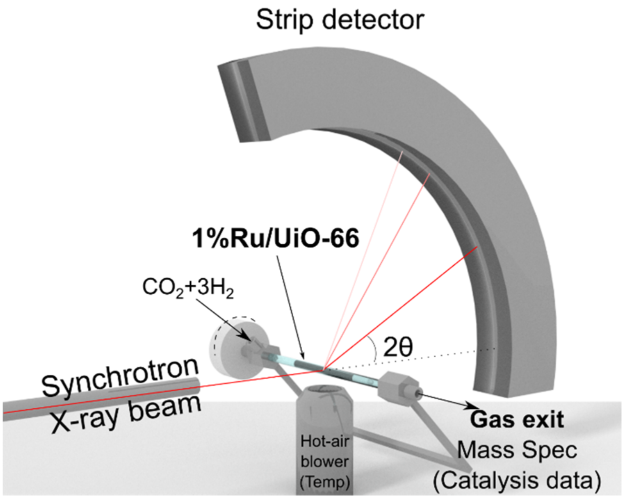

Figure 2: Simplified illustration of in operando PXRD set-up. The template MOF was loaded in the capillary (blue), which was kept oscillating 40° during data acquisition. The gas feed (CO_2+H_2) was connected upstream as indicated and the effluent gases flowed through a nylon tubing connected to the mass spectrometer.

4.4.2.2. *In operando* PXRD sample conditions

Firstly, the sample was dried under a stream of N_2 while increasing the temperature to 200 °C at 10 °C/min. Upon reaching 200 °C the sample was held at this temperature for 1 hour and then the gas feed switched to the reactive mixture of CO_2 and H_2 and temperature varied according to the profile displayed in Figure 5B. This process broadly simulated the same activation and reaction conditions encountered by the materials during their use in catalytic investigations.

4.4.3. Rietveld refinement

Phase identification was performed using the search and match algorithm in X'pert Highscore Plus (PANalytical, the Netherlands). The identified phases were quantified via Rietveld refinement based quantitative phase analysis[37] using Topas V5 software (Bruker AXS, Germany).[38] Batch analysis for the quantification of the crystalline and amorphous phases is described in details in the SI.

4.4.4. Heat treatment under controlled atmosphere

UiO-66 and **1%Ru/UiO-66** were pre-reduced in a tube furnace. The samples were loaded into quartz crucibles, and placed in a tube furnace. The tube furnace consists of a quartz tube with sealed ends placed on the furnace ceramic. The tube ends are connected to gas lines to allow the gases to flow in and out of the furnace. The crucibles were placed in one of the three hot zones, each zone is independently controlled by a Series 96 1/16 DIN temperature controller (Watlow, USA). The furnace temperature was calibrated with a K-type thermocouple with an 1100 °C model digital thermometer prior to the experiment. The upstream end was connected to a cylinder of 5% H_2 in Ar and the downstream end connected to an oil bubbler, to ensure unidirectional flow. The samples were treated at 350 °C for 8 h under continuous gas flow (heating and cooling ramp rate set to 2 °C/min).

4.4.5. Surface area analysis

Nitrogen adsorption isotherms were collected at 77.3 K using a micromeritics ASAP 2020 Surface Area & Porosity Analyser and for BET surface area analysis. The samples were degassed under vacuum (90 mtorr) for 72 h at 110 °C prior to analysis.

4.4.6. Catalysis testing

The catalytic performance testing was performed in a custom-built high-throughput catalyst testing rig, Flowrence^{TM} (Avantium, the Netherlands), described in Lippi *et al.*[21] The rig is capable of simultaneously testing 48 fixed-bed microreactors, which are distributed in 3 different blocks with independent temperature control. All reactors at a given time are subjected to identical conditions of gas flow, composition and pressure. For validation purposes, all experiments included positive and negative (filled with 50 mg of SiC) controls.

20 mg of the relevant PSM-MOF precatalysts were loaded into the micro-reactors, except for samples heat-treated in 5% H_2/Ar prior to the experiment, 20 mg of the sample derived from the heat-treatment was loaded. Samples were first dried in pure N_2 at 200 °C (2 °C/min), then each reactor was exposed to reactive conditions: 2.08 mL H_2, 0.52 mL CO_2, 0.31 mL Ar, 350 °C (5 °C/min) and 4 bar.

4.4.7. Electron microscopy

High resolution TEM and High-angle annular dark-field (HAADF) images were collected using a probe-corrected JEOL ARM200F (USA) equipped with a cold field emission gun operating at 200 kV.

4.5. Results and discussion

4.5.1. Ex-situ activation

The majority of reported MOF-templated catalysts are generated *ex situ*, i.e. under conditions different than the catalytic conditions. Previously, we have reported the synthesis of a highly active catalyst under CO_2 methanation reaction conditions (i.e. *in situ*).[21] To assess the influence of the atmosphere in templating the active catalyst, **UiO-66** and **1%Ru/UiO-66** were treated in a tube furnace under a flow of 5% H_2/Ar and compared to the catalysts derived from **UiO-66** and **1%Ru/UiO-66** activated *in situ*. The XRD patterns collected after the indicated treatment are displayed in Figure 3A. It is evident that the samples treated in 5% H_2 display structures different from the samples tested for catalysis. When activated under catalytic conditions, **1%Ru/UiO-66** yielded a mixture of monoclinic (m-) and tetragonal (t-) ZrO_2 phases and did not display reflections that could be attributed to Ru phases. However, under 5% H_2 in Ar, the resulting sample was composed of tetragonal ZrO_2 and RuO_2. The control sample, **UiO-66** also displayed different phases depending on the treatment, resulting in an amorphous phase when activated under catalytic conditions and in tetragonal ZrO_2 when treated in 5% H_2 in Ar.

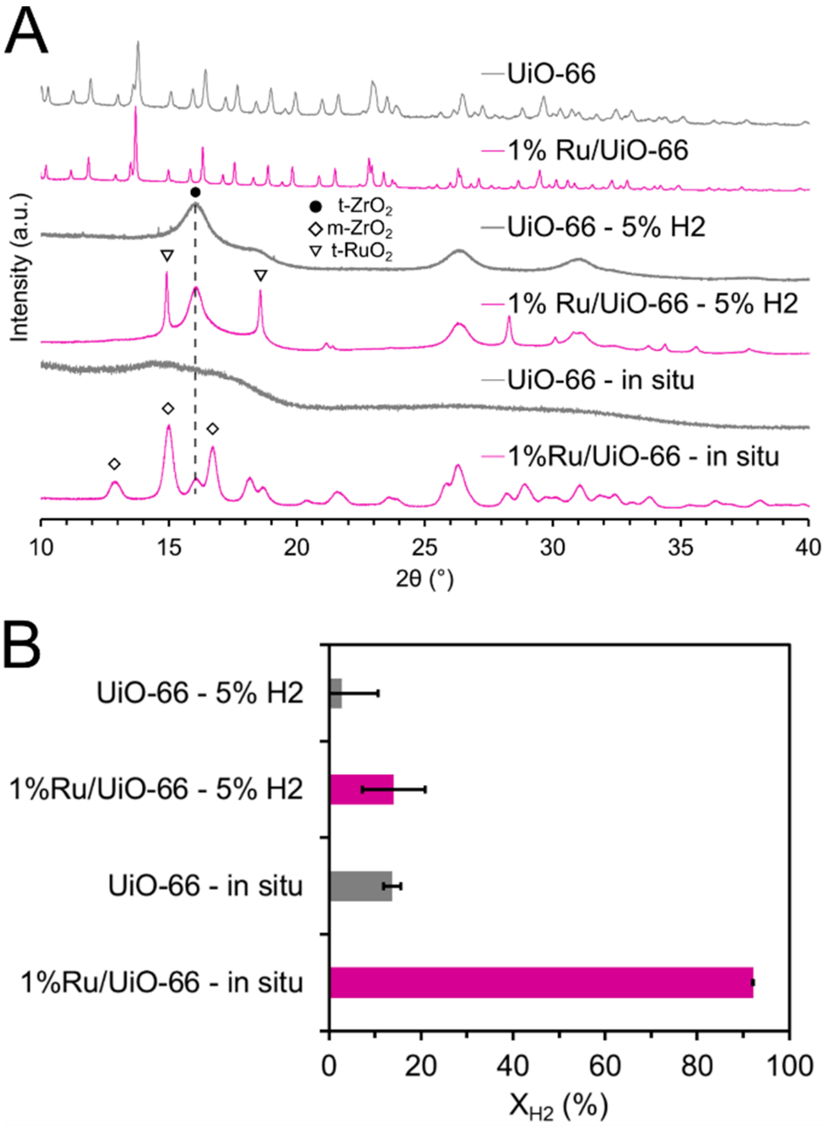

Figure 3: A) PXRD patterns of the catalyst templates UiO-66 (grey) and Ru/UiO-66 (magenta), of the samples resulting from thermal treatment under 5%H_2/Ar and 350 °C ("5% H2") and for the samples treated under CO_2 methanation reaction conditions ("in situ"). B) Average H_2 conversion during catalytic testing. The samples labelled "5% H2" were activated prior to the catalysis testing under a flow of 5% H_2/Ar at 350 °C. Whereas, the samples labelled "in situ" were templated during the catalysis testing (*in situ* templating). Error bars indicate standard deviation of the data.

In addition to identifying the phases, using the position and relative intensities of the reflections, the pattern profile also contains other useful information. For example, the presence of broad peaks is easily observed in the PXRD patterns of **UiO-66 – 5%H_2**, **1%Ru/UiO-66 – 5%H_2**, and **1%Ru/UiO-66 – in situ** (Figure 3). These result from the presence of phases with small crystallite sizes in the samples. By analysing the peak width it is possible to extract the crystallite domain size (Lvol-IB) from full-pattern PXRD analysis. The calculated crystallite domain size can also be indicative of the apparent crystallite size, although the true crystallite size will depend on the particle morphology.

Quantification of the crystalline phases of the sample derived from **1%Ru/UiO-66 – 5%H_2** resulted in 87.7wt% tetragonal-ZrO_2 (9.9 nm) and 12.3wt% RuO_2 (43 nm); the high relative amount of Ru quantified indicates the additional presence of an amorphous Zr-containing phase. In contrast, **1%Ru/UiO-66 – in situ** was composed of 84wt% monoclinic-ZrO_2 and 16wt% of t-ZrO_2. Ru phases were not quantified using this method due to the very small crystallite size of Ru^0 (2-5 nm), low loading (approximately 3wt%) and presence of amorphous Ru nanoparticles. Apart from the evident phase composition differences, the catalytic performance of the samples also varied significantly (Figure 3B). The catalysts activated under 5%H_2/Ar (**1%Ru/UiO-66 – 5%H_2**) displayed H_2 conversion of 14% when tested under the same conditions as the catalyst activated under CO_2 methanation reaction conditions (**1%Ru/UiO-66 – in situ**), which displayed H_2 conversion of 92%. These results further support the hypothesis that a H_2 rich environment is required to template the highly active catalyst.

4.5.2. Amorphous Ru nanoparticles

The presence of Ru^0 nanoparticles (NPs) has been previously confirmed by high magnification EDS mapping of catalysts formed under these conditions.[21] The absence of reflections for a Ru phase in the XRD patterns prompted HR-TEM investigations which revealed the presence of both single crystal and amorphous (or multi-twinning) Ru^0 nanoparticles in the range of 2 to 5 nm (Figure 4A-D). It has been reported that in case of platinum nanoparticles, amorphous nanoparticles can provide a different surface density of catalytic active sites when compared to single crystals.[39] The effect of amorphous arrangement in Ru nanoparticles on catalytic sites in unknown. In addition, TEM evidence of Ru^0 nanoparticles in an amorphous phase is rarely reported. The presence of amorphous Ru^0 nanoparticles in this catalyst is hypothesised to underpin the high catalytic of this catalyst.

The transition from amorphous to single crystal was observed in real time during TEM experiment (Figure 4D). The presence of single crystal in addition to amorphous nanoparticles encouraged us to investigate its contribution to the diffraction pattern. A synchrotron powder X-ray diffraction pattern was collected for 1%Ru/UiO-66 after catalysis testing and full pattern Rietveld refinement quantitative analysis was performed considering hexagonal Ru^0, cubic Ru^0, or tetragonal RuO_2; in addition to m-ZrO_2, t-ZrO_2. Among the Ru phases, only hexagonal Ru^0 (h-Ru^0) improved the fitting of the calculated pattern (Figure 4F), supporting the presence of hexagonal Ru^0 in the active catalyst, even after exposure to air.

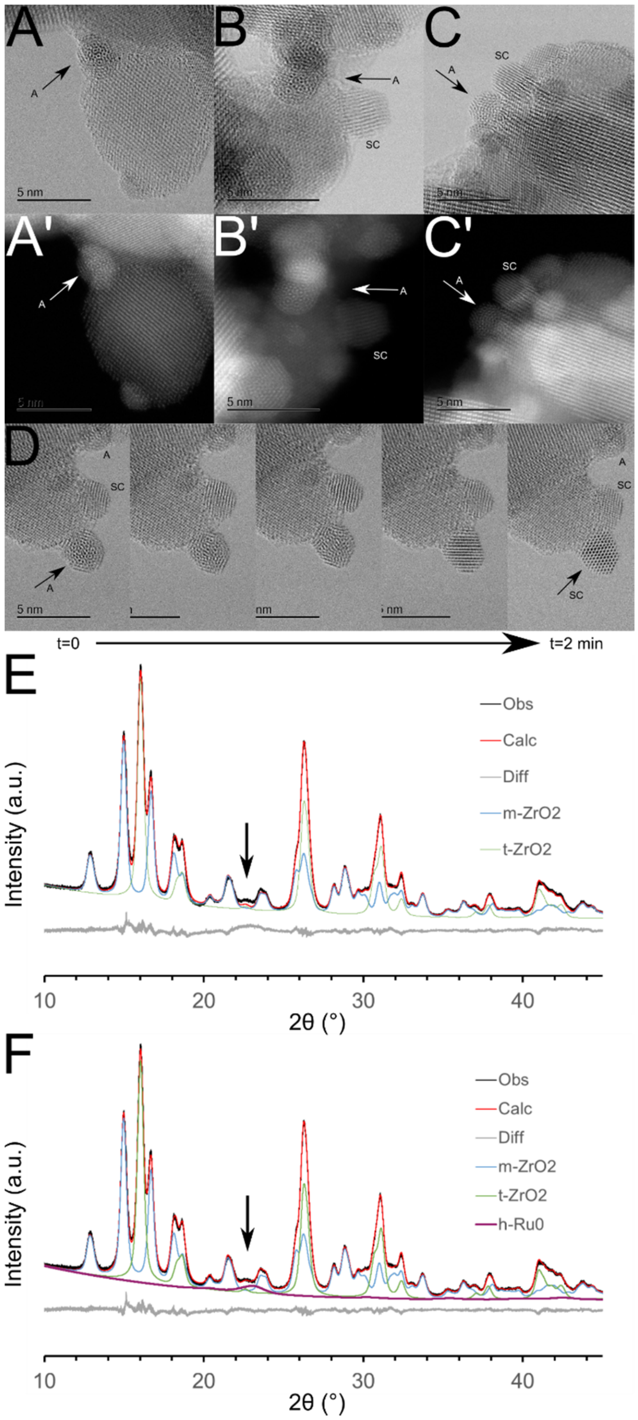

Figure 4: High Resolution TEM (A-C) and HAADF (A'-C') images of the catalyst derived from **1Ru%/UiO-66**. The arrows and labels indicate amorphous ("A") and single crystal ("SC") nanoparticles. D) A series of TEM images acquired during a 2 min period, where an amorphous nanoparticle ("A") transitions to single crystal ("SC") due to the beam high energy. Scale bars indicate magnification. E-F) XRD pattern collected ("Obs") for the catalyst derived from **1Ru%/UiO-66**, the resulting Rietveld refinement calculated pattern ("Calc"), difference curve ("Diff") and refined individual phase contributions for monoclinic-ZrO_2, tetragonal-ZrO_2 and hexagonal-Ru^0 as indicated in the legend. The arrow indicates a misfit between the observed and

calculated pattern which is corrected by the addition of h-Ru^0 phase (t-RuO_2 and c-Ru^0 were also evaluated for the refinement, but did not improve the fitting of the pattern).

4.5.3. *In situ* activation (*in operando* PXRD)

As the thermal reduction of **1%Ru/UiO-66** by 5% H_2/Ar produced a much less active, and structurally different, catalyst to the material templated *in situ*, the phase transition during CO_2 methanation reaction conditions was studied. Accordingly, the catalyst template was subjected to simulated CO_2 methanation conditions in a controlled atmosphere and temperature variable ("*in situ*") PXRD experiment.[21] The collapse of the crystalline MOF structure was observed at 330 °C resulting in an amorphous phase, which remained stable for 8 hours of experiment with no formation of ZrO_2 or Ru phases.

An *in operando* PXRD experiment was performed using a mass spectrometer for the simultaneous analysis of the capillary effluent gas. The 700 patterns collected over 33 hours of experiment are displayed in Figure 5A. The temperature profile during the experiment is shown in Figure 5B and the lowercase letters indicate changes during the experiment and are described in Table 1 together with our observations,

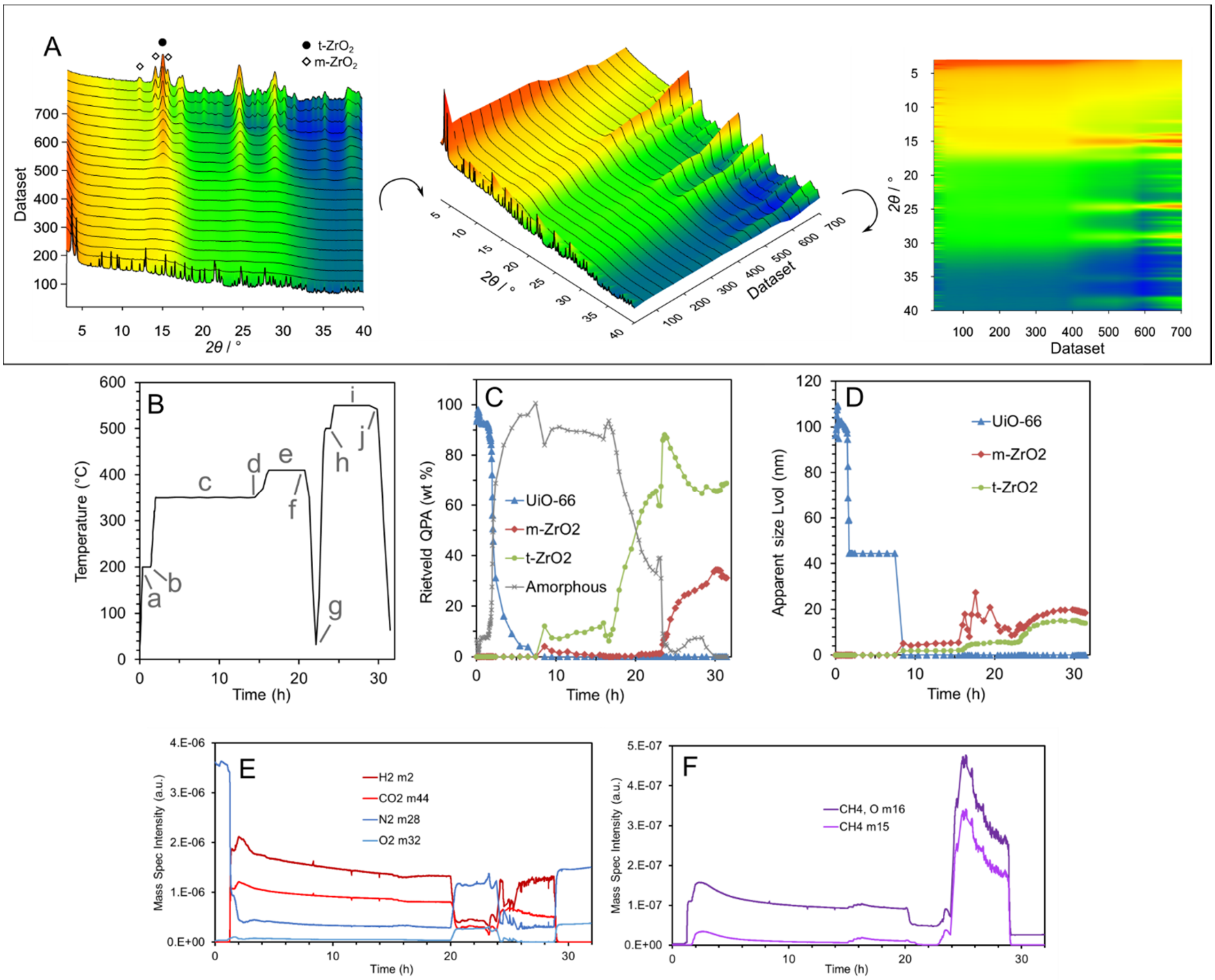

Figure 5: A) Three different views of XRD patterns offset according to dataset axis. B) Temperature profile during the experiment, the lowercase letters indicate events and observations described in Table 1. C) Quantitative phase analysis obtained via Rietveld refinement of datasets displayed in A (details in SI). D) Crystallite domain size or Apparent size (Lvol) calculated via Rietveld refinement of the crystalline phases for datasets displayed in A. E) Mass spectrometry results for the components in the gas feed: N_2, H_2 and CO_2. Mass 32 for O_2 was added to indicate periods when the mass spec was disconnected from the capillary and was exposed to atmospheric air, the sample was constantly kept under either N_2 or H_2 and CO_2 flow. F) Mass spectrometry results for mass 15 and 16. Mass 16 refers to CH_4 and O, whilst mass 15 refers to the CH_3 fragment from CH_4. The production of CH_4 should be observed by the combination of these two masses.

Table 1: *In operando* PXRD experimental conditions and observations for different steps of displayed in Figure 5B.

Step	Temperature	Gas flow	PXRD phase observations	Mass spectrometry observations
a	Ramp to 200 °C (10 °C /min) Held at 200 °C for 1 hour	N_2 (≈10 ml/min)	UiO-66 (indicative of catalyst template **1%Ru/UiO-66)**	Release of solvents (water, DMF and ethanol)
b	Held at 200 °C Ramp to 350 °C (10 °C/min)	75% H_2 + 25% CO_2 (≈5 ml/min)	UiO-66 <330 °C Amorphous phase >330 °C	During MOF collapse, several organic fragments were observed in the gas effluent, in addition to CH_4 (Figure 5F).
c	Held at 350 °C for >10 h	75% H_2 + 25% CO_2 (≈5 ml/min)	Amorphous phase *in agreement with our previous report[21]	Minor production of CH_4
d	At 15 h temperature ramp to 400 °C	75% H_2 + 25% CO_2 (≈5 ml/min)	Decrease of the contribution of amorphous phase and the formation of t-ZrO_2.	Increase in the production of CH_4
e	400 °C	75% H_2 + 25% CO_2 (≈5 ml/min)	Increase of t-ZrO_2 phase and decrease of amorphous phase	Drop in CH_4 production*
f	Cooling to room temperature	75% H_2 + 25% CO_2 (≈5 ml/min)	t-ZrO_2 and amorphous phase	Atmospheric air*
g	Ramp to 500 °C	75% H_2 + 25% CO_2 (≈5 ml/min)	Increase of t-ZrO_2 phase and decrease of amorphous phase below 40 wt%	Increase in CH_4 production
h	Ramp to 550 °C	75% H_2 + 25% CO_2 (≈5 ml/min)	t-ZrO_2 (90 wt%)	Further increase in CH_4 production
i	550 °C	75% H_2 + 25% CO_2 (≈5 ml/min)	t-ZrO_2 and formation of m-ZrO_2 (up to 30 wt%)	higher rates of CH_4 synthesis **
j	Cooling to room temperature	75% H_2 + 25% CO_2 (≈5 ml/min)	t- and m-ZrO_2 are kept constant as well as their crystallite sizes.	N/A (mass spectrometer disconnected)

* Condensation of H_2O (side-product of CO_2 methanation) was noted to be blocking the effluent gas line, obstructing mass spectrometer sampling (Figure S10). The experiment was paused (step f) in order to dry the nylon tubing connecting the flow-through cell to the mass spectrometer. For safety reasons, temperature was required to drop to room temperature before disconnecting the line from both the capillary and the mass spectrometer. PXRD data was collected during the cooling period. After drying the nylon tubing under a stream of high purity N_2, it was reconnected to the mass spectrometer and to the capillary and the experiment was resumed. ** Condensation of H_2O was again observed and affected sampling by the mass spectrometer. Mass spectrometer is disconnected (step j).

The temperature during the experiment was increased from 350 to 550 °C to assess the hypothesis that the flow of cold gas through the catalyst plug, caused the real temperature of the sample to be lower than the set temperature. This hypothesis was based on our previous report on the effect of temperature (250, 300 and 350 °C) in the MOF-templating of Ru^0/ZrO_2 via *ex situ* PXRD analysis,[21] it was observed that at lower temperatures, poorly crystalline t-ZrO_2 is formed alone and at higher temperatures, t-ZrO_2 and m-ZrO_2 are formed with slightly larger apparent crystallite size. Furthermore, according to the thermodynamic equilibrium calculations by Gao *et al.* and assuming a consistent catalytic phase, the CH_4 yield at the thermodynamic equilibrium conditions is less favourable with increasing temperatures: 90% at 350 °C and 60% at 500 °C at 1 bar.[40] Although the real temperature could not be defined, these reports support our hypothesis that heat-transfer of the cold gas flow affecting the real temperature of the sample. Setting higher temperatures (500 and 550 °C) we are able to observe the formation of phases that correspond to the highly active MOF-derived catalyst and observe a drastic increase in catalytic activity.

The crystalline structure of the post-synthetically modified MOF **1%Ru/UiO-66** collapses at 330 °C (set temperature) in the presence of the reactive gases (80%H_2/CO_2) with the release of different organic fragments.[21] The remaining solid is amorphous which gives rise to an increase in the background contribution of the XRD patterns. This contribution from the amorphous phase to the patterns was quantified by modelling the background increase via Rietveld refinement and considered in the quantitative phase analysis (details in SI). The quantitative phase analysis demonstrated that the amorphous phase is stable for over 10 h at 350 °C (set temperature). We note that this phase was inactive for the production of CH_4 (Figure 5F, mass 15). Upon increasing the temperature, the amorphous phase undergoes a transition to form ZrO_2 nanoparticles, initially t-ZrO_2 is formed and the catalyst begins to show moderate CH_4 production. At even higher temperatures, m-ZrO_2 is formed in addition to t-ZrO_2 and the amorphous phase is no longer observed. The increase in temperature also caused the growth of the crystallite sizes, although they remained below 20 nm, considerably smaller than the crystallite size of the template. In addition, the catalytic production of CH_4 is almost five times greater. While a direct correlation between the high catalytic activity and the formation of nano-ZrO_2 was observed, this experiment cannot attribute catalytic activity to it. Since no Ru crystalline phases (Ru^0 or RuO_2) were identified, it is reasonable to assume that they are in an amorphous form, in agreement with the used catalyst (Figure 4).

4.5.4. Loading of Ru in UiO-66

PXRD patterns of materials formed from different loadings of Ru in the UiO-66 MOF-template are displayed in Figure 6. The effect of the precatalyst's Ru loading on the catalytic performance has been previously reported,[21] and these results are reproduced in Figure 6, alongside new structural data of the derived catalysts. In the absence of Ru (i.e. 0% loading), **UiO-66** produces an amorphous phase, which remains stable during the entire catalysis testing (over 90 hours) even after exposure to atmospheric air. Ruthenium is the catalytic metal and its presence, even in small amounts, is sufficient to drive the crystallisation of ZrO_2. For example, as little as **0.25%Ru/UiO-66** generated ZrO_2 nanocrystals of 6.3 nm apparent size (64% t-ZrO_2 and 36% m-ZrO_2). The low content of Ru caused the catalyst to display low catalytic activity (H_2 conversions of 16%). Higher H_2 conversions were observed with increasing the amount of Ru in the template-MOF; for example, the catalyst derived from **1%Ru/UiO-66** shows H_2 conversion of 95%. The structure of this catalyst, **1%Ru/UiO-66**, is also composed of ZrO_2 nanoparticles (9.6 nm), however it presents a higher monoclinic ZrO_2 content (84% monoclinic and 16% tetragonal). Considering that the catalyst was achieving the thermodynamic equilibrium of the CO_2 methanation reaction, it is not possible to affirm that a higher amount of Ru did not lead to catalyst deactivation, however, no decrease in the overall H_2 conversion was observed for samples derived from **1.25%** to **2% Ru/UiO-66**. The samples **1.5%** and **2% Ru/UiO-66** were selected as examples of higher loading for the structural evaluation. These two samples displayed very similar structures, exhibiting 7.6 and 7.3 nm average ZrO_2 nanoparticle sizes for **1.5%** and **2%Ru/UiO-66**, respectively, and composition of 70% m-ZrO_2 and 30% t-ZrO_2. These results indicate that, under CO_2 methanation conditions, ZrO_2 formation is assisted by the presence of Ru; a low amount of Ru directs the formation of t-ZrO_2 and higher loadings of Ru cause the final sample to have higher amounts of m-ZrO_2.

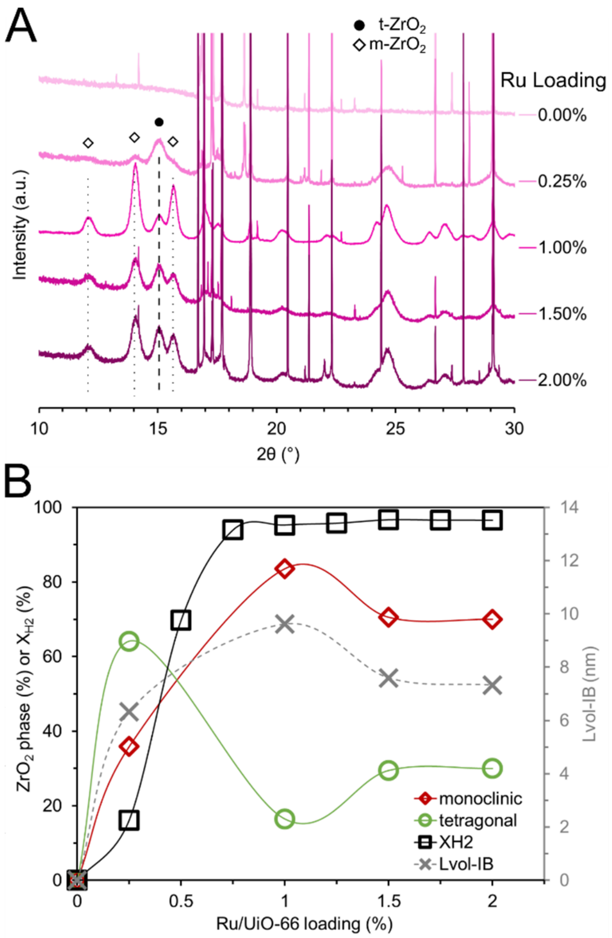

Figure 6: A) *Ex situ* XRD patterns of the catalysts derived from MOFs with different loading of Ru/UiO-66. The dashed lines indicate peak position of m-and t-ZrO_2. (The sharp peaks are from the highly crystalline SiC used as a catalyst diluent during the catalysis tests). B) Catalytic H_2 conversion (X_{H2}) observed for the catalysts derived from different loadings of Ru/UiO-66, quantification of m- and t-ZrO_2 phases, and average apparent crystallite size (Lvol).

4.5.5. Linker changes in Zr-MOFs

Functionalization of linkers has been demonstrated to provide benefits for the composition control of MOFs and for MOF-derived catalysts. For example, amine groups in MOFs have been strategically used to improve the dispersion of secondary metal precursors within the framework pores for the encapsulation of metal nanoparticles in MOFs.[41-42] In MOF-derived materials, pyrolysis of MOFs with N-containing linkers has been demonstrated to produce N-doped carbon matrices.[26] We hypothesised that linker functionalization could influence the final catalyst structure by affecting dispersion of Ru within the template MOF and the derived support. Accordingly, the templating of Ru/ZrO_2 catalysts was evaluated by synthesising Zr-MOFs with the linkers displayed in Figure 7A. The structure of the synthesised Zr-MOFs were evaluated by means of XRD analysis. Crystalline **UiO-66**, **UiO-67**, **UiO-66-NH$_2$** were successfully synthesised. The synthesis of **UiO-66-(OH)$_2$** and **UiO-66-SO$_3$H** yielded coordination polymers with low surface area (11 and 29 m^2/g, respectively) and low crystallinity observed by the significantly broaden reflections relative to UiO-66, but with the same relative intensities. The synthesis of **UiO-66-PYDC** with HCl as modulator yielded an amorphous coordination polymer. Amorphous UiO-66-PYDC has been recently synthesised by Wang *et al.* in the absence of a modulator, whereas they obtained crystalline UiO-66-PYDC using acetic acid as modulator.[43] Lastly, **UiO-66-PZDC**, also displayed medium surface area (139 m^2/g) lower crystallinity, although the broad reflections obtained in XRD diffractograms were found to have similar relative intensities to UiO-66. A Zr-PZDC MOF (CAU-22) was recently synthesised by Waitschat *et al.*[44] However, in order to obtain a crystalline material, formic acid was used as a modulator resulting in a topology dependent on presence of 2 formate anions per hexanuclear Zr-node. This topology was significantly different from UiO-66 and from the material we obtained, verified by comparing XRD patterns with the reported structure.

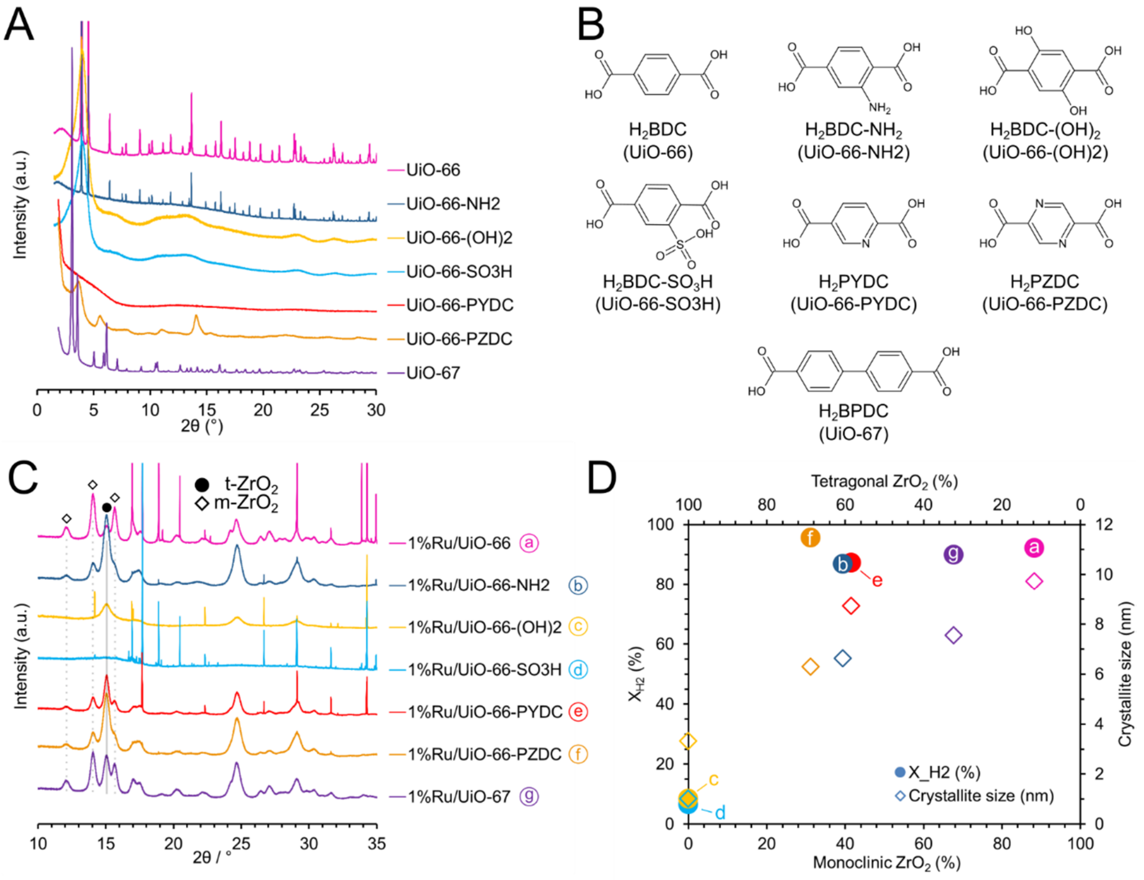

Figure 7: A) XRD patterns of the synthesised Zr-MOFs. B) MOF ligands and respective MOF label in brackets. C) XRD patterns of the catalysts templated from the respective Ru-impregnated Zr-MOFs. D) Catalytic activity represented by H_2 conversion (left y-axis) versus ZrO_2 phase's relative composition (m-ZrO_2 bottom x-axis and t-ZrO_2 top x-axis) and composition weighted average crystallite size (right y-axis). Lowercase letters refer to the different samples as indicated in B.

These zirconium MOFs and coordination polymers were impregnated with $RuCl_3$ via IWI method (Figure S2) to achieve loading of 1wt% Ru/MOF. Next, they were loaded into microreactors for the activation of the catalysts and for the parallel catalytic performance testing. Both were carried at 350 °C and 4 bar. Figure 7D presents the H_2 conversion results (left axis) during CO_2 methanation for the samples indicated by the lowercase letters. High H_2 conversions were observed for the catalysts derived from **1%Ru** on **UiO-66** (92%), **UiO-66-NH$_2$** (87%), **UiO-66-PYDC** (87%), **UiO-66-PZDC** (96%) and **UiO-67** (90%). The catalytic activity was not affected by the use of 4,4'-biphenyldicarboxylate, or N-containing linkers when comparing to BDC. Furthermore, the catalytic activity was also independent of the crystallinity of the MOF. In fact, among these samples, the highest conversions were observed for the catalyst derived from **1%Ru/UiO-66-PZDC**, with average conversion of 96%. Catalysts derived from **1%Ru/UiO-66-(OH)$_2$** and **1%Ru/UiO-66-SO$_3$H** showed the lowest conversions of the set, 8% and 7% respectively.

The MOF-derived catalysts were characterized by XRD (Figure 7C). The most active samples (**1%Ru** on **UiO-66-NH$_2$**, **UiO-66-PYDC**, **UiO-66-PZDC** and **UiO-67**) were composed of a mixture of monoclinic and tetragonal ZrO_2 with apparent crystallite sizes between 6 and 10 nm (Figure 7C-D), whereas the material derived from **1%Ru/UiO-66-(OH)$_2$** was composed only of t-ZrO_2 with very small apparent size (3 nm). The **1%Ru/UiO-66-SO$_3$H** produced an amorphous phase, similar to bare UiO-66 (Figure 6 – 0%Ru loading). To explain this lower activity of catalysts derived from these two MOFs, we first considered some of their physical properties; both MOFs have very low surface area, are non-porous (Figure S3) and have low crystallinity. However, these properties do not seem to dictate the quality of the derived catalysts as **1%Ru/UiO-66-PYDC** is amorphous, non-porous and has a low surface area, but templates a highly active catalyst. That led us to hypothesise that steric effects of the functional groups (SO_3H and OH) may obstruct the pores, inhibiting the dispersion of Ru^{3+} salt through the coordination polymer, and also affecting the crystallisation of ZrO_2. In the case of **1%Ru/UiO-66-NH2**, the functional group is much smaller and the material is crystalline, ensuring the presence of channels that facilitate the impregnation of the Ru^{3+} solution. In the specific case of **1%Ru/UiO-66-SO$_3$H** we acknowledge the possibility of poisoning of Ru by sulfur, but further experiments would be necessary for confirmation.

The N-containing linkers yielded catalysts with lower relative content of m-ZrO_2 (from 31 to 42%, with the remaining being t-ZrO_2) than the catalysts derived from **1Ru%/UiO-66** (88%) and from **1Ru%/UiO-67** (68%). Interestingly, the templates with linkers containing 1 N atom (**1%Ru/UiO-66-NH2** and **1%Ru/UiO-66-PYDC**) produced catalysts with very similar relative composition monoclinic to tetragonal, whereas the template **1Ru%/UiO-66-PZDC**, containing 2 N atoms per linker, displayed the lowest amount of m-ZrO_2 (31% m-ZrO_2). Lastly, the use of a template with the same topology as UiO-66, but longer linker (**1%Ru/UiO-67**) yielded a highly active catalyst composed of 68% m-ZrO_2 and average crystallite size of 7.5 nm (compared to **1%Ru/UiO-66** with 88% m-ZrO_2 and 9.7 nm). These differences might be caused by the higher amount of carbon in the sample or larger distances between the inorganic nodes, however the variance is small and more experimentation would be necessary to be conclusive on the effect.

This study demonstrated how the linker functional groups can affect the final catalysts. Crystallinity of the MOF-template was not needed to produce highly active catalysts. However, large functional groups in poorly crystalline MOFs are hypothesised to obstruct infiltration and distribution of Ru precursor solution and lead to low activity catalysts with structures distinct from the active catalysts in both phase composition and crystallite size. Templates with linkers containing N produced catalysts with higher content of t-ZrO_2, irrespective of their crystallinity, but with activity as good as to the positive control **1%Ru/UiO-66**.

4.5.6. Impregnated Metal in UiO-66

The effect of the impregnated metal in the synthesis and performance of catalysts via MOF-templating route was evaluated by impregnating UiO-66 with different metals commonly used in catalysis. For this study, $RuCl_3$, $Zn(NO_3)_2$, $FeCl_3$, $CuCl_2$, or $Co(NO_3)_2$ were impregnated within UiO-66 via IWI to yield 1wt% Metal/UiO-66. These post-synthetically modified MOFs were then subjected to CO_2 methanation reaction conditions (350 °C and 4 bar) for *in situ* templating of the catalysts and for subsequent evaluation of catalytic performance. The catalytic performance and structure of the derived catalysts were evaluated and are discussed below.

The activity of the catalysts was evaluated by considering their H_2 conversion efficiency. For the metals trialled here, Ru exhibited the highest conversion efficiency. The activity order from higher to lowest was Ru (92%), Fe (11%), Co(10%), Zn(9.6%), and Cu(5%) (Figure 8B). This order of activity is in agreement with previous observations on hydrogenation capacity.[45-46] In addition to differences in conversion, the product distribution also varied depending on the metal. Notably, the catalyst derived from **1%Ru/UiO-66** displayed the highest production rate of CH_4 (0.89 mmol/min) while also having the lowest production rate of CO (0.0005 mmol/min), indicative of the very high selectivity to CH_4 already reported for this system.[21] The catalysts derived from other metals displayed much lower production rate for CH_4 and higher production rate for CO. In addition, C_3H_8 (0.4 μmol/min) and ethanol (0.05 μmol/min) were produced in trace amounts for the catalysts derived from **1%Zn/UiO-66** and **1%Fe/UiO-66**, respectively (Figure 8C).

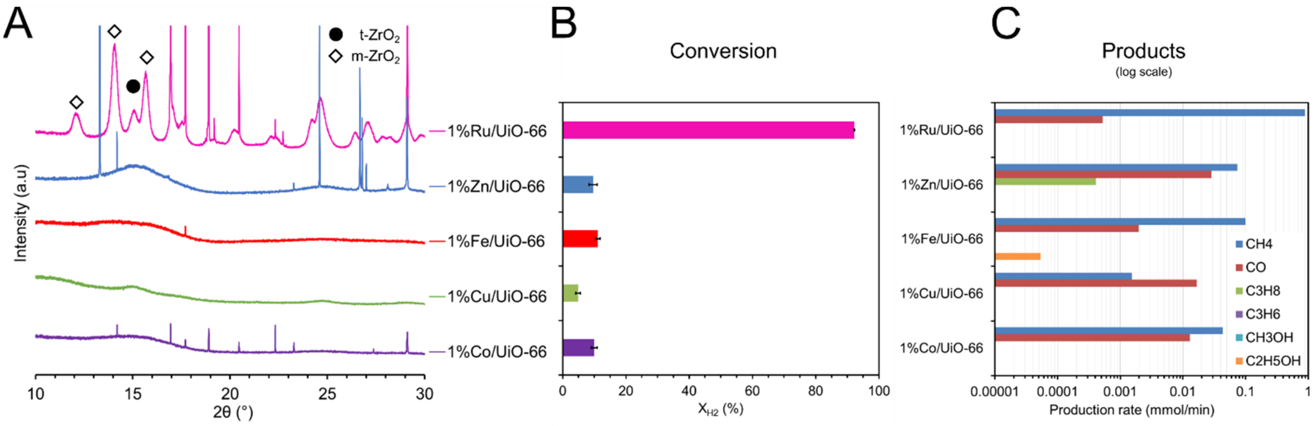

Figure 8: A) XRD patterns for MOF-derived catalysts from **1wt%Metal/UiO-66** (where **Metal** was Ru^{3+}, Zn^{2+}, Fe^{3+}, Cu^{2+}, or Co^{2+}) after catalytic testing. B) H_2 conversion results for the MOF-derived catalysts. C) Production rate observed for different hydrocarbons as presented in the legend). Logarithm scale was used for the evaluation of trace amounts. Sharp reflections were investigated and are due the presence of SiC, used as catalyst diluent.

XRD analysis of the used catalysts confirmed the absence of reflections corresponding to UiO-66, indicating the complete collapse of the MOF. However, only the catalyst derived from **1%Ru/UiO-66** contained clear reflections for ZrO_2. The catalysts derived from **1%Zn/UiO-66** displayed broad peaks with positions suggestive of the presence of poorly ordered t-ZrO_2. For the other metals, the final phase was amorphous and similar to a material derived from pure UiO-66 (Figure 6 – 0%Ru loading).

The clear formation of ZrO_2 for the sample containing Ru and the different degrees of formation of t-ZrO_2, may be correlated to the hydrogenation activity of the metals. Ru is significantly more active for hydrogenation than the other metals tested in this work.[46] This may have consequence not only for the final catalyst, but also for the templating mechanism of the catalyst. For instance, in Chapter 2 the impregnated active metal was demonstrated to assist in the decomposition of the organic linkers of the MOF; when the active metal was absent, the template generated an amorphous phase rich in carbon and nitrogen (both atoms present in the linker). Therefore, a less active metal, or the absence of metal, will be less efficient in the volatilisation of the organic linkers to facilitate the crystallisation of the support metal oxide (e.g. ZrO_2). Furthermore, the generation of a C-rich amorphous phase may lead to covering of the active metal, decreasing the overall access of gases to the active metal and yielding a low-performing catalyst. This study supports the hypothesis that for the **Ru/UiO-66** systems, the role of the active metal in the templating is to decompose the organic linkers to facilitate the crystallisation of ZrO_2.

4.5.7. MOF node metal – templating a different metal-oxide support

To investigate the possibility of templating Ru catalysts using different metal oxides as supports, a cerium(IV)-based MOF with structure analogous to UiO-66 (**Ce-UiO-66**) was synthesised (Figure 9A) and impregnated with $RuCl_3$ to yield **1%Ru/Ce-UiO-66**. This sample was compared to **1%Ru/UiO-66** for its catalytic performance for CO_2 methanation. In addition, non-impregnated versions of the MOFs, **Ce-UiO-66** and **UiO-66**, were also tested as controls (Figure 9B-C).

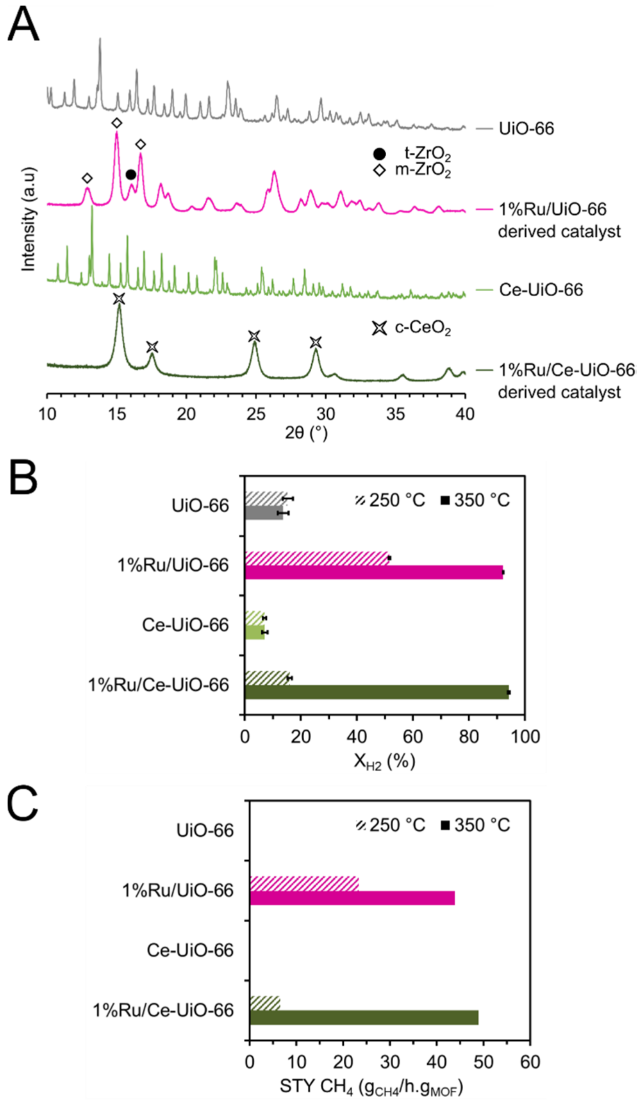

Figure 9: A) XRD patterns of UiO-66 and Ce-UiO-66 and of the templated catalysts derived from 1%Ru/MOF. The MOFs, UiO-66 and Ce-UiO-66, display analogous structures. The MOF templated samples produced nanocrystalline metal oxides of the respective template metal nodes (m- and t-ZrO_2 and cubic-CeO_2). In both cases, reflections indicative of Ru phases were absent. B) Average H_2 conversion for catalysts derived from MOFs and Ru/MOFs, specified in the y-axis. Error bars indicate standard deviation of the data. C) Production of CH_4 during the catalytic testing for catalysts derived from MOFs and Ru/MOFs, specified in the y-axis. Samples were *in situ* activated at 350 °C prior to testing at 250 °C.

The catalytic performance testing indicated that the MOF-templated catalyst Ru/ZrO_2 performed better than Ru/CeO_2 at 250 °C, but had similar performance at 350 °C.

(Figure 9B-C), achieving H_2 conversions over 90%, close to the thermodynamic equilibrium. The controls, **UiO-66** and **Ce-UiO-66** generated catalysts with very low H_2 conversions (13 and 7%, respectively, at 350 °C), and only trace amounts of CH_4.

The structure of the catalyst derived from **1%Ru/Ce-UiO-66** was analysed using PXRD (Figure 9A). The final structure was composed of nanosized cubic CeO_2 with no crystalline Ru phases observed. The sample derived from bare **Ce-UiO-66** was amorphous. These results were in agreement with the samples prepared with Zr-UiO-66, where the sample derived from bare **UiO-66** transformed into an amorphous phase and the sample of **1%Ru/UiO-66** formed nano-ZrO_2 (Figure 6). The MOF-templating of Ru/CeO_2 was assessed in a second in operando PXRD experiment (Figure S11) using **1%Ru/Ce-UiO-66** as starting material observed under CO_2 methanation reaction conditions. The study demonstrated similarities between the two samples: collapse of the MOF forms an amorphous phase which at higher temperatures crystallises into nanosized ceria; increase in the activity is observed during the crystallisation of the sample; and absence of Ru phases' reflections throughout the experiment.

This study provides evidence that this MOF templating route can be used for the synthesis of metal nanoparticles supported on different metal-oxides. In addition, it also indicates similarities in the templating process, where the active metal is necessary to assist with the crystallisation of the support metal oxide.

4.5.8. Support ZrO_2 phase

Thermal decomposition of UiO-66 in air has been previously studied to form mainly t-ZrO_2 as the decomposition product;[47-49] the m-ZrO_2 phase has also been observed in small amounts after treatment at 800 °C.[49] These examples show that t-ZrO_2 is the phase preferentially formed from the decomposition of UiO-66. We observed that the catalyst derived from **1%Ru/UiO-66** during CO_2 methanation reaction conditions produced a catalyst with over

80% m-ZrO_2. Previously, the high content of m-ZrO_2 has been assigned to the transformation that tetragonal ZrO_2 undergoes at high temperatures in the presence of water, a side-product of the CO_2 methanation.[21, 50] However, it has not been yet been established if the monoclinic phase of ZrO_2 is directly correlated to the high activity of the catalyst. In the study of different linkers of Zr-MOFs, we noted that catalysts derived from N-containing linkers displayed H_2 conversion from 87 to 96%, while having less than 42% m-ZrO_2, evidence that high catalytic performance can be achieved even with lower amounts of m-ZrO_2. However, we note that the catalysts were operating at the thermodynamic equilibrium of CO_2 methanation, and differences in catalytic activity may not have been observed for this reason. When comparing different metal oxide supports, the study with Ru/Ce-UiO-66 has shown that the MOF-templated Ru/CeO_2 displays H_2 conversion of 16% at 250 °C, against 52% by the MOF-templated Ru/ZrO_2. This result confirms the importance of the support ZrO_2 for the high activity of the Ru catalyst. We are currently pursuing studies that will define the most ZrO_2 polymorph.

4.6. Conclusions

This work has described a systematic study of the MOF-templated catalyst Ru^0/ZrO_2 derived from **1%Ru/UiO-66** by evaluating the catalytic performance and structural information of different samples. A H_2-rich atmosphere was required for the activation of the highly active Ru^0/ZrO_2 catalyst. During templating in 75%H_2/CO_2, the MOF structure collapsed forming a catalytically inactive amorphous phase, which at higher temperatures crystallised into a mixture of t-ZrO_2 and m-ZrO_2 with high catalytic activity. The lack of PXRD reflections of Ru^0 has been attributed to the size of Ru^0 nanoparticles and to their presence also in amorphous (or multi-twinning) states. Other synthesis methods, direct impregnation[21] of Ru precursor on ZrO_2 and MOF-templating in 5% H_2/Ar, have led to catalysts with poor performance, demonstrating the importance of MOF-templating in a H_2-rich atmosphere strategy for the phase and morphology control the high-performing catalyst.

Variations in Ru loading in the template MOF demonstrated that Ru, even in small amounts dictated the formation of ZrO_2, due to its hydrogenation properties. In the absence of Ru under the same templating conditions UiO-66 formed an amorphous phase. This amorphous phase was similar to the materials derived from UiO-66 impregnated with metals that are less active for hydrogenation. The use of different linker for template Zr-MOFs demonstrated that linkers can influence the final catalyst structure and performance. Highly active catalysts were templated from MOFs containing linkers with N irrespective of their crystallinity, however, these catalysts contained a lower content of m-ZrO_2 than catalysts derived from Ru/UiO-66 and Ru/UiO-67. The Zr-MOFs with linkers H_2BDC-$(OH)_2$ and H_2BDC-SO_3H were observed to inhibit the synthesis of the highly active catalyst, we hypothesise that steric effects caused by the functional groups cause poor distribution of Ru precursor in the template MOF and we are further investigating the template and derived materials to elucidate these results. Lastly, the use of a Ce-based MOF analogous to UiO-66 was demonstrated to also produce a Ru^0/CeO_2 catalyst also active for CO_2 methanation. The catalysts displayed several similarities with the Zr-analogue, including the nanoparticulate nature of the support, the lack of Ru PXRD reflections and the transition undergone by the MOF during catalyst templating, demonstrating that different support materials can be achieved by the selection of appropriate MOFs.

4.7. Acknowledgements

Aspects of this work were undertaken at the Australian Synchrotron (Proposal M11125). The authors acknowledge CSIRO and the University of Adelaide for funding this research. RL acknowledges The University of Adelaide for the Beacon of enlightenment PhD Scholarship and the CSIRO for top-up scholarship. The authors acknowledge Ashley Murphy, Ben Muir, Krystina Lamb, Samuel Yick, Robert Madiona for assistance in experiments, Thomas Bennett for TGA, and Yunxia Yang for surface area analysis.

4.8. References

1. Batten, S. R.; Champness, N. R.; Chen, X. M.; Garcia-Martinez, J.; Kitagawa, S.; Ohrstrom, L.; O'Keeffe, M.; Suh, M. P.; Reedijk, J., Terminology of Metal-Organic Frameworks and Coordination Polymers (Iupac Recommendations 2013). *Pure Appl. Chem.* **2013**, *85*, 1715-1724.

2. Sumida, K.; Rogow, D. L.; Mason, J. A.; McDonald, T. M.; Bloch, E. D.; Herm, Z. R.; Bae, T.-H.; Long, J. R., Carbon Dioxide Capture in Metal–Organic Frameworks. *Chem. Rev.* **2011**, *112*, 724-781.

3. Suh, M. P.; Park, H. J.; Prasad, T. K.; Lim, D.-W., Hydrogen Storage in Metal–Organic Frameworks. *Chem. Rev.* **2011**, *112*, 782-835.

4. Peng, Y.; Krungleviciute, V.; Eryazici, I.; Hupp, J. T.; Farha, O. K.; Yildirim, T., Methane Storage in Metal–Organic Frameworks: Current Records, Surprise Findings, and Challenges. *J. Am. Chem. Soc.* **2013**, *135*, 11887-11894.

5. Mason, J. A.; Veenstra, M.; Long, J. R., Evaluating Metal-Organic Frameworks for Natural Gas Storage. *Chem. Sci.* **2014**, *5*, 32-51.

6. He, Y.; Zhou, W.; Qian, G.; Chen, B., Methane Storage in Metal-Organic Frameworks. *Chem. Soc. Rev.* **2014**, *43*, 5657-5678.

7. Li, J.-R.; Sculley, J.; Zhou, H.-C., Metal–Organic Frameworks for Separations. *Chem. Rev.* **2011**, *112*, 869-932.

8. Van de Voorde, B.; Bueken, B.; Denayer, J.; De Vos, D., Adsorptive Separation on Metal-Organic Frameworks in the Liquid Phase. *Chem. Soc. Rev.* **2014**, *43*, 5766-5788.

9. Kang, Z.; Fan, L.; Sun, D., Recent Advances and Challenges of Metal-Organic Framework Membranes for Gas Separation. *J. Mater. Chem. A* **2017**, *5*, 10073-10091.

10. Lee, J.; Farha, O. K.; Roberts, J.; Scheidt, K. A.; Nguyen, S. T.; Hupp, J. T., Metal-Organic Framework Materials as Catalysts. *Chem. Soc. Rev.* **2009**, *38*, 1450-9.

11. Liu, J.; Chen, L.; Cui, H.; Zhang, J.; Zhang, L.; Su, C.-Y., Applications of Metal-Organic Frameworks in Heterogeneous Supramolecular Catalysis. *Chem. Soc. Rev.* **2014**, *43*, 6011-6061.

12. Garcia-Garcia, P.; Muller, M.; Corma, A., MOF Catalysis in Relation to Their Homogeneous Counterparts and Conventional Solid Catalysts. *Chem. Sci.* **2014**, *5*, 2979-3007.

13. Xia, W.; Mahmood, A.; Zou, R.; Xu, Q., Metal-Organic Frameworks and Their Derived Nanostructures for Electrochemical Energy Storage and Conversion. *Energy Environ. Sci.* **2015**, *8*, 1837-1866.

14. Song, Y.; Li, X.; Sun, L.; Wang, L., Metal/Metal Oxide Nanostructures Derived from Metal-Organic Frameworks. *RSC Adv.* **2015**, *5*, 7267-7279.

15. Shen, K.; Chen, X.; Chen, J.; Li, Y., Development of MOF-Derived Carbon-Based Nanomaterials for Efficient Catalysis. *ACS Catal.* **2016**, *6*, 5887-5903.

16. Cao, X.; Tan, C.; Sindoro, M.; Zhang, H., Hybrid Micro-/Nano-Structures Derived from Metal-Organic Frameworks: Preparation and Applications in Energy Storage and Conversion. *Chem. Soc. Rev.* **2017**, *46*, 2660-2677.

17. Xie, Z.; Xu, W.; Cui, X.; Wang, Y., Recent Progress in Metal–Organic Frameworks and Their Derived Nanostructures for Energy and Environmental Applications. *ChemSusChem* **2017**, *10*, 1645-1663.

18. Zhao, S.-N.; Song, X.-Z.; Song, S.-Y.; Zhang, H.-j., Highly Efficient Heterogeneous Catalytic Materials Derived from Metal-Organic Framework Supports/Precursors. *Coord. Chem. Rev.* **2017**, *337*, 80-96.

19. Oar-Arteta, L.; Wezendonk, T.; Sun, X.; Kapteijn, F.; Gascon, J., Metal Organic Frameworks as Precursors for the Manufacture of Advanced Catalytic Materials. *Mater. Chem. Front.* **2017**, *1*, 1709-1745.

20. Kaneti, Y. V.; Tang, J.; Salunkhe, R. R.; Jiang, X. C.; Yu, A. B.; Wu, K. C. W.; Yamauchi, Y., Nanoarchitectured Design of Porous Materials and Nanocomposites from Metal-Organic Frameworks. *Adv. Mater.* **2017**, *29*.

21. Lippi, R., et al., Highly Active Catalyst for CO_2 Methanation Derived from a Metal Organic Framework Template. *J. Mater. Chem. A* **2017**, *5*, 12990-12997.

22. Santos, V. P., et al., Metal Organic Framework-Mediated Synthesis of Highly Active and Stable Fischer-Tropsch Catalysts. *Nat. Commun.* **2015**, *6*, 6451.

23. Wang, H.; Liu, M.; Guo, S.; Wang, Y.; Han, X.; Bai, Y., Efficient Oxidation of O-Xylene over CeO2 Catalyst Prepared from a Ce-MOF Template: The Promotion of K+ Embedding Substitution. *Mol. Catal.* **2017**, *436*, 120-127.

24. Chen, D.; Huang, M.; He, S.; He, S.; Ding, L.; Wang, Q.; Yu, S.; Miao, S., Ru-MOF Enwrapped by Montmorillonite for Catalyzing Benzene Hydrogenation. *Appl. Clay Sci.* **2016**, *119*, 109-115.

25. Wang, Z.; Li, X.; Yang, Y.; Cui, Y.; Pan, H.; Wang, Z.; Chen, B.; Qian, G., Highly Dispersed Beta-Nis Nanoparticles in Porous Carbon Matrices by a Template Metal-Organic Framework Method for Lithium-Ion Cathode. *J. Mater. Chem. A* **2014**, *2*, 7912-7916.

26. Long, J.; Shen, K.; Chen, L.; Li, Y., Multimetal-MOF-Derived Transition Metal Alloy NPs Embedded in an N-Doped Carbon Matrix: Highly Active Catalysts for Hydrogenation Reactions. *J. Mater. Chem. A* **2016**, *4*, 10254-10262.

27. Abney, C. W.; Patterson, J. T.; Gilhula, J. C.; Wang, L.; Hensley, D. K.; Chen, J.; Foo, G. S.; Wu, Z.; Dai, S., Controlling Interfacial Properties in Supported Metal Oxide Catalysts through Metal-Organic Framework Templating. *J. Mater. Chem. A* **2017**, *5*, 13565-13572.

28. Wang, P.; Feng, J.; Zhao, Y.; Wang, S.; Liu, J., MOF-Derived Tungstated Zirconia as Strong Solid Acids toward High Catalytic Performance for Acetalization. *ACS Appl. Mater. Interfaces* **2016**, *8*, 23755-23762.

29. Xu, D.; Pan, Y.; Chen, M.; Pan, Q.; Zhu, L.; Xue, M.; Zhang, D.; Fang, Q.; Qiu, S., Synthesis and Application of a MOF-Derived Ni@C Catalyst by the Guidance from an in Situ Hot Stage in Tem. *RSC Adv.* **2017**, *7*, 26377-26383.

30. *Powder Diffraction: Theory and Practice*; The Royal Society of Chemistry: Cambridge, UK, 2008; Vol. 24, p 2-3.

31. Madsen, I. C.; Grey, I. E.; Mills, S., In Situ Diffraction Studies: Thermal Decomposition of a Natural Plumbojarosite and the Development of Rietveld-Based Data Analysis Techniques. *Mater. Sci. Forum* **2010**, *651*, 37-64.

32. Katz, M. J.; Brown, Z. J.; Colón, Y. J.; Siu, P. W.; Scheidt, K. a.; Snurr, R. Q.; Hupp, J. T.; Farha, O. K., A Facile Synthesis of UiO-66, UiO-67 and Their Derivatives. *Chem. Commun.* **2013**, *49*, 9449-51.

33. Foo, M. L.; Horike, S.; Fukushima, T.; Hijikata, Y.; Kubota, Y.; Takata, M.; Kitagawa, S., Ligand-Based Solid Solution Approach to Stabilisation of Sulphonic Acid Groups in Porous Coordination Polymer Zr6o4(OH)(4)(Bdc)(6) (UiO-66). *Dalton Trans.* **2012**, *41*, 13791-13794.

34. Lammert, M.; Wharmby, M. T.; Smolders, S.; Bueken, B.; Lieb, A.; Lomachenko, K. A.; Vos, D. D.; Stock, N., Cerium-Based Metal Organic Frameworks with UiO-66 Architecture: Synthesis, Properties and Redox Catalytic Activity. *Chem. Commun.* **2015**, *51*, 12578-12581.

35. Schmitt, B.; Bronnimann, C.; Eikenberry, E. F.; Gozzo, F.; Hormann, C.; Horisberger, R.; Patterson, B., Mythen Detector System. *Nucl. Instrum. Methods Phys. Res., Sect. A* **2003**, *501*, 267-272.

36. Jong, L.; Ruben, G.; Spear, K. *Powder Diffraction Visualisation Processing and Reporting (Pdviper)*, Synchrotron Light Source Australia Pty Ltd. : 2014.

37. Madsen, I. C.; Scarlett, N. V. Y.; Riley, D. P.; Raven, M. D., Quantitative Phase Analysis Using the Rietveld Method. In *Modern Diffraction Methods*, Wiley-VCH Verlag GmbH & Co. KGaA: 2012; pp 283-320.

38. *Topas V5: General Profile and Structure Analysis Software for Powder Diffraction Data*, Bruker AXS GmbH: Karlsruhe, Germany, 2012.

39. Barron, H.; Opletal, G.; Tilley, R.; Barnard, A. S., Predicting the Role of Seed Morphology in the Evolution of Anisotropic Nanocatalysts. *Nanoscale* **2017**, *9*, 1502-1510.

40. Gao, J. J.; Wang, Y. L.; Ping, Y.; Hu, D. C.; Xu, G. W.; Gu, F. N.; Su, F. B., A Thermodynamic Analysis of Methanation Reactions of Carbon Oxides for the Production of Synthetic Natural Gas. *RSC Adv.* **2012**, *2*, 2358-2368.

41. Hwang, Y. K.; Hong, D. Y.; Chang, J. S.; Jhung, S. H.; Seo, Y. K.; Kim, J.; Vimont, A.; Daturi, M.; Serre, C.; Ferey, G., Amine Grafting on Coordinatively Unsaturated Metal Centers of MOFs: Consequences for Catalysis and Metal Encapsulation. *Angew. Chem. Int. Ed.* **2008**, *47*, 4144-4148.

42. Zheng, S.; Yang, P.; Zhang, F.; Chen, D.-L.; Zhu, W., Pd Nanoparticles Encaged within Amine-Functionalized Metal-Organic Frameworks: Catalytic Activity and Reaction Mechanism in the Hydrogenation of 2,3,5-Trimethylbenzoquinone. *Chem. Eng. J.* **2017**, *328*, 977-987.

43. Wang, Z.; Huang, Y.; Yang, J.; Li, Y.; Zhuang, Q.; Gu, J., The Water-Based Synthesis of Chemically Stable Zr-Based MOFs Using Pyridine-Containing Ligands and Their Exceptionally High Adsorption Capacity for Iodine. *Dalton Trans.* **2017**, *46*, 7412-7420.

44. Waitschat, S.; Reinsch, H.; Stock, N., Water-Based Synthesis and Characterisation of a New Zr-MOF with a Unique Inorganic Building Unit. *Chem. Commun.* **2016**, *52*, 12698-12701.

45. Vannice, M. A., The Catalytic Synthesis of Hydrocarbons from H2co Mixtures over the Group Viii Metals: I. The Specific Activities and Product Distributions of Supported Metals. *J. Catal.* **1975**, *37*, 449-461.

46. Gao, J.; Liu, Q.; Gu, F.; Liu, B.; Zhong, Z.; Su, F., Recent Advances in Methanation Catalysts for the Production of Synthetic Natural Gas. *RSC Adv.* **2015**, *5*, 22759-22776.

47. Liu, S.-C.; Yue, Z.-F.; Liu, Y., Mesoporous Carbon–ZrO2 Composites Prepared Using Thermolysis of Zirconium Based Metal–Organic Frameworks and Their Adsorption Properties. *J. Porous Mater.* **2015**, *22*, 465-471.

48. Yan, X.; Lu, N.; Fan, B.; Bao, J.; Pan, D.; Wang, M.; Li, R., Synthesis of Mesoporous and Tetragonal Zirconia with Inherited Morphology from Metal-Organic Frameworks. *CrystEngComm* **2015**, *17*, 6426-6433.

49. DeCoste, J. B.; Peterson, G. W.; Jasuja, H.; Glover, T. G.; Huang, Y. G.; Walton, K. S., Stability and Degradation Mechanisms of Metal-Organic Frameworks Containing the Zr6o4(OH)(4) Secondary Building Unit. *J. Mater. Chem. A* **2013**, *1*, 5642-5650.

50. Xie, S.; Iglesia, E.; Bell, A. T., Water-Assisted Tetragonal-to-Monoclinic Phase Transformation of ZrO2 at Low Temperatures. *Chem. Mater.* **2000**, *12*, 2442-2447.

4.9. Supporting information

What happens during MOF-templating? Synchrotron in operando PXRD study and systematic evaluation of MOF components for the synthesis of CO_2 methanation catalysts

A. Experimental methods

A.1 Materials

zirconium (IV) chloride anhydrous ($ZrCl_4$) 99.99% Sigma Aldrich (Australia), Ammonium cerium(IV) nitrate ($Ce(NH_4)_2(NO_3)_6$) 98.5% Sigma Aldrich (Australia), Zinc nitrate hexahydrate ($Zn(NO_3)_2 \cdot 6H_2O$) 98% Sigma Aldrich (Australia), Copper(II) chloride dehydrate ($CuCl_2 \cdot 2H_2O$) 99% Sigma Aldrich (Australia), Cobalt(II) nitrate hexahydrate ($Co(NO_3)_2 \cdot 6H_2O$) 98% Sigma Aldrich (Australia), Iron(III) chloride hexahydrate ($FeCl_3 \cdot 6H_2O$) 98% Sigma Aldrich (Australia), ruthenium(III) chloride trihydrate ($RuCl_3 \cdot 3H_2O$) 99% PMO Pty Ltd (Australia), terephthalic acid (H_2BDC) 99% Acros Organics (Great Britain), Biphenyl-4,4′-dicarboxylic acid (H_2BPDC) 97% Sigma Aldrich (Australia), 2-aminoterephthalic acid ($H_2BDC\text{-}NH_2$) 99% Sigma Aldrich (Australia), 2,5-dihydroxyterephthalic acid ($H_2BDC\text{-}(OH)_2$) 98% Sigma Aldrich (Australia), 2-Sulfoterephthalic Acid Monosodium Salt ($H_2BDC\text{-}SO_3Na$) 98% Tokyo Chemical Industry Co Ltd (Japan), 2,5-pyridinedicarboxylic acid (H_2PYDC) 98% Sigma Aldrich (Australia), 2,5-Pyrazinedicarboxylic acid dihydrate (H_2PYRC) 96% Sigma Aldrich (Australia), N-N-dimethylformamide (DMF) 99.8% Merck Pty. Ltd. (Australia), diethyl ether (DEE) for analysis Merck Pty. Ltd. (Australia), hydrochloric acid (HCl) 32% Merck Pty. Ltd. (Australia), acetic acid 100% Merck Pty. Ltd. (Australia),

A.2 MOF syntheses

Table S1: Quantities used for the synthesis of the MOFs.

MOF sample	ligand	ligand (mmol)	ligand (mg)	Metal precursor	Metal precursor (mmol)	Metal precursor (mg)	Modulator	Modulator volume (mL)	DMF (mL)
UiO-66	H_2BDC	3.75	623	$ZrCl_4$	2.7	629	HCl	5	75
UiO-66-NH_2	H_2BDC-NH_2	3.75	679	$ZrCl_4$	2.7	629	HCl	5	75
UiO-66-$(OH)_2$	H_2BDC-$(OH)_2$	5.05	1000	$ZrCl_4$	5.05	1177	Acetic acid	16	148
UiO-66-(SO_3H)	H_2BDC-SO_3Na	3.73	1000	$ZrCl_4$	3.73	869	Acetic acid	16	148
UiO-66-PYDC	H_2PYDC	0.75	125	$ZrCl_4$	0.54	126	HCl	1	15
UiO-66-PZDC	H_2PZDC	0.75	153	$ZrCl_4$	0.54	126	HCl	1	15
UiO-67	H_2BPDC	3.75	908	$ZrCl_4$	2.7	629	HCl	5	75
Ce-UiO-66	H_2BDC	1.92	319	$(NH_4)_2Ce(NO_3)_6$	1.92	1051	H_2O	3.6	10.8

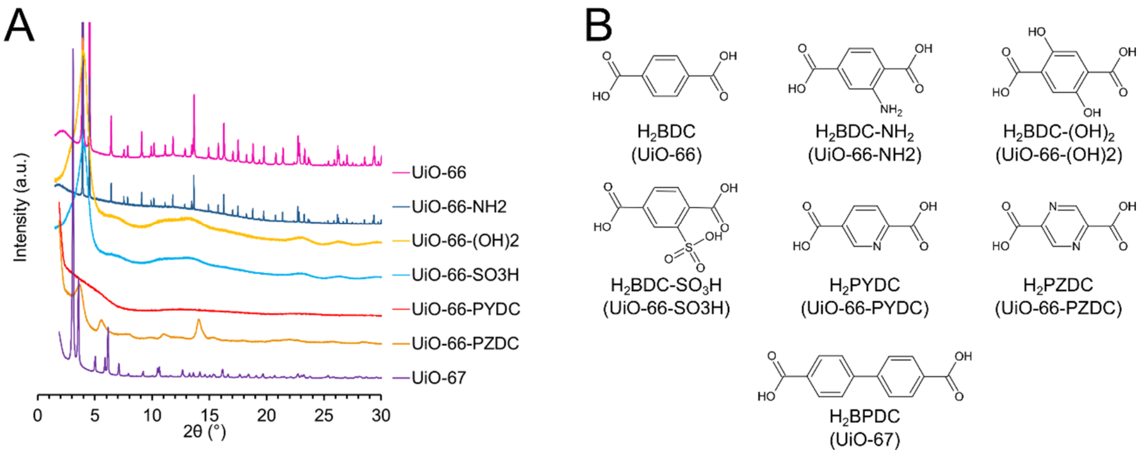

Figure S1: A) PXRD of the synthesised Zr-MOFs and B) the ligands used for each of the respective MOFs in brackets.

A.3 Post-synthetic modification

A.3.1 Incipient wetness impregnation (IWI) method

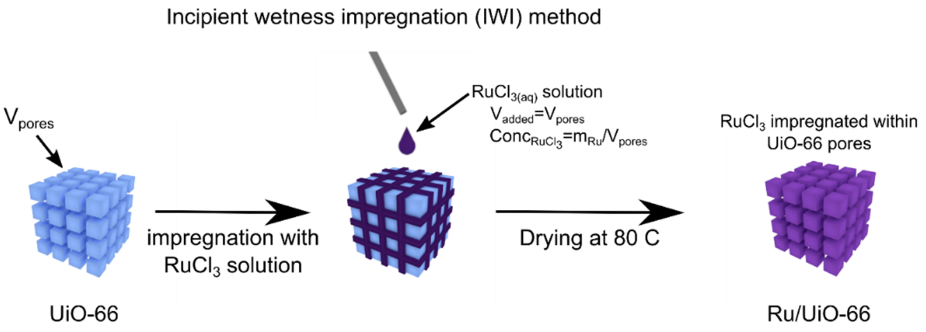

Figure S2: Scheme showing the incipient wetness impregnation method used to obtain Ru/UiO-66 and MOFs impregnated with other metal precursors.

A.3.2 Loading

Table S2: Quantities used for the impregnation of UiO-66 with different loadings of Ru.

sample	Ru loading (%)	Mass $RuCl_3.3H_2O$ (mg)	Mass support UiO-66 (mg)	H_2O vol (µL)
1.00%Ru/UiO-66	1.00	6.5	250	345
0.25%Ru/UiO-66	0.25	1.6	250	345
0.50%Ru/UiO-66	0.50	3.2	250	345
0.75%Ru/UiO-66	0.75	4.9	250	345
1.25%Ru/UiO-66	1.25	8	250	345
1.50%Ru/UiO-66	1.50	9.7	250	345
1.75%Ru/UiO-66	1.75	11.3	250	345
2.00%Ru/UiO-66	2.00	12.9	250	345

A.3.3 Ligands and MOFs

Table S3: Quantities used for the impregnation of MOFs with 1% loadings of Ru.

sample	MOF sample	Ru loading (wt%)	Mass $RuCl_3.3H_2O$ (mg)	Mass MOF (mg)	H_2O vol (µL)
1%Ru/UiO-66-NH2	UiO-66-NH_2	1	6.5	250	345
1%Ru/UiO-66-$(OH)_2$	UiO-66-$(OH)_2$	1	6.5	250	345
1%Ru/UiO-66-(SO_3H)	UiO-66-(SO_3H)	1	6.5	250	345
1%Ru/UiO-66- PYDC	UiO-66-PYDC	1	6.5	250	345
1%Ru/UiO-66-PZDC	UiO-66-PZDC	1	6.5	250	345
1%Ru/UiO-67	UiO-67	1	6.5	250	345
1%Ru/Ce-UiO-66	Ce-UiO-66	1	6.5	250	345

A.3.4 Metal

Table S4: Quantities used for the impregnation of UiO-66 with 1% loadings of different metals.

Sample	Metal loading (wt%)	Metal precursor	Mass (mg)	Mass UiO-66)	H_2O vol (µL)
1%Zn/UiO-66	1	$Zn(NO_3)_2 \cdot 6H_2O$	11.37	250	345
1%Fe/UiO-66	1	$FeCl_3 \cdot 6H_2O$	12.1	250	345
1%Cu/UiO-66	1	$CuCl_2 \cdot 2H_2O$	6.71	250	345
1%Co/UiO-66	1	$Co(NO_3)_2 \cdot 6H_2O$	12.35	250	345

B. Porosity

With regards to surface area, different batches of **UiO-66**, **UiO-67** and **UiO-66-NH$_2$** displayed high surface area and isotherms in agreement with previous reports[1-2] **UiO-66-(OH)$_2$** and **UiO-66-SO$_3$H** displayed type IV isotherms with mild hysteresis type H4, indicating the presence of some micro-mesoporosity.[3] **UiO-66-PYDC** displayed type II isotherms indicating a non-porous material.[3] Lastly, **UiO-66-PZDC** displayed a type IV isotherm with hysteresis type H2(a), indicating the presence of complex pore structures.[3] CAU-22 (Zr-PZCD) reported by Waitschat et al.[4] did not display the same hysteresis, further supporting differences between the two structures.

Table S5: BET surface area values.

Sample	BET Surface area (m^2/g)
UiO-66-(OH)$_2$	11.3502
UiO-66-SO$_3$H	28.3089
UiO-66-PYDC	50.2142
UiO-66-PZDC	138.9884

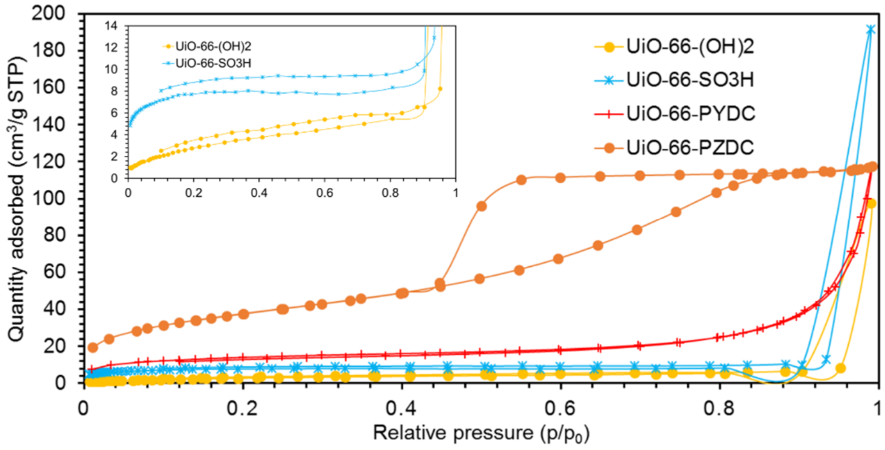

Figure S3: N_2 sorption isotherms.

C. TGA in N_2

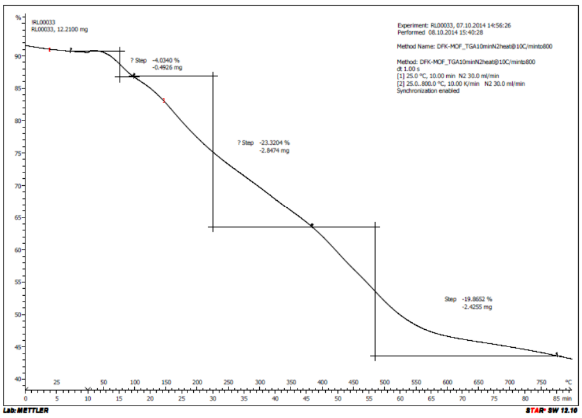

Figure S4: TGA of UiO-66-$(OH)_2$.

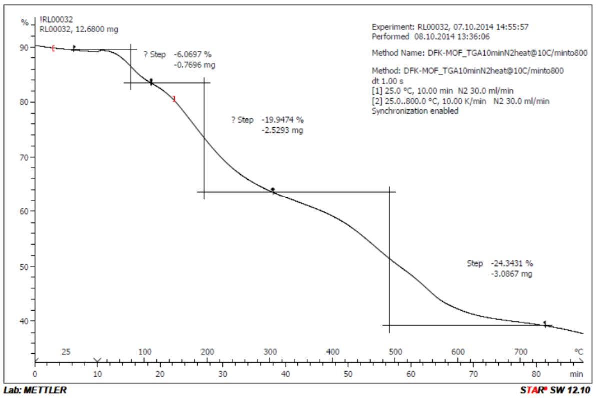

Figure S5: TGA of UiO-66-SO_3H.

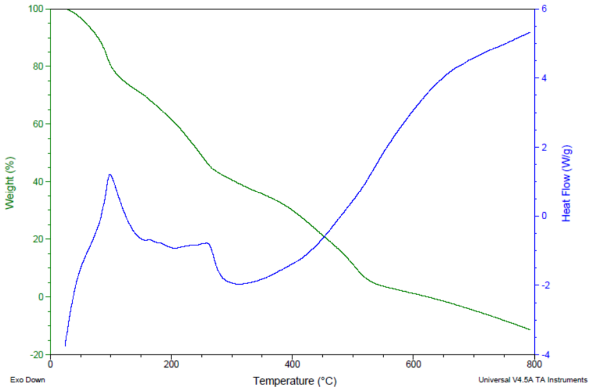

Figure S6: TGA of UiO-66-PYDC.

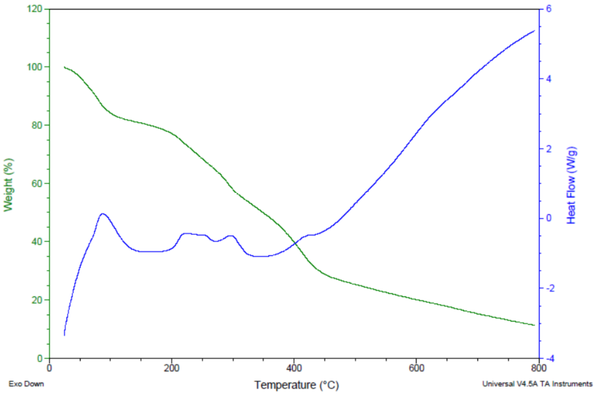

Figure S7: TGA of UiO-66-PZDC.

D. Powder X-ray diffraction

Powder X-ray diffraction patterns were collected with synchrotron and with laboratory source X-rays. The X-ray source and respective energy for each image presented in the manuscript are described below:

- Figure 4A: Synchrotron 15 keV
- Figures 6, 7A, 8B, 9A and 10A: Synchrotron 16 keV
- In Figure 8A, the energy used for the samples analysed in synchrotron source or lab source are described below:
    - UiO-66, UiO-66-NH2, UiO-66-(OH)2, UiO-66-SO3H: synchrotron radiation E = 15 keV
    - UiO-66-PYDC, UiO-66-PZDC and UiO-67 collected with lab source Cu radiation E = 8.04 keV

For comparison, the diffractograms of UiO-66-PYDC, UiO-66-PZDC and UiO-67 displayed in Figure 8A collected using lab source at 8.04 keV were plotted for E = 15 keV using Eq. 6:

Planck–Einstein relation

$$E = h\nu \Rightarrow E = h\frac{c}{\lambda} \tag{Eq. 1}$$

$$\left| \begin{array}{l} E_1 = h\frac{c}{\lambda_1} \\ E_2 = h\frac{c}{\lambda_2} \end{array} \right. \Rightarrow E_1\lambda_1 = E_2\lambda_2 \Rightarrow \frac{E_1}{E_2} = \frac{\lambda_2}{\lambda_1} \tag{Eq. 2}$$

Bragg’s law

$$n\lambda = 2d \cdot sin\theta \tag{Eq. 3}$$

$$d = \frac{n\lambda}{2 \cdot sin\theta} \Rightarrow d_1 = d_2 \Rightarrow \frac{n\lambda_1}{2 \cdot sin\theta_1} = \frac{n\lambda_2}{2 \cdot sin\theta_2} \Rightarrow \frac{\lambda_2}{\lambda_1} = \frac{sin(\theta_2)}{sin(\theta_1)} \tag{Eq. 4}$$

Combining Eq. 2 and 4

$$\frac{E_1}{E_2} = \frac{\lambda_2}{\lambda_1} = \frac{sin(\theta_2)}{sin(\theta_1)} \Rightarrow sin\left(\frac{2\theta_2}{2}\right) = sin\left(\frac{2\theta_1}{2}\right) \cdot \frac{E_1}{E_2} \tag{Eq. 5}$$

$$2\theta_2 = sin^{-1}\left(sin\left(\frac{2\theta_1}{2}\right) \cdot \frac{E_1}{E_2}\right) \cdot 2 \tag{Eq. 6}$$

D.1 Rietveld refinement

Rietveld refinement is a least-squares method to refine a calculated model based on the observed pattern profile.[5] The method seeks to minimize the difference between observed and calculated patterns (R_wp). For the models to be calculated the structures and background functions should be manually defined and selected structural parameters and individual phase scale factor are refined. Here, the crystalline structures considered are: monoclinic ZrO_2, tetragonal ZrO_2 and UiO-66.[6] Parameters refined include: scale factor, unit cell parameters, and Lvol (Lvol values were extracted from peak width and shape using Integral breadth).

D.1.1 Amorphous phases fitting

Using the pattern of first dataset, which presented the starting materials, UiO-66, in the most crystalline form, the capillary background was refined using six pseudo-voigt peaks. Once the capillary background was refined for this patter, the relative intensities of this *capillary phase* were fixed and associated with a *scale factor*, capable of multiplying intensity of the peaks while keeping the relative intensities constant. Next, the first completely amorphous dataset pattern was selected and refined only with the capillary phase. A misfit between the calculated and observed data was observed, which was due to the amorphisation of the sample, to assign the contribution another phase was created by adding a total of five pseudo-voigt peaks and they were refined to improve the fit of the phase. Once the relative intensities were adequate to comprise the amorphous phase, the relative intensities of these 5 peaks were fixed and another scale factor was assigned to the *amorphous phase*. The peaks group of the amorphous phase was verified on other datasets of the amorphous region before the batch refinement.

D.1.2 Batch Rietveld refinement

As over 700 datasets were collected in total, 93 patterns were selected to be representative of the total phase transition. Where phase transitions were observed, more datasets were selected and where the phase was stable, less datasets were selected for the analysis. In total 5 phases were refined: UiO-66, monoclinic ZrO_2, tetragonal ZrO_2, amorphous peak phase and capillary peak phase. The datasets were evaluated for the presence of crystalline phase. Accordingly, datasets collected in the first 8 hours, were refined for UiO-66, amorphous peak phase and capillary peak phase, whereas datasets collected after the first 8 hours of experiment were refined for m-ZrO_2, t-ZrO_2, amorphous peak phase and capillary peak phase. The datasets were refined in sequence using the launch mode of TOPAS V5.[7] The refined values of the previous dataset were used as starting point for the refinement of the subsequent dataset. An example of input file is presented at the end of this document.

D.1.3 Indirect quantitative phase analysis

Direct quantitative phase analysis via Rietveld refinement is only possible for crystalline phases,[8] however, as the amorphous phase contribution is observable and the sample is contained within the capillary (i.e. no material added or removed), the indirect quantitative phase analysis of this amorphous phase is possible. In this work, the maximum scale factor (Figure S7 A) observed for the amorphous phase was defined as 100 wt% amorphous phase content, with proportional values for other values of scale factor.

The results from the direct quantitative phase analysis of the crystalline phases (UiO-66, m-ZrO_2 and t-ZrO_2) were considered for the remaining phases (i.e. not-amorphous content). When considering the crystalline phases, misquantification of phases was noted due to the amorphisation of the sample. Apparent crystallite sizes (Lvol-IB) close to the minimum limit are evidence of the misquantification (Figure S7 C and D). Figure S7 C shows the independent quantification of the amorphous phase and the crystalline phases and Figure S7 D shows the apparent crystallite size (Lvol-IB) constant and value on the minimum limit.

Therefore, the quantification of the phases, including the amorphous phase was calculated using the following equation:

$$W\%_{Crys\ phase\ real} = W\%_{Crys\ phase\ Rietveld} \cdot \left(\frac{100 - \frac{SF_{Amorphous} \cdot 100}{SF_{Amorphous\ MAX}}}{100} \right)$$

Where:

- $W\%_{Crys\ phase\ real}$ is the weight percentage considering the amorphous phase, presented in Figure 7;
- $W\%_{Crys\ phase\ Rietveld}$ is the weight percent of a crystalline phase calculated directly via Rietveld refinement (Figure S7 C);
- $SF_{Amorphous\ MAX}$ is the maximum scale factor observed for the amorphous phase (1.08), where the sample is completely amorphous;
- $SF_{Amorphous}$ is the scale factor for the respective dataset.

No other manipulation was performed in the data.

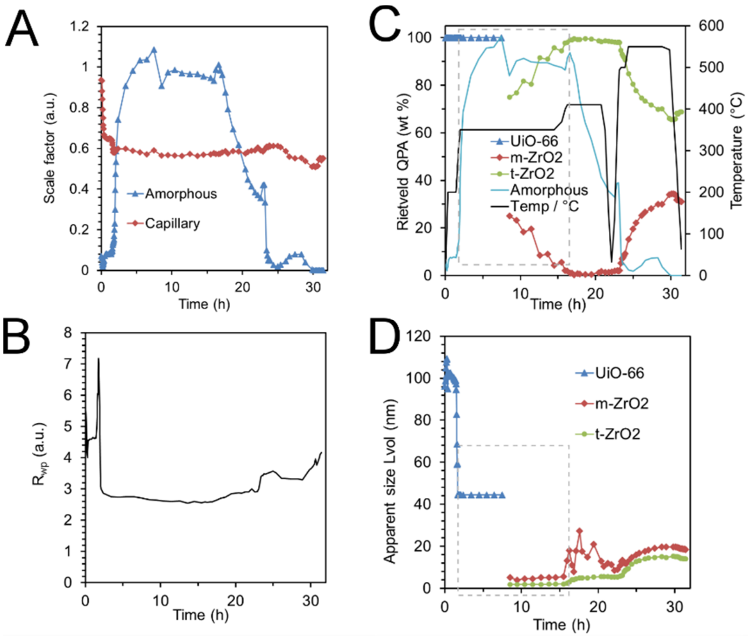

Figure S8: Rietveld refinement results: A) Scale factors for the two fitted amorphous phases: capillary and MOF-derived amorphous phase; B) Weighted profile R (R_{wp}); C) Quantitative phase analysis as obtained from the refinement; D) Apparent crystallite size (lvol).

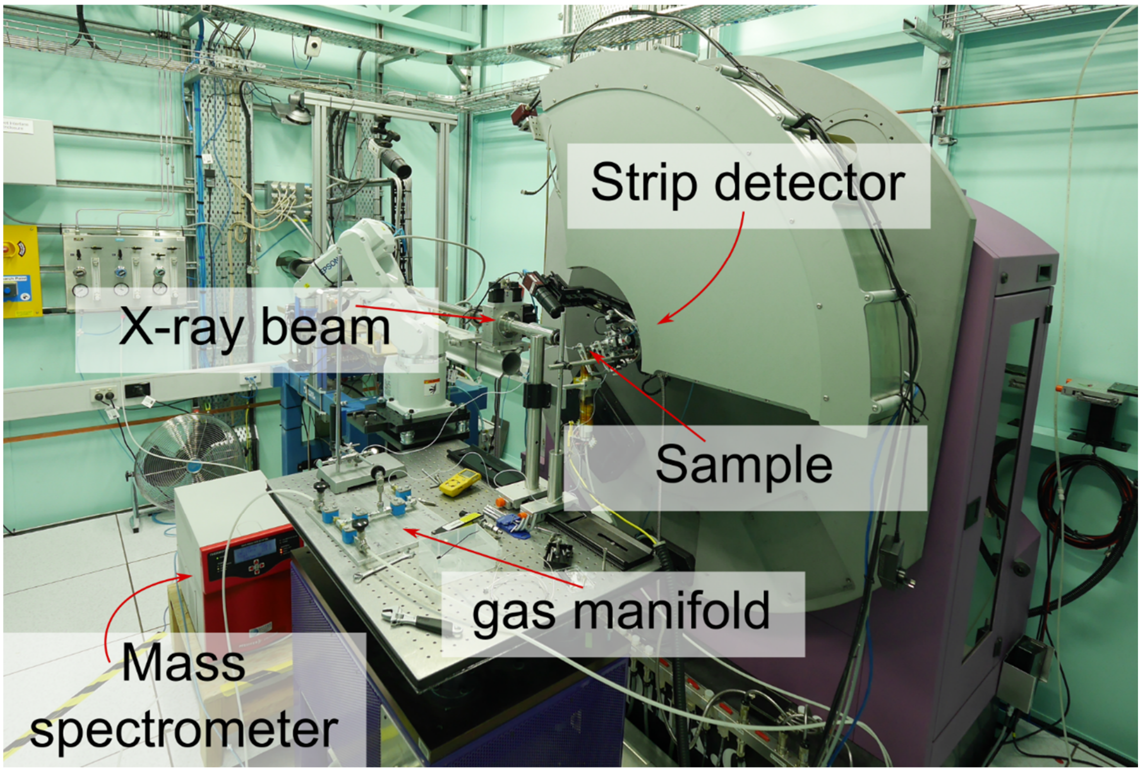

Figure S9: Photo of *in operando* PXRD set-up.

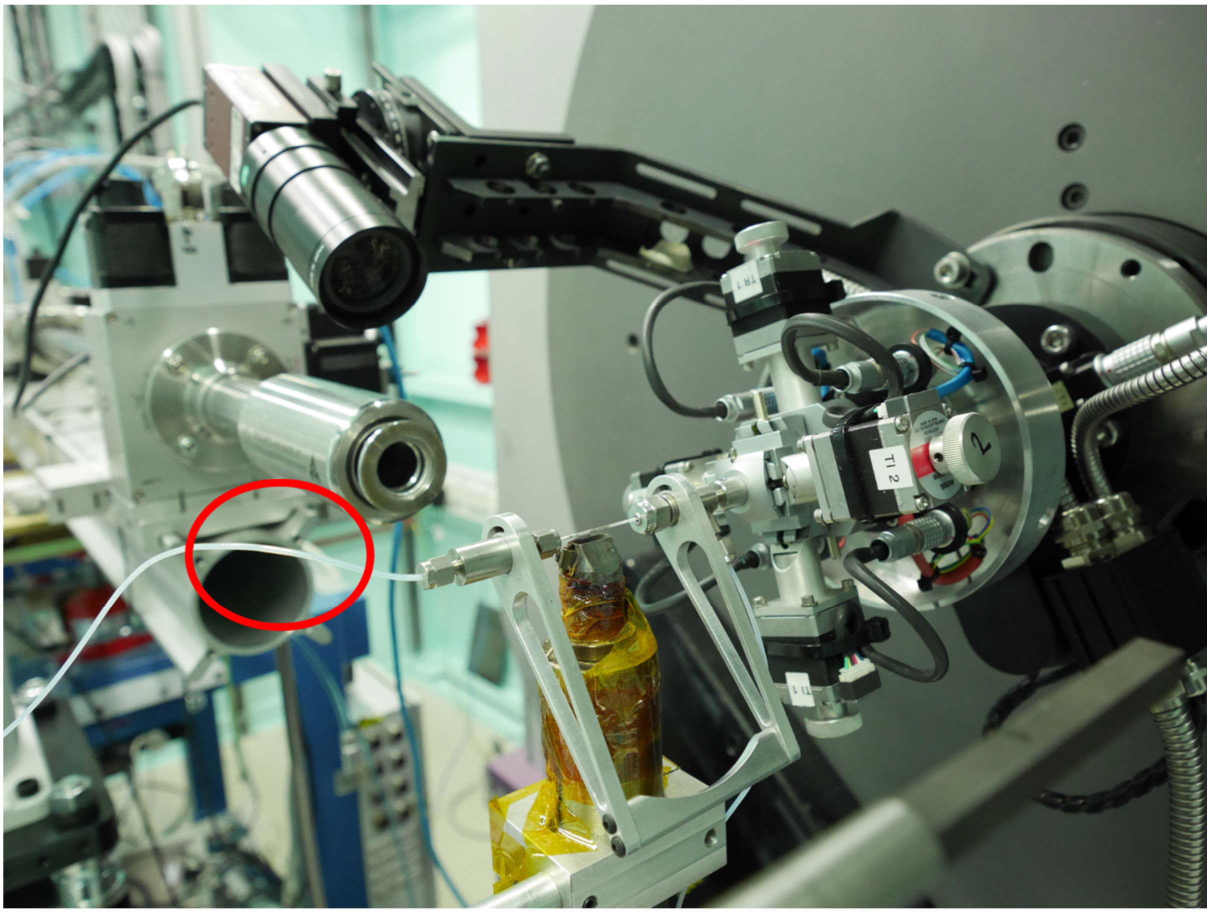

Figure S10: Photo of water drop in effluent gas nylon tubing, affecting mass spectrometry data collection.

D.2 *In operando* PXRD of Ru/Ce-UiO-66

The collapse of the Ce-UiO-66 could be observed by the simultaneous decrease in the amount of the MOF (Figure S9 B) and Lvol (column weighted volume length) values (Figure S9 C). The collapse of the MOF triggered the production of methane (Figure S9 D); the CH_4 production rate increased with the amount of CeO_2 present in the phase. The associated H_2O production caused the gas effluent line to be obstructed by condensation (Figure S9 D, dashed line 4). Even with the interruption of the MS analysis, the subsequent observation of droplets in the line was an indicative of the high CH_4 production. The final phase agreed with the MOF-templated catalysts (Figure 10). The data indicates that around 250 °C an amorphous phase is formed, and after 2 hours it crystallizes into cubic ceria nanoparticles (Lvol-integral breadth = 9 nm).

Throughout the experiment, no Ru phase was observed. The apparent presence of RuO_2 (Figure S9 B) should be disregarded as inspection of the results indicated the phase was fitted as contributing to the background and not improving reflection fit. The absence of the Ru crystalline phased in the diffractograms suggested that the presence of Ru NPs or amorphous Ru.

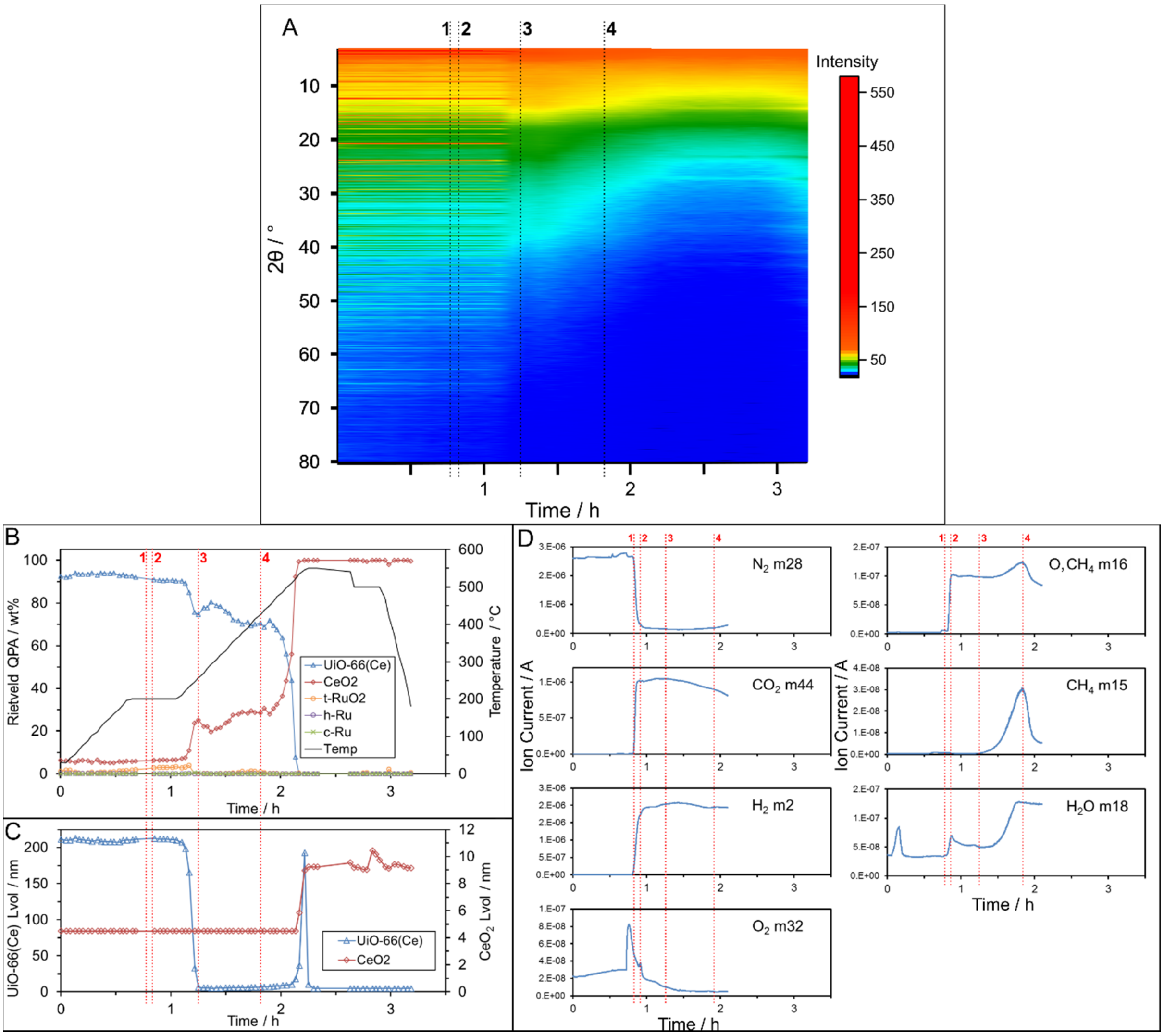

Figure S11: Catalyst MOF-templating *Operando* PXRD results. A) PXRD diffractograms stacked horizontally along time axis. Colours in heat-map indicate intensity counts; B) Rietveld quantitative phase analysis, QPA, and temperature; C) apparent crystallite size, Lvol; and D) mass spectra of different species collected during the experiment. Dashed vertical lines indicate key transitions: 1 and 2) change of gas flow from N_2 to CO_2+H_2, 3) collapse of UiO-66(Ce) structure, 4) end of mass spec reading due to H_2O condensation in the line obstructing effluent gas analysis.

E. Catalysis results

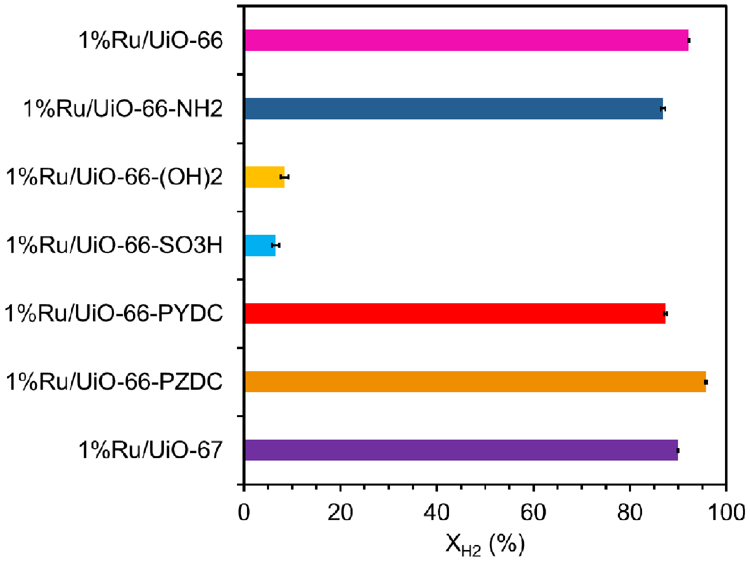

Figure S12: Catalysis results displayed in Figure 8 C with error bars indicating standard deviation of the data.

Table S6: Catalytic performance and XRD phase analysis results displayed in Figure 8 C.

Precatalyst	X_{H2} (%)	SD_{XH2} (%)	m-ZrO_2 (wt%)	t-ZrO_2 (wt%)	lvol m-ZrO_2 (nm)	lvol t-ZrO_2 (nm)	Weighted average apparent crystallite size (nm)
1%Ru/UiO-66	92.2	0.13	88.2	11.8	10.0	7.7	9.7
1%Ru/UiO-66-NH2	86.8	0.51	39.4	60.6	7.5	6.1	6.6
1%Ru/UiO-66-(OH)2	8.4	0.80	0	100	0	3.3	3.3
1%Ru/UiO-66-SO3H	6.6	0.73	0	100	0	1.0	1.0
1%Ru/UiO-66-PYDC	87.3	0.28	41.6	58.4	9.0	8.5	8.7
1%Ru/UiO-66-PZDC	95.7	0.12	31.2	68.8	7.6	5.7	6.3
1%Ru/UiO-67	89.9	0.08	67.6	32.4	7.9	6.9	7.6

* Weighted Average apparent crystallite size: lvol averaged considering relative phase (m/t-ZrO_2) content.

F. Example of Topas™ input file used for Rietveld refinement

```
macro outfile {"temp.txt"}
no_LIMIT_warnings
' -------------------------------------------------
' Control Zone                 ' {{{
            #define synchrotronRad

#ifndef BATCH
            #define m-ZrO2
            #define t-ZrO2
            #define UiO66
            macro file {"file.xye"}
#endif
            #define CapillaryPeaks
            #define Amorphous
' -------------------------------------------------
#ifdef BATCH
            do_errors
#endif
' }}}
' -------------------------------------------------
xdd file

  r_exp  2.72080154 r_exp_dash  4.14841348 r_wp  2.63597063 r_wp_dash  4.01907156 r_p  2.04521568 r_p_dash  3.15556484
weighted_Durbin_Watson  0.792196708 gof  0.968821354
  x_calculation_step 0.002
  bkg  @  526.046457` -307.455628`  134.671438` -47.8918283`  18.4268181`
  One_on_X(@, 20558.17843`)
  start_X  8
  ' -------------------------------------------------
 #ifdef synchrotronRad '{{{
  lam
    ymin_on_ymax  0.0001
    la  1 lo  0.7735184 lh  0.1

                        Zero_Error(  0.00051 )
                        LP_Factor( 90)
                        Rp 0
                        Rs 0
                        Cylindrical_2Th_Correction(@, 0.09993` min -0.1 max 0.1)     ' ICM min/max added
                                    User_Defined_Dependence_Convolution(lor_fwhm, , , 0.00010)
                          User_Defined_Dependence_Convolution(gauss_fwhm, , , 0.01251)
                          User_Defined_Dependence_Convolution(hat,,, 0.00010)
                          User_Defined_Dependence_Convolution(circles_conv,,,-0.00445 max =0;)
#endif '}}}
' -------------------------------------------------
#ifdef m-ZrO2                ' {{{
             str
   local csg 4.82781`      min 2          max 9999
   local csl  9967.68064`                 min 2    max 9999
              local  msg  0.25373` min 0.0001 max 0.30
              local  msl  0.00039` min 0.0001 max 0.30
   local  lvol = 1 / IB_from_CS(csg, csl);    :  4.53311`
              local  e0 = Voigt_FWHM_GL(msg, msl) .25;   :  0.06349`
            CS_L(csl)
                        CS_G(csg)
                        Strain_L(msl)
                        Strain_G(msg)
   LVol_FWHM_CS_G_L( 1, 4.53311`, 0.89, 4.29554`,,csg,, csl) 'LVol_FWHM_CS_G_L( 1, 6.107792147, 0.89, 9.594097469,,,@, csl)
   r_bragg  0.815480905
   phase_MAC  20.4881463
   phase_name "m-ZrO2"
   MVW( 492.891, 140.274`, 81.62285685)
   scale @  3.00722525e-005`
   weight_percent @  23.212`
   space_group P21/c
   Phase_LAC_1_on_cm( 119.54315`)
   Phase_Density_g_on_cm3( 5.83475`)
   a  @  5.120000` min 5.12  max 5.19     'a  5.145
   b  @  5.181465` min 5.17  max 5.23     'b  5.2075
   c  @  5.360000` min 5.29  max 5.36     'c  5.3107
   be @  99.43000` min 99.03 max 99.43    'be  99.23
   site Zr num_posns  4 x  0.2758 y  0.0411  z  0.2082   occ Zr    1 beq 1.0                  ' ICM - chnaged to 1.0
```

```
   site O1 num_posns  4 x  0.0703 y  0.3359  z  0.3406   occ O-2   1 beq 1.0              ' ICM - chnaged to 1.0
   site O2 num_posns  4 x  0.4423 y  -0.2451 z  0.4789   occ O-2   1 beq 1.0              ' ICM - chnaged to 1.0

  #ifdef BATCH  Out_Quant_3prm(outfile)  #endif

#endif      ' }}}

#ifdef t-ZrO2                  ' {{{
            str
            local csg    2.06747`         min 2        max 9999
   local csl  8837.19237`                 min 2        max 9999
            local  msg  0.06161` min 0.0001  max 0.50
            local  msl  0.00059` min 0.0001  max 0.50
   local  lvol = 1 / IB_from_CS(csg, csl);    :  1.94178`
            local  e0 = Voigt_FWHM_GL(msg, msl) .25;   :  0.01549`
             CS_L(csl)
                      CS_G(csg)
                      Strain_L(msl)
                      Strain_G(msg)
   LVol_FWHM_CS_G_L( 1, 1.94178`, 0.89, 1.83980`,, csg,, csl)
   r_bragg  0.548681646
   phase_MAC  20.4881463
   phase_name "t-ZrO2"
   MVW( 246.446, 65.259`, 18.37714315)
   scale @  0.000368070248`
   weight_percent @  66.086`
   space_group P42/nmc:2
   Phase_LAC_1_on_cm( 128.47927`)
   Phase_Density_g_on_cm3( 6.27091`)
   Tetragonal( @  3.544902` min 3.5449 max 3.6449 , @  5.193160` min 5.125 max 5.225) 'Tetragonal( 3.595777173, 5.17) '(a,c)
   site Zr num_posns  2   x  0.75 y  0.25 z  0.25   occ Zr   1 beq   1.53628
   site O  num_posns  4   x  0.25 y  0.25 z  0.454  occ O-2  1 beq   2.14827

  #ifdef BATCH  Out_Quant_3prm(outfile)  #endif

#endif      ' }}}

#ifdef UiO66                   ' {{{

  str

                      local csg      99.00000`                 min 99      max 9999
                      local csl      99.00000`                 min 99      max 9999
                      local  msg  0.10000`                   min 0.0001 max 0.10
                      local  msl  0.10000`                   min 0.0001 max 0.10
                      local  lvol = 1 / IB_from_CS(csg, csl);    :  44.44615`
                      local  e0 = Voigt_FWHM_GL(msg, msl) .25;   :  0.04101`
           CS_L(csl)
                      CS_G(csg)
                      Strain_L(msl)
                      Strain_G(msg)
                      LVol_FWHM_CS_G_L( 1, 44.44615`, 0.89, 53.70658`,,csg,, csl)


    r_bragg  1.08658846
    phase_MAC  9.83390778
    phase_name "UiO-66"
    MVW( 6543.354, 8607.563`, 100)
    scale @  1.70202257e-008`
    weight_percent @  10.702`
    space_group Fm-3m
    Phase_LAC_1_on_cm( 12.41354`)
    Phase_Density_g_on_cm3( 1.26232`)
    Cubic( a_uio66  20.494000` min 20.494 max 20.894)

    site Zr  num_posns  24 x  0.1204 y  0        z  0       occ Zr  1 beq   1.11559
    site O1  num_posns  96 x  0.1726 y  0        z  0.096   occ O   1 beq   2.78938
    site O2  num_posns  32 x  0.0561 y  -0.0561  z  -0.0561 occ O   1 beq   3.11801
    site C11 num_posns  48 x  0.1473 y  0        z  -0.1473 occ C   1 beq   1.0
    site C12 num_posns  48 x  0.2019 y  0        z  0.2019  occ C   1 beq   1.0
    site C13 num_posns  96 x  0.2643 y  0        z  0.1841  occ C   1 beq   1.0

  #ifdef BATCH  Out_Quant_3prm(outfile)  #endif
'          view_structure

#endif '}}}
```

```
#ifdef CapillaryPeaks     ' {{{
 ' ------------------------------------------------------------------------------
            xo_Is
              phase_name Capillary_peaks

              scale     scpeaks  0.561318996` min  0.0000000001

                        peak_type pv
      pv_lor     !lor1  0.875176188 min 0.001 max 0.999
      pv_fwhm    !wid1  6.80993837 min 3 max 12

                        xo      10.7686286 min  8 max 11  I      61.81976 min 0.001
                        xo      11.9996389 min 11 max 13  I      60.88785 min 0.001
                        xo      14.0521764 min 13 max 16  I      60.79769 min 0.001
                        xo      28.3161141 min 27 max 30  I      155.51446 min 0.001
                        xo      39.9874426 min 36 max 40  I      3.67647 min 0.001
                        xo      42.7635267 min 41 max 44  I      174.51989 min 0.001

            #ifdef BATCH  Out_peak_phase(outfile)  #endif 'RL added output macro

#endif '}}}

#ifdef Amorphous          ' {{{
 ' ------------------------------------------------------------------------------
            xo_Is
              phase_name Amorphous_peaks

              scale     scpeaks2  0.939639376` min  0.0000000001

                        peak_type pv
      pv_lor     !lor2  0.00100190355` min 0.001 max 0.999
      pv_fwhm    !wid2  3.55937145`    min 3     max 12

                        xo      14.999958`          min 12 max 15  I      49.23024` min 0.001
                        xo      16.0000019` min 16 max 18  I      16.13496` min 0.001
                        xo      21.9960938` min 20 max 22  I      13.64560` min 0.001
                        xo      25.0769558` min 22 max 26  I      48.34264` min 0.001
                        xo      29`         min 27 max 29  I      61.82307` min 0.001

            #ifdef BATCH  Out_peak_phase(outfile)  #endif

#endif '}}}
```

G. References

1. Cavka, J. H.; Jakobsen, S.; Olsbye, U.; Guillou, N.; Lamberti, C.; Bordiga, S.; Lillerud, K. P., A New Zirconium Inorganic Building Brick Forming Metal Organic Frameworks with Exceptional Stability. J. Am. Chem. Soc. 2008, 130, 13850-1.

2. Katz, M. J.; Brown, Z. J.; Colón, Y. J.; Siu, P. W.; Scheidt, K. a.; Snurr, R. Q.; Hupp, J. T.; Farha, O. K., A Facile Synthesis of UiO-66, UiO-67 and Their Derivatives. Chem. Commun. 2013, 49, 9449-51.

3. Thommes, M.; Kaneko, K.; Neimark, A. V.; Olivier, J. P.; Rodriguez-Reinoso, F.; Rouquerol, J.; Sing, K. S. W., Physisorption of Gases, with Special Reference to the Evaluation of Surface Area and Pore Size Distribution (Iupac Technical Report). Pure Appl. Chem. 2015, 87, 1051-1069.

4. Waitschat, S.; Reinsch, H.; Stock, N., Water-Based Synthesis and Characterisation of a New Zr-MOF with a Unique Inorganic Building Unit. Chem. Commun. 2016, 52, 12698-12701.

5. Rietveld, H., A Profile Refinement Method for Nuclear and Magnetic Structures. J. Appl. Crystallogr. 1969, 2, 65-71.

6. Valenzano, L.; Civalleri, B.; Chavan, S.; Bordiga, S.; Nilsen, M. H.; Jakobsen, S.; Lillerud, K. P.; Lamberti, C., Disclosing the Complex Structure of UiO-66 Metal Organic Framework: A Synergic Combination of Experiment and Theory. Chem. Mater. 2011, 23, 1700-1718.

7. Topas V5: General Profile and Structure Analysis Software for Powder Diffraction Data, Bruker AXS GmbH: Karlsruhe, Germany, 2012.

8. Madsen, I. C.; Scarlett, N. V. Y.; Riley, D. P.; Raven, M. D., Quantitative Phase Analysis Using the Rietveld Method. In Modern Diffraction Methods, Wiley-VCH Verlag GmbH & Co. KGaA: 2012; pp 283-320.

Chapter 5

In situ MOF-templating route to Ru/CeO_2 catalysts for NH_3 synthesis

Renata Lippi,[†‡] Shaun C. Howard,[‡] Christopher J. Sumby,[†] Christian J. Doonan,*[†] Danielle F. Kennedy*[‡]

[‡]CSIRO Manufacturing, Clayton, Victoria 3168, Australia.
[†]Centre for Advanced Nanomaterials, Department of Chemistry, The University of Adelaide, Adelaide, South Australia 5005, Australia.

Submitted manuscript

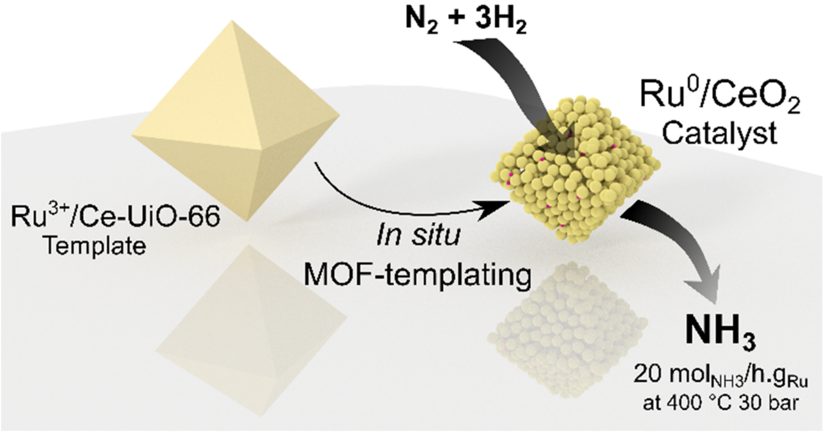

5.1. Summary

The remarkable morphology control and catalytic activity for CO_2 methanation provided by the MOF-templated Ru^0/ZrO_2 described in Chapter 3 and 4 encouraged expansion of this synthesis route to catalysts for NH_3 synthesis. In the NH_3 synthesis reaction, ruthenium catalysts have been proposed as a low pressure alternative to Fe-based catalysts. However, their stability, availability, and cost usually discourage application. Therefore, obtaining stable catalysts that maximise NH_3 yield per mass of Ru are desirable. This chapter describes the use of $RuCl_3$/Ce-UiO-66 as template for NH_3 synthesis catalysts. The MOF-templating of the catalyst occured *in situ*, i.e. 80% H_2 and 20% N_2, with the final catalyst structure investigated and demonstrated to be composed of Ru^0 nanoparticles supported on CeO_2. The MOF-derived catalyst was tested alongside Fe and Ru catalysts and displayed high catalytic activity. The high activity is hypothesised to be a result of the morphology control and homogeneous Ru distribution provided by the MOF-templating route.

Statement of Authorship

Title of Paper	In situ MOF-templating route to Ru/CeO_2 catalysts for NH_3 synthesis	
Publication Status	☐ Published ☒ Submitted for Publication	☐ Accepted for Publication ☐ Unpublished and Unsubmitted work written in manuscript style
Publication Details	Submitted to Chemical Communications on 24/11/2017.	

Principal Author

Name of Principal Author (Candidate)	Renata Lippi		
Contribution to the Paper	Design, preparation and execution of experiments, synthesis of materials, catalysis tests, catalysis data analysis, XRD experiments and analysis, electron microscopy experiments, preparation of manuscript.		
Overall percentage (%)	80%		
Certification:	This paper reports on original research I conducted during the period of my Higher Degree by Research candidature and is not subject to any obligations or contractual agreements with a third party that would constrain its inclusion in this thesis. I am the primary author of this paper.		
Signature		Date	29/11/2017

Co-Author Contributions

By signing the Statement of Authorship, each author certifies that:

i. the candidate's stated contribution to the publication is accurate (as detailed above);

ii. permission is granted for the candidate in include the publication in the thesis; and

iii. the sum of all co-author contributions is equal to 100% less the candidate's stated contribution.

Name of Co-Author	Shaun C. Howard		
Contribution to the Paper	Intellectual input in planning and operation of high-throughput catalysis testing rig and synchrotron experimental set up		
Signature		Date	20-Nov-2017

Name of Co-Author	Cristopher J. Sumby		
Contribution to the Paper	Intellectual input in project design, manuscript revisions		
Signature		Date	23/11/17

Name of Co-Author	Christian J. Doonan		
Contribution to the Paper	Intellectual input in project design, manuscript revisions		
Signature		Date	23/11/17

Name of Co-Author	Danielle F. Kennedy		
Contribution to the Paper	Intellectual input in project design, High-throughput catalysis screening method development, assistance in synchrotron experiments, manuscript revisions		
Signature		Date	26/11/2017

5.2. Abstract

A Ru-impregnated Ce-based MOF was used as a sacrificial template for the preparation of an NH3 synthesis catalyst. Formation under reaction conditions gave a catalyst with remarkable performance in comparison to benchmark catalysts. The MOF-templating route was found to provide excellent control over the size and distribution of both the metal oxide support and the active metal components.

5.3. Introduction

Ammonia (NH_3) synthesis via the Haber-Bosch process is widely applied in industry for the production of artificial fertilizers.[1-2] This process involves the reaction of N_2 and H_2 over heterogeneous catalysts. The reaction is endothermic and equilibrium controlled, thus high pressures and temperatures are necessary to shift the equilibrium towards NH_3 production.[3] For example, Fe-based catalysts are typically employed in industry under operating conditions of 500 °C and 200 bar.[2] This energy intensive process is estimated to consume 2% of energy produced globally.[4] As a result, decreasing the energy requirements for the large scale production of NH_3 is an on-going challenge.[5-6] To this end supported Ru nanoparticles have been explored as an alternative to Fe-based catalysts as they show higher reactivity at significantly lower pressures.[7] However, stability, availability and cost have discouraged their commercial use.[5, 8] Fundamental studies have shown that the efficiency of Ru catalysts is structure dependent.[8] Therefore, synthesis methods that offer control over the final catalyst structure may help to maximise the production of ammonia per unit mass of Ru.[8-10] Additonally, the composition of the catalyst support material is also critical to the efficiency of the reaction. Although the support materials do not present significant catalytic activity alone, their physicochemical properties do influence the activity of catalytic systems.[7, 11] Support materials commonly used include: carbon, MgO_2, Al_2O_3, and CeO_2.[11-13] Of these, CeO_2 is reported to be an effective support material for Ru-based catalysts,[9a] as the presence of the reversible redox pair Ce^{4+}/Ce^{3+} can increase the electron density on Ru^0 and facilitate N_2 activation.[12, 14-15]

The synthetic approach used to generate heterogeneous catalysts can have a significant effect on their performance, especially with respect to the morphologies and surface chemistry of Ru and CeO_2.[10, 16-17] For example, nanoparticles with a high number of reactive surface sites are desired in heterogeneous catalysts.[9] However, synthesising nanoparticles of specific size and distribution on the support can be challenging, as they tend to aggregate and sinter under operating conditions. Iwamoto *et al*. have demonstrated preparation of Ru/MgO catalysts via sol-gel methods, where both the support and the active metal were synthesised simultaneously, and were able to achieve a homogeneous distribution of Ru on the support and high NH_3 production rates.[18]

Metal-organic frameworks (MOFs) are hybrid materials composed of inorganic nodes connected by organic linkers.[19] The wide variety of organic and inorganic building units gives rise to an expansive number of possible structures that possess diverse chemical functionality and physical properties.[20] MOFs have been widely explored as porous catalysts,[21-23] however; recent reports have described the advantage of using the tailored structures of MOFs as templates for functional materials including novel catalysts.[24-26] In the examples reported, the MOF template engendered specific elemental distributions and structures that could not be obtained by other synthetic approaches. Furthermore, the templating method led to enhanced catalytic performance.[27-32]

5.4. Results and discussion

Previously, we have described the application of MOF-templating for the production of a highly active Ru/ZrO_2 nanostructured catalyst for CO_2 methanation.[27] The high activity was attributed to the homogeneous distribution of size-controlled Ru nanoparticles on the nanostructured ZrO_2 support. Here, we report a MOF-templating route for the synthesis of a highly active Ru/CeO_2 catalyst for NH_3 synthesis. The templated catalyst was compared to a series of controls, including a Ru-based literature reported catalyst, a commercial Wustite catalyst (Amomax-10), other MOF-derived catalysts, and samples of analogous chemical composition synthesised by other methods. The Cerium-based MOF, Ce-UiO-66, which is structurally analogous to UiO-66 was employed as the template to afford a CeO_2 support and $RuCl_3$ was introduced into the pores of the MOF via Impregnation to provide the active catalyst (Figure 1).

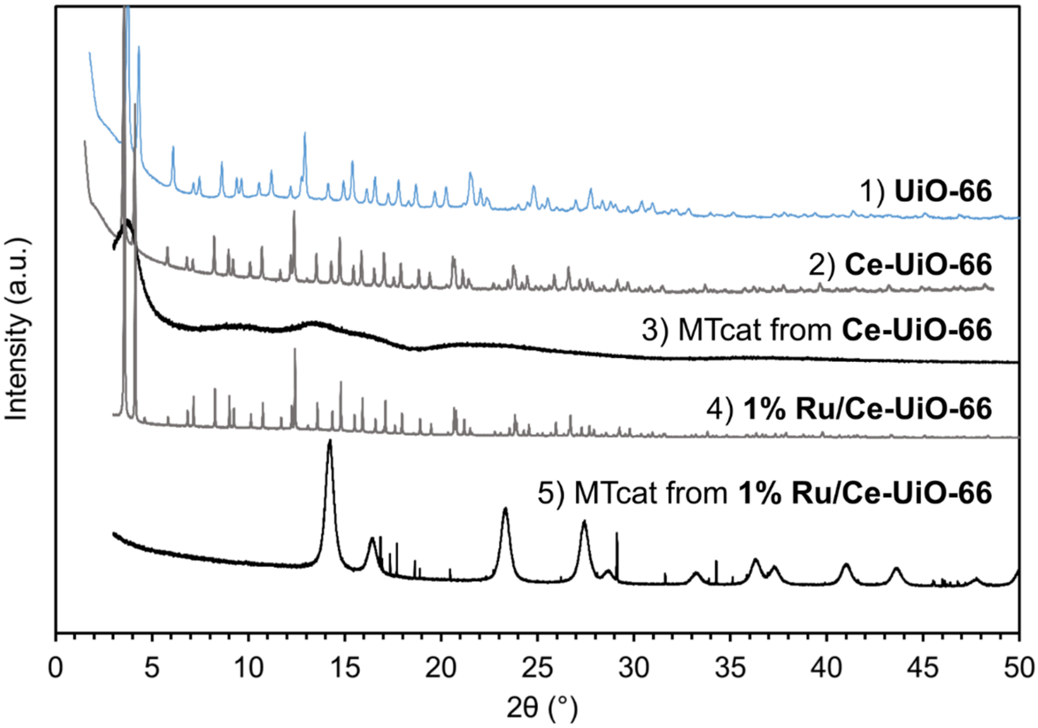

Figure 1: PXRD patterns of 1) UiO-66; 2) Ce-UiO-66; 3) MOF-templated catalyst (MTcat) derived from Ce-UiO-66; 4) 1% Ru/Ce-UiO-66; and 5) active catalyst, MTcat derived from 1% Ru/Ce-UiO-66. The crystalline structure of the MOF is clearly observed in is the patterns 1, 2, and 4. MTcat testing from

Ce-UiO-66 generated an amorphous phase (3). In contrast, 1%Ru/Ce-UiO-66 templated an active catalyst composed mostly of cubic CeO_2 (5), the broad peaks are a result of the small crystallite size formed. The sharp peaks are from highly crystalline SiC used as catalyst diluent (Figure S6).

Comparing the performance of literature reported catalysts is challenging as the test conditions used are variable (e.g. gas velocity, catalyst mass, reactor design). Furthermore, different methods of analysis (e.g. gas chromatography, titration) can be employed. To overcome this issue, we selected a commercially available benchmark NH_3 synthesis catalyst Wustite (FeO) (Amomax-10, Sud-Chemie) and synthesised, the well known, highly active low-pressure Ru-based catalyst developed by Aika *et al.*[11] for intitial screening studies. Using a multi-channel catalysis rig,[27] we were able to test these samples under the same conditions as the MOF-templated catalysts and controls reported in this study.

The initial catalyst screening included a fresh sample of **1%Ru/Ce-UiO-66**, catalysts derived from **1%Ru/UiO-66** and **2%Ru/UiO-66** templated previously, and Amomax-10 (Figure 2). All catalysts were subjected to the activation conditions required for Amomax-10 (pure H_2 flow, at 475 °C and 1 bar). After this activation procedure all the catalysts displayed stable conversion for approximately 30 hours under reaction conditions (H_2, 1.875 mL/min; N_2, 0.625 mL/min; Ar, 0.417 mL/min; at 475 °C and 160 bar). Amomax-10 showed the highest NH_3 production per unit of catalyst mass, however; among the MOF-derived catalysts, the Ce-based catalyst significantly outperformed its Zr analogues. The lower performance of Ru/ZrO_2 compared to Ru/CeO_2 is in agreement with previous reports, which describe the negative impact that the acidic nature of ZrO_2 has on ammonia synthesis.[33] On the other hand, a basic support will assist the reaction by donating electrons to Ru.[33]

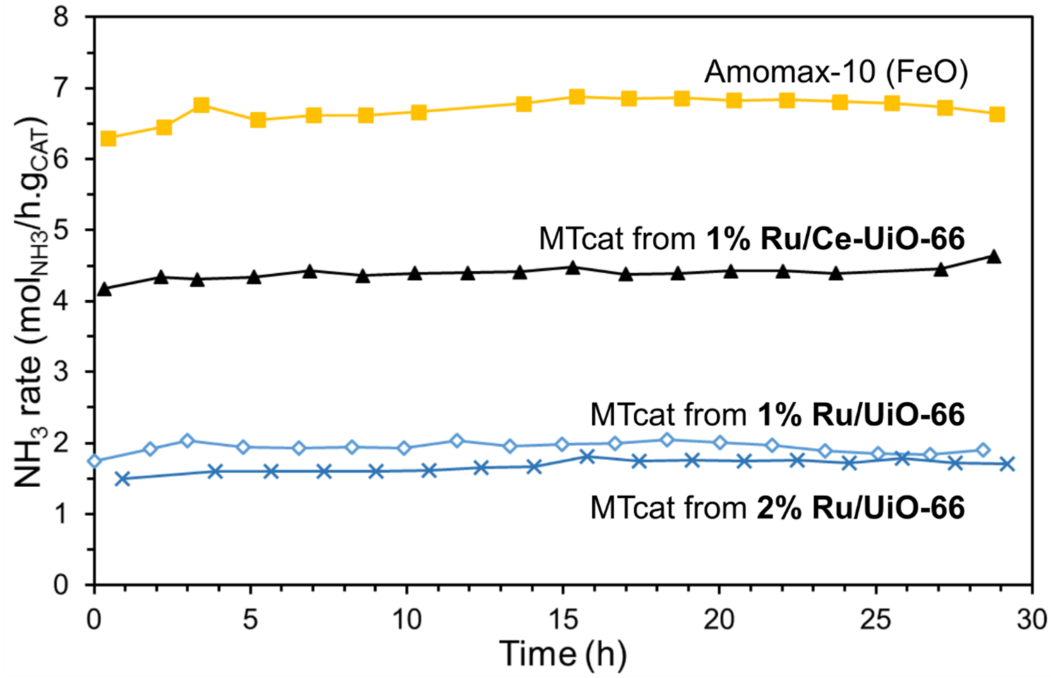

Figure 2: Catalytic performance of FeO and MOF-templated catalysts (MTcat) at 475 °C and 160 bar.

High temperatures and pressures are necessary to ensure high activity for Amomax-10. Thus if, Ru-based catalysts operate at milder conditions, they may offer an energetic advantage for NH_3 production. Accordingly, a systematic comparison of the Ru-based samples was performed at lower temperatures and pressures. In these experiments, a low pressure benchmark catalyst reported by Aika *et al.*, that is composed of of Ru supported on MgO and promoted with Cs (**2%Ru-Cs/MgO**), was included.[11] A series of $RuCl_3$-impregnated Ce-UiO-66 samples with different Ru loadings were prepared: varying from 0.25 to 2 wt% Ru/Ce-UiO-66. Furthermore, a series samples composed of $RuCl_3$-impregnated directly on pre-made cubic CeO_2 (10 nm) were prepared with loadings of 0.5, 1, 1.5 and 2% Ru/CeO_2.

At temperatures lower than or equal to 350 °C and pressures of 10, 30, and 50 bar we did not detect ammonia production, even for the benchmark catalyst. However, the previous report by Aika *et al*. indicated that the **2%Ru-Cs/MgO** catalyst does display activity under these conditions.[11] We posit that variances in NH_3 detection range among effluent analysis techniques used may explain this discrepancy.

When the reaction temperature was elevated to 400˚C the Ru/Ce-UiO-66 templated catalyst displayed remarkable activity (Figure 1B). The most active MOF-templated catalyst was derived from **0.75% Ru/Ce-UiO-66**, producing 14, 20.5 and 22.9 $mol_{NH3}/h.g_{Ru}$ at 10, 30 and 50 bar, respectively. It is noteworthy, that at 30 and 50 bar the MOF derived catalyst outperformed the benchmark **2% Ru-Cs/MgO**, which generates 18.1, 18.1 and 16.1 $mol_{NH3}/h.g_{Ru}$ at 10, 30 and 50 bar, respectively. Additionally, the family of MOF-templated catalysts also display increasing conversion at higher pressures, indeed the error bars in Figure 1B obscure an increasing conversion with time (Figure S5), whereas the conversion by the **2% Ru-Cs/MgO** catalyst was not affected by the pressure increase, in agreement with previous reports.[34] It is noteworthy that at 30 and 50 bar MOF-templated catalysts composed of of **0.75**, **1** and **1.25% Ru/Ce-UiO-66** outperformed the positive control **2% Ru-Cs/MgO**. The catalysts prepared via direct impregnation of $RuCl_3$ on pre-made CeO_2 did not produce detectable amounts of NH_3 at any of the tested conditions. The use of metal precursors that contain Cl are usually avoided in the synthesis of NH_3 catalysts as Cl is known to have a poisoning effect,[35] although there is no consensus on the poisoning mechanism by Cl atoms. Notably, the presence of Cl in the precatalysts $RuCl_3$/Ce-UiO-66 did not inhibit catalytic activity of the derived catalysts.

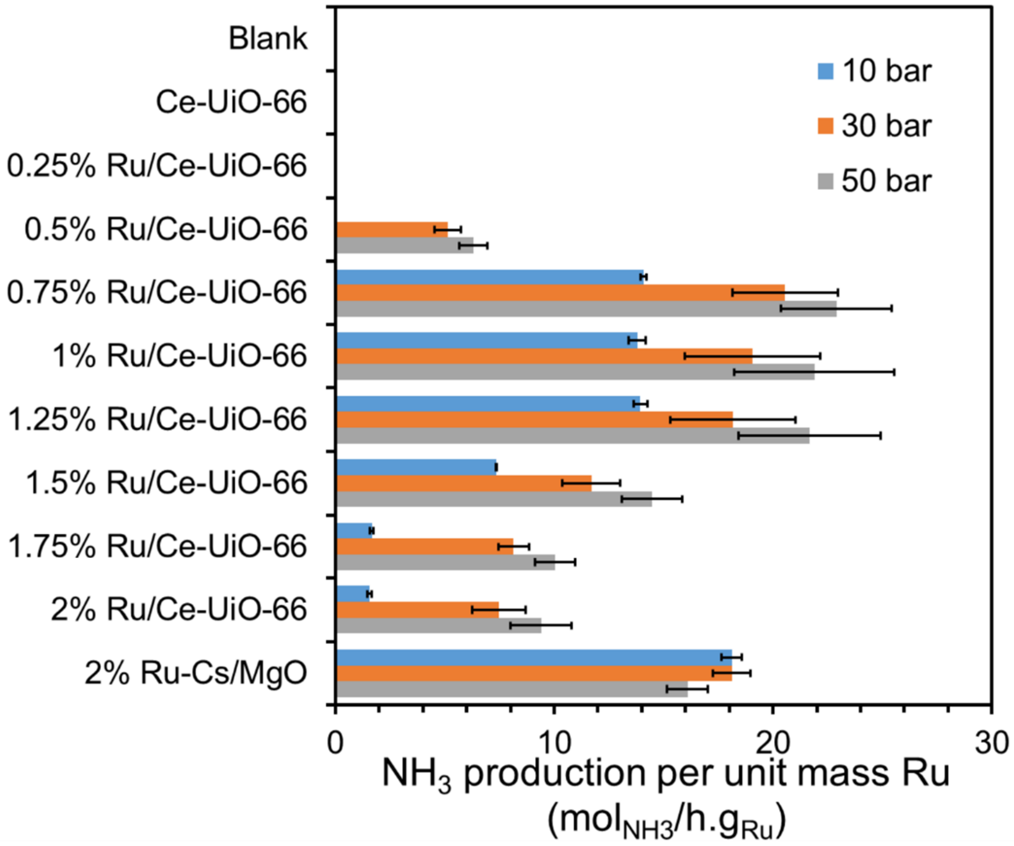

Figure 3: NH_3 production per unit mass of Ru during catalyst testing at 400 °C with variable pressure. $RuCl_3$ was impregnated onto Ce-UiO-66 at different loadings as indicated. The chart indicated the performance of the catalyst derived from these precursors. 2% Ru-Cs/MgO catalyst was prepared according to Aika *et al.*[11] Error bars show standard deviation of the 3 measurements.

The structure of the Ce-MOF templated catalyst was studied by powder X-ray diffraction (PXRD), transmission electron microscopy (TEM), energy dispersive spectroscopy (EDS) and electron diffraction to determine the chemistry underpinning its efficacy. The MOF-templated catalyst (MTcat) from **1% Ru/Ce-UIO-66** was analysed using synchrotron X-ray powder diffraction to obtain high resolution diffractograms (Figure 1). The peak positions and broadness suggest that the catalyst is composed of nano-sized cubic CeO_2.[36] The integral breadth apparent size (Lvol-IB) is used in XRD to estimate crystallite domain sizes, although actual crystallite sizes will depend on the morphology of the particle.[37] For the templated catalyst, the Lvol-IB for cubic CeO_2 was 6 nm. No reflections corresponding to a Ru phase were observed in the synchrotron source diffractograms which is consistent with our previous studies on the MOF-templating of a Ru/ZrO_2 catalyst.[27] We attribute the absence of Ru peaks to its low loading on the support and to the small size of the nanoparticles. Nevertheless, diffraction studies indicate that Ru is crucial to directing the structure of the catalyst. For example, neat **Ce-UiO-66** processed under analogous conditions gave rise to an amorphous phase rather than nanostructured CeO_2.

TEM performed on the active catalyst was in agreement with the PXRD analysis, indicating the presence of CeO_2 nanocrystals in the rage of 4-6 nm (Figure 4 and S7). These crystals were found to agglomerate into large clusters approximately 130-170 nm in size. It is noteworthy that these clusters are similar in size to the apparent crystallite size (Lvol-IB) of 200 nm for the parent MOF, Ce-UiO-66. This suggests that CeO_2 nanoparticle clusters are formed directly from the collapse of the MOF crystals. In agreement with our previous observations,[27] on the MOF-templating of Ru/ZrO_2.

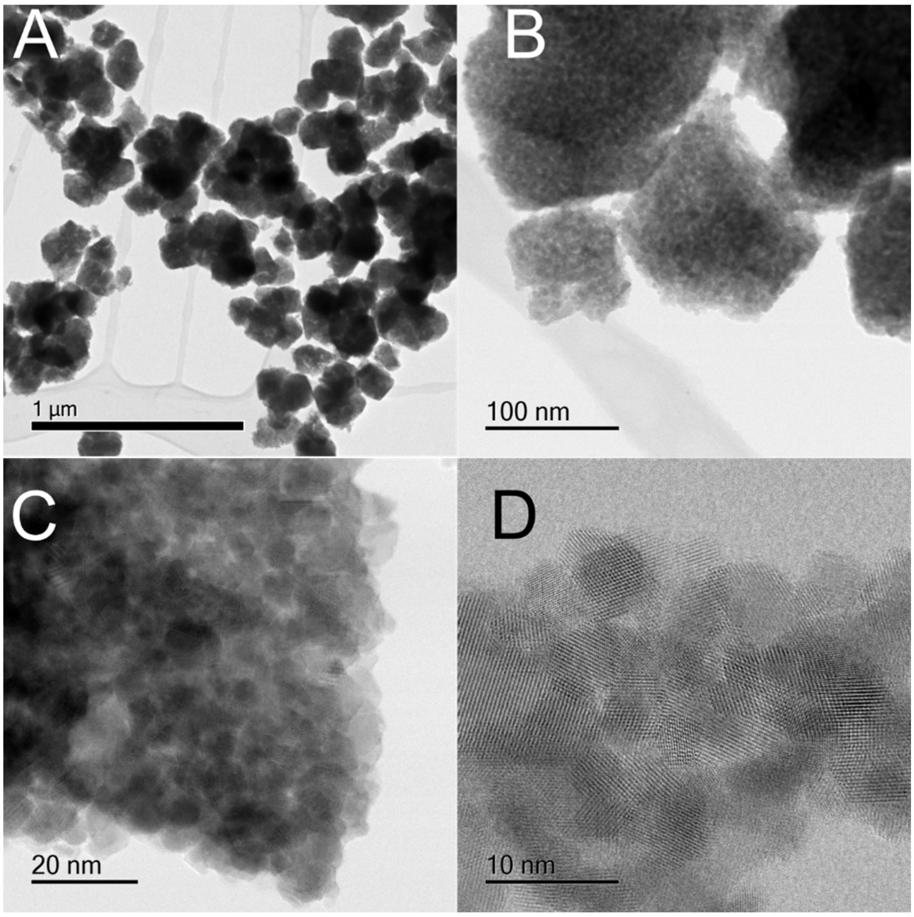

Figure 4: A-D) High resolution TEM of the catalyst templated by 1%Ru/Ce-UiO-66 at different magnifications. It is possible to observe that the catalyst is composed of clusters of nanoparticles (A and B). Within these clusters, nanocrystals can be observed (C and D).

Due to the high electron density of Ce, Ru cannot be clearly distinguished using TEM. Thus, in order to evaluate the distribution of Ru NPs in the catalyst we employed electron dispersive X-ray spectroscopy (EDS) (Figure 5). The EDS maps indicated the Ru nanoparticles are evenly distributed throughout the CeO_2 nanoparticles (**Figure** 5). Additionally, the Ru NPs were approximately 2 nm in size, significantly smaller than the CeO_2 support. Electron diffraction identified hexagonal close-packed Ru^0 (Figure S9) and no evidence of RuO_2 phases even after storage in air. These results confirm that the bulk of the Ru^0 nanoparticles may be stabilised on the CeO_2 support by intimate integration with the CeO_2 nanocrystals.

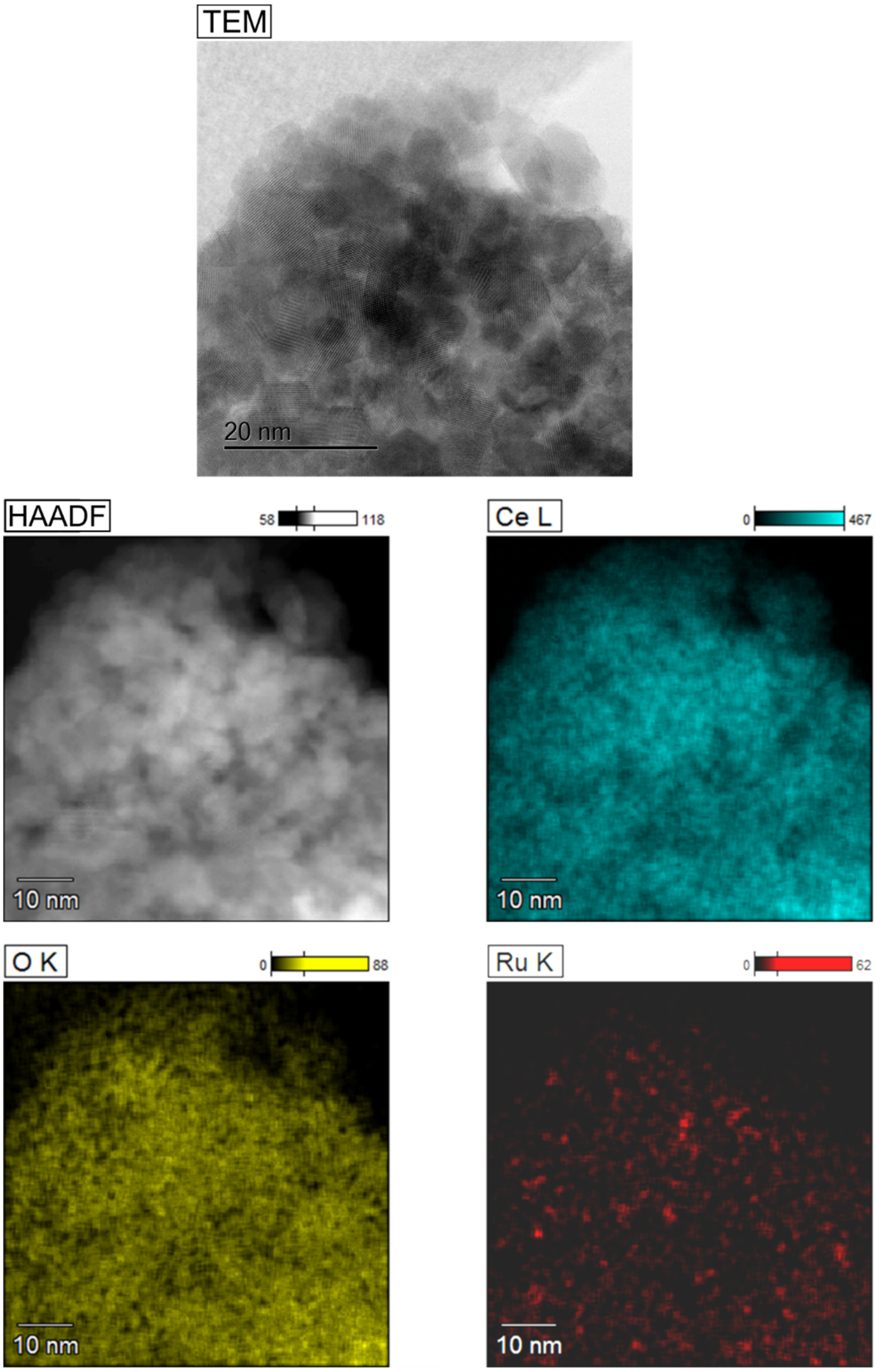

Figure 5: TEM, HAADF (high-angle annular dark-field) and EDS (Energy dispersive spectroscopy) mapping for the MOF-templated catalyst derived from 1%Ru/Ce-UiO-66. The elemental maps show small clusters of Ru (less than 2 nm) evenly dispersed on the CeO_2. For clarification, contrast was improved on Ru map.

We attribute the high activity of the MOF-templated catalyst to its unique composite nanostructure. For example, CeO_2 is considered an efficient support due to its facile redox activity (Ce^{4+}/Ce^{3+}), with the presence of this redox pair is believed to modulate the electron density on the surface of Ru nanoparticles and improve the activation of N_2.[10, 38] The small size of the templated CeO_2 crystals may be key to allow a higher amount of Ce^{4+} to be reduced and the consequent creation of surface O vacancies. These results are in agreement with other recent reports on MOF-templated CeO_2 based oxidation catalysts, which also demonstrated the successful synthesis of smaller CeO_2 particles and a significant increase in the overall catalytic activity.[31-32] Furthermore, it is known that for Ru-based catalysts, the presence of B_5-type sites on Ru^0 nanoparticles may facilitate ammonia synthesis.[9] These sites are typically found on the edges of crystals, and the proportion of B_5-type sites per mass of Ru is known to be higher for Ru^0 nanoparticles in the range of 2 to 2.5 nm.[8, 39] We conclude that the high activity of the **Ru/Ce-UIO-66** derived catalyst can be attributed to the homogeneous dispersion of such Ru NPs on the CeO_2 support.

5.5. Conclusions

In summary, we employed a Ru-impregnated Ce-MOF (**x% Ru/Ce-UiO-66**) as a template for an NH_3 synthesis catalyst. Compared to the control catalyst, **2% Ru-Cs/MgO** at 50 bar, the MOF templated catalysts, **0.75% Ru/Ce-UiO-66** and **1% Ru/Ce-UiO-66,** showed 42% and 36% higher activity per mass of Ru, respectively. We note that this high performance is the result of the unique catalyst structure that can only be achieved via the MOF-templating route. We employed diffraction and microscopy to elucidate the catalyst structure and found that it was composed of small Ru^0 nanoparticles (~2 nm) homogeneously distributed on CeO_2 nanoparticles 4 to 6 nm in size. In summary, this work exemplifies how the MOF-templating route can be applied to synthesis of highly active catalysts.

5.6. Acknowledgements

Aspects of this research were undertaken on the Powder Diffraction beamline at the Australian Synchrotron, Victoria, Australia. This work was supported by CSIRO and The University of Adelaide. R. Lippi acknowledges The University of Adelaide for the Beacon of Enlightenment Ph.D. Scholarship. The authors acknowledge Ruth Fischer for synthesising the positive control.

5.7. References

1. Smil, V., Detonator of the Population Explosion. Nature 1999, 400, 415-415.

2. Kandemir, T.; Schuster, M. E.; Senyshyn, A.; Behrens, M.; Schlogl, R., The Haber-Bosch Process Revisited: On the Real Structure and Stability of "Ammonia Iron" under Working Conditions. Angew. Chem. Int. Ed. 2013, 52, 12723-12726.

3. Larson, A. T., The Ammonia Equilibrium at High Pressures. J. Am. Chem. Soc. 1924, 45, 367-372.

4. Pfromm, P. H., Towards Sustainable Agriculture: Fossil-Free Ammonia. *J. Renew. Sustain. Energy* **2017**, *9*.

5. Saadatjou, N.; Jafari, A.; Sahebdelfar, S., Ruthenium Nanocatalysts for Ammonia Synthesis: A Review. *Chem. Eng. Commun.* **2015**, *202*, 420-448.

6. Shipman, M. A.; Symes, M. D., Recent Progress Towards the Electrosynthesis of Ammonia from Sustainable Resources. *Catal. Today* **2017**, *286*, 57-68.

7. Muhler, M.; Rosowski, F.; Hinrichsen, O.; Hornung, A.; Ertl, G., Ruthenium as Catalyst for Ammonia Synthesis. *Stud. Surf. Sci. Catal.* **1996**, *101*, 317-326.

8. Jacobsen, C. J. H.; Dahl, S.; Hansen, P. L.; Törnqvist, E.; Jensen, L.; Topsøe, H.; Prip, D. V.; Møenshaug, P. B.; Chorkendorff, I., Structure Sensitivity of Supported Ruthenium Catalysts for Ammonia Synthesis. *J. Mol. Catal. A: Chem.* **2000**, *163*, 19-26.

9. Dahl, S.; Logadottir, A.; Egeberg, R. C.; Larsen, J. H.; Chorkendorff, I.; Törnqvist, E.; Nørskov, J. K., Role of Steps in N2 Activation on Ru(0001). *Phys. Rev. Lett.* **1999**, *83*, 1814-1817.

10. Ma, Z.; Zhao, S.; Pei, X.; Xiong, X.; Hu, B., New Insights into the Support Morphology-Dependent Ammonia Synthesis Activity of Ru/CeO2 Catalysts. *Catal. Sci. Technol.* **2017**, *7*, 191-199.

11. Aika, K.-i.; Takano, T.; Murata, S., Preparation and Characterization of Chlorine-Free Ruthenium Catalysts and the Promoter Effect in Ammonia Synthesis. *J. Catal.* **1992**, *136*, 126-140.

12. Niwa, Y.; Aika, K.-i., The Effect of Lanthanide Oxides as a Support for Ruthenium Catalysts in Ammonia Synthesis. *J. Catal.* **1996**, *162*, 138-142.

13. Forni, L.; Molinari, D.; Rossetti, I.; Pernicone, N., Carbon-Supported Promoted Ru Catalyst for Ammonia Synthesis. *Appl. Catal., A* **1999**, *185*, 269-275.

14. Ma, Z.; Xiong, X.; Song, C.; Hu, B.; Zhang, W., Electronic Metal-Support Interactions Enhance the Ammonia Synthesis Activity over Ruthenium Supported on Zr-Modified CeO2 Catalysts. *RSC Adv.* **2016**, *6*, 51106-51110.

15. Campbell, C. T.; Peden, C. H. F., Oxygen Vacancies and Catalysis on Ceria Surfaces. *Science* **2005**, *309*, 713-714.

16. Song, Z.; Cai, T.; Hanson, J. C.; Rodriguez, J. A.; Hrbek, J., Structure and Reactivity of Ru Nanoparticles Supported on Modified Graphite Surfaces: A Study of the Model Catalysts for Ammonia Synthesis. *J. Am. Chem. Soc.* **2004**, *126*, 8576-8584.

17. Fernández, C.; Sassoye, C.; Debecker, D. P.; Sanchez, C.; Ruiz, P., Effect of the Size and Distribution of Supported Ru Nanoparticles on Their Activity in Ammonia Synthesis under Mild Reaction Conditions. *Appl. Catal., A* **2014**, *474*, 194-202.

18. Iwamoto, J.; Itoh, M.; Kajita, Y.; Saito, M.; Machida, K.-i., Ammonia Synthesis on Magnesia Supported Ruthenium Catalysts with Mesoporous Structure. *Catal. Commun.* **2007**, *8*, 941-944.

19. Furukawa, H.; Cordova, K. E.; O'Keeffe, M.; Yaghi, O. M., The Chemistry and Applications of Metal-Organic Frameworks. *Science* **2013**, *341*, 1230444.

20. Chung, Y. G.; Camp, J.; Haranczyk, M.; Sikora, B. J.; Bury, W.; Krungleviciute, V.; Yildirim, T.; Farha, O. K.; Sholl, D. S.; Snurr, R. Q., Computation-Ready, Experimental Metal–Organic Frameworks: A Tool to Enable High-Throughput Screening of Nanoporous Crystals. *Chem. Mater.* **2014**, *26*, 6185-6192.

21. Bloch, W. M.; Burgun, A.; Coghlan, C. J.; Lee, R.; Coote, M. L.; Doonan, C. J.; Sumby, C. J., Capturing Snapshots of Post-Synthetic Metallation Chemistry in Metal–Organic Frameworks. *Nat. Chem.* **2014**, *6*, 906-912.

22. Nguyen, H. G. T.; Schweitzer, N. M.; Chang, C. Y.; Drake, T. L.; So, M. C.; Stair, P. C.; Farha, O. K.; Hupp, J. T.; Nguyen, S. T., Vanadium-Node-Functionalized UiO-66: A Thermally Stable MOF-Supported Catalyst for the Gas-Phase Oxidative Dehydrogenation of Cyclohexene. *ACS Catal.* **2014**, *4*, 2496-2500.

23. Burgun, A.; Coghlan, C. J.; Huang, D. M.; Chen, W.; Horike, S.; Kitagawa, S.; Alvino, J. F.; Metha, G. F.; Sumby, C. J.; Doonan, C. J., Mapping-out Catalytic Processes in a Metal–Organic Framework with Single-Crystal X-Ray Crystallography. *Angew. Chem. Int. Ed.* **2017**, *56*, 8412-8416.

24. Song, Y.; Li, X.; Sun, L.; Wang, L., Metal/Metal Oxide Nanostructures Derived from Metal-Organic Frameworks. *RSC Adv.* **2015**, *5*, 7267-7279.

25. Zhang, L.; Wu, H. B.; Lou, X. W., Metal–Organic-Frameworks-Derived General Formation of Hollow Structures with High Complexity. *J. Am. Chem. Soc.* **2013**, *135*, 10664-10672.

26. Zhao, S.-N.; Song, X.-Z.; Song, S.-Y.; Zhang, H.-j., Highly Efficient Heterogeneous Catalytic Materials Derived from Metal-Organic Framework Supports/Precursors. *Coord. Chem. Rev.* **2017**, *337*, 80-96.

27. Lippi, R., et al., Highly Active Catalyst for CO_2 Methanation Derived from a Metal Organic Framework Template. *J. Mater. Chem. A* **2017**, *5*, 12990-12997.

28. Santos, V. P., et al., Metal Organic Framework-Mediated Synthesis of Highly Active and Stable Fischer-Tropsch Catalysts. *Nat. Commun.* **2015**, *6*, 6451.

29. Wang, P.; Feng, J.; Zhao, Y.; Wang, S.; Liu, J., MOF-Derived Tungstated Zirconia as Strong Solid Acids toward High Catalytic Performance for Acetalization. *ACS Appl. Mater. Interfaces* **2016**, *8*, 23755-23762.

30. Yang, J.; Zhang, F.; Wang, X.; He, D.; Wu, G.; Yang, Q.; Hong, X.; Wu, Y.; Li, Y., Porous Molybdenum Phosphide Nano-Octahedrons Derived from Confined Phosphorization in Uio-66 for Efficient Hydrogen Evolution. *Angew. Chem. Int. Ed.* **2016**, *55*, 12854-12858.

31. Abney, C. W.; Patterson, J. T.; Gilhula, J. C.; Wang, L.; Hensley, D. K.; Chen, J.; Foo, G. S.; Wu, Z.; Dai, S., Controlling Interfacial Properties in Supported Metal Oxide Catalysts through Metal-Organic Framework Templating. *J. Mater. Chem. A* **2017**, *5*, 13565-13572.

32. Wang, H.; Liu, M.; Guo, S.; Wang, Y.; Han, X.; Bai, Y., Efficient Oxidation of O-Xylene over CeO2 Catalyst Prepared from a Ce-MOF Template: The Promotion of K+ Embedding Substitution. *Mol. Catal.* **2017**, *436*, 120-127.

33. Wang, Z.-q.; Ma, Y.-c.; Lin, J.-x., Ruthenium Catalyst Supported on High-Surface-Area Basic ZrO2 for Ammonia Synthesis. *J. Mol. Catal. A: Chem.* **2013**, *378*, 307-313.

34. Rosowski, F.; Hornung, A.; Hinrichsen, O.; Herein, D.; Muhler, M.; Ertl, G., Ruthenium Catalysts for Ammonia Synthesis at High Pressures: Preparation, Characterization, and Power-Law Kinetics. *Appl. Catal., A* **1997**, *151*, 443-460.

35. Lin, B.; Wang, R.; Lin, J.; Ni, J.; Wei, K., Effect of Carbon and Chlorine on the Performance of Carbon-Covered Alumina Supported Ru Catalyst for Ammonia Synthesis. *Catal. Commun.* **2011**, *12*, 1452-1457.

36. Scherrer, P., Bestimmung Der Größe Und Der Inneren Struktur Von Kolloidteilchen Mittels Röntgenstrahlen. *Nachr. Ges. Wiss. Gottingen, Math.-Phys. Kl.* **1918**, *1918*, 98-100.

37. Langford, J. I.; Louer, D.; Scardi, P., Effect of a Crystallite Size Distribution on X-Ray Diffraction Line Profiles and Whole-Powder-Pattern Fitting. *J. Appl. Crystallogr.* **2000**, *33*, 964-974.

38. Zhang, L.; Lin, J.; Ni, J.; Wang, R.; Wei, K., Highly Efficient Ru/Sm2o3-CeO2 Catalyst for Ammonia Synthesis. *Catal. Commun.* **2011**, *15*, 23-26.

39. Honkala, K.; Hellman, A.; Remediakis, I. N.; Logadottir, A.; Carlsson, A.; Dahl, S.; Christensen, C. H.; Nørskov, J. K., Ammonia Synthesis from First-Principles Calculations. *Science* **2005**, *307*, 555-558.

5.8. Supporting information

In situ MOF-templating route to Ru/CeO_2 catalysts for NH_3 synthesis

A. Materials

All chemicals were used as provided by the manufacturer. Chemicals and suppliers: terephthalic acid (H_2BDC) 99% Acros Organics (Great Britain), N-N-dimethylformamide (DMF) 99.8% Merck Pty. Ltd. (Australia), cerium (IV) ammonium nitrate ($Ce(NH_4)_2(NO_3)_6$) 98.5% Sigma Aldrich (Australia), ethanol Merck Pty. Ltd, cerium oxide nanoparticles/nanopowder (99.99% CeO_2, 10 nm) US Nano (USA), magnesium oxide nanoparticles (99+% MgO, 40 nm) US Nano (USA), ruthenium(III) chloride trihydrate ($RuCl_3 \cdot 3H_2O$) 99% PMO Pty Ltd (Australia), triruthenium dodecacarbonyl ($Ru_3(CO)_{12}$) Strem Chemicals (USA), cesium nitrate ($CsNO_3$) Sigma Aldrich (Australia), tetrahydrofuran (THF) Merck (Australia), zirconium chloride ($ZrCL_4$) 99.5% Sigma-Aldrich (Australia), hydrochloric acid (HCl) 32% Merck Pty. Ltd. (Australia), Amomax-10 (wustite with promoters) Süd Chemie AG (Germany), Silicon Carbide (SiC) 99% 300-355 μm Beijing HWRK Chem Co., Ltd. (China). Water was deionized by reverse osmosis. All gases used were supplied by Coregas (Australia) including custom made mixtures: nitrogen (N5); Argon (N5); Helium (N5); Hydrogen (N5); 25vol% carbon dioxide with H_2 balance; 2.5vol% NH_3, 2.5vol%Ar, 15vol% H_2 with N_2 balance.

B. Synthesis

B.1 Ce-UiO-66

Ce-UiO-66 was synthesised according to Lammert et al.[1] The synthesis was scaled-up 9x from the literature report. In a 20 mL glass vial with Teflon-lined screw cap, H_2BDC (0.3186 g, 1918 μmol) was dissolved in DMF (10.8 mL) using a magnetic stirrer bar. An aqueous solution of $Ce(NH_4)_2(NO_3)_6$ (0.5333 mol/L) was prepared and stored. The terephthalic acid solution was placed in an aluminium block on a hot-plate stirrer with temperature control, and was preheated to 100 °C. Next, the Ce salt solution (3.6 mL, 1918 μmol) was added to the terephthalic acid solution, sealed, and vigorously stirred at 100 °C for 15 min. The dark orange solution quickly became lighter and a light yellow precipitate was formed. After 15 min the precipitate was centrifuged (1000 rpm for 10 min) and washed (2x 15 mL with DMF and 4x 15 mL with ethanol). The solid was dried at 80 °C for 24 h. XRD and TGA of the MOF were in agreement with the literature report.

B.2 UiO-66

UiO-66 (or Zr-UiO-66) was synthesised according to Katz et al.[2] as described in details in our previous work.[3] The catalysts derived from the **1%Ru/UiO-66** and **2%Ru/UiO-66** were activated in 75% H_2 and 25% CO_2 at 1 bar and 350 °C for several hours prior to testing for NH_3 synthesis.

B.3 Post-synthetic metalation (PSM)

Post-synthetic metalation (PSM) of the MOFs were carried via incipient wetness impregnation (IWI) with $RuCl_3$. For 1 wt% Ru(III) on Ce-UiO-66, 100 mg of Ce-UiO-66 was placed in an 8 mL glass vial and 137 μL of $RuCl_3$ aqueous solution (0.143 mol/L) was slowly added with a pipette. The sample was mixed with a spatula to homogenize the slurry formed. The sample was dried at 100 °C for 24 h to yield **1% Ru/Ce-UiO-66**. To achieve different loadings, $RuCl_3$ solutions with the appropriate concentrations were prepared. Among the controls, $RuCl_3$ on pre-made CeO_2 nanoparticles was prepared in the same fashion, these samples are referred as **x%Ru/CeO$_2$**.

B.4 2%Ru-Cs/MgO

2%Ru-Cs/MgO was synthesised according to the procedure reported by Aika et al.[4]

C. Thermogravimetric analysis

Samples were loaded into Al_2O_3 crucibles and evaluated using a Mettler Toledo TGA 2. **Ce-UiO-66**, as synthesized, was heated to 600 °C in N_2 atmosphere to analyse its thermal stability. The sample was heated to 600 °C at 10 °C/min under N_2 purge gas at 30 mL/min. The sample was allowed to equilibrate at 25 °C in N_2 before the analysis, this section is not shown in the thermogram, however a significant loss of solvent (~40wt%) during this period was observed.

Samples of the catalysts derived from **Ce-UiO-66** and **1%Ru/Ce-UiO-66** were heated to 800 °C in air to evaluate the catalysts carbon content. These samples were heated to 800 °C at 10 °C/min under air purge gas at 40 mL/min.

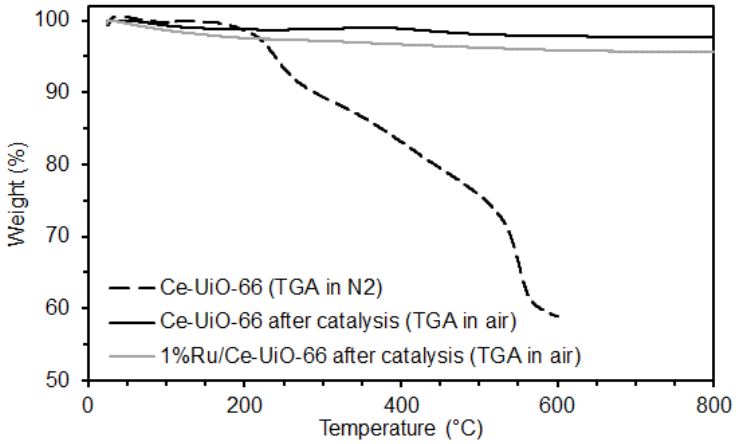

Figure S1: Thermogravimetric analysis of Ce-UiO-66, and catalysts derived from Ce-UiO-66 and 1%Ru/Ce-UiO-66. The synthesised Ce-UiO-66 displayed good thermal stability, but decomposes losing a substantial amount of mass. The catalysts derived from Ce-UiO-66 and 1%Ru/Ce-UiO-66 displayed mass loss of less than 5 wt%, indicating that the derived catalysts are mostly free of carbon.

D. Catalyst testing for NH_3 synthesis

The catalysts were evaluated for NH_3 synthesis using an Avantium Flowrence multi-channel(48) microreactor testing rig described in details in our previous work.[3] About 20 mg of each sample was mixed with 50 mg of SiC and loaded into fixed-bed microreactors. Catalysis experiments used stoichiometric ratio of reactants (H_2:N_2=3:1) and Ar as tracer gas. The gas feed flow was 2.9 mL/min per reactor (H_2, 1.875 mL/min; N_2, 0.625 mL/min; Ar, 0.417 mL/min) in addition, by-passing diluent gas (N_2, 13.33 mL/min per reactor) was mixed with the reactor effluent gases before GC analysis (**Figure S2**).

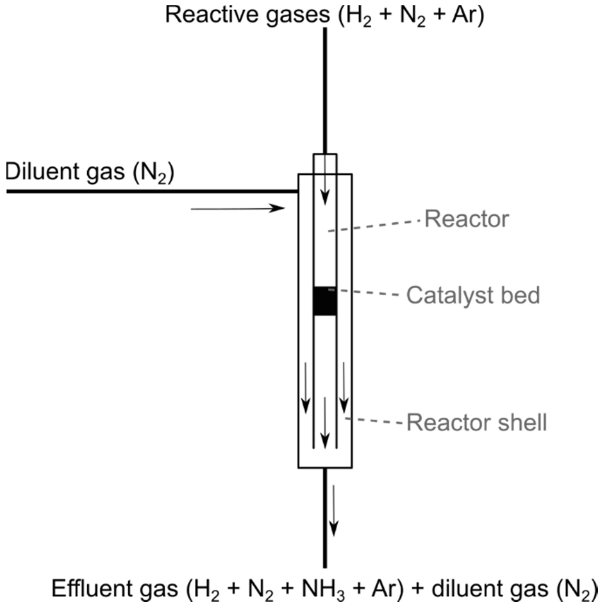

Figure S2: Scheme of an individual reactor. The multi-channel reactor contains 48 reactors in 48 individual reactor shells. A stream of N_2 is used to dilute the reactor effluent gases prior to analysis. Consequently, the total effluent gas (Reactants, products, tracer gas and diluent gas) were analyzed using an online gas chromatograph (GC).

In a first screening (Figure 3A), the MOF-based catalysts were tested alongside a commercially available Fe-catalyst (Amomax-10); therefore all of the samples were activated and tested under the same conditions as required for the Fe-based catalyst. Activation was carried under a pure H_2 stream at 475 °C and 1 bar until water was not detected in the effluent stream and testing was carried at 475 °C and 160 bar.

In a second experiment (Figure 3B), different loadings of Ru on Ce-UiO-66 and on CeO_2 were compared to a Ru-based high performing catalyst reported by Aika et al.[4] Since operation at lower temperature and pressure are some of the advantages of Ru catalysts, the screening was performed at temperatures from 200 to 400 °C and pressures of 10, 30 and 50 bar. The parallel testing of all these samples started with an activation step with the reactive gas mixture at 400 °C and 10 bar for 7 h. Next, the activated catalysts were evaluated for NH_3 synthesis. First, at 10 bar at different temperatures: 200, 250, 300, 350 and 400 °C, then temperature was dropped to 200 °C and the pressure was increased to 30 bar, catalysts were tested at the same temperatures. Lastly, pressure was increased to 50 bar and catalysts were submitted to the same temperatures. Upon reaching each set temperature and pressure, the system was allowed to stabilize for 15 min prior to the start of effluent analysis. The reactors, which were distributed randomly within the rig, were sampled 3 times at each condition step. At all times the catalysts were under constant flow of reactive gases (H_2:N_2=3:1).

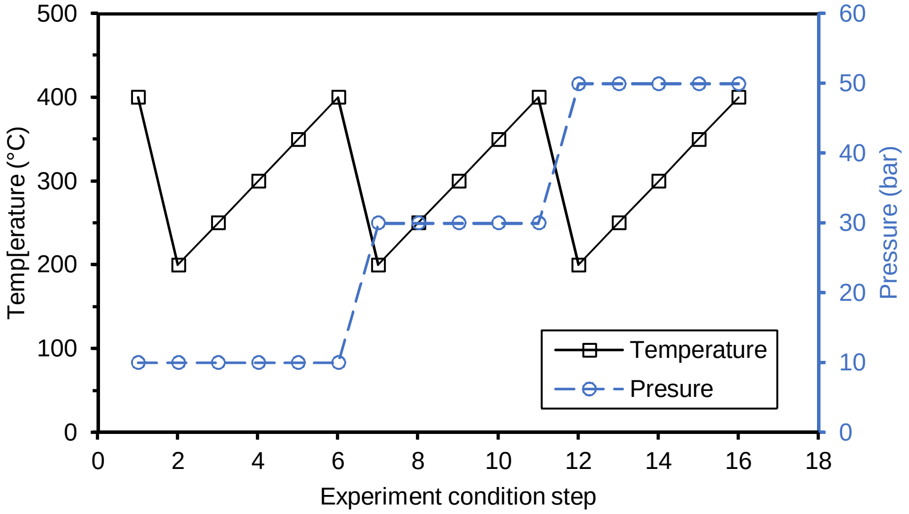

Figure S3: Experimental conditions for the second screening (Figure 3B). The 1st conditioning step shows the conditions for the activation step and the following steps the conditions during the testing. For all samples, including the positive control NH_3 was only detected at 400 °C.

D.1 Quantification of NH_3 in the gas effluent

According to the calibration curve displayed in **Figure S4**, the volumetric fraction of NH3 in the gas sample can be correlated to the integrated area using Eq. 1

$$x_{NH_3}(\%) = 1.1114 \cdot 10^{-12} \cdot {A_{NH_3}}^2 + 1.7609 \cdot 10^{-6} \cdot A_{NH_3} \qquad \text{(Eq. 1)}$$

This volumetric fraction can be correlated to the effluent flow composition:

$$\dot{V}_{feed\ total} = \dot{V}_{N_2\ in} + \dot{V}_{H_2\ in} + \dot{V}_{N_2\ diluent} \qquad \text{(Eq. 2)}$$

$$\dot{V}_{effluent\ total} = \dot{V}_{N_2\ out} + \dot{V}_{H_2\ out} + \dot{V}_{NH_3\ produced} + \dot{V}_{N_2\ diluent} \qquad \text{(Eq. 3)}$$

Since the maximum concentration obtained for ammonia was below 0.4 vol% for $\dot{V}_{effluent\ total}$, the total gas flow is approximately constant, therefore:

$$\dot{V}_{NH_3\ produced} \cong \dot{V}_{feed\ total} \cdot x_{NH_3} \qquad \text{(Eq. 4)}$$

Considering density of NH3 (ρ_{NH_3}) as 771.3 g/m^3 at 0 °C and 1.013 bar, we obtained the mass of NH3 produced per unit of time:

$$\dot{m}_{NH_3\ produced} = \dot{V}_{NH_3\ produced} \cdot \rho_{NH_3} \qquad \text{(Eq. 5)}$$

Considering the molar mass of NH3 (M_{NH_3}) as 17.031 g/mol, we were able to determine the number of mols of NH3 produced per unit of time:

$$\dot{n}_{NH_3\ produced} = \dot{m}_{NH_3\ produced} \cdot M_{NH_3} \qquad \text{(Eq. 6)}$$

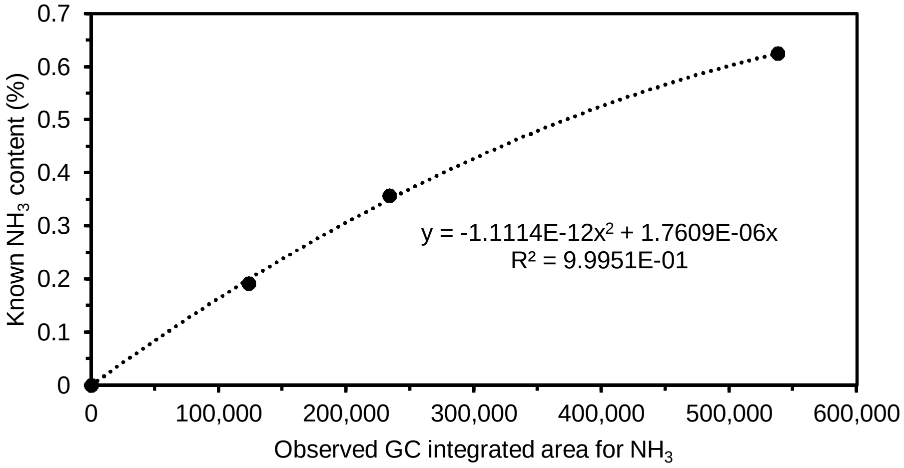

Figure S4: Gas chromatograph calibration curve for NH3. During the catalysis experiment the integrated area results for NH3 were in the range of 0 to 270,000.

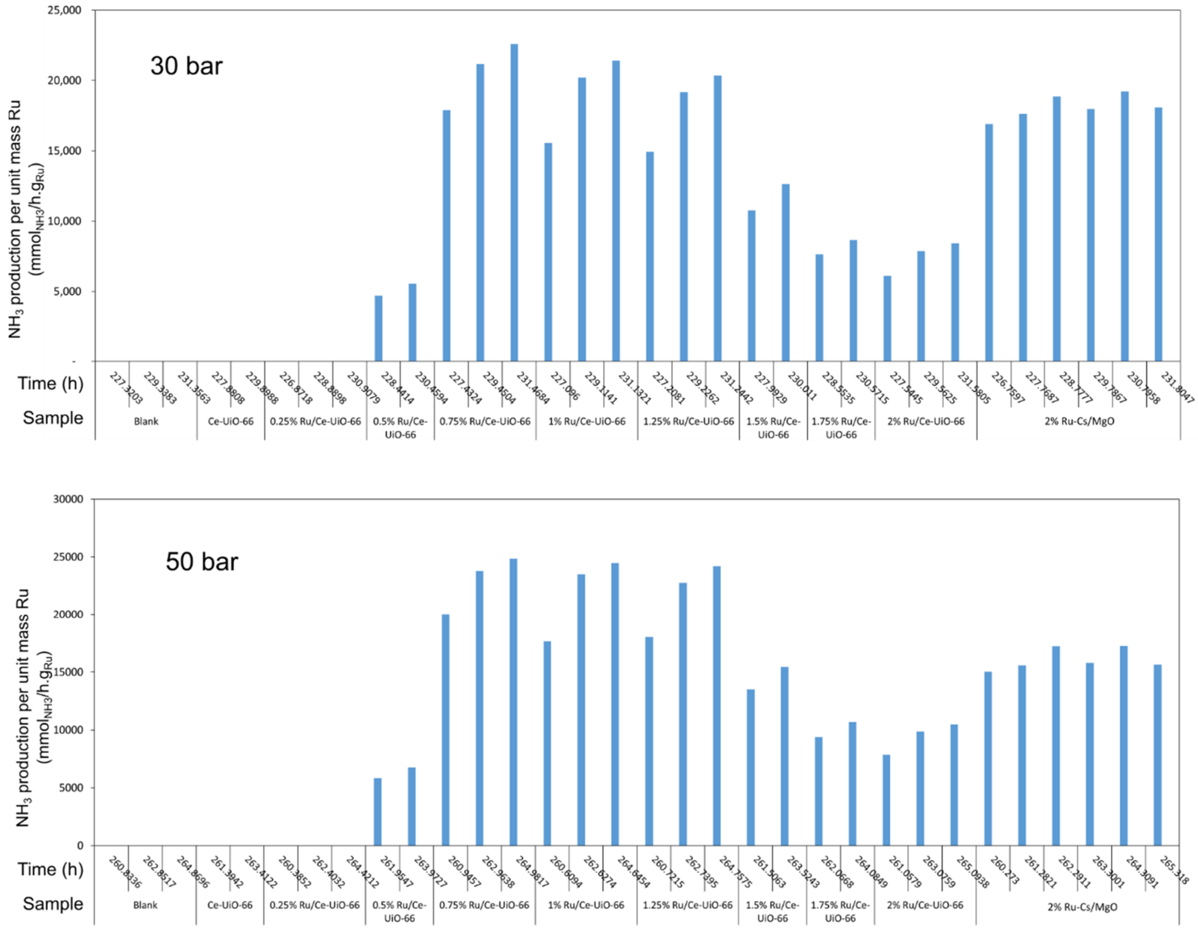

Figure S5: NH_3 production results for the MTcat derived from x% Ru/Ce-UiO-66, as indicated, at different time points. Data presented in Fig. 3B is the average of these values. Sample 2% Ru-Cs/MgO was tested in replicate.

E. Powder X-ray diffraction

XRD data was collected using different instruments as described below. In order to compare samples analysed at different wavelengths in Figure 2, the data was transformed to the same energy. The formula used is also described below.

E.1 Laboratory source XRD

Samples were back-loaded into sample holders prior to the collection of XRD traces to minimize texture. A Bruker D8 Advance X-ray Diffractometer operating under CuKα radiation (40kV, 40mA) or CoKα radiation (35kV, 45mA) equipped with a LynxEye detector was employed to obtain the XRD patterns. Samples were scanned over the 2θ range 3.5° to 130°

with a step size of 0.02° and acquisition time of 0.4 second per step. 173/192 of the sensor strips on the LynxEye detector were used, to give an equivalent count time of 69.2 seconds per step.

In Figure 2, the radiation used to analyse the samples using the lab source diffractometers are described below:

1) “UiO-66” Cu radiation Kα = 8.046 keV
2) “Ce-UiO-66” Co radiation Kα = 6.931 keV

E.2 Synchrotron source XRD

XRD experiments carried at the Powder Diffraction Beamline at the Australian Synchrotron used a Mythen microstrip detector[5] for data collection. The samples were loaded into special glass 0.7 mm wide capillaries (The Charles Supper Company, USA). The capillary was kept rotating during acquisition. The beam energy during data acquisition was 16.0172 keV with a current of 200 mA.

In Figure 2, the beam energy used for the samples analysed in synchrotron source are described below:

3) “MTcat from Ce-UiO-66” synchrotron radiation E = 16.0172 keV
4) “1% Ru/Ce-UiO-66” synchrotron radiation E = 16.0172 keV
5) “MTcat from 1% Ru/Ce-UiO-66” synchrotron radiation E = 16.0172 keV

For comparison, the diffractograms displayed in Figure 2 collected using lab source were plotted for E = 16.0172 keV using Eq. 12:

Planck–Einstein relation

$$E = h\nu \Rightarrow E = h\frac{c}{\lambda} \tag{Eq. 7}$$

$$\left| \begin{array}{l} E_1 = h\frac{c}{\lambda_1} \\ E_2 = h\frac{c}{\lambda_2} \end{array} \right. \Rightarrow E_1\lambda_1 = E_2\lambda_2 \Rightarrow \frac{E_1}{E_2} = \frac{\lambda_2}{\lambda_1} \tag{Eq. 8}$$

Bragg's law

$$n\lambda = 2d \cdot sin\theta \tag{Eq. 9}$$

$$d = \frac{n\lambda}{2 \cdot sin\theta} \Rightarrow d_1 = d_2 \Rightarrow \frac{n\lambda_1}{2 \cdot sin\theta_1} = \frac{n\lambda_2}{2 \cdot sin\theta_2} \Rightarrow \frac{\lambda_2}{\lambda_1} = \frac{sin(\theta_2)}{sin(\theta_1)} \tag{Eq. 10}$$

Combining Eq. 8 and 10

$$\frac{E_1}{E_2} = \frac{\lambda_2}{\lambda_1} = \frac{sin(\theta_2)}{sin(\theta_1)} \Rightarrow sin\left(\frac{2\theta_2}{2}\right) = sin\left(\frac{2\theta_1}{2}\right) \cdot \frac{E_1}{E_2} \tag{Eq. 11}$$

$$2\theta_2 = sin^{-1}\left(sin\left(\frac{2\theta_1}{2}\right) \cdot \frac{E_1}{E_2}\right) \cdot 2 \tag{Eq. 12}$$

E.3 Rietveld refinement

The quantitative phase and microstructure analysis of the powder diffraction data was performed using a whole-pattern, Rietveld based approach. The Rietveld method involves producing a model which is used to generate a calculated XRD pattern. The model includes parameters such as the crystal structure model for each phase, pattern background, wavelength, sample and instrument aberrations, etc. The calculated pattern is then compared with the observed data and the difference between observed and calculated is minimised through a least squares method by adjusting selected parameters in the model. These calculations were performed using the software TOPAS V5[6].

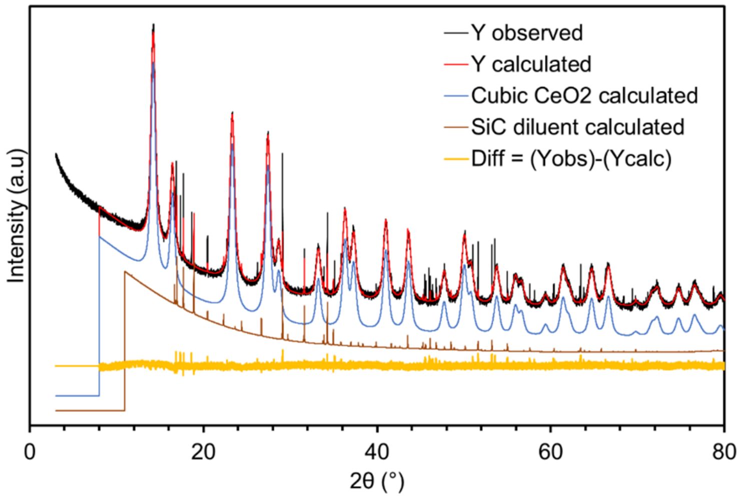

Figure S6: Observed diffractogram (Y observed), complete diffractogram calculated via Rietveld Refinement (Y calculated), CeO_2 contribution to calculated diffractogram, SiC (catalyst diluent) contribution to the calculated diffractogram, and difference between observed and calculated data.

Table S1: Results from Rietveld refinement displayed in the figure above.

Phase name	CeO_2
R-Bragg	1.607
Space group	Fm-3m
Wt% - Rietveld	96.46
Double-Voigt approach	
Cry size Lorentzian	12.3
Cry size Gaussian	15.3
Lvol-IB (nm)	6.006
Lattice parameters a (Å)	5.415132
Rwp	7.235

G. Electron Microscopy

TEM/STEM investigation was performed using a probe-corrected JEOL ARM200F (JEOL, USA) equipped with a cold field emission gun operating at 200 kV. High-angle annular dark-field (HAADF) images were acquired with inner and outer collection angles of 68 and 280 mrad, respectively, while bright field images were acquired with a maximum collection angle of 17 mrad. All images were acquired with a 20 ms dwell time and convergence angle of 25 mrad, resulting in a probe size about 0.1 nm and a current of 40 pA. The Energy-dispersive X-ray Spectroscopy (EDS) maps were acquired with a probe current of 155 uA.

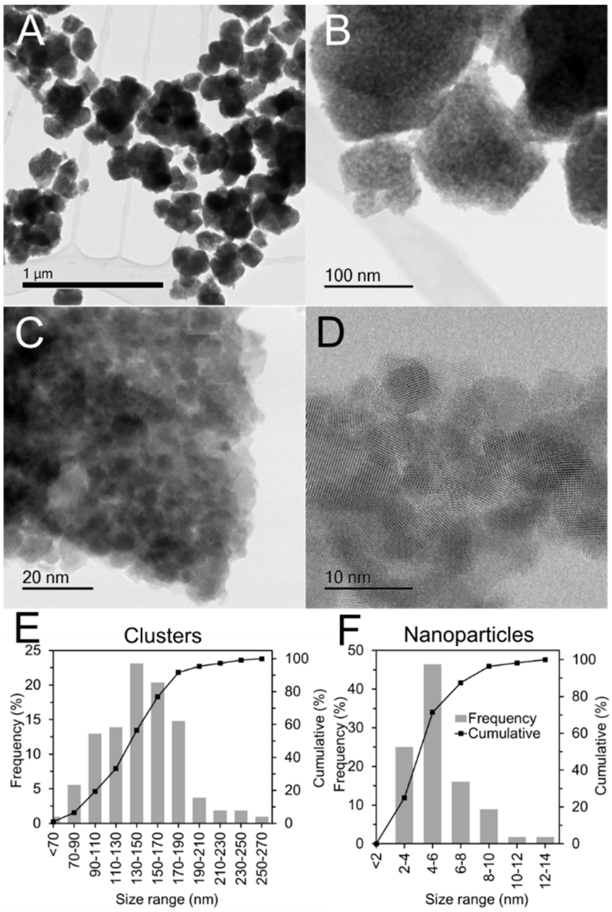

Figure S7: A-D) High resolution TEM of the catalyst templated by 1%Ru/Ce-UiO-66 at different magnifications. It is possible to observe that the catalyst is composed of clusters of nanoparticles (A and B). Within these clusters, nanocrystals can be observed (C and D). E) Histogram of cluster sizes and F) Histogram of nanocrystal sizes.

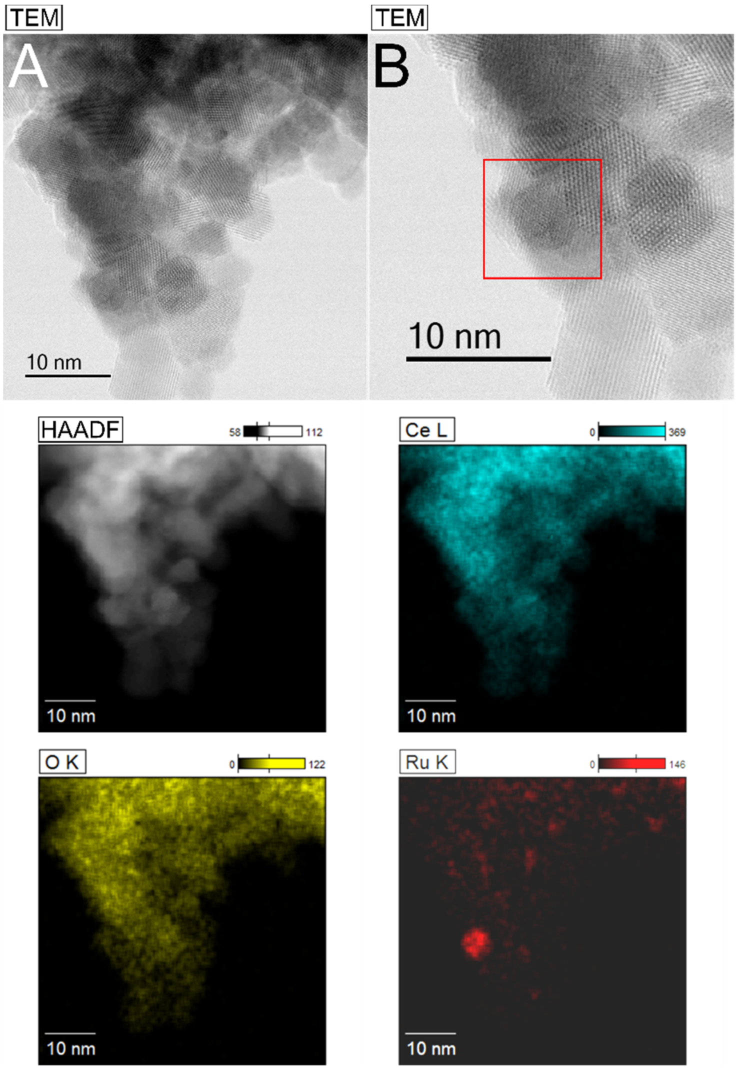

Figure S8: TEM (A and B), HAADF (high-angle annular dark-field) and EDS (Energy dispersive spectroscopy) mapping for the MOF-templated catalyst derived from 1%Ru/Ce-UiO-66. B) Enlargement of part of image A, where an apparently amorphous Ru^0 nanoparticle (5 nm) is highlighted by the red square.

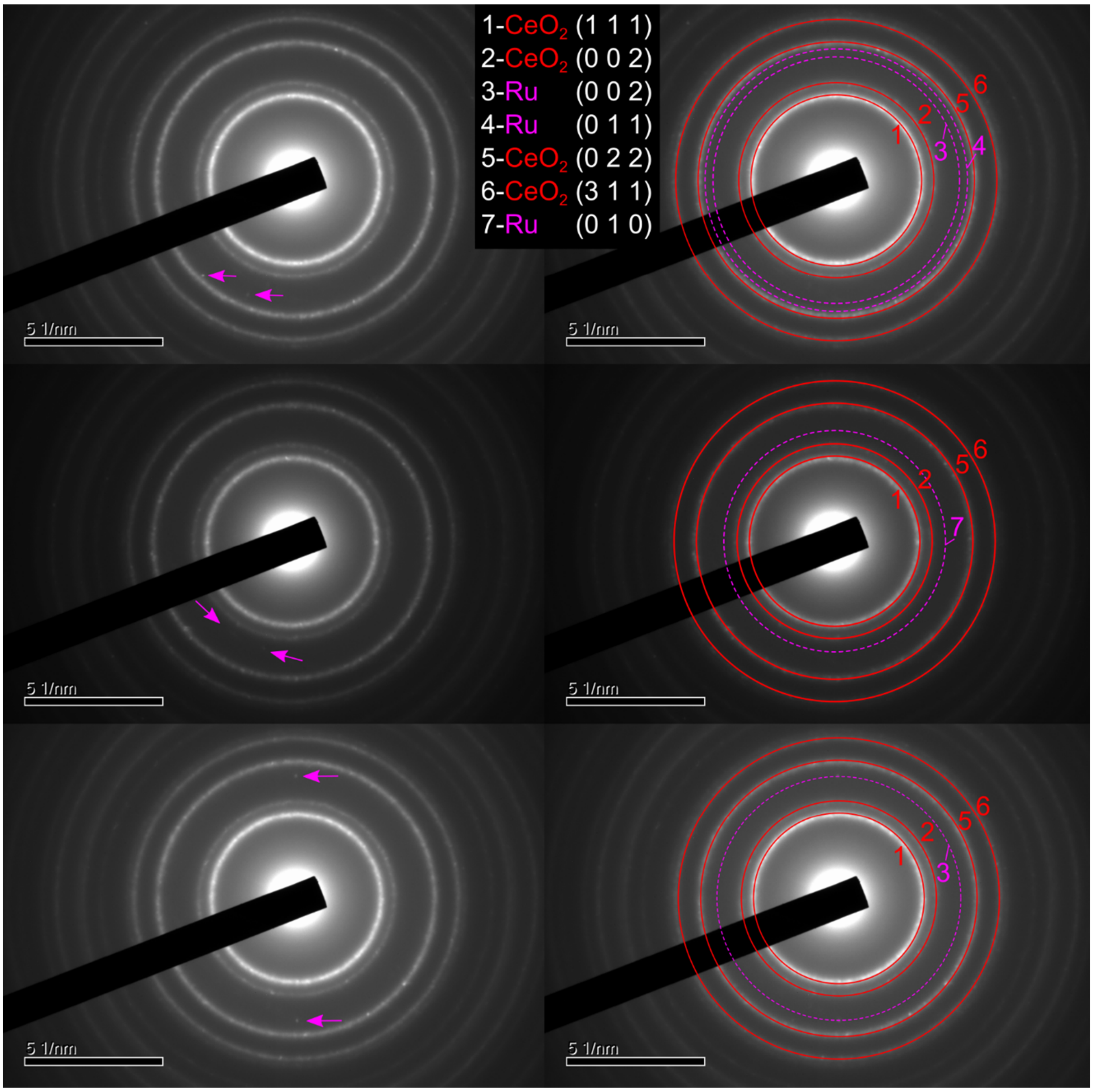

Figure S9: Electron diffraction imaged for MOF-templated catalyst derived from **1% Ru/Ce-UiO-66** (left) and images superimposed by rings indicating the phases present (right). As the CeO_2 phase was confirmed by XRD, this phase was used as reference for the precise measurement of the d-spacing. As Ru was in much lower abundance than CeO_2, and there is evidence that some of the Ru nanoparticles are amorphous, the dots indicated by the pink arrows were used to identify the Ru phase present. The phases considered were: cubic Ru^0, tetragonal RuO_2 and hexagonal Ru^0. The distances measured only correlated to the hexagonal Ru^0. Therefore, we could conclude that the templated catalyst contained Ru^0/CeO_2. This sample was free of SiC.

Table S2: Space groups and d-spacing observed in the electron diffraction images (Figure S9).

Ring	Colour	Phase	Space Group	h	k	l	d (Å)
1	red	CeO_2	Fm-3m	1	1	1	3.13
2	red	CeO_2	Fm-3m	0	0	2	2.71
3	pink	Ru	P63/mmc	0	0	2	2.14
4	pink	Ru	P63/mmc	0	1	1	2.05
5	red	CeO_2	Fm-3m	0	2	2	1.91
6	red	CeO_2	Fm-3m	3	1	1	1.63
7	pink	Ru	P63/mmc	0	1	0	2.34

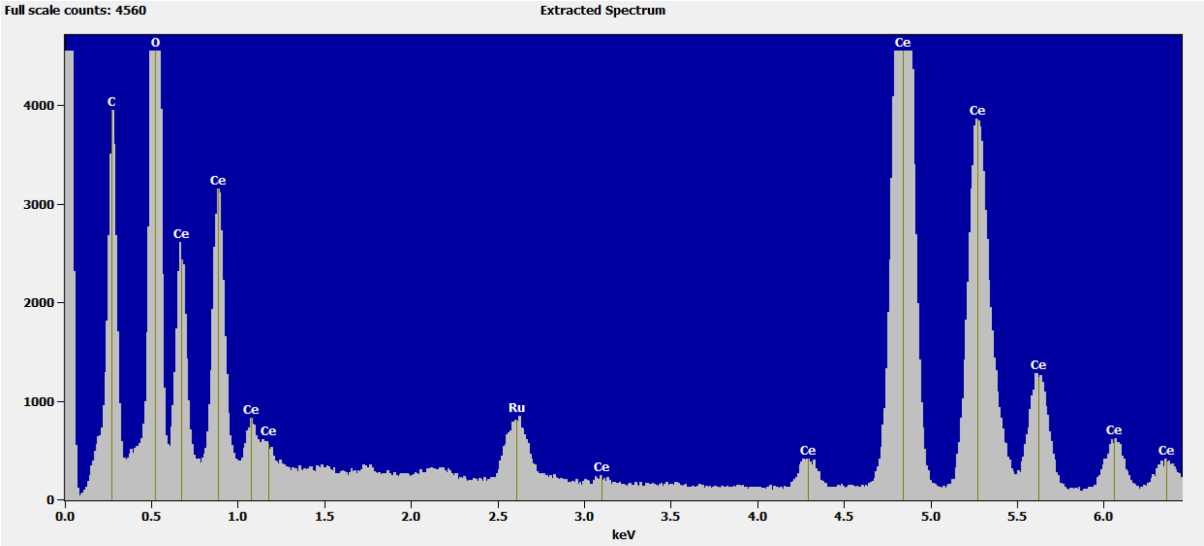

Figure S10: EDS spectrum confirming the presence of Ru.

I. References

1. Lammert, M.; Wharmby, M. T.; Smolders, S.; Bueken, B.; Lieb, A.; Lomachenko, K. A.; Vos, D. D.; Stock, N., Cerium-Based Metal Organic Frameworks with UiO-66 Architecture: Synthesis, Properties and Redox Catalytic Activity. Chem. Commun. 2015, 51, 12578-12581.

2. Katz, M. J.; Brown, Z. J.; Colón, Y. J.; Siu, P. W.; Scheidt, K. a.; Snurr, R. Q.; Hupp, J. T.; Farha, O. K., A Facile Synthesis of UiO-66, UiO-67 and Their Derivatives. Chem. Commun. 2013, 49, 9449-51.

3. Lippi, R., et al., Highly Active Catalyst for CO2 Methanation Derived from a Metal Organic Framework Template. J. Mater. Chem. A 2017, 5, 12990-12997.

4. Aika, K.-i.; Takano, T.; Murata, S., Preparation and Characterization of Chlorine-Free Ruthenium Catalysts and the Promoter Effect in Ammonia Synthesis. J. Catal. 1992, 136, 126-140.

5. Schmitt, B.; Bronnimann, C.; Eikenberry, E. F.; Gozzo, F.; Hormann, C.; Horisberger, R.; Patterson, B., Mythen Detector System. Nucl. Instrum. Methods Phys. Res., Sect. A 2003, 501, 267-272.

6. Topas V5: General Profile and Structure Analysis Software for Powder Diffraction Data, Bruker AXS GmbH: Karlsruhe, Germany, 2012.

Chapter 6

6. Conclusions

This thesis explored the use of metal-organic frameworks as templates for highly active gas phase heterogeneous catalysts. Synthesis of inorganic materials mediated by metal-organic frameworks has attracted interest from applied fields such as, nanomaterials and catalysts where controlled synthesis methods have been a long-standing challenge.[1-5] Chapter 1 identified opportunities and challenges for MOF-derived materials and presented the research questions underlying this thesis. These were focused on the use of reducing atmospheres in the synthesis of MOF-templated catalysts for gas phase reactions and investigating the MOF-templating mechanism. The following sections discuss the contribution, limitations and future directions identified in this work.

6.1. MOF-templating in H_2

MOF-templated materials are often obtained via thermal treatment of the parent MOF in an inert or oxidising atmosphere. This generally leads to the synthesis of metal/metal-oxide nanoparticles embedded in carbon or to metal-oxide nanoparticles, respectively. In contrast, MOF-templating in H_2 has not been largely explored, with only a few examples of thermal treatment of MOFs in a reducing atmosphere.[6-7] High temperature reduction is a common treatment for the synthesis or activation of catalysts, as it leads to metallic species. Thus, MOF-templating in H_2 had been hypothesised to assist the formation of metal nanoparticles not achieved by pyrolysis.

Chapters 2 and 3 explored the *in situ* MOF-templating of catalysts for CO_2 hydrogenation, *i.e.* 80% H_2 and 20% CO_2 at 350 °C. In Chapter 2, a Mn-MOF metalated with rhodium was used as template for the synthesis of Rh^0 nanoparticles of controlled size; these nanoparticles were arranged as a porous mesh surrounding $MnCO_3$ and MnO crystals derived from the MOF nodes (Figure 1). In addition, the effect of a low H_2 concentration (5% H_2/Ar) was also evaluated and the synthesis of Rh^0 nanoparticles evenly distributed in a partially decomposed framework was demonstrated. The successful synthesis of Rh^0 nanoparticles via MOF-templating in H_2 provides an alternative route to prepare Rh^0 catalysts and demonstrates the use of MOF-templating to synthesise metallic species with controlled morphology.

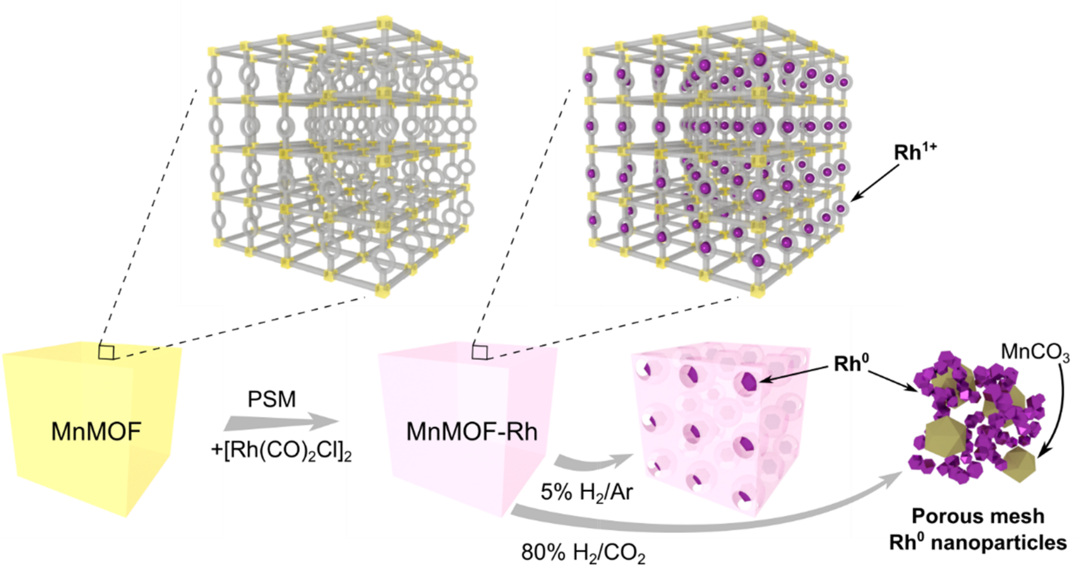

Figure 1: Illustration of MnMOF and post synthetically metalated MnMOF with Rh (MnMOF-Rh) and derived products from templating in H_2-containing atmosphere.

Furthermore, in Chapter 3, the synthesis of Ru^0 supported on ZrO_2 was achieved using a $RuCl_3$ impregnated Zr-MOF as a template (Figure 2). The templating process occurred under CO_2 methanation conditions (80% H_2 and 20% CO_2 at 350 °C), thus not requiring an additional step for the activation of the catalyst. Once activated, the catalyst displayed remarkable stability, H_2 conversion, and selectivity to CH_4 for over 160 h and could be exposed to air in between runs without loss in activity.

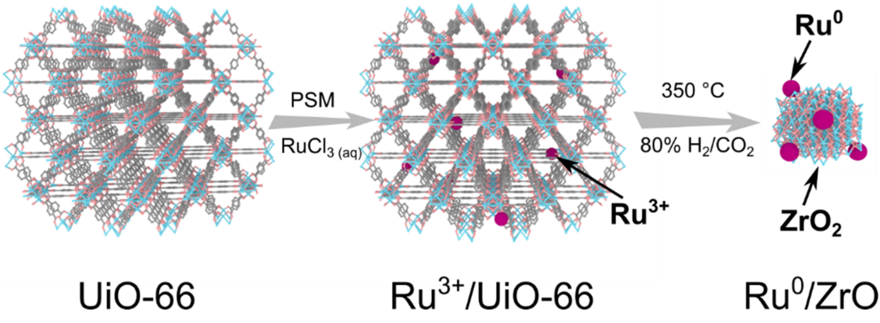

Figure 2: Illustration of UiO-66 and Ru^{3+}-impregnated UiO-66 and *in situ* MOF-templated catalyst, Ru^0/ZrO_2.

Chapter 5 presented the templating of MOF-derived Ru^0/CeO_2 catalysts in 75% H_2 and 25% N_2 (Figure 3). During the course of this research project we speculated that CO_2 played a critical role in the templating of the active catalyst, but the successful synthesis of this catalyst under NH_3 synthesis conditions (reducing environment and high pressure regime) confirmed H_2 as the main agent of the linker decomposition leading to MOF-templating this class of metals supported on metal-oxides. Attempts to activate catalysts in 5% H_2 were discussed in Chapters 2 and 4, in both cases, the low concentration of H_2 led to the production of materials that differ in composition and morphology than their counterparts templated in higher concentrations of H_2. The combined results demonstrate that the H_2 concentration is an important parameter for the complete decomposition of the framework.

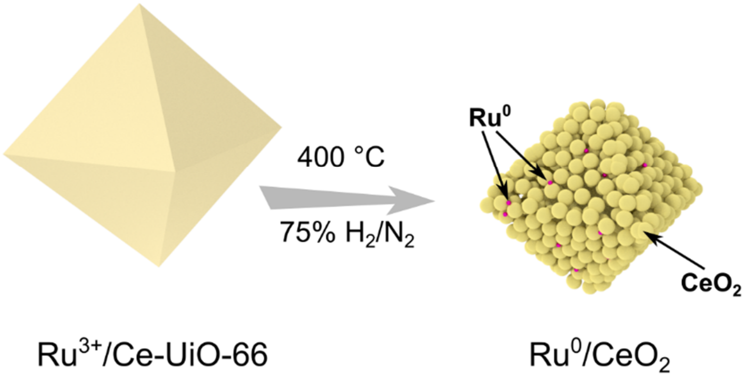

Figure 3: Illustration of Ru^{3+}-impregnated Ce-UiO-66 and *in situ* MOF-templated catalyst, Ru^0/CeO_2.

6.2. MOF-templated catalysts for gas phase reactions

MOFs and MOF-derived catalysts have been largely applied for liquid phase reactions.[2] This thesis demonstrated the use of three different MOFs for the synthesis of catalysts for gas phase reactions. The post-synthetically metalated MOFs (Mn-MOF metalated with Rh, Ru-impregnated Zr-MOF and Ru-impregnated Ce-MOF) acted as sacrificial templates for the synthesis of Rh^0, Ru^0/ZrO_2 and Ru^0/CeO_2 catalysts. Among these catalysts, MOF-derived Ru^0/ZrO_2 was shown in Chapter 3 to be a highly active catalyst for CO_2 methanation. This high activity resulted from the controlled morphology and Ru distribution derived from the MOF-templating route, as demonstrated by the significantly lower catalytic performance of samples with the equivalent chemical composition. Thus Chapter 3 not only exemplified MOF-templating as a synthetic route for metal supported on metal oxide catalysts, but also showed that this route was critical for the synthesis of a highly active and selective catalyst.

As shown in Chapter 2, the catalyst derived from Mn-MOF metalated with Rh, a mesh of Rh^0 nanoparticles, displayed mild activity for CO_2 hydrogenation. In spite of its catalytic performance, its final structure has potential to be applied for other reactions. The catalysts activated *in situ* were characterised after 90 h under continuous reaction conditions demonstrating good stability against agglomeration. Other methods to synthesise Rh^0 nanoparticles use stabilisers or supports to avoid agglomeration; [8-9] however, stabilisers can affect the catalytic activity of these catalysts.[8] The unusual structure of this MOF-templated catalyst may potentially find application in other reactions.

Lastly, Chapter 4 and Chapter 5 reported the use of MOF-templated Ru^0/CeO_2 for CO_2 methanation and NH_3 synthesis, respectively. As presented in chapter 4, this catalyst displayed high activity for CO_2 methanation at 350 °C which was comparable to MOF-templated Ru^0/ZrO_2. However, at lower temperature, 250 °C, Ru^0/CeO_2 showed significantly inferior catalytic performance than its Zr counterpart. Chapter 5, focused on MOF-templated catalysts for ammonia synthesis and demonstrated Ru^0/CeO_2 as a highly active catalyst for this gas phase reaction, even when compared to MOF-templated Ru^0/ZrO_2 and to a benchmark catalyst. In addition, catalysts prepared with $RuCl_3$ directly impregnated on CeO_2 nanoparticles displayed inferior performance then the MOF-templated analogue. These results further demonstrate the relevance of MOFs in the synthesis of catalysts for gas phase reactions.

6.3. Templating mechanism

The lack of understanding of the mechanism of MOF-templating has been identified as a limitation for improving the control over the synthesis of these materials.[1-5, 10-12] MOFs have a high degree of structural variability owing to the expansive library of organic and inorganic components readily available. Therefore, understanding the transformation from MOF to functional material and the role of each component may lead to more rational design of MOF-templates.

As reported in Chapter 2, the MOF-templating mechanism was studied using a Mn-based MOF and its Rh-metalated version, with the MOFs subjected to heat treatment under different concentrations of H_2. The short-term exposure of the MOFs to 5% H_2 at 350 °C yielded a partially decomposed MOF, whereas long-term exposure to 80% H_2 at 350 °C led to complete decomposition of the MOF and the templating of the Rh^0 nanoparticle mesh. The comparison of these two MOFs at different stages of templating process revealed that the different compositions substantially affected the final materials; as an example, rhodium was identified to promote the removal of the organic linkers. The knowledge provided by this study was valuable for the selection and evaluation of the other MOF-templates investigated during this project.

As discussed in Chapter 3, MOF-templating of Ru^0/ZrO_2 was studied at different temperatures, revealing that temperature affects the removal of the organic linkers. At temperatures below the threshold for the removal of the organic linkers, the derived catalysts showed poor crystallinity and catalytic performance. This indicates that removal of the organic linkers is a relevant step for the templating of the active catalyst. The final catalyst was observed to have an excellent distribution of Ru on the ZrO_2 particles. DFT calculations indicated the possibility of Ru binding to inorganic nodes of UiO-66 where an organic linker is missing. As missing linker defects are commonly found in UiO-66, we hypothesise that this interaction of Ru with the node may be key for the homogeneous dispersion of Ru in the template MOF. However, experimental observation is necessary to confirm this phenomenon.

The templating of the Ru^0/ZrO_2 catalyst was further examined in an *in operando* PXRD experiment described in Chapter 4. This experiment unveiled the structural transition during MOF-templating:

1. Initial crystalline state of Ru^{3+}/UiO-66
2. Collapse of the crystalline structure and loss of organic fragments at ≈330 °C;

3. resulting amorphous phase occurred over a wide temperature range for an extensive time period;
4. at increasing temperatures the amorphous phase crystallised into nanosized tetragonal ZrO_2 alongside remnants of the amorphous phase;
5. at even higher temperatures, the amorphous phase was completely consumed and monoclinic ZrO_2 was found to form.

Reflections from Ru crystalline phases were not evident in the PXRD patterns and high-resolution TEM demonstrated the presence of single crystal and amorphous Ru^0 nanoparticles. Although the templating mechanism is not yet fully elucidated, these experiments provide interesting insights to refine the current hypothesis. The controlled size of the ZrO_2 support, may be a consequence of the inorganic nodes of UiO-66 acting as regularly spaced seeds for the crystallization of ZrO_2.

Furthermore, Chapter 4 reported an evaluation of the effect of different MOF components on the structure and catalytic performance of MOF-templated CO_2 methanation catalysts. The study of the loading of Ru in UiO-66 revealed that Ru, even at small quantities, promoted the crystallization of ZrO_2. In addition, UiO-66 impregnated with Zn, Fe, Co or Cu did not promote crystallization of ZrO_2, indicating that the catalytic properties of Ru may facilitate the removal of the organic linkers as observed in the case of Rh in Chapter 2. The effect of the linker in the MOF templating mechanism was investigated by the use of Zr-MOFs with various linkers. Contrary to our expectations, the crystallinity of the MOFs did not dictate the quality of the catalyst, with amorphous MOFs yielding highly active catalysts. In addition, the use of a longer linker did not significantly affect the size of the ZrO_2 nanocrystals. On the other hand, some linkers inhibited the catalytic activity on the templated catalysts, demonstrating the importance of the selection of an appropriate linker in MOF-templating.

6.4. Future directions

This thesis focused on the synthesis of Rh^0 and Ru^0 nanoparticles for application as catalysts. One limitation of the approach presented is that it is highly dependent on the metal. For example, Chapter 4, presented the evaluation of different metals impregnated in UiO-66, including Fe, Zn, Cu and Co, subjected to the same conditions used for the templating of Ru^0/ZrO_2. Under those conditions, no sample displayed formation of ZrO_2, instead, they presented a phase similar to the material derived from pristine UiO-66; this behaviour is attributed to differences in the hydrogenolysis properties of the different metals.[13] Therefore, conditions may have to be optimised for different metals, including an increase in temperature and loading of metal. The hypothesis that Ru is dispersed through the framework by interacting with the inorganic node should be experimentally investigated. In addition, this type of interaction should be investigated for different metals, and the distribution of other metals though the framework may have to be optimised by post-synthetic metalation of the linkers. With regards to the MOF-templated Rh^0 nanoparticles, the investigation of other Mn-MOFs may be of interest for the evaluation of the role of linkers, coordination groups and even Mn node structure in the templating of the final composite.

The MOF-derived catalysts evaluated, particularly MOF-templated Ru^0/ZrO_2 and Ru^0/CeO_2, prove how gas phase reactions can benefit from MOF-mediated synthesis of catalysts. Interestingly, the chemical composition of the MOF-templated catalysts presented are simpler in composition than most of their counterparts:[14-15] for example, catalyst promoters were not part of the scope of this research. Future directions in this area may include the evaluation of more complex compositions, including the addition of promoters and metal oxide dopants for example. Furthermore, other well-stablished catalyst compositions for gas phase reactions may benefit from the morphology and elemental distribution control provided by MOF-templating to further enhance their catalytic performance. Development of a protocol to apply MOF-mediated synthesis for catalysts of pre-defined composition is proposed as a way forward in the field of MOF-templated catalysts.

Suggestions for future directions on the investigation of the MOF-templating mechanism for Ru^0/ZrO_2 catalysts include evaluation of the ZrO_2 phase's contribution to catalytic activity by a follow-up *in operando* PXRD experiment. This would specifically involve starting with the MOF-templating in pure hydrogen or in 75% H_2/Ar, to observe phase formation and subsequently switching gas feed to the synthesis gas (80%H_2 and 20%CO_2) in order to identify the isolated effects of H_2 in the templating phase transformation and the effect of water on the formation of monoclinic ZrO_2. In addition, temperature calibration with the appropriate gas flow and improved insulation of effluent gas line (whilst allowing for capillary oscillation) to mass spectrometer would be necessary. The amorphous phase obtained after the MOF collapse can be, in the future, investigated by scanning and transmission electron microscopy (STEM), energy-dispersive X-ray spectroscopy (EDS), and *in situ* or *in operando* pair distribution function (PDF) analysis. Lastly, investigation of the CO_2 methanation mechanism on this specific catalyst using, for example, infra-red techniques is recommended.

6.5. References

1. Song, Y.; Li, X.; Sun, L.; Wang, L., Metal/Metal Oxide Nanostructures Derived from Metal-Organic Frameworks. RSC Adv. 2015, 5, 7267-7279.

2. Shen, K.; Chen, X.; Chen, J.; Li, Y., Development of MOF-Derived Carbon-Based Nanomaterials for Efficient Catalysis. ACS Catal. 2016, 6, 5887-5903.

3. Zhao, S.-N.; Song, X.-Z.; Song, S.-Y.; Zhang, H.-j., Highly Efficient Heterogeneous Catalytic Materials Derived from Metal-Organic Framework Supports/Precursors. Coord. Chem. Rev. 2017, 337, 80-96.

4. Oar-Arteta, L.; Wezendonk, T.; Sun, X.; Kapteijn, F.; Gascon, J., Metal Organic Frameworks as Precursors for the Manufacture of Advanced Catalytic Materials. Mater. Chem. Front. 2017, 1, 1709-1745.

5. Kaneti, Y. V.; Tang, J.; Salunkhe, R. R.; Jiang, X. C.; Yu, A. B.; Wu, K. C. W.; Yamauchi, Y., Nanoarchitectured Design of Porous Materials and Nanocomposites from Metal-Organic Frameworks. Adv. Mater. 2017, 29.

6. Chen, D.; Huang, M.; He, S.; He, S.; Ding, L.; Wang, Q.; Yu, S.; Miao, S., Ru-MOF Enwrapped by Montmorillonite for Catalyzing Benzene Hydrogenation. Appl. Clay Sci. 2016, 119, 109-115.

7. Wang, Z.; Li, X.; Yang, Y.; Cui, Y.; Pan, H.; Wang, Z.; Chen, B.; Qian, G., Highly Dispersed Beta-Nis Nanoparticles in Porous Carbon Matrices by a Template Metal-Organic Framework Method for Lithium-Ion Cathode. J. Mater. Chem. A 2014, 2, 7912-7916.

8. Yan, N.; Yuan, Y.; Dyson, P. J., Rhodium Nanoparticle Catalysts Stabilized with a Polymer That Enhances Stability without Compromising Activity. Chem. Commun. 2011, 47, 2529-2531.

9. Yuan, Y.; Yan, N.; Dyson, P. J., Advances in the Rational Design of Rhodium Nanoparticle Catalysts: Control via Manipulation of the Nanoparticle Core and Stabilizer. ACS Catal. 2012, 2, 1057-1069.

10. Xia, W.; Mahmood, A.; Zou, R.; Xu, Q., Metal-Organic Frameworks and Their Derived Nanostructures for Electrochemical Energy Storage and Conversion. Energy Environ. Sci. 2015, 8, 1837-1866.

11. Cao, X.; Tan, C.; Sindoro, M.; Zhang, H., Hybrid Micro-/Nano-Structures Derived from Metal-Organic Frameworks: Preparation and Applications in Energy Storage and Conversion. Chem. Soc. Rev. 2017, 46, 2660-2677.

12. Xie, Z.; Xu, W.; Cui, X.; Wang, Y., Recent Progress in Metal–Organic Frameworks and Their Derived Nanostructures for Energy and Environmental Applications. ChemSusChem 2017, 10, 1645-1663.

13. Sinfelt, J. H., Catalytic Hydrogenolysis over Supported Metals. Catalysis Reviews 1970, 3, 175-205.

14. Aziz, M. A. A.; Jalil, A. A.; Triwahyono, S.; Ahmad, A., CO2 Methanation over Heterogeneous Catalysts: Recent Progress and Future Prospects. Green Chem. 2015, 17, 2647-2663.

15. Saadatjou, N.; Jafari, A.; Sahebdelfar, S., Ruthenium Nanocatalysts for Ammonia Synthesis: A Review. Chem. Eng. Commun. 2015, 202, 420-448.

Appendix 1

A. Rietveld refinement

Rietveld refinement is a least-squares method to refine a calculated model based on the observed pattern profile.[1] The method seeks to minimize the difference between observed and calculated patterns (R_{wp}) using the following equation:

$$R_{wp} = \left[\frac{\sum_i w_i (y_{i\ observed} - y_{i\ calculated})^2}{\sum_i (w_i y_{i\ observed}^2)}\right]^{\frac{1}{2}} \qquad \text{(Eq. 1)}$$

Where:

- R_{wp} is weighted profile R;
- w_i is the weighting at step i;
- $y_{i\ observed}$ is the observed intensity at step i;
- $y_{i\ calculated}$ is the calculated intensity at step i.

The calculated intensity is given by the following equation, which includes phase parameters and background contribution.

$$y_{i\ calculated} = \sum_{k=k1}^{kn} G_{ik} I_k + y_{i\ background} \qquad \text{(Eq. 2)}$$

Where:

- $y_{i\ calculated}$ refers to the intensity calculated at a given $2\theta_i$ range;
- G_{ik} is the peak profile function;
- I_k is the intensity of the kth Bragg reflection;
- LP is the Lorentz polarization factor;

- kn is a reflection contributing at $2\theta_i$;
- $y_{i\,background}$ is the background contribution at $2\theta_i$.

$$I_k = s \cdot \left(M_k \cdot LP_k \cdot P_k \cdot |F_{hkl}|_k{}^2\right) \qquad \text{(Eq. 3)}$$

Where:

- I_k is the intensity of the kth Bragg reflection;
- s is the scale factor;
- M_k is the multiplicity of the reflection, related to the crystal symmetry;
- LP_k is the Lorentz polarisation factor, related to instrument geometry;
- P_k is the preferred orientation factor, related to crystallite morphology;
- $|F_{hkl}|_k$ is the structure factor; related to the atomic composition and arrangement of the unit cell.

The method involves the use of a model to calculate a profile, the calculated pattern is compared to the observed data by calculating R_{wp}, the model is altered by refinement of selected parameters followed by several iterations of calculating pattern, comparing and refining. Several software packages are available to perform Rietveld refinement. For this research, TOPAS™ (Total Pattern Analysis System)[2] has been used. This software allow two operating modes: graphical user interface (GUI) and Launch mode. Launch mode lets the user to write codes that include TOPAS™ functionalities and other logical commands which allow for analyses flexibility.

B. Rietveld refinement-based quantitative phase analysis

For a sample containing multiple crystalline phases, Rietveld refinement can assist in their quantification. As described by Madsen et al.[3], considering a crystalline phase α, the Rietveld scale factor is given by:

$$s_\alpha = \left[\frac{K}{V_\alpha^2}\right] \cdot \left[\frac{W_\alpha}{\rho_\alpha}\right] \cdot \frac{1}{\mu_m^*} \qquad \text{(Eq. 4)}$$

Where:

- s_α is the Rietveld scale factor for α;
- K is an experiment constant;
- V_α is the volume of the unit cell for α;
- W_α is the weight fraction for α;
- ρ_α is the density of α;

μ_m^* is the overall sample mass absorption coefficient.

Rearranging Eq. 4 in order to have weight fraction as a function of the scale factor:

$$W_\alpha = \frac{s_\alpha \cdot \rho_\alpha \cdot V_\alpha^2 \cdot \mu_m^*}{K} \qquad \text{(Eq. 5)}$$

The density of a crystalline phase (ρ_α) can be calculated by the following equation:

$$\rho_\alpha = \frac{ZM_\alpha}{V_\alpha} . f \qquad \text{(Eq. 6)}$$

Where:

- ZM_α is the mass of the unit cell contents;
- V_α is the volume of the unit cell;
- $f = 1.66054$ is the conversion factor from AMU/Å to g/cm^3.

Substituting Eq. 6 in Eq. 5:

$$W_\alpha = \frac{s_\alpha \cdot \frac{ZM_\alpha}{V_\alpha} \cdot V_\alpha^2 \cdot \mu_m^*}{K} = \frac{s_\alpha \cdot (ZMV)_\alpha \cdot \mu_m^*}{K} \qquad \text{(Eq. 7)}$$

A solid sample can be composed of a combination of amorphous and crystalline phases, therefore, the sum of the weight fractions of individual phases is:

$$W_{amorphous} + \sum_j^n W_j = 1 \qquad \text{(Eq. 8)}$$

By disregarding the absolute amount of amorphous phase (i.e. “matrix”) in a sample containing more than one crystalline phase, the Matrix Flushing method can be used for the relative quantification of the crystalline phases.[4-5] Therefore:

$$W_{amorphous} = 0 \Rightarrow \sum_j^n W_j = 1 \qquad \text{(Eq. 9)}$$

Where:

- j indicates crystalline phases

This method can be applied to Rietveld refinement-based quantification.[6-7] Considering Eq. 7, K and μ_m^* will remain unchanged within the same sample and the addition of another constrain such as Eq. 9, implies the following equation:

$$W_\alpha = \frac{s_\alpha \cdot (ZMV)_\alpha}{\sum_j^n s_j \cdot (ZMV)_j} \qquad \text{(Eq. 10)}$$

Eq. 10 is independent of factors that require additional experimental measurements and can be used to evaluate the relative composition among identified crystalline phases in the same sample, but does not consider the amount of an amorphous phase or unidentified crystalline phases which may also be present in the sample.

C. References

1. Rietveld, H., A Profile Refinement Method for Nuclear and Magnetic Structures. J. Appl. Crystallogr. 1969, 2, 65-71.

2. Topas V5: General Profile and Structure Analysis Software for Powder Diffraction Data, Bruker AXS GmbH: Karlsruhe, Germany, 2012.

3. Madsen, I. C.; Scarlett, N. V. Y.; Riley, D. P.; Raven, M. D., Quantitative Phase Analysis Using the Rietveld Method. In Modern Diffraction Methods, Wiley-VCH Verlag GmbH & Co. KGaA: 2012; pp 283-320.

4. Chung, F. H., Quantitative Interpretation of X-Ray Diffraction Patterns of Mixtures. I. Matrix-Flushing Method for Quantitative Multicomponent Analysis. J. Appl. Crystallogr. 1974, 7, 519-525.

5. Chung, F. H., Quantitative Interpretation of X-Ray Diffraction Patterns of Mixtures. Ii. Adiabatic Principle of X-Ray Diffraction Analysis of Mixtures. J. Appl. Crystallogr. 1974, 7, 526-531.

6. Hill, R. J.; Howard, C. J., Quantitative Phase-Analysis from Neutron Powder Diffraction Data Using the Rietveld Method. J. Appl. Crystallogr. 1987, 20, 467-474.

7. Bish, D. L.; Howard, S. A., Quantitative Phase-Analysis Using the Rietveld Method. J. Appl. Crystallogr. 1988, 21, 86-91.

Journal of
Materials Chemistry A

PAPER

View Article

Check for updates

Cite this: *J. Mater. Chem. A*, 2017, **5**, 12990

Highly active catalyst for CO_2 methanation derived from a metal organic framework template†

R. Lippi,[ab] S. C. Howard,[a] H. Barron,[c] C. D. Easton,[a] I. C. Madsen,[d] L. J. Waddington,[a] C. Vogt,[ae] M. R. Hill,[a] C. J. Sumby,[b] C. J. Doonan*[b] and D. F. Kennedy*[a]

Received 30th January 2017
Accepted 26th May 2017

DOI: 10.1039/c7ta00958e

rsc.li/materials-a

The conversion of CO_2 into chemicals of commercial interest is a rapidly expanding area of research. Here, we present a highly active and stable CO_2 methanation catalyst that is derived from a Ru-impregnated zirconium-based metal organic framework (MOF) material. The Ru-doped MOF is transformed, under reaction conditions, into an active catalyst which yields CO_2 conversions of 96% and a CH_4 selectivity of 99%. We demonstrate that the final catalyst was composed of a mixture of Ru-nanoparticles supported on monoclinic and tetragonal ZrO_2 nanoparticles. Notably, such catalytic activity has only been achieved using the MOF templating strategy. Catalysts of the same composition were synthesized *via* different methods but were less active for CO_2 methanation.

Introduction

In the past two decades, anthropogenic carbon dioxide (CO_2) emissions have become a major environmental concern. This can be attributed to the effect of atmospheric CO_2 concentrations on the global climate patterns.[1,2] Accordingly, efforts from the international community are underway to limit the increase in average global temperature to a maximum of 2 °C.[3] One strategy for controlling CO_2 emissions is Carbon Capture and Utilization (CCU). However, for CCU to be economically viable, an energy efficient processes must be developed for utilising CO_2 as a carbon source which will enable its use for producing commodity chemicals aligned to industrial needs.[4]

One pathway to CO_2 utilisation is hydrogenation to value added products.[5] The Sabatier reaction (also known as CO_2 methanation), fully reduces CO_2, over a catalyst, to produce methane which can be directly used as a fuel.[6] This reaction may find use in the future as part of power-to-gas technology where hydrogen is produced from renewable energy sources such as wind or solar power.[7,8] A key challenge for the realisation of this process is improvement in existing catalyst technologies. For example, directions in this field include the synthesis of high surface area catalysts, improving CO_2 conversion, minimising unwanted CO production, addressing poor long-term catalyst stability, low methane production rates and reducing the reaction temperatures.[9 11] Nickel catalysts on various supports have been widely studied due to nickel's natural abundance and relatively low cost. However, most Ni catalysts suffer from deactivation due to carbon deposition, sintering, and chemical poisoning.[9 12] Given these limitations other metals, such as ruthenium,[13] have been explored as potential catalysts. Although, ruthenium-based catalysts are relatively more expensive, they are very stable and known to be highly active for CO_2 methanation.[9 11,14,15] With respect to catalytic supports, Al_2O_3, TiO_2, SiO_2, CeO_2 and ZrO_2 are most common.[9 11,16 19] The metal-oxide support has a significant impact on the activity of catalysts in the CO_2 methanation reaction. A salient example is ZrO_2, which exists in three phases: monoclinic, tetragonal and cubic. Studies have shown that the respective phases affect CO_2 conversion for Ni-based catalysts.[16,18,19] Indeed, supports comprised of a combination of two ZrO_2 phases were shown to yield more active catalysts.[19]

Metal organic frameworks (MOFs) are well-known for their applications in gas absorption, molecular separation,[20,21] sensors and catalysis.[20] Recent reports have shown that these materials can be used as templates to synthesise catalysts with unique morphologies.[22 25] For example, Santos *et al.* have recently reported the synthesis of highly active MOF-derived iron carbide catalyst for Fischer Tropsch synthesis.[26,27] It is noteworthy that the novel structure of the MOF derived catalyst described in that work could not be obtained by other methods.[26] Additionally, MOF-derived catalysts have also been reported for photocatalytic hydrogen production, the reduction of nitro aromatics and for the aerobic oxidation of alcohols,

---

[a] *CSIRO Manufacturing, Clayton, Victoria 3168, Australia. E-mail: danielle.kennedy@csiro.au*

[b] *Centre for Advanced Nanomaterials, Department of Chemistry, The University of Adelaide, Adelaide, South Australia 5005, Australia. E-mail: christian.doonan@adelaide.edu.au*

[c] *CSIRO Data61, Docklands, Victoria 3008, Australia*

[d] *CSIRO Mineral Resources, Clayton, Victoria 3168, Australia*

[e] *School of Chemistry, Monash University, Clayton, Victoria 3800, Australia*

† Electronic supplementary information (ESI) available: Experimental section and more structure and performance characterization. See DOI: 10.1039/c7ta00958e

respectively.[28 31] These previous studies led us to hypothesise that a Ru-impregnated Zr-MOF may yield a composite active towards CO_2 methanation. Accordingly, here we report that infiltrating the pores of UiO-66 with $RuCl_3$ gives rise to a precursor of a highly active, stable and selective, *in situ* generated MOF-derived catalyst for CO_2 methanation at low pressure and mid-range temperature.

Experimental

Catalyst precursor synthesis

The methanation catalyst precursors are defined as xRu/UiO-66, where $x = 0.25$, 0.5, 0.75, 1, 1.25, 1.5, 1.75 or 2 wt% of Ru on the zirconium terephthalate MOF, UiO-66. They were synthesised by addition of $RuCl_3$ into the pores of activated UiO-66 *via* the Incipient Wetness Impregnation (IWI) method[32] to achieve the desired loading x. Detailed method in ESI.†

CO_2 methanation reaction catalysis

The catalysts were activated *in situ* under methanation reaction conditions. We then evaluated the catalytic performance of the xRu/UiO-66 derived catalyst for CO_2 methanation under different pressure and temperature conditions. In a typical experiment, 20 mg of xRu/UiO-66 was loaded into a fixed-bed microreactor and, after an *in situ* drying step, the synthesis gas mixture was flowed through the bed. The synthesis gas mixture contained either a stoichiometric ratio of H_2 and CO_2 ($H_2 : CO_2 = 4 : 1$) and Ar tracer gas (H_2, 77.6 vol%; CO_2, 19.4 vol%; Ar, 3 vol%), or $H_2 : CO_2 = 3.5 : 1$ with Ar as tracer gas (H_2, 75.44 vol%; CO_2, 21.56 vol%; Ar, 3 vol%). The ratios used for each experiment are indicated in the figure captions. Throughout the experiments the temperature and pressure were controlled and effluent gas samples were analysed by a gas chromatograph. Considering that CO_2 is less expensive and more abundant, the limiting reactant in the Sabatier reaction is H_2, which would ideally be obtained from non-fossil-based sources. For this reason, performance was evaluated at stoichiometric ratios of H_2 and CO_2 and with a slight excess of CO_2. Thus, the authors chose to discuss performance in terms of H_2 conversion. Catalyst carbon content, CH_4 production and CO_2 conversion were evaluated for validation of the reported H_2 conversion. Other details can be found in the ESI.†

Results and discussion

Catalyst activation

Fig. 1A shows an initial increase in hydrogen conversion (X_{H_2}) that can be attributed to catalyst activation. During this activation period, 60% mass loss was observed (Table S3†) and mass spectrometry confirmed the loss of organic fragments from the precatalyst 1Ru/UiO-66 at 330 °C (Fig. S14†). After the activation, carbon products were derived from CO_2, as the carbon content of the MOF-derived catalyst was less than 2 wt% (Fig. S11†). High and stable H_2 conversions were observed from the MOF-derived CO_2 methanation catalysts. In particular, Fig. 1A indicates that activation conditions above 330 °C afford X_{H_2} above 94% and independent of pressure. However, 1Ru/UiO-66 derived catalysts activated and monitored at 250 and 300 °C took 13 h to stabilize, showing X_{H_2} below 25% throughout the experiment. We note that increasing the reaction pressure at 350 °C reduced the activation period but had little impact on optimal conversion. Additionally, the catalyst showed remarkable selectivity for methane (S_{CH_4}); 99.9% at all conditions tested (Fig. 2C and D). The only by-product observed during this work was CO at very low concentrations (S_{CO} < 0.1%).

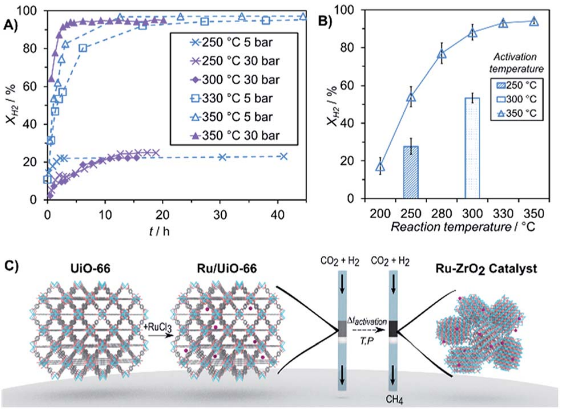

Fig. 1 (A) H_2 conversion (X_H) during CO_2 methanation reactions using 1Ru/UiO-66 as the precatalyst under different reaction conditions. Reaction conditions: 20 mg of 1Ru/UiO-66, $H_2 : CO_2 = 4 : 1$, Weight Hourly Space Velocity (WHSV) = 25 L h^{1} g^{1}. (B) X_{H_2} at different reaction temperatures and 5 bar for catalysts activated at 250, 300 or 350 °C. Reaction conditions: activation at 30 bar for 22 hours, 50 mg of 1Ru/UiO-66, $H_2 : CO_2 = 4 : 1$, WHSV = 43 L h^{1} g^{1}. (C) Scheme of Ru/UiO-66 synthesis and *in situ* transformation into the MOF derived catalyst. Δt_{act} = activation period.

Catalyst performance

To confirm that Ru is necessary for catalytic activity we carried out an analogous set of experiments with pure UiO-66. Under all conditions tested no X_{H_2} was detected from this control. In addition, we found that X_{H_2} was dependent on Ru loading. Fig. 2A shows that conversions above 93% were observed for loadings higher than 0.75 wt% of Ru on UiO-66. Accordingly, 1 wt% Ru/UiO-66 (1Ru/UiO-66) was used for all other experiments. As a production rate indicator, we report the Weight Hourly Space Velocity (WHSV) in Fig. 2B, which is the gas feed flow per catalyst mass unit. From an industrial perspective, it is desirable to maximize the production of methane using as little precious metal catalyst as possible. Therefore, a high WHSV associated with high X_{H_2} is representative of an optimal catalyst. It is worth mentioning that 20 mg of 0.25Ru/UiO-66 yielded a catalyst with X_{H_2} of 16% (Fig. 2A) while, under the same conditions, 5 mg of 1Ru/UiO-66 provided X_{H_2} of 78% (Fig. 2B). Given that both reactors contained a total of 0.05 mg Ru these results confirm that the high activity of the MOF-templated catalyst is not achieved simply by the absolute amount of Ru, but depends on the structure of the catalyst.

In order to evaluate the performance of the 1Ru/UiO-66-derived catalyst a number of control samples were prepared

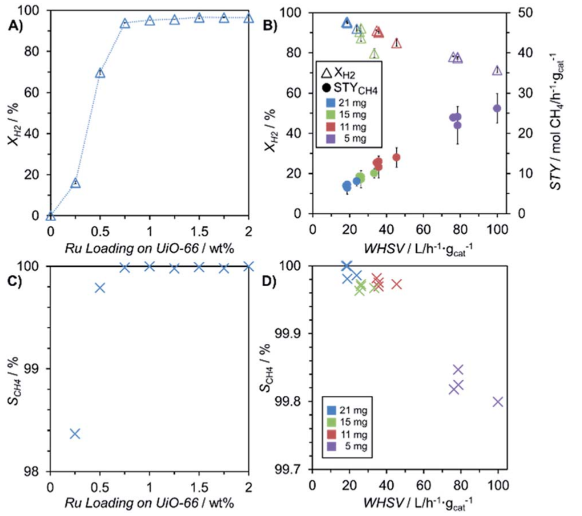

Fig. 2 (A) H_2 conversions (X_{H_2}) and (C) CH_4 selectivity (S_{CH_4}) for catalysts derived from different loadings (*x*) of Ru on UiO-66. Reaction conditions: 20 mg of *x*Ru/UiO-66, $H_2 : CO_2 = 4 : 1$, WHSV = 19 L h^{-1} g^{-1}, 350 °C and 5 bar. (B) X_{H_2} and space time yield for CH_4 (STY_{CH_4}) for the MOF-derived catalysts and (D) S_{CH_4} for different conditions of WHSV (gas feed flow per catalyst mass unit), achieved using the indicated amounts of 1Ru/UiO-66 and different gas flows. Reaction conditions: $H_2 : CO_2 = 4 : 1$, 350 °C and 5 bar. Error bars represent standard deviation over 40 h periods. CO was the only by-product observed.

(Fig. 3). Ru was loaded onto several pre-made supports using identical IWI conditions to the MOF-based precatalyst; pre-made monoclinic zirconia (pmZrO_2), activated carbon (C), and mesoporous silica (SBA-15), to yield 1 wt% Ru loading. These control samples were then assessed for their catalytic performance for CO_2 methanation alongside 1Ru/UiO-66 and a commercially available Methanizer catalyst. We note that the MOF-based precatalyst undergoes significant mass loss during the *in situ* templating of the active catalyst. To ensure consistency, 20 mg of 1% Ru loaded on the different supports was used so that the absolute amount of Ru was equivalent in all experiments undertaken with different support materials. In all conditions tested, a significantly greater X_{H_2} was observed for the MOF-derived catalyst (Fig. 3). Furthermore, this catalyst was the most selective for methane and inhibited formation of the by-product CO which is commonly present in CO_2 methanation.[9–11] The catalyst's remarkable stability over isopressure periods of 40 h is evidenced by the small standard deviation bars, Fig. 3, and the consistent conversion X_{H_2} in Fig. 1. Even after shutdown and exposure to air, deactivation was not observed for the derived catalyst (Fig. S15†).

In addition to high stability, the 1Ru/UiO-66-derived catalyst showed comparable or better activity than high-performing CO_2 methanation catalysts reported in the literature[14,18,19,33–36] and achieved conversions equivalent to the thermodynamic equilibrium of the Sabatier reaction (Fig. S15†). The 1Ru/UiO-66-derived catalyst can be considered superior based on its combined performance characteristics: it requires a very small amount of catalyst to convert CO_2-rich streams at high gas flows conditions, it displays stable conversion in excess of 160 h, it is very selective for CH_4, has extremely low CO by-product formation, and operates at medium range temperatures (Fig. 1B).

It is evident that the composition, in addition to the Ru loading, of the MOF-derived catalyst underpins its exceptional activity. This was confirmed by performing studies that showed,

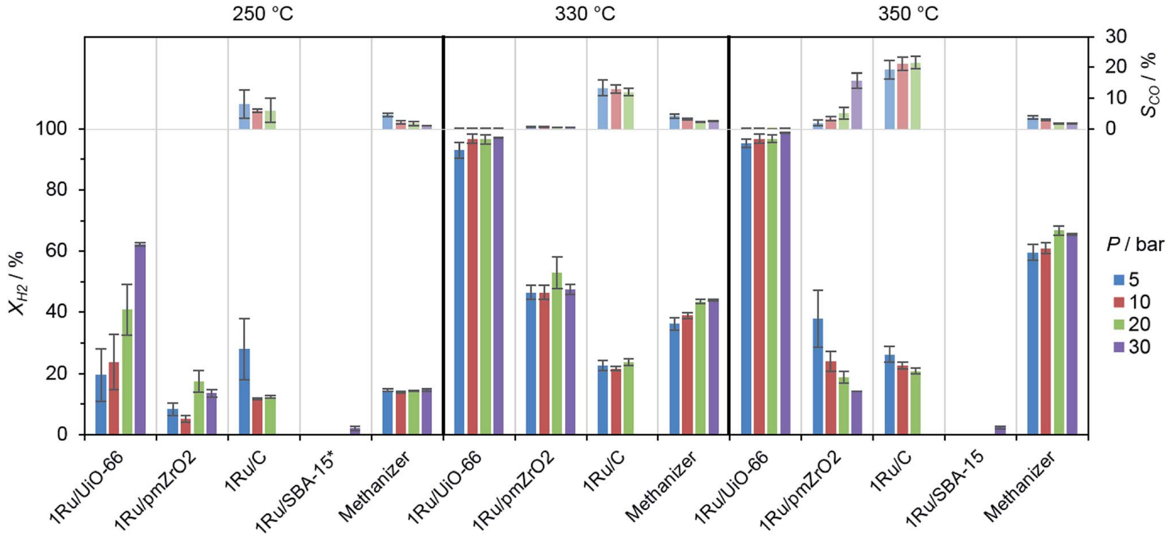

Fig. 3 Average H_2 conversion (X_{H_2}) and selectivity for CO (S_{CO}) by-product for samples at 250, 330 and 350 °C (left to right) with increasing reaction pressure conditions indicated by the colored bars. Average conversion values were obtained across isopressure periods of ~40 h. Total experiment time: 160 h. Reaction conditions: 20 mg of fresh sample as above, $H_2 : CO_2 = 3.5 : 1$, gas flow = 14.3 mL min^{-1}. Error bars represent standard deviation across an average of 3–4 measurements. * Tested at 270 °C.

even at low concentrations, the presence of Ru was critical for catalytic performance; UiO-66 with no further treatment was inactive for CO_2 methanation. We also investigated whether the catalytic activity depended on the morphology of the template, UiO-66, in addition to the chemical composition. Accordingly, we prepared a solid mixture with the MOF precursors: $ZrCl_4$ and terephthalic acid (H_2BDC) in the molar ratio present in UiO-66, and then added $RuCl_3$ to produce a sample with chemical composition equivalent to the 1Ru/UiO-66. The catalytic activity of this sample was assessed at 350 °C and 5 bar and no methane production or H_2 conversion was detected. This provides strong evidence that the UiO-66 framework plays an important role in templating the structure of the active catalyst. This result is in agreement with previous studies[26] and is a further demonstration that MOFs can confer unique architectures to solid-state catalysts.

Powder X-ray diffraction

To elucidate the structure of the MOF-derived catalyst we performed a series of X-ray diffraction (XRD) experiments. We activated and tested the 1Ru/UiO-66 pre-catalyst at 250 °C, 300 °C and 350 °C (Fig. 1B) and then recorded XRD patterns representative of each temperature after 20 and 100 hours on stream (Fig. 4). Rietveld refinement based quantitative phase analysis of the data indicates that both monoclinic (m-ZrO_2) and tetragonal (t-ZrO_2) phases of ZrO_2 are present with their respective ratios varying with reaction temperature and time. However, there were no peaks that could be attributed to the presence of a Ru^0 or RuO_2 phase. XRD reflections in diffractograms are affected by the relative amount of a phase, crystallinity and crystallite size. The catalyst contains only 3 wt% of Ru and Ru^0 nanoparticles are commonly found in an amorphous form.[37,38] Therefore, microscopy and elemental mapping were used to investigate the Ru phase (below). The MOF-derived catalyst activated at 350 °C yielded a greater proportion of m-ZrO_2 than the one activated at 250 °C. In addition, the catalyst activated at 350 °C performed better at 250 °C than the sample activated and kept at 250 °C. This infers a correlation between the amount of m-ZrO_2 present and activity (Fig. 1A and B and 4). Catalyst samples activated and tested at 300 and 250 °C were less active (Fig. 1A and B), and contained more t-ZrO_2 (Fig. 4). For these lower activation temperatures, the reaction time was observed to have an effect on composition and microstructure as well as on the conversion. This variation can be explained by the existence of a temperature threshold for the fast decomposition of 1Ru/UiO-66 under synthesis gas flow. Fig. S14† shows the effluent composition during the activation of the MOF-derived catalyst in a single channel reactor connected to a mass spectrometer. An increasing loss of organic fragments was observed from 300 to 330 °C, at which point it reached a maxima, subsequently the conversion of the reagents and the production of CH_4 increased drastically. To further understand the changes in morphology under simulated reaction conditions, we performed controlled atmosphere and variable temperature (*in situ*) XRD of the precatalyst. This study at 1 bar confirmed that the MOF structure collapsed at 330 °C, in agreement with the loss of fragments observed by mass spectrometry, giving rise to an amorphous phase (Fig. 5). This disordered phase, caused by the loss of the organic linkers, crystallizes into the ZrO_2 tetragonal and monoclinic phases at different rates depending on the temperature (Fig. 4) to produce the active catalyst. Thermal decomposition of UiO-66 in air[39] and in N_2 (ref. 40) atmosphere typically produce tetragonal ZrO_2. The high content of monoclinic ZrO_2 in the catalyst is explained by the presence of H_2O,[41] which is produced *via* CO_2 methanation during activation. This highlights the importance of the activation under reactive conditions to generate an active catalyst.

Electron microscopy

The microstructure of the MOF-derived catalyst was studied by Transmission Electron Microscopy (TEM) and Energy-

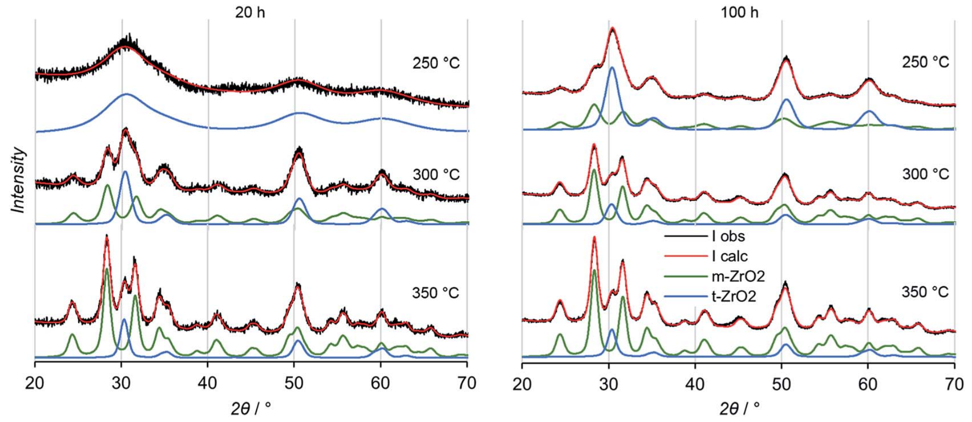

Fig. 4 Diffractograms of MOF-derived catalysts activated at 250, 300 and 350 °C at 30 bar, after 20 h and after 100 h. Black lines indicate the collected data; red lines, the calculated profile from Rietveld quantitative phase analysis; and green and blue lines the individual contribution of each phase calculated by the Rietveld method (ESI†). Diffractograms are offset for clarification.

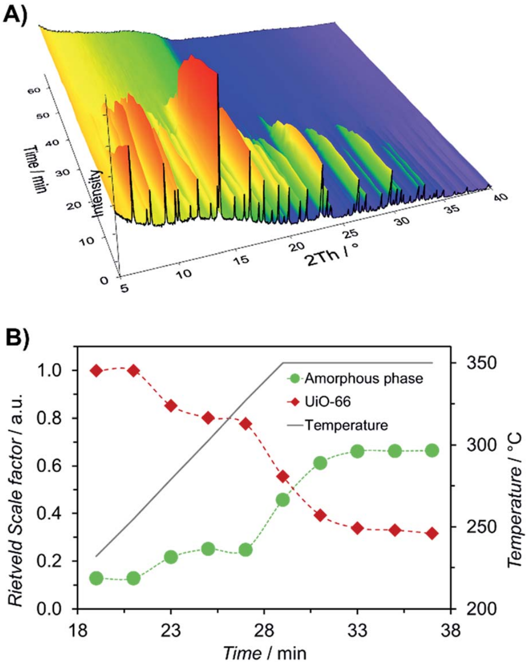

Fig. 5 (A) Controlled atmosphere and variable temperature (*in situ*) PXRD of 1Ru/UiO-66 in simulated reaction conditions. (B) Rietveld refinement scale factor *versus* time and temperature for UiO-66 crystalline phase and the resulting amorphous phase. Experimental details can be found in the ESI.†

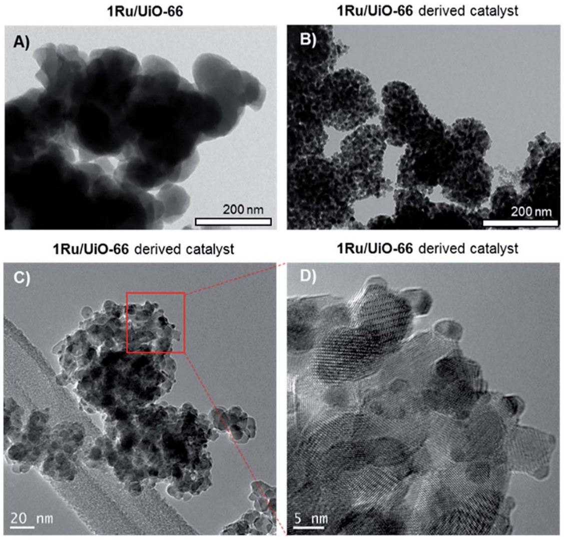

Fig. 6 (A) TEM of 1Ru/UiO-66 and of (B) 1Ru/UiO-66 derived catalyst, the final catalyst is made of nanoparticle clusters which resemble the UiO-66 particles. (C and D) HR-TEM of 1Ru/UiO-66 derived catalyst displaying the Ru particles (2 5 nm) supported on the ZrO_2 particles (10 20 nm). The MOF-derived catalyst was activated and tested at 350 °C, 30 bar for 100 h.

Dispersive X-ray Spectroscopy (EDS). The activated catalyst consisted of a hierarchical nanostructure. Nanoparticles of ZrO_2 in the range of 10 to 20 nm, in agreement with crystallite domain size obtained from XRD, were organized in clusters from 100 to 200 nm (Fig. 6B). These clusters resembled the precursor 1Ru/UiO-66 crystals in size and shape (Fig. 6A). Smaller Ru nanoparticles (Ru NPs) in the range of 2 to 5 nm were observed on the surface of the ZrO_2 particles (Fig. 6C and D). EDS mapping infers that the Ru NPs are homogeneously dispersed on the ZrO_2 surfaces (Fig. 7). The observed distribution of Ru is most likely due to the precursor MOF as a control sample of 1Ru/pmZrO_2 (pm = pre-made) does not show the same spatial coincidence of Ru and Zr (Fig. 7). Elemental mapping at higher magnification confirmed the presence of Ru NPs, additionally, the different spatial location of oxygen and Ru suggests that the nanoparticles consist of elemental Ru rather than Ru oxide (Fig. 8 and S21†). In summary, the microscopy data provide evidence that the MOF-derived catalyst is composed of larger ZrO_2 nanoparticles (10 20 nm) decorated by smaller Ru^0 NPs (2 5 nm).

X-ray photoelectron spectroscopy

The surface of the MOF-derived catalyst was examined by X-ray photoelectron spectroscopy (XPS). The high resolution spectra peak shape and binding energy position of the Ru is consistent with RuO_2 (Fig. S24 and Table S7†).[42] These results are in contrast to EDS maps that indicate the bulk of the nanoparticles consist of Ru^0, the presence of surface RuO_2 can be explained by oxidation of the surface Ru^0 atoms upon exposure to air.[43,44] The amount of Ru and Zr on the catalyst surface was quantified by XPS elemental analysis which afforded a Ru : Zr atomic ratio of 1 : 9. This value is significantly higher to the bulk Ru : Zr elemental quantification of 1 : 24 and provides further confirmation that the Ru nanoparticles supported on the ZrO_2 surface.

DFT calculations

To provide insight into the structure of the catalyst precursor, Density Functional Theory (DFT) calculations were performed to evaluate the interaction between a Ru atom and the UiO-66 secondary building unit (SBU) (Fig. 9). Cation exchange between Zr and Ru atoms during IWI was considered unlikely as the solvent is dried at 80 °C just after the addition of the $RuCl_3$ solution, not allowing a substantial amount of time for the exchange.[45] According to Table 1, the most favourable site for the 1Ru/UiO-66 is the configuration A, where the Ru atom is bonded to one oxygen and two zirconium atoms before the relaxation (high negative values of $\delta E_{\min}$ imply that some configurations are not allowed or stable, while low values indicate favourable configurations). Configuration B is the second most probable with an energy difference of 14 eV. This small energy difference is attributed to the fact that the final position of the Ru atom is similar to the initial configuration in both cases and remains bonded to the same atoms with very small change of configurations; while configurations C, D, and

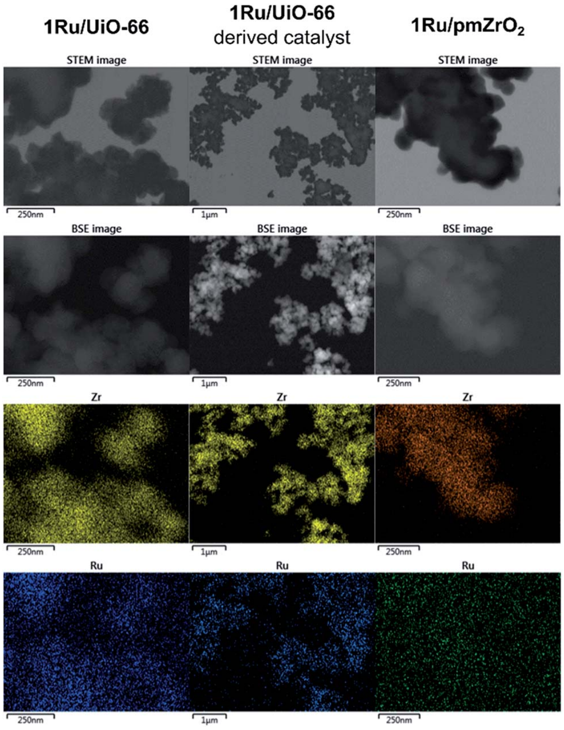

Fig. 7 Microscopy images including STEM, backscattered electrons (BSE) and EDS elemental mapping of Zr and Ru for the precursor MOF, MOF-templated catalyst and Ru impregnated on pre-made monoclinic zirconia catalyst (1Ru/pmZrO$_2$). The elemental mapping of 1Ru/UiO-66 and the MOF-templated catalyst exhibited a great dispersion of Ru on the ZrO$_2$ particles. This level of dispersion was not observed for the 1Ru/pmZrO$_2$ catalyst, which presented most ZrO$_2$ particles Ru-free.

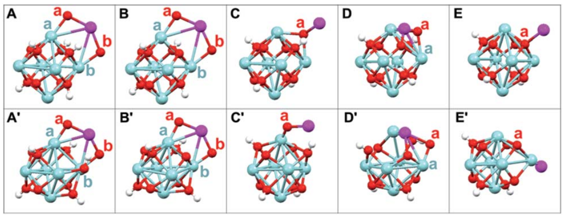

Fig. 9 Initial (top) and final (bottom) configurations for the geometry optimization of different locations of Ru binding to the SBU. The spheres indicate atom position (Ru, magenta; O, red; Zr, blue and H, white). The most energetically favourable configurations A and B undergo subtle changes during the optimization, while configurations C, D and E undergo major changes.

E undergo substantial configuration changes (Fig. 9 and Table 1). Configurations A and B suggest that the Ru atom is coordinated to the metal node in a position normally occupied by a terephthalate linker. We note that this is consistent with previous studies which show that metal node defect sites in UiO-66 preferentially bind to other metals.[46,47] In this system, the post-synthetic metalation[48] of these defect sites may lead to the controlled distribution of Ru throughout the framework of the catalyst precursor MOF (Fig. 7).

Upon the MOF collapse, during the activation period, the MOF loses its organic linkers and the MOF SBUs form a disordered (amorphous) phase before they rearrange to form ZrO$_2$ nanoparticles. Nanocrystalline ZrO$_2$ presents an excess of oxygen vacancies[49] which are responsible for the adsorption of CO$_2$ in the methanation process.[18,19] Ru species previously dispersed through the precursor MOF (1Ru/UiO-66) migrate to the surface of the nano-ZrO$_2$ and form Ru NPs. The high level of Ru NPs dispersion in the final catalyst is owed to the dispersion

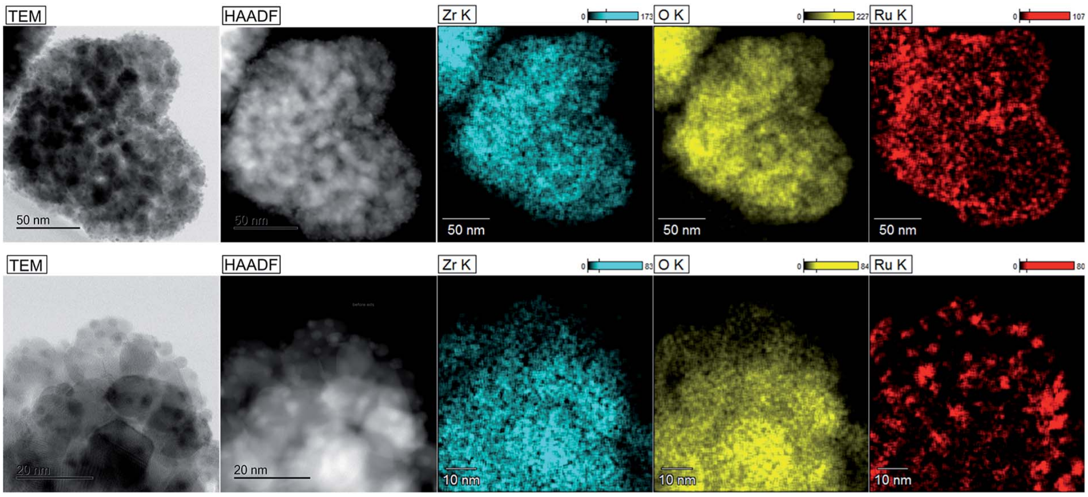

Fig. 8 High resolution TEM, high-angle annular dark-field (HAADF) and EDS elemental mapping of 1Ru/UiO-66 templated catalyst. The MOF-templating method yielded a catalyst containing Ru nanoparticles (2–5 nm) supported on ZrO$_2$ nanoparticles (10–20 nm). The oxygen map does not correlate with the Ru location, indicating the ruthenium to be Ru^0. Catalyst activated and tested at 350 °C and 30 bar.

Table 1 Geometrical features and calculated energy for the configurations displayed in Fig. 9[a]

Initial	D_i Ru O	D_i Ru Zr	Final	D_f Ru O	D_f Ru Zr	E_Total/eV	δE_min/eV
A	2.2a, 2.2b	3.4a, 3.4b	A′	2.0a, 2.0b	3.0a, 3.0b	5681	0
B	2.2a, 2.2b	3.4a, 3.4b	B′	2.1a, 2.1b	3.0a, 3.0b	5667	14
C	2.1a	0.0a	C′	2.1a	0.0a	5229	452
D	2.1a, 0.0b	0.0a, 0.0b	D	2.1a, 2.4b	2.8a, 2.9b	5226	455
E	0.0a	0.0a, 0.0b	E′	2.1b	2.8a, 2.9b	4762	919

[a] $D_\text{i,f}$: initial and final distances in A. Sub-indexes a and b correspond to neighbouring atoms of each element (Fig. 9). δE_min relates the maximum energy deviations observed from the lowest energy configuration with respect to Ru position.

of Ru in the precursor MOF. In this study, the distribution of Ru NPs on nano-ZrO_2 matrix may underpin the exceptional activity of the MOF-derived catalyst. Accordingly, when the oxygen vacancies are associated with the hydrogenation properties of Ru NPs, a high activity for the CO_2 methanation was observed even at low Ru loading and at high WHSV.

Conclusions

We have identified a highly active catalyst for CO_2 methanation derived from Ru impregnated UiO-66. The final Ru/ZrO_2 catalyst displayed CO_2 conversions in the range of 96 to 98% when operating under high gas flow rates. In addition, it showed remarkable stability and high selectivity to methane for more than 160 h of testing. The combination of these reactive properties assures this catalyst superiority when comparing it to other cutting edge catalysts, however, poisoning tests have not yet been performed for this material. This work highlights that MOFs can confer unique morphology to heterogeneous catalyst systems *via* a templating strategy. Such *in situ* generation of the active catalyst by MOF-templating has the advantage of not requiring a calcination step at high temperatures or caustic chemical processing.[18,19,24,26,35,50 52] Furthermore, the precise spatial control of metal-oxide and organic components offered by MOF chemistry provides excellent potential for the design of new solid-state catalysts.

Acknowledgements

The authors would like to thank Nathan Brosnahan, Kaycee Low and Hao Wei. Aspects of this research were undertaken on the Powder Diffraction beamline at the Australian Synchrotron, Victoria, Australia. This work was supported by CSIRO and the Science and Industry Endowment Fund is thanked for funding this research. R. Lippi acknowledges The University of Adelaide for the Beacon of Enlightenment Ph.D. Scholarship.

References

1 C. S. Song, *Catal. Today*, 2006, **115**, 2 32.
2 IPCC, in *Climate Change 2013: The Physical Science Basis. Contribution of Working Group I to the Fifth Assessment Report of the Intergovernmental Panel on Climate Change*, ed. T. F. Stocker, D. Qin, G.-K. Plattner, M. Tignor, S. K. Allen, J. Boschung, A. Nauels, Y. Xia, V. Bex and P. M. Midgley, Cambridge University Press, Cambridge, United Kingdom and New York, NY, USA, 2013, pp. 1 30, DOI: 10.1017/CBO9781107415324.004.
3 G. C. Iyer, J. A. Edmonds, A. A. Fawcett, N. E. Hultman, J. Alsalam, G. R. Asrar, K. V. Calvin, L. E. Clarke, J. Creason, M. Jeong, P. Kyle, J. McFarland, A. Mundra, P. Patel, W. Shi and H. C. McJeon, *Environ. Res. Lett.*, 2015, **10**, 125002.
4 M. Aresta, A. Dibenedetto and A. Angelini, *Chem. Rev.*, 2014, **114**, 1709 1742.
5 C. Ampelli, S. Perathoner and G. Centi, *Philos. Trans. R. Soc. London, A*, 2015, 373.
6 K. R. Thampi, J. Kiwi and M. Gratzel, *Nature*, 1987, **327**, 506 508.
7 F. Gutierrez-Martin and L. M. Rodriguez-Anton, *Int. J. Hydrogen Energy*, 2016, **41**, 19290 19303.
8 M. Götz, J. Lefebvre, F. Mörs, A. McDaniel Koch, F. Graf, S. Bajohr, R. Reimert and T. Kolb, *Renewable Energy*, 2016, **85**, 1371 1390.
9 M. A. A. Aziz, A. A. Jalil, S. Triwahyono and A. Ahmad, *Green Chem.*, 2015, **17**, 2647 2663.
10 J. Gao, Q. Liu, F. Gu, B. Liu, Z. Zhong and F. Su, *RSC Adv.* 2015, **5**, 22759 22776.
11 S. Ronsch, J. Schneider, S. Matthischke, M. Schluter, M. Gotz, J. Lefebvre, P. Prabhakaran and S. Bajohr, *Fuel* 2016, **166**, 276 296.
12 F. Ocampo, B. Louis, L. Kiwi-Minsker and A.-C. Roger, *Appl. Catal., A*, 2011, **392**, 36 44.
13 W. Sheng, W. Shudong, L. Tao, G. Diannan and W. Mingzhe, *China Pat.*, CN104148065B, Dalian Institute of Chemical Physics, Chinese Academy of Sciences, 2017.
14 S. Sharma, Z. Hu, P. Zhang, E. W. McFarland and H. Metiu, *J. Catal.*, 2011, **278**, 297 309.
15 S. Carenco, C. Sassoye, M. Faustini, P. Eloy, D. P. Debecker, H. Bluhm and M. Salmeron, *J. Phys. Chem. C*, 2016, **120** 15354 15361.
16 M. Yamasaki, H. Habazaki, T. Yoshida, E. Akiyama, A. Kawashima, K. Asami, K. Hashimoto, M. Komori and K. Shimamura, *Appl. Catal., A*, 1997, **163**, 187 197.
17 N. Perkas, G. Amirian, Z. Zhong, J. Teo, Y. Gofer and A. Gedanken, *Catal. Lett.*, 2009, **130**, 455 462.
18 H. Takano, Y. Kirihata, K. Izumiya, N. Kumagai, H. Habazaki and K. Hashimoto, *Appl. Surf. Sci.*, 2016, **388**, 653 663.

19 H. Takano, H. Shinomiya, K. Izumiya, N. Kumagai, H. Habazaki and K. Hashimoto, *Int. J. Hydrogen Energy*, 2015, **40**, 8347 8355.

20 H. Furukawa, K. E. Cordova, M. O'Keeffe and O. M. Yaghi, *Science*, 2013, **341**, 1230444.

21 Y. Cui, B. Li, H. He, W. Zhou, B. Chen and G. Qian, *Acc. Chem. Res.*, 2016, **49**, 483 493.

22 Y. Song, X. Li, L. Sun and L. Wang, *RSC Adv.*, 2015, **5**, 7267 7279.

23 W. Xia, A. Mahmood, R. Zou and Q. Xu, *Energy Environ. Sci.*, 2015, **8**, 1837 1866.

24 J. Yang, F. Zhang, X. Wang, D. He, G. Wu, Q. Yang, X. Hong, Y. Wu and Y. Li, *Angew. Chem., Int. Ed.*, 2016, **55**, 12854 12858.

25 K. Shen, X. Chen, J. Chen and Y. Li, *ACS Catal.*, 2016, **6**, 5887 5903.

26 V. P. Santos, T. A. Wezendonk, J. J. D. Jaen, A. I. Dugulan, M. A. Nasalevich, H. U. Islam, A. Chojecki, S. Sartipi, X. Sun, A. A. Hakeem, A. C. J. Koeken, M. Ruitenbeek, T. Davidian, G. R. Meima, G. Sankar, F. Kapteijn, M. Makkee and J. Gascon, *Nat. Commun.*, 2015, **6**, 6451.

27 T. A. Wezendonk, V. P. Santos, M. A. Nasalevich, Q. S. E. Warringa, A. I. Dugulan, A. Chojecki, A. C. J. Koeken, M. Ruitenbeek, G. Meima, H.-U. Islam, G. Sankar, M. Makkee, F. Kapteijn and J. Gascon, *ACS Catal.*, 2016, **6**, 3236 3247.

28 K. E. deKrafft, C. Wang and W. Lin, *Adv. Mater.*, 2012, **24**, 2014 2018.

29 H. Y. Niu, S. L. Liu, Y. Q. Cai, F. C. Wu and X. L. Zhao, *Microporous Mesoporous Mater.*, 2016, **219**, 48 53.

30 X. Sun, A. I. Olivos-Suarez, L. Oar-Arteta, E. Rozhko, D. Osadchii, A. Bavykina, F. Kapteijn and J. Gascon, *ChemCatChem*, 2017, **9**, 1854 1862.

31 B. R. Kim, J. S. Oh, J. Kim and C. Y. Lee, *Catal. Lett.*, 2016, **146**, 734 743.

32 J. M. Campelo, D. Luna, R. Luque, J. M. Marinas and A. a. Romero, *ChemSusChem*, 2009, **2**, 18 45.

33 G. Garbarino, D. Bellotti, P. Riani, L. Magistri and G. Busca, *Int. J. Hydrogen Energy*, 2015, **40**, 9171 9182.

34 B. Lu and K. Kawamoto, *Fuel*, 2013, **103**, 699 704.

35 W. L. Zhen, B. Li, G. X. Lu and J. T. Ma, *Chem. Commun.* 2015, **51**, 1728 1731.

36 H. H. Shin, L. Lu, Z. Yang, C. J. Kiely and S. McIntosh, *ACS Catal.*, 2016, **6**, 2811 2818.

37 J. Ohyama, T. Sato, Y. Yamamoto, S. Arai and A. Satsuma, *J. Am. Chem. Soc.*, 2013, **135**, 8016 8021.

38 T. Si Yin, L. Coryl Jing Jun, D. Saman Safari, L. Szu Cheng, W. Evan Laurence, L. He-Kuan, C. Dongzhi, T. S. A. Hor and H. Ming-Yong, *Nanotechnology*, 2015, **26**, 415401.

39 J. B. DeCoste, G. W. Peterson, H. Jasuja, T. G. Glover, Y. G. Huang and K. S. Walton, *J. Mater. Chem. A*, 2013, **1** 5642 5650.

40 S.-C. Liu, Z.-F. Yue and Y. Liu, *J. Porous Mater.*, 2015, **22**, 465 471.

41 S. Xie, E. Iglesia and A. T. Bell, *Chem. Mater.*, 2000, **12**, 2442 2447.

42 D. J. Morgan, *Surf. Interface Anal.*, 2015, **47**, 1072 1079.

43 R. Bavand, A. Yelon and E. Sacher, *Appl. Surf. Sci.*, 2015, **355** 279 289.

44 Q. Yao, Z.-H. Lu, K. Yang, X. Chen and M. Zhu, *Sci. Rep.* 2015, **5**, 15186.

45 M. Kim, J. F. Cahill, H. H. Fei, K. A. Prather and S. M. Cohen, *J. Am. Chem. Soc.*, 2012, **134**, 18082 18088.

46 H. G. T. Nguyen, N. M. Schweitzer, C. Y. Chang, T. L. Drake, M. C. So, P. C. Stair, O. K. Farha, J. T. Hupp and S. T. Nguyen, *ACS Catal.*, 2014, **4**, 2496 2500.

47 D. Yang, S. O. Odoh, T. C. Wang, O. K. Farha, J. T. Hupp, C. J. Cramer, L. Gagliardi and B. C. Gates, *J. Am. Chem. Soc.*, 2015, **137**, 7391 7396.

48 J. D. Evans, C. J. Sumby and C. J. Doonan, *Chem. Soc. Rev.* 2014, **43**, 5933 5951.

49 Y. Cong, B. Li, S. Yue, D. Fan and X.-j. Wang, *J. Phys. Chem. C* 2009, **113**, 13974 13978.

50 S. Toemen, W. A. W. Abu Bakar and R. Ali, *J. CO2 Util.*, 2016, **13**, 38 49.

51 W. A. W. Abu Bakar, R. Ali and S. Toemen, *J. Nat. Gas Chem.* 2011, **20**, 585 594.

52 W. A. W. Abu Bakar, R. Ali and S. Toemen, *Sci. Iran.*, 2012, **19** 525 534.

Journal Name

COMMUNICATION

In situ MOF-templating route to Ru/CeO_2 catalysts for NH_3 synthesis

R. Lippi,[a,b] S. C. Howard,[a] C. J. Sumby,[b] C. J. Doonan,*[b] D. F. Kennedy*[a]

Received 00th January 20xx,
Accepted 00th January 20xx

DOI: 10.1039/x0xx00000x

www.rsc.org/

A Ru-impregnated Ce-based MOF was used as a sacrificial template for the preparation of an NH_3 synthesis catalyst. Formation under reaction conditions gave a catalyst with remarkable performance in comparison to benchmark catalysts. The MOF-templating route was found to provide excellent control over the size and distribution of both the metal oxide support and the active metal components.

Ammonia (NH_3) synthesis via the Haber-Bosch process is widely applied in industry for the production of artificial fertilizers.[1] This process involves the reaction of N_2 and H_2 over heterogeneous catalysts. The reaction is endothermic and equilibrium controlled, thus high pressures and temperatures are necessary to shift the equilibrium towards NH_3 production.[2] For example, Fe-based catalysts are typically employed in industry under operating conditions of 500 °C and 200 bar.[1b] This energy intensive process is estimated to consume 2% of energy produced globally.[3] As a result, decreasing the energy requirements for the large scale production of NH_3 is an on-going challenge[4] To this end, supported Ru nanoparticles have been explored as an alternative to Fe based catalysts as they show higher reactivity at significantly lower pressures.[5] However, stability, availability and cost have discouraged their commercial use.[4a, 6] Fundamental studies have shown that the efficiency of Ru catalysts is structure dependent.[6] Therefore, synthesis methods that offer control over the final catalyst structure may help to maximise the production of ammonia per unit mass of Ru.[6] [7] Additonally, the composition of the catalyst support material is also critical to the efficiency of the reaction. Although the support materials do not present significant catalytic activity alone, their physicochemical properties do influence the activity of catalytic systems[5, 8] Support materials commonly used include: carbon, MgO_2, Al_2O_3, and CeO_2.[8] [9] Of these, CeO_2 is reported to be an effective support material for Ru based catalysts,[9a] as the presence of the reversible redox pair Ce^{4+}/Ce^{3+} can increase the electron density on Ru^0 and facilitate N_2 activation.[9a, 10]

The synthetic approach used to generate heterogeneous catalysts can have a significant effect on their performance, especially with respect to the morphologies and surface chemistry of Ru and CeO_2.[7b, 11] For example, nanoparticles with a high number of reactive surface sites are desired in heterogeneous catalysts.[7a] However, synthesising nanoparticles of specific size and distribution on the support can be challenging, as they tend to aggregate and sinter under operating conditions. Iwamoto *et al.* have demonstrated preparation of Ru/MgO catalysts via sol gel methods, where both the support and the active metal were synthesised simultaneously. This approach led to a homogeneous distribution of Ru on the support and high NH_3 production rates.[12]

Metal-organic Frameworks (MOFs) are hybrid materials composed of inorganic nodes connected by organic linkers.[13] The wide variety of organic and inorganic building units gives rise to an expansive number of possible structures that possess diverse chemical functionality and physical properties.[14] MOFs have been widely explored as porous catalysts,[15] however; recent reports have described the advantage of using the tailored structures of MOFs as templates for functional materials including novel catalysts.[16] In the examples reported, the MOF template engendered specific elemental distributions and structures that could not be obtained by other synthetic approaches. Furthermore, the templating method led to enhanced catalytic performance.[17]

Previously, we have described the application of MOF templating for the production of a highly active Ru/ZrO_2 nanostructured catalyst for CO_2 methanation.[17a] The high activity was attributed to the homogeneous distribution of size

---

[a] *CSIRO Manufacturing, Clayton, Victoria 3168, Australia.*
E mail: danielle.kennedy@csiro.au
[b] *Centre for Advanced Nanomaterials and Department of Chemistry, The University of Adelaide, Adelaide, South Australia 5005, Australia.*
E mail: christian.doonan@adelaide.edu.au

Electronic Supplementary Information (ESI) available: Experimental details for materials synthesis, catalysis testing and characterization techniques. See DOI: 10.1039/x0xx00000x controlled Ru nanoparticles on the nanostructured ZrO_2 support. Here, we report a MOF templating route for the synthesis of a highly active Ru/CeO_2 catalyst for NH_3 synthesis. The templated catalyst was compared to a series of controls, including a Ru based literature reported catalyst, a commercial Wustite catalyst (Amomax-10), other MOF-derived catalysts, and samples of analogous chemical composition synthesised by other methods. The Cerium-based MOF, Ce-UiO-66, which is structurally analogous to UiO-66[18] was employed as the template to afford a CeO_2 support and $RuCl_3$ was introduced into the pores of the MOF via Impregnation to provide the active catalyst (Fig. 1).

Comparing the performance of literature reported catalysts is challenging as the test conditions used are variable (e.g. gas velocity, catalyst mass, reactor design). Furthermore, different methods of analysis (e.g. gas chromatography, titration) can be employed. To overcome this issue, we selected a commercially available benchmark NH_3 synthesis catalyst Wustite (FeO) (Amomax-10, Sud Chemie) and synthesised, the well known, highly active low pressure Ru based catalyst developed by Aika *et al*.[8] for intitial screening studies Using a multi-channel catalysis rig,[17a] we were able to test these samples under the same conditions as the MOF templated catalysts and controls reported in this study.

The initial catalyst screening included a fresh sample of **1%Ru/Ce-UiO-66**, catalysts derived from **1%Ru/UiO-66** and **2%Ru/UiO 66** templated previously, and Amomax 10 (Fig. 2A) All catalysts were subjected to the activation conditions required for Amomax-10 (pure H_2 flow, at 475 °C and 1 bar). After this activation procedure all the catalysts displayed stable conversion for approximately 30 hours under reaction conditions (H_2, 1.875 mL/min; N_2, 0.625 mL/min; Ar, 0.417 mL/min; at 475 °C and 160 bar). Amomax 10 showed the highest NH_3 production per unit of catalyst mass, however; among the MOF derived catalysts, the Ce-based catalyst significantly outperformed its Zr analogues. The lower performance of Ru/ZrO_2 compared to Ru/CeO_2 is in agreement with previous reports, which describe the negative impact that the acidic nature of ZrO_2 has on ammonia synthesis.[19] On the other hand, a basic support will assist the reaction by donating electrons to Ru.[19]

High temperatures and pressures are necessary to ensure high activity for Amomax 10. Thus if, Ru based catalysts operate at milder conditions, they may offer an energetic advantage for NH_3 production. Accordingly, a systematic comparison of the Ru-based samples was performed at lower temperatures and pressures. In these experiments, a low pressure benchmark catalyst reported by Aika *et al*., that is composed of of Ru supported on MgO and promoted with Cs (**2%Ru Cs/MgO**), was included.[8] A series of $RuCl_3$-impregnated Ce-UiO-66 samples with different Ru loadings were prepared: varying from 0.25 to 2 wt% Ru/Ce UiO-66. Furthermore, a series samples composed of $RuCl_3$ impregnated directly on pre made cubic CeO_2 (10 nm) were prepared with loadings of 0.5, 1, 1.5 and 2% Ru/CeO_2.

At temperatures lower than or equal to 350 °C and pressures of 10, 30, and 50 bar we did not detect ammonia production, even for the benchmark catalyst. However, the previous report by Aika *et al*. indicated that the **2%Ru-Cs/MgO** catalyst does display activity under these conditions.[8] We posit that variances in NH_3 detection range among effluent analysis techniques used may explain this discrepancy.

When the reaction temperature was elevated to 400°C the Ru/Ce-UiO 66 templated catalyst displayed remarkable activity (Fig. 2B). The most active MOF-templated catalyst was derived

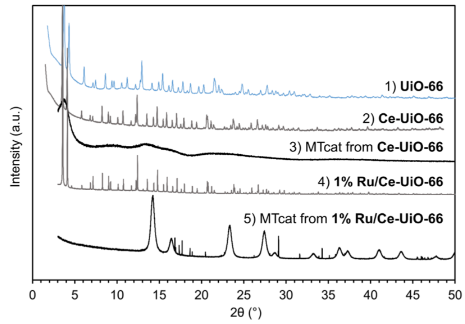

Fig. 1: PXRD patterns of 1) UiO 66; 2) Ce UiO 66; 3) MOF templated catalyst (MTcat) derived from Ce-UiO 66; 4) 1% Ru/Ce UiO 66; and 5) active catalyst, MTcat derived from 1% Ru/Ce UiO 66. The crystalline structure of the MOF is clearly observed in is the patterns 1, 2, and 4. MTcat testing from Ce UiO 66 generated an amorphous phase (3). In contrast, 1%Ru/Ce UiO-66 templated an active catalyst composed mostly of cubic CeO_2 (5), the broad peaks are a result of the small crystallite size formed. The sharp peaks are from highly crystalline SiC used as catalyst diluent (Fig. S6).

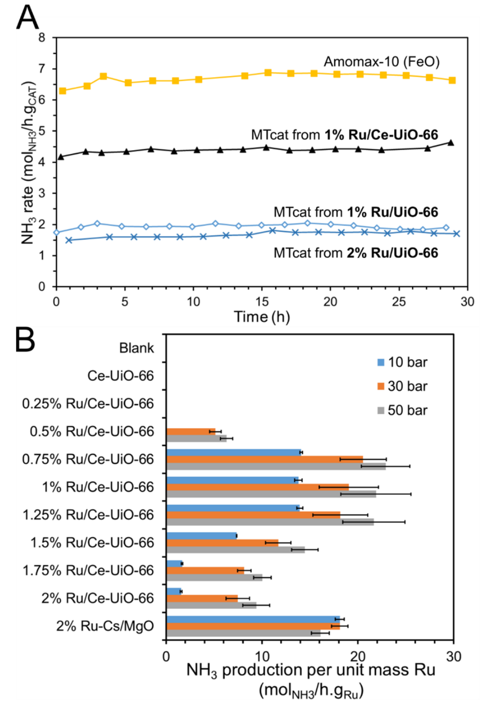

Fig. 2: A) Catalytic performance of FeO and MOF templated catalysts (MTcat) at 475 °C and 160 bar. B) NH3 production per unit mass of Ru during catalyst testing at 400 °C with variable pressure. $RuCl_3$ was impregnated onto Ce UiO 66 at different loadings as indicated. The chart indicated the performance of the catalyst derived from these precursors. 2% Ru Cs/MgO catalyst was prepared according to Aika *et al* Error bars show standard deviation of the 3 measurements

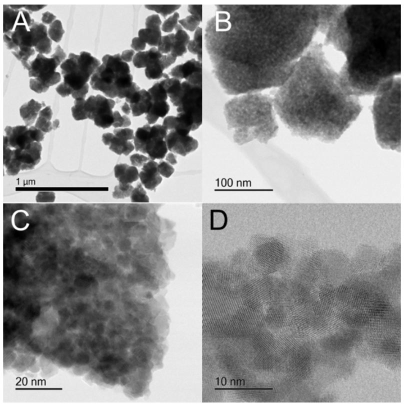

Fig. 3: A D) High resolution TEM of the catalyst templated by 1%Ru/Ce UiO 66 at different magnifications. It is possible to observe that the catalyst is composed of clusters of nanoparticles (A and B). Within these clusters, nanocrystals can be observed (C and D).

from **0.75% Ru/Ce-UiO-66**, producing 14, 20.5 and 22.9 $mol_{NH3}/h.g_{Ru}$ at 10, 30 and 50 bar, repsectively. It is noteworthy, that at 30 and 50 bar the MOF derived catalyst outperformed the benchmark **2% Ru-Cs/MgO**, which generates 18.1, 18.1 and 16.1 $mol_{NH3}/h.g_{Ru}$ at 10, 30 and 50 bar, respectively. Additionally, the family of MOF templated catalysts also display increasing conversion at higher pressures, indeed the error bars in Fig. 2B obscure an increasing conversion with time (Figure S5), whereas the conversion by the **2% Ru-Cs/MgO** catalyst was not affected by the pressure increase, in agreement with previous reports.[20] It is noteworthy that at 30 and 50 bar MOF templated catalysts composed of of **0.75**, **1** and **1.25% Ru/Ce-UiO-66** outperformed the positive control **2% Ru-Cs/MgO**. The catalysts prepared via direct impregnation of $RuCl_3$ on pre-made CeO_2 did not produce detectable amounts of NH_3 at any of the tested conditions. The use of metal precursors that contain Cl are usually avoided in the synthesis of NH_3 catalysts as Cl is known to have a poisoning effect,[21] although there is no consensus on the poisoning mechanism by Cl atoms. Notably, the presence of Cl in the precatalysts $RuCl_3$/Ce UiO 66 did not inhibit catalytic activity of the derived catalysts.

The structure of the Ce MOF templated catalyst was studied by powder X-ray diffraction (PXRD), transmission electron microscopy (TEM), energy dispersive spectroscopy (EDS) and electron diffraction to determine the chemistry underpinning its efficacy. The MOF templated catalyst (MTcat) from **1% Ru/Ce-UIO-66** was analysed using synchrotron X-ray powder diffraction to obtain high resolution diffractograms (Fig. 1). The peak positions and broadness suggest that the catalyst is composed of nano sized cubic CeO_2.[22] The integral breadth apparent size (Lvol-IB) is used in XRD to estimate crystallite domain sizes, although actual crystallite sizes will depend on the morphology of the particle.[23] For the templated catalyst, the Lvol IB for cubic CeO_2 was 6 nm. No reflections corresponding to a Ru phase were observed in the synchrotron source diffractograms which is consistent with our previous studies on the MOF templating of a Ru/ZrO_2 catalyst.[17a] We attribute the absence of Ru peaks to its low loading on the support and to the small size of the nanoparticles. Nevertheless, diffraction studies indicate that Ru is crucial to directing the structure of the catalyst. For example, neat **Ce-UiO-66** processed under analogous conditions gave rise to an amorphous phase rather than nanostructured CeO_2.

TEM performed on the active catalyst was in agreement with the PXRD analysis, indicating the presence of CeO_2 nanocrystals in the rage of 4-6 nm (Fig. 3 and S7). These crystals were found to agglomerate into large clusters approximately 130 170 nm in size. It is noteworthy that these clusters are similar in size to the apparent crystallite size (Lvol IB) of 200 nm for the parent MOF, Ce-UiO-66. This suggests that CeO_2 nanoparticle clusters are formed directly from the collapse of the MOF crystals. In agreement with our previous observations,[17a] on the MOF templating of Ru/ZrO_2.

Due to the high electron density of Ce, Ru cannot be clearly distinguished using TEM. Thus, in order to evaluate the distribution of Ru NPs in the catalyst we employed electron dispersive X ray spectroscopy (EDS) (Fig. 4). The EDS maps indicated the Ru nanoparticles are evenly distributed throughout the CeO_2 nanoparticles (Fig. 4). Additionally, the Ru NPs were approximately 2 nm in size, significantly smaller than the CeO_2 support. Electron diffraction identified hexagonal close-packed Ru^0 (Fig. S9) and no evidence of RuO_2 phases even after storage in air. These results confirm that the bulk of the Ru^0 nanoparticles may be stabilised on the CeO_2 support by intimate integration with the CeO_2 nanocrystals.

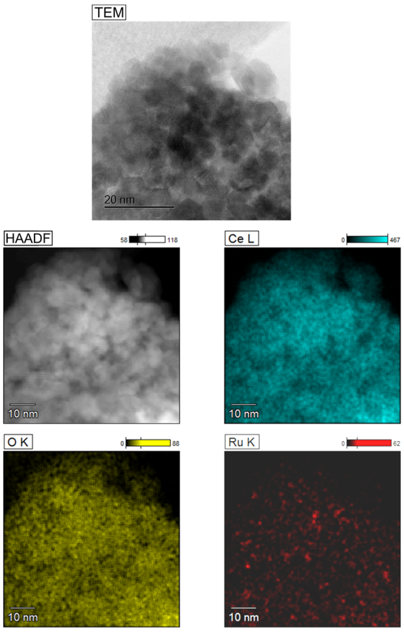

Fig. 4: TEM, HAADF (high angle annular dark field) and EDS (Energy dispersive spectroscopy) mapping for the MOF templated catalyst derived from 1%Ru/Ce UiO 66. The elemental maps show small clusters of Ru (less than 2 nm) evenly dispersed on the CeO_2 For clarification, contrast was improved on Ru map.

We attribute the high activity of the MOF templated catalyst to its unique composite nanostructure. For example, CeO_2 is considered an efficient support due to its facile redox activity (Ce^{4+}/Ce^{3+}), with the presence of this redox pair is believed to modulate the electron density on the surface of Ru nanoparticles and improve the activation of N_2[7b, 24] The small size of the templated CeO_2 crystals may be key to allow a higher amount of Ce^{4+} to be reduced and the consequent creation of surface O vacancies These results are in agreement with other recent reports on MOF-templated CeO_2 based oxidation catalysts, which also demonstrated the successful synthesis of smaller CeO_2 particles and a significant increase in the overall catalytic activity[17d, e] Furthermore, it is known that for Ru based catalysts, the presence of B_5-type sites on Ru^0 nanoparticles may facilitate ammonia synthesis.[7a] These sites are typically found on the edges of crystals, and the proportion of B_5 type sites per mass of Ru is known to be higher for Ru^0 nanoparticles in the range of 2 to 2.5 nm[6, 25] We conclude that the high activity of the **Ru/Ce UIO 66** derived catalyst can be attributed to the homogeneous dispersion of such Ru NPs on the CeO_2 support.

In summary, we employed a Ru-impregnated Ce-MOF (**x% Ru/Ce UiO 66**) as a template for an NH_3 synthesis catalyst. Compared to the control catalyst, **2% Ru-Cs/MgO** at 50 bar, the MOF templated catalysts, **0.75% Ru/Ce UiO 66** and **1% Ru/Ce-UiO-66,** showed 42% and 36% higher activity per mass of Ru, respectively. We note that this high performance is the result of the unique catalyst structure that can only be achieved via the MOF templating route. We employed diffraction and microscopy to elucidate the catalyst structure and found that it was composed of small Ru^0 nanoparticles (~2 nm) homogeneously distributed on CeO_2 nanoparticles 4 to 6 nm in size. In summary, this work exemplifies how the MOF templating route can be applied to synthesis of highly active catalysts.

Aspects of this research were undertaken on the Powder Diffraction beamline at the Australian Synchrotron, Victoria, Australia. This work was supported by CSIRO and The University of Adelaide. R. Lippi acknowledges The University of Adelaide for the Beacon of Enlightenment Ph.D. Scholarship. The authors acknowledge Ruth Fischer for synthesising the positive control.

Conflicts of interest

There are no conflicts to declare

Notes and references

1 a) V. Smil, *Nature*, 1999, **400**, 415 415; b) T. Kandemir, M. E. Schuster, A. Senyshyn, M. Behrens and R. Schlogl, *Angew. Chem. Int. Ed.*, 2013, **52**, 12723–12726.

2 A. T. Larson, *J. Am. Chem. Soc.*, 1924, **45**, 367 372.

3 P. H. Pfromm, *J. Renew. Sustain. Energy*, 2017, **9**.

4 a) N. Saadatjou, A. Jafari and S. Sahebdelfar, *Chem. Eng. Commun.*, 2015, **202**, 420 448; b) M. A. Shipman and M. D. Symes, *Catal. Today*, 2017, **286**, 57 68.

5 M. Muhler, F. Rosowski, O. Hinrichsen, A. Hornung and G. Ertl, *Stud. Surf. Sci. Catal.*, 1996, **101**, 317 326.

6 C. J. H. Jacobsen, S. Dahl, P. L. Hansen, E. Törnqvist, L. Jensen, H. Topsøe, D. V. Prip, P. B. Møenshaug and I. Chorkendorff, *J. Mol. Catal. A: Chem.*, 2000, **163**, 19 26.

7 a) S. Dahl, A. Logadottir, R. C. Egeberg, J. H. Larsen, I. Chorkendorff, E. Törnqvist and J. K. Nørskov, *Phys. Rev. Lett.*, 1999, **83**, 1814 1817; b) Z. Ma, S. Zhao, X. Pei, X. Xiong and B. Hu, *Catal. Sci. Technol.*, 2017, **7**, 191 199.

8 K. i. Aika, T. Takano and S. Murata, *J. Catal.*, 1992, **136**, 126 140.

9 a) Y. Niwa and K. i. Aika, *J. Catal.*, 1996, **162**, 138–142; b) L. Forni, D. Molinari, I. Rossetti and N. Pernicone, *Appl. Catal., A*, 1999, **185**, 269 275.

10 a) Z. Ma, X. Xiong, C. Song, B. Hu and W. Zhang, *RSC Adv.*, 2016, **6**, 51106 51110; b) C. T. Campbell and C. H. F. Peden, *Science*, 2005, **309**, 713–714.

11 a) Z. Song, T. Cai, J. C. Hanson, J. A. Rodriguez and J. Hrbek, *J. Am. Chem. Soc.*, 2004, **126**, 8576 8584; b) C. Fernández, C. Sassoye, D. P. Debecker, C. Sanchez and P. Ruiz, *Appl. Catal., A*, 2014, **474**, 194 202.

12 J. Iwamoto, M. Itoh, Y. Kajita, M. Saito and K. i. Machida, *Catal. Commun.*, 2007, **8**, 941–944.

13 H. Furukawa, K. E. Cordova, M. O'Keeffe and O. M. Yaghi, *Science*, 2013, **341**, 1230444.

14 Y. G. Chung, J. Camp, M. Haranczyk, B. J. Sikora, W. Bury, V. Krungleviciute, T. Yildirim, O. K. Farha, D. S. Sholl and R. Q. Snurr, *Chem. Mater.*, 2014, **26**, 6185 6192.

15 a) W. M. Bloch, A. Burgun, C. J. Coghlan, R. Lee, M. L. Coote, C. J. Doonan and C. J. Sumby, *Nat. Chem.*, 2014, **6**, 906 912; b) H. G. T. Nguyen, N. M. Schweitzer, C. Y. Chang, T. L. Drake, M. C. So, P. C. Stair, O. K. Farha, J. T. Hupp and S. T. Nguyen, *ACS Catal.*, 2014, **4**, 2496 2500; c) A. Burgun, C. J. Coghlan, D. M. Huang, W. Chen, S. Horike, S. Kitagawa, J. F. Alvino, G. F. Metha, C. J. Sumby and C. J. Doonan, *Angew. Chem. Int. Ed.*, 2017, **56**, 8412 8416.

16 a) Y. Song, X. Li, L. Sun and L. Wang, *RSC Adv.*, 2015, **5**, 7267–7279; b) L. Zhang, H. B. Wu and X. W. Lou, *J. Am. Chem. Soc.*, 2013, **135**, 10664 10672; c) S. N. Zhao, X. Z. Song, S. Y. Song and H. j. Zhang, *Coord. Chem. Rev.*, 2017, **337**, 80 96; d) L. Oar Arteta, T. Wezendonk, X. Sun, F. Kapteijn and J. Gascon, *Mater. Chem. Front.*, 2017, **1**, 1709 1745.

17 a) R. Lippi, S. C. Howard, H. Barron, C. D. Easton, I. C. Madsen, L. J. Waddington, C. Vogt, M. R. Hill, C. J. Sumby, C. J. Doonan and D. F. Kennedy, *J. Mater. Chem. A*, 2017, **5**, 12990 12997; b) V. P. Santos, T. A. Wezendonk, J. J. D. Jaen, A. I. Dugulan, M. A. Nasalevich, H. U. Islam, A. Chojecki, S. Sartipi, X. Sun, A. A. Hakeem, A. C. J. Koeken, M. Ruitenbeek, T. Davidian, G. R. Meima, G. Sankar, F. Kapteijn, M. Makkee and J. Gascon, *Nat. Commun.*, 2015, **6**, 6451; c) P. Wang, J. Feng, Y. Zhao, S. Wang and J. Liu, *ACS Appl. Mater. Interfaces*, 2016, **8**, 23755–23762; d) C. W. Abney, J. T. Patterson, J. C. Gilhula, L. Wang, D. K. Hensley, J. Chen, G. S. Foo, Z. Wu and S. Dai, *J. Mater. Chem. A*, 2017, **5**, 13565 13572; e) H. Wang, M. Liu, S. Guo, Y. Wang, X. Han and Y. Bai, *Mol. Catal.*, 2017, **436**, 120 127.

18 M. Lammert, M. T. Wharmby, S. Smolders, B. Bueken, A. Lieb, K. A. Lomachenko, D. D. Vos and N. Stock, *Chem. Commun.*, 2015, **51**, 12578 12581.

19 Z. q. Wang, Y. c. Ma and J. x. Lin, *J. Mol. Catal. A: Chem.*, 2013, **378**, 307 313.

20 F. Rosowski, A. Hornung, O. Hinrichsen, D. Herein, M. Muhler and G. Ertl, *Appl. Catal., A*, 1997, **151**, 443 460.

21 B. Lin, R. Wang, J. Lin, J. Ni and K. Wei, *Catal. Commun.*, 2011, **12**, 1452 1457.

22 P. Scherrer, *Nachr. Ges. Wiss. Gottingen, Math. Phys. Kl.*, 1918, **1918**, 98–100.

23 J. I. Langford, D. Louer and P. Scardi, *J. Appl. Crystallogr.*, 2000, **33**, 964 974.

24 L. Zhang, J. Lin, J. Ni, R. Wang and K. Wei, *Catal. Commun.*, 2011, **15**, 23 26.

25 K. Honkala, A. Hellman, I. N. Remediakis, A. Logadottir, A. Carlsson, S. Dahl, C. H. Christensen and J. K. Nørskov, *Science*, 2005, **307**, 555 558.